Dépôt chimique (CVD/ALD) assisté par plasma et intégration de Ti(Al)N et Ta(Al)N pour les métaux de grille sub-20nm

Fabien Piallat

UNIVERSITÉ DE GRENOBLE

THESIS

In order to get the grade of

DOCTOR OF GRENOBLE UNIVERSITY

Speciality: **Micro and Nano Electronics**

Ministerial order: 7 Août 2006

Presented by

Fabien Piallat

Thesis directed by **Christophe Vallée**
and co-directed by **Remy Gassilloud and Pierre Caubet**

prepared at **Laboratoire d'Electronique et des Technologies de l'Information (LETI) du CEA Grenoble**
in the **Ecole Doctorale *Electronique, Electrotechnique, Automatisme & Traitement du Signal***

Plasma assisted chemical deposition (CVD/ALD) and integration of Ti(Al)N and Ta(Al)N for sub-20 nm metal gate

Thesis publicly defended the **4th of June 2014**,
in front of the jury composed by:

Elisabeth Blanquet
SIMAP, St Martin d'Hères, Examinator
Olivier Thomas
IM2NP, Marseille, Examinator
Agnès Granier
IMN, Nantes, Reporter
Brice Gautier
INL, Lyon, Reporter
Christophe Vallée
CNRS-LTM, Grenoble, Thesis Director
Remy Gassilloud
CEA-Leti Minatec, Grenoble, Thesis Supervisor
Pierre Caubet
STMicroelectronics, Crolles, Thesis Co-Supervisor

"There is no hard work, only badly trained workers and unadapted tools."

Someone who never undertook to write a thesis work.

Acknowledgements

Je tiens à remercier humblement tous ceux et toutes celles qui de près ou de loin, m'ont permis de mener à bien cette étude. Je suis intimement persuadé qu'ils se reconnaîtront sans qu'il soit nécessaire de se livrer au traditionnel exercice de style que sont "les remerciements"...

Et j'ajouterais une pensée toute particulière à ceux dont j'aurais pu oublier le nom.

Contents

Abbreviations

ALD	**A**tomic **L**ayer **D**eposition
AR-XPS	**A**ngle **R**esolved - **XPS**
a.u.	**a**rbritary **u**nit
C-V	**C**apacity - **V**oltage
CCP	**C**apacitively **C**oupled **P**lasma
CVD	**C**hemical **V**apor **D**eposition
DF	**D**ual **F**requency Plasma
EOT	**E**quivalent **O**xide **T**hickness
FWHM	**F**ull **W**idth at **H**alf **M**aximum
HKMG	**H**igh-κ **M**etal **G**ate
LF	**L**ow **F**requency Plasma
I-V	**C**urrent - **V**oltage
IC	**I**ntegrated **C**ircuit
ITRS	**I**nternational **T**echnology **R**oadmap for **S**emiconductors
MOCVD	**M**etal **O**rganic **CVD**
OES	**O**ptical **E**mission **S**pectroscopy
PEALD	**P**lasma **E**nhanced **ALD**
PEMOCVD	**P**lasma **E**nhanced **MOCVD**
$\mathbf{R^2}$	Square **R**esistivity
RF	**R**adio **F**requency Plasma
sccm	**s**tandard **c**ubic **c**entimeter per **m**inute
SEM	**S**canning **E**lectron **M**icroscopy
Ta(C)N	**Ta**ntalum(**C**arbo)**N**itride
TBTDET	**T**ertiary-**B**utylimido**T**ris(**D**i**E**thylamino)**T**antalum
TDEAT	**T**etrakis(**D**i**E**thyl**A**mido)**T**itanium
TEM	**T**ransmission **E**lectron **M**icroscopy
Ti(C)N	**Ti**tanium(**C**arbo)**N**itride
TMA	**T**ri**M**ethyl**A**luminium
UHV	**U**ltra **H**igh **V**acuum
XPS	**X**-Ray **P**hotoelectron **S**pectroscopy
XRD	**X** - **R**ay **D**iffraction
XRR	**X** - **R**ay **R**eflection

Chapter 1

MOSFET transistors: technological challenges

"We're so accustomed to the marvels of everyday thought that we never wonder about it."
Marvin Minsky, scientist

1.1 Microelectronic and improvements

Over the past few decades, semiconductor industry has witnessed dramatic rise in the performance of integrated circuits and in the subsequent financial market growth. Performance improvement at lower cost in microelectronic integrated circuits (ICs) has been achieved by increasing transistor speed, reducing transistor size and packing more transistors onto a single chip.
This trend was first foreseen by Intel co-founder Gordon Moore, who, in his article in the year 1965 observed that the number of components in integrated circuits has doubled every year from the invention of the integrated circuit in 1958, by Jack Kilby (Nobel prize in 2000) [1], until 1965. G. Moore predicted that this trend would continue "for at least ten years" [2]. From the beginning of mass production, the number of transistors that the industry was able to place on a computer chip did double every two years (figure 1.1) [3]. This prediction, now known as the Moore's law, is responsible for the evolution of today's complementary metal-oxide-semiconductor (CMOS) technology. Recognition of this observation has proven to be accurate, in part because the law is now used in the semiconductor industry to guide long-term planning and to set targets for research and development, resulting in the auto-fulfilling of the hypothesis made by G. Moore. Thus, the transistor has shrunk from the size of a pencil eraser to smaller than a bacterium for the latest generation.

Transistor has become the workhorse component of almost every electronic device after it was invented by John Bardeen, Walter Brattain and independently by William Schokley at the Bell Laboratories in 1947. They shared a Nobel Prize in 1956 for their classic discovery of point-contact transistors and bipolar transistors [4].
The salient feature of transistors which fuels the rapid growth of the information technology industry is the incredible increase in their speed and drop in cost per component as their

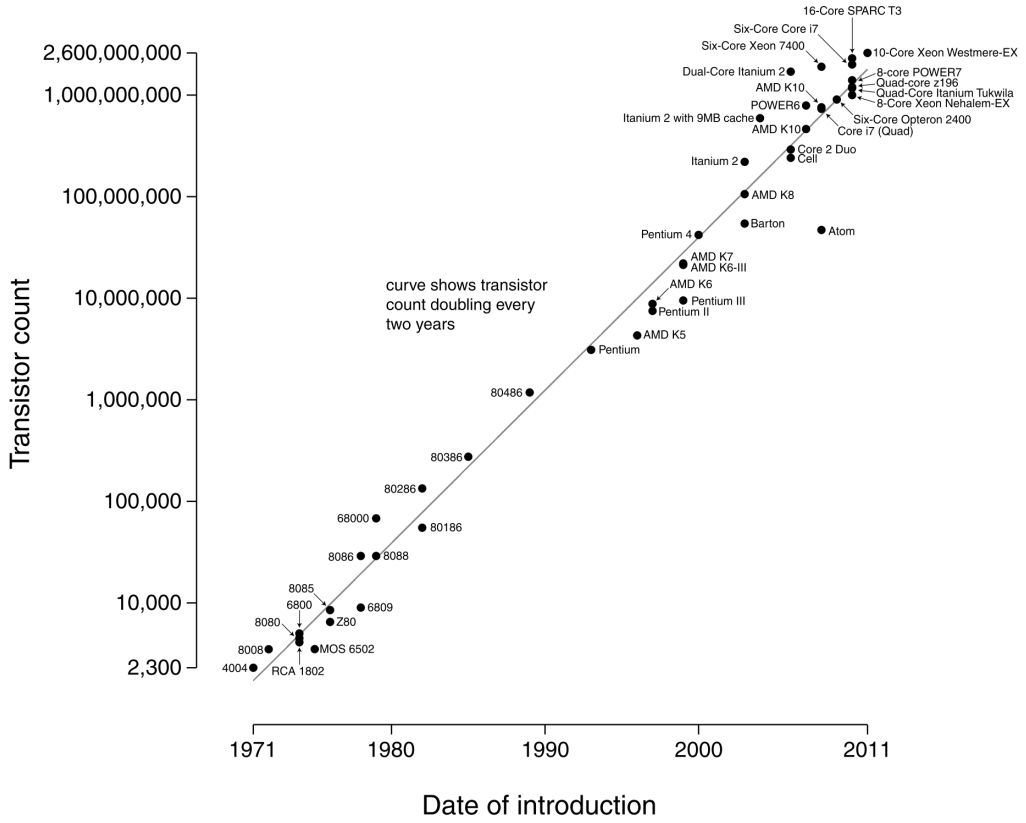

FIGURE 1.1: *Evolution of the number of transistors placed on a chip*

size is reduced.

In simple terms, a transistor can be described as a three terminal semiconductor device in which the input signal controls the output current and which performs the functions of switching and amplifying. Use of transistor is extended in areas like amplifying low frequency radio signals, analog to digital signal transformation and *vice versa*, high speed computers, etc. Increase in the processor performance results not only from increase in the transistor density but also from the improvement in the transistor functionality. Transistor can be improved both through materials and architecture changes. Based on design and operating behaviour, transistors are classified into two major types: bipolar junction transistor and Field-Effect Transistor (FET) [5], presented in figure 1.2 left and right respectively.
In the 1960s, the IC market was broadly based on bipolar transistors due to their high switching speed and low power consumption at smaller sizes. But since 1975, integration of FETs prevailed even though they were found to be slower switching devices than the bipolar transistors [6]. This was caused by the failure of bipolar transistors to demonstrate rapid decrease in the power per circuit compared to FETs. As linear dimensions reached the half-micron level in the early 1990s, the performance advantage of bipolar transistor was outweighed by FET (more specifically MOSFET, a modern and more practical variant of FET), then used in the CMOS circuit production till today.

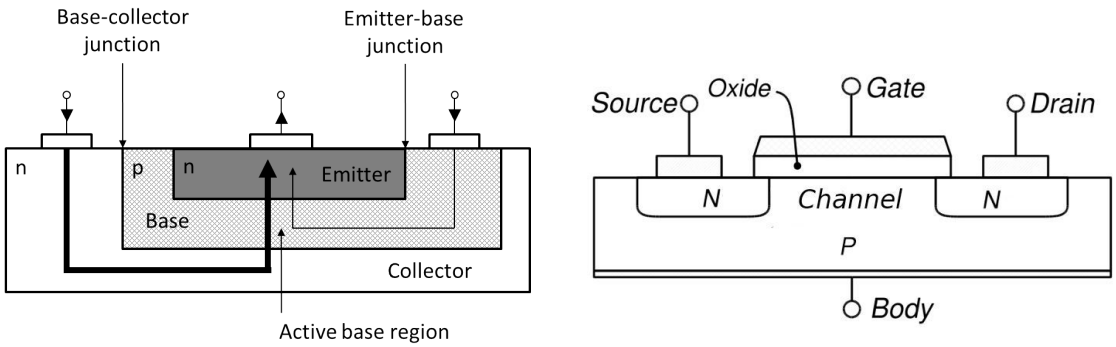

FIGURE 1.2: *Bipolar (left) and MOSFET (right) transistors schemas*

The choice of FET over bipolar was also comforted by:

a. the ease of scaling. Whereas the drain current of bipolar devices has an exponential dependence on base-emitter voltage, the MOSFET drain current depends on the ratio of its geometry (width/length). Thus, the MOSFET characteristics remain the same as far as the W/L is kept same; necessarily leading to easier scaling down of the device.
b. the lower power. CMOS logic consumes less power compared to bipolar. This is due to the fact that complementary logic in MOS gives zero static power dissipation, which is not the case for bipolar junction.
c. the ease of production. MOSFET fabrication is easier because bipolar junction requires complex processes which includes buried layer.

Improvements can be applied to different aspects of the devices for ever competitive devices. First one coming into mind is the scaling, i.e. the size reduction of the structures. Then architecture is adapted to the new thickness before the development of new materials. These three points are investigated in next sections of this chapter.

1.1.1 MOSFET: fundamental device in the CMOS technology

Metal-oxide-semiconductor FET (MOSFET) is essentially a metal-insulator-semiconductor junction provided with a source and a drain, as shown in figure 1.2. In a MOSFET structure, a dielectric material (mainly silicon dioxide, SiO_2) is used as the insulation layer, called a gate oxide, which is placed between the gate electrode and the semiconductor, called channel, made of silicon in the crystalline state. The diagram, in figure 1.3, makes easier the understanding of MOSFET operating, assuming that the substrate is a p-type semiconductor which has positively charged mobile holes as carriers, and that the source and drain are made of doped n-type (denoted by n^+) material, as presented in figure 1.3a. When a positive voltage is applied on the gate (V_g), figure 1.3b, an electric field causes the holes to be repelled from the interface, creating a depletion region containing immobile negatively charged acceptor ions. A further increase in the gate voltage above the threshold voltage (V_{th}), figure 1.3c, eventually causes electrons to appear at the interface, in what is called an inversion layer, or channel. Electrons can now move from the source to the drain in the

inversion layer (n-MOS).

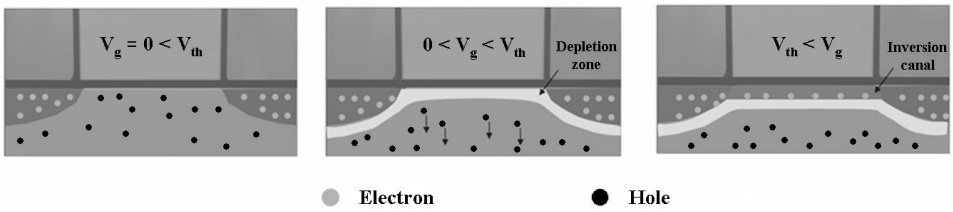

FIGURE 1.3: *CMOS working conditions schema, a: off conditions, b: depletion condition, c: inversion canal creation condition*

FETs evolved from p-type MOSFETs (p-MOS) in the 1960s to n-type MOSFETs (n-MOS) in the 1970s and then to CMOS in the 1980s and 1990s. CMOS circuits combine both n-MOS and p-MOS in a way which greatly reduces consumption of power. Other architectures were proposed to replace CMOS but never made it to the production maturity.

1.1.2 Improved performance via scaling

'Scaling' is a practice term invented to describe reduction in the size of the device dimensions in order to fit more components on a single microchip. Calculated reduction of transistor geometries as well as the capacitor cell area in the IC has demonstrated spectacular expansion in the technology and communication markets [7]. The prime elements which enable the scaling of the Si-based MOSFET are the materials properties associated with the dielectric employed to isolate the transistor gate from silicon channel.
Early CMOS devices mainly consisted of thermally grown amorphous silicon dioxide as the gate dielectric which is the smallest feature of the device. SiO_2 layer has a major influence on the device electrical behaviour, it acts as a perfect insulator between the gate and the channel, thus preventing short circuits. As the transistor feature size is shrinking, the corresponding gate dielectric thickness is also decreasing rapidly. The problem associated with thinning of the oxide layer is its inability to store or to flow large amount of current in it, thus greater leakage current occurs through the dielectric layer. In an ideal situation, the gate dielectric acts as a perfect insulator, but as it is made ever thinner in order to improve the device performance, huge amounts of current leaks through it thereby resulting in higher power consumption, and turning the device cost ineffective. This problem became even more determining with the apparition of mobile devices which have limited power but need more and more calculation power.
At normal device operating condition, the typical leakage current of SiO_2 at a gate bias of 1 Volt, changes from 10^{-12} A.cm^{-2} at 35 Å to 1 A.cm^{-2} at gate oxide thickness of 15 Å. To avoid high leakage currents and still achieve the required gate capacitance, a material with higher permittivity is needed.
The formula equation 1.1 shows the device parameters that determine the resulting gate

capacitance (**C**):

$$C = \frac{\varepsilon \varepsilon_0 A}{t} \tag{1.1}$$

where ε is the dielectric constant (also referred to as the relative permittivity) of the material, ε_0 is the permittivity of free space (8.85x10^{-12} F.m^{-1}), A is the area of the capacitor and t is the thickness of the dielectric. To keep similar behaviour of the devices, C has to be kept constant, so as mentioned earlier, parameter A will be growing only smaller in the future semiconductor technologies if no change is made to the architecture of the transistor. Thus to keep C constant with a decreasing A, t can be decreased or ε be increased. However, if t is reduced the leakage current will grow, and from equation 1.1 it is apparent that the dielectric layer thickness t can be increased in order to avoid high leakage currents, only when a material with higher relative permittivity ε is used. These materials with higher relative permittivity are called high-κ materials and represent one of the main parameters investigated for new technology nodes.

In order to compare the dielectric layer of different materials, the use of the equivalent oxide thickness (EOT or t_{eq}) parameter was introduced. The term t_{eq} characterises the theoretical thickness of SiO_2 that would provide a particular capacitance density assuming standard dielectric constant of 3.9 (disregarding issues like leakage current and reliability). Therefore, equation 1.1 for capacitance can be rewritten in terms of t_{eq} and ε_{ox} (3.9, the dielectric constant of SiO_2) of the capacitor as follows:

$$\frac{t_{eq}}{\varepsilon_{ox}} = \frac{t_{high-\kappa}}{\varepsilon_{high-\kappa}} \tag{1.2}$$

or simply:

$$t_{eq} = \frac{\varepsilon_{SiO_2}}{\varepsilon_{high-\kappa}} t_{high-\kappa} = \frac{3.9}{\varepsilon_{high-\kappa}} t_{high-\kappa} \tag{1.3}$$

From equation 1.3, it appears that a gate oxide material having a dielectric constant of ~ 25 affords to have a physical thickness of ~ 64 Å to obtain t_{eq} of 10 Å.

In the real world some interactions happen between the dielectric and the substrate or metal. Thus the equation becomes:

$$EOT = t_{eq} = t_{SiO_2} + \sum_i \frac{3.9}{\varepsilon_i} t_{dielectric_i} \tag{1.4}$$

where t_{SiO_2} is the physical thickness of the SiO_2 interface layer, also referred to as IL, $t_{dielectric_i}$ is the physical thickness of the dielectric i, ε_i the dielectric constant of the film and the summation over *"i"* is for stacks that do not have an uniform profile or are made of several dielectrics.
To further reduce the EOT one could think that t_{SiO2} could be reduced or even removed from the device. However, nucleation of the dielectric is favoured by the presence of SiO_2 at the surface [8–10] and due to the deposition of a dielectric, which is an oxide, there is

generally creation of silicon oxide at the silicon/dielectric interface. The removal of SiO_2 also results in the degradation of mobility and reliability of the devices due to the direct contact of the high-κ with silicon. Still, if a Si wafer is cleaned before dielectric deposition, a natural oxidation of the wafer's extreme surface happens when in contact with the air. This oxidation, about 5-6 Å may continue to grow during device manufacturing. Thus, in order to control this SiO_2 IL and obtain a good quality oxide, with 3.9 dielectric constant and avoid any regrowth, a chemical oxide is formed at the surface of the sample, with a thickness stabilised around 7-8 Å.

It appears that today, the continuous scaling of microelectronic devices has reached more or less its limits with the known materials. New materials are needed to meet the requirements of the coming technologies. As introduced, high-dielectric constant materials have already partially replaced silicon dioxide together with metal-gates replacing polycrystalline silicon.

1.1.3 Improved performance via electrode tuning

If EOT and current leakage are mainly controlled by the dielectric properties, threshold voltage, work function and interfacial defects can be tuned by carefully choosing the material used for the electrode. For a long time, polycrystalline silicon was used for the creation of electrode due to the easiness of doping Si to obtain n-type or p-type material. In ultra-thin oxide systems, when EOT reaches less than 2 nm in thickness, the parasitic capacitance induced by poly gate depletion becomes a first order phenomenon. It leads to a capacitance in series with the gate oxide, which results in the increase of the EOT. One solution is to highly dope the polysilicon, but the ionised dopants and the parasitic charge density increase with increased doping. These parasitic gate charges act as charge centres in the gate and scatter the carriers in the channel thus degrading the device performance, an effect called Remote Coulomb Scattering (RCS). Since parasitic gate charge density should be decreased, a reduction of gate doping concentration is necessary. Thus, it is clear that the effects of polygate depletion and/or RCS are unavoidable in conventionally doped gate CMOS devices. To improve device performance, it appeared that the gate depletion must be completely eliminated. Hence metal gate provides a solution to eliminate poly gate depletion effect. Also, to ease integration and avoid interactions from superior metal layers deposition or reaction, metals with good chemical barrier properties have to be chosen. The gate in CMOS devices is generally of the same type as that of the source/drain, i.e. the NMOSFET has a n-gate and PMOSFET has a p-gate.
Some of the most extensively studied and most promising materials are titanium and tantalum alloys [11–13], in particular nitrides, thanks to their high thermal stability [14], low reactivity [15, 16], low electrical resistivity [11, 17, 18] and their wide range of work function [12, 14, 17, 19–21]. Moreover, creation of new alloys, based on these metals, can lead to the fine tuning of the work function. In particular, carbides or aluminium alloying can significantly shift the effective work function of the metal [22, 23].

Although much work has been done so far on the understanding of metals, more studies need to be conducted on the interactions taking place at the metal / dielectric interface. Moreover, materials deposited later on during the integration flow are equivalent to a low temperature annealing, and so can enhance the interactions and the damages created at the interface.

To ease the integration of new materials in the production chain, different architectures can be chosen to lower the process constraints.

1.1.4 Improved performance via architecture

If material tuning is one solution to allow a reduction of the devices size, changes in the architecture and flow is another. MOS transistors have been built, for many generations, using a gate-first approach. In this approach the metal forming the gate is deposited before the formation of the drain and source by implantation, and subsequent the high temperature anneal performed to activate the dopants in the Si substrate. This high temperature activation anneal can strongly impact the integrity of the dielectric/metal stack. Even if data on the effect of process temperature on work function are clear [24, 25], the advantage of the already existing work flow has kept focus on gate first approaches. However, given the need to reduce gate dielectric current leakage, to reduce the metal gate depletion and considering the interactions taking place at the metal/dielectric interface, the benefits of a lower thermal budget are immediate and integration of the high-κ/metal gate stack into the transistor flow is mandatory for new technology nodes. Such approach is referred to as the replacement gate process or gate-last flow (in opposition to gate-first), which enables decoupling of the junction formation from the dielectric/metal gate formation step. In this flow, a sacrificial poly gate is used and then removed after the junctions formation. Consequently, the gate dielectric and the metal gate are deposited after the high temperature anneal. A comparison of unique steps in metal gate-first and gate-last process flows is given table 1.1, with the key differences highlighted in bold. Because of its low thermal budget, the gate-last integration flow opens new possibility to carefully tune the work function and to provide devices with the desired threshold voltages.

The gate-last architecture was first introduced in mass production by Intel in 2007 for the 45 nm technology node [26].

A more complete description and comparison of Gate-First and Gate-Last approaches is presented Appendix A, page 171.
On top of these two approaches, a plethora of modifications to the gate first or gate last methodologies have been and continue to be discussed in the scientific literature.

Another way to improve the performance by architecture modification is the introduction of Silicon On Insulator (SOI) substrate. SOI substrates are layered silicon-insulator-silicon and

TABLE 1.1: *Comparison of Gate-First and Gate-Last flows*

Gate-First	**Gate-last**
Isolation	Isolation
High-κ gate deposition	High-κ gate deposition
Dual Metal-Gate deposition	**Sacrificial Poly-Silicon gate deposition/patterning**
Poly-Silicon gate deposition	Source/Drain formation
Poly-Silicon/metal etch	Salicide/Contact etch stop
Source/Drain formation	**Sacrificial Poly-Silicon gate removal**
Salicide/Contact etch stop	**Dual Metal-Gate deposition**
1^{st} Inter-Layer Dielectric deposition/polish	Contact formation
Contact formation	

replace the conventional silicon substrate: schematic description is given in figure 1.4. The benefits of SOI relative to conventional silicon includes: low parasitic capacitance due to the isolation from the bulk silicon, which improves power consumption at matched performance; and resistance to short-circuit due to complete isolation of the n- and p-well structures. SOI substrates can easily be integrated in the current technology without modifications of the process flow.

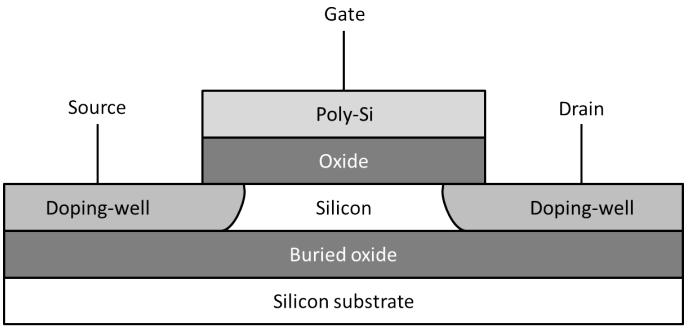

FIGURE 1.4: *SOI schema*

Introduction of 3D architecture, also called Tri-gate, in the last half-decade was investigated as a possible solution [27]. 3D transistors employ a single gate stacked on top of multiple vertical gates, as visible in figure 1.5, allowing to duplicate the surface area at which the electrons can travel. And as introduced in equation 1.1, increase of the transistor surface area allows to increase the gate capacitance. Reports showing that 3D transistors reduce leakage and consume far less power than current transistors have been made. This allows up to 37% higher speed, or a power consumption at under 50% of the previous type of planar transistor [28, 29]. Additional control over the gate enable as much transistor current flowing as possible when the transistor is in the 'on' state (for performance), and as close to zero as possible when it is in the 'off' state (to minimise power loss), and enable the transistor to switch very quickly between the two states (again, for performance).

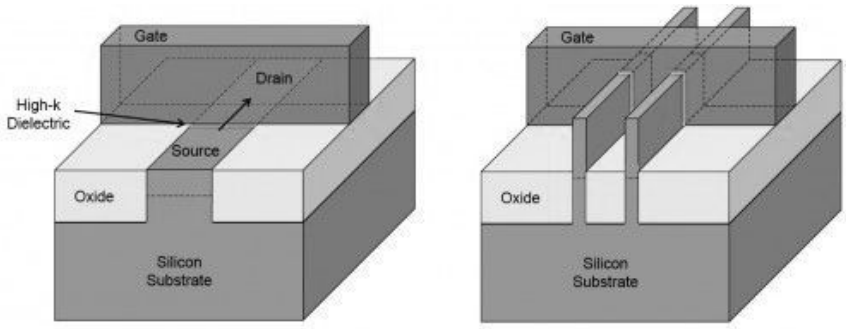

FIGURE 1.5: *Planar and 3D transistors schema*

This architecture has opened new opportunities but new difficulties also rose with it. One of the most challenging difficulty is the need of conformal and uniform deposition on all the surfaces of the structures with a layer as thin as one nanometre [30]. Conformal deposition leads to the need of a non-directive, non-preferential method, thus to surface reactant depositions. Depositions based on chemical principle are hence preferred to the physical one, with a particular interest for metal-organic chemical vapour deposition to keep the cost down and to be easily industrialised.

Once the material matching the aimed physical characteristics is obtained and the architecture of the device is known, some work has to be done on the integration. Interactions between the various materials of the device can lead to unwanted and negative effects, resulting in the degradation of the electrical properties. To limit these interactions, lowly reacting materials but also soft processes have to be chosen for device fabrication.

1.2 Material integration for device fabrication

As explained in the previous paragraphs, a transistor, which is the basic component of any device, can be described as a precise superposition of materials, which are controlled at the atomic level, which are deposited as thin films on a semiconductor substrate and which are interacting between each other. Due to the ever-decreasing size of ICs, interactions between the materials are becoming more and more important and they now define the general behaviour of the devices. Therefore, thin film deposition has evolved to become a stringent, meticulous field within surface science: deposited films in ICs require sub-nanometre dimensions and extremely low levels of contamination (to avoid altering the properties of the deposited materials) [31–37].
Paradoxically, the solution for the first problem, the use of chemical deposition methods, has worsened the second.

Initially, deposition was mainly performed through evaporation or sputtering methods (known as physical vapour deposition PVD), where a source of pure material was vaporised, using electron beam, ion beam or plasma, and deposited on a substrate [38–40]. However, the direction-dependency of these methods led to some unsolvable problems with smaller size

devices. The use of volatile molecular compounds instead of solid sources allowed an homogeneous growth of the layers, even on demanding aspect ratios. Originally, inorganic compounds were chosen (metal halides were the most used), but they required rather high temperatures and the byproducts were corrosive [40, 41]. Although these drawbacks were overcome with the use of metalorganic precursors, [41, 42] an inherent problem was the introduction of undesired elements (in particular carbon) into the growing film [40, 43].
Moreover, due to this choice toward Chemical Vapour Deposition (CVD), pure materials cannot be obtained anymore. Only alloys, such as oxides, nitrides or carbides, are deposited and require new developments for integration.

CVD is a surface reactant deposition, which implies that the deposited material is interacting with the under-layer. And because of thickness reduction of the layers the surface-volume ratio is reducing, leading to more and more significant surface interactions for the definition of the devices behaviour, compared to the previous generations of CMOS. These surface interactions compel the choice of lowly reactive materials and deposition methods, especially when plasma is introduced in the process. Concessions have to be done when choosing the best material with the lowest interactions.

This thesis took place in the described context and some of the previously mentioned challenges and opportunities were investigated. Part of the results, from a three years long work, are presented in this thesis.

1.3 Outline

As introduced in the previous sections, alternative candidates for metal gate with suitable properties and limited interactions with dielectric, are needed for future generations of CMOS technology. To achieve this, new materials, or new processes to tune the characteristics of these metals, have to be investigated. Then, it is necessary to have a better understanding of the physico-chemical phenomenons taking place at interfaces during deposition. Moreover, a correlation has to be done between material changes and possible changes of the electrical behaviour of the complete devices.
MOCVD-deposited titanium and tantalum alloys are widely investigated as potential replacement of the actual titanium nitride PVD metal gate, in order to fulfil the conformity demand. MOCVD allows conformal deposition, important for gate-last and FinFET integration, but also results in nitride and/or carbide alloys and contamination, whose levels are important to control.

MOCVD is a general naming which includes several deposition methods, all based on the chemical reaction of metal-organic precursor with the substrate and a reactant gas. Thus, Atomic Layer Deposition (ALD), Liquid Injected MOCVD (LIMOCVD) and Plasma Enhanced LIMOCVD (PELIMOCVD) are part of the MOCVD group. A description of these

techniques is given in the *Chapter 2*, with an emphasis on the differences of reaction mechanism paths.
To study the deposited metals in terms of physical and chemical properties several characterisations techniques are used. Hence, the physical characteristics of the layers, i.e. density, thickness, roughness are obtained by X-Ray Reflection, resistivity and crystallography, by four points probes and X-Ray Diffraction measurements respectively. Composition and chemical interactions are investigated by means of X-ray Photoelectron Spectroscopy. These characterization techniques and the corresponding methodologies are described in *Chapter 2*.

In *Chapter 3*, influences of the deposition process on the deposited metal properties, during MOCVD and ALD are studied. Effects of the variation of substrate and injectors temperature, reactant gas, pressure and other process parameters are discussed. These parameters are carefully tuned to achieve a full understanding of the changes in the properties of the deposited material. The characteristics closely looked at are the deposition rate, density, roughness, resistivity, composition and bonding environment of the species. Depending on the variation of the previously mentioned characteristics deposition reaction mechanisms are discussed and linked to the deposition parameters.

Similar methodology is used in the *Chapter 4*, for an investigation of the plasma in PEMOCVD or PEALD modes. The influence of each of the plasma parameters on the deposition reaction path is studied. Then, the addition of low frequency plasma for better decomposition of the precursor in PEMOCVD is reviewed in details. Using optical emission spectroscopy the modifications of the plasma are correlated to the modifications of the deposited material. In the last part of this chapter plasma is introduced for densification of Ta(C)N, in a PEALD mode. Evolution of the physical properties are linked to the chemical evolution of Ta(C)N when the plasma power is increased.

Then, because there is a thickness reduction of the deposited materials, the volume/surface ratio is also reducing and it gives an ever rising importance to surface reactions. Indeed, at thicknesses of two nanometres and below, more than half of the atoms composing a layer are in contact with bottom or top materials. An investigation of these interactions happening at the metal-dielectric interface is presented in *Chapter 5*.
By carefully choosing the deposition process it is also possible to promote some interactions, such as oxide removal or nitrogen addition, resulting in the improvement of the stack properties. MOCVD deposition reaction mechanisms are based on chemical affinity of the precursor with the reactant gas and with the substrate, thereby reactions with the underlayer cannot be avoided. Illustration of the point will be done by a study of the Ta(C)N interaction with TiN in *Chapter 5*.
Reciprocity is valid, the substrate have an influence on the nucleation of a new material.

Finally, in *Chapter 6* the first results concerning Al doping of TaN deposited by PVD and MOCVD are compared. Complete investigation of PVD-TaAl and PVD-TaAlN highlighted the important role of Al for passivation of the film, thus limiting the oxygen diffusion in

the volume of the layer. Successful deposition of MOCVD-AlN and PEMOCVD-AlC is used to acquire some knowledge about MOCVD doping, and used as reference for comparison with MOCVD-TaAlN deposition. ARXPS analysis of MOCVD-TaAlN layer confirmed the Al_2O_3 passivation layer formation, supposed from the study of PVD-TaAl and PVD-TaAlN. Then, to limit the creation of AlN, observed at the deposition of MOCVD-TaAlN, multistack materials containing Al-Al and AlC are developped and compared to MOCVD-TaN. The electrical results are discussed in relation to the physico-chemical characterisations and to Al doping behaviour in PVD-Ta.

Chapter 2

Deposition and characterisation tools

"Do not wait; the time will never be just right. Start where you stand, and work with whatever tools you may have at your command, and better tools will be found as you go along."

Napoleon Hill, author

2.1 Introduction

Since the introduction of IC to mass production, in the late 1960s, new deposition methods have been developed to answer the specific needs of this demanding industry. At the same time, to understand the phenomenons taking place during the deposition, improvement of the characterisation tools was achieved.

Today this pair, deposition/characterization, allows to create, control and characterise layers at the atomic level. A new world of possibilities and understanding is now at reach. This change was confirmed by the evolution of the number of publications concerning surface and interface studies. Indeed, in the last forty years it rocketed up from less than 100 up to almost 3000 (figure 2.1).

In this chapter are presented the tools used for deposition and characterization of the investigated metals and of the interactions with the substrate taking place during deposition. For each tool the physico-chemical principle is described and a discussion is given on the advantages, limitations and constraints consecutive to the metal-gate thematic. Emphasis is laid on Metal Organic Chemical Vapour Deposition and X-Ray Photoelectron Spectroscopy, the most used deposition and characterization methods of this work.

2.2 Deposition tools

The tools used for deposition during this thesis were industrial or pre-industrial modules, it implies that the recipes are already provided by the manufacturer in the industrial module,

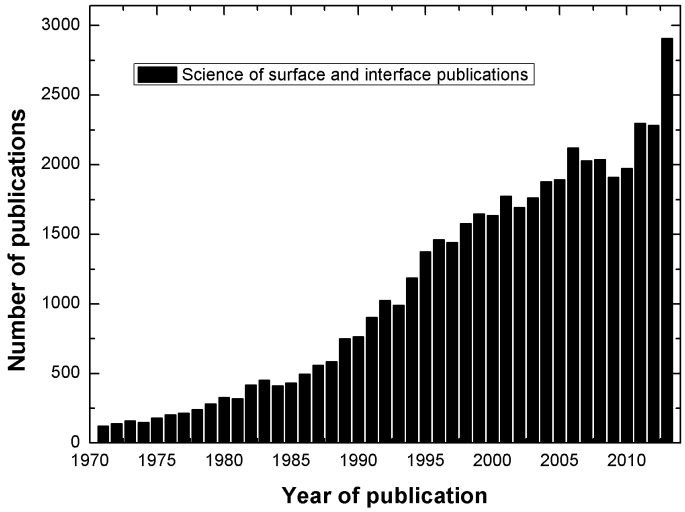

FIGURE 2.1: *Evolution of the number of publications in surface and interface science referenced in ScienceDirect database*

whereas no process is included with pre-industrial module. A direct consequence is that modifications of the process, to extreme conditions, are much easier with the pre-industrial module. However, reaction mechanism used in industrial modules have to noticeable advantage of being stable, reproducible and already investigated in details.

2.2.1 Precursors for CVD and ALD

CVD and ALD are based on chemical reactions; every reaction needs reactants to obtain the products. In the case of metal deposition the reactants consist of the metallic atoms in solution, called a precursor, and a reactive gas. As introduced Chapter 1 section 1.2, the best metal compounds for metal gate application are the metalorganic precursors.
Metalorganic precursor is defined as a chemical compound that contain metal and organic ligands. Metalorganic compounds exclude species with direct metal-carbon bonds, which are classified as organometalic compounds.

Metalorganic precursors have several advantages for film growth compared to the elemental sources that are used in physical vapour deposition processes and to the metal halides that are often used in CVD processes. Most importantly, metalorganic precursors tend to be much more volatile than many metal halides and most metals in their elemental form, which allows easy precursor delivery systems. Since film growth occurs by a succession of chemical reactions, the precursor chemistry can be designed to favour the desired inorganic phase, minimise undesirable element incorporation into the final material, control the deposition temperature and avoid corrosive by-products that might damage the reactor or the substrate on which the film is grown. Metalorganic precursors can also be obtained in high chemical purity, which is important for microelectronic application. Indeed ultra pure metalorganics are required, with purity of the order of 99.9999% or greater.

Many different types of ligands have been employed to create volatile metalorganic precursors for film growth. In general, the ligands are anionic, with carbon, oxygen or nitrogen donor atoms. In some cases, neutral donor ligands are present. Many CVD processes entail the reaction between a metalorganic precursor with basic ligands and a co-reactant that contains acidic element-hydrogen bonds. Mixing of these reactants in the gas phase results in protonation[1] reactions that eliminate the basic ligand in its protonated form and in the formation of a new metal-element bond (equation 2.1) [35, 42, 44].

$$M - R + EH_n \xrightarrow[-RH]{CVD\ reactor} M - EH_{n-1} \tag{2.1}$$

with M the metal atom or heteroatom, E the reactant atom such as O, N, S.

The co-reactant with acidic element-hydrogen bonds is generally chosen so that the element corresponds to one of the atoms required for the final film material. Examples of this type of reactant include ammonia and water for the deposition of nitrides and oxides, respectively. A second type of strategy that is used to eliminate excess hydrocarbon groups from the metalorganic precursor is β-hydrogen elimination [45, 46]. Hydrocarbon groups such as Et, ^{n}Pr, ^{i}Pr, ^{n}Bu and ^{i}Bu, when bonded to a metal atom or a heteroatom, can eliminate an alkene through a low-energy decomposition pathway [46, 47]. This β-hydrogen elimination often provides an efficient pathway through which carbon groups are removed from precursors. If a precursor is properly designed, the carbon incorporation in the film material can be minimised.
Deposition by MOCVD and ALD was reported for many elements of the periodic table, a list of these elements and the deposited materials is presented Appendix B, page B.

MOCVD and ALD appear as a viable solution for microelectronic but critically rely upon the availability of suitable high-purity precursors with sufficient volatility and stability. Articles, books and reviews addressing this subject have been widely published in the past few years. The role of molecular chemistry in influencing the physical properties of the precursor leading to robust thin films has been widely discussed [35, 36, 44–48]. To be compatible with microelectronic applications the precursor must possess the following properties:

- Appreciable volatility and molecular stability of the vapours to avoid pre-gas phase reactions or decomposition of the vapours, and to achieve film growth at moderate deposition temperatures.
- Adequate temperature window between precursor evaporation and decomposition to get high quality deposits preferably at lower substrate temperatures.
- Clean fragmentation of the organic matter at the surface of the substrate during film growth, to limit the by-products contamination.
- Easily synthesised and purified in high yields at reduced cost, convenient during handling and transportation, preferably a low degree of toxicity to easier the maintenance

[1] Protonation is the addition of a proton (H^+) to an atom, molecule or ion, forming the conjugate acid.

of the deposition tool.

Of course, such a precursor do not exist and compromises have to be done. Vapour pressure of a metalorganic precursor is the crucial parameter that governs the concentrations of metalorganic precursors entering the reactor, and subsequently the growth rate of deposition process. Also low vapour pressure allows to limit the necessary temperature of the system, including the capillary tubes from the canister to the deposition chamber.
Thus choosing a precursor is not an easy task and should not be underestimated.

One precursor of both tantalum and titanium were chosen to match the deposition constraints of the metal for high-κ/metal gate deposition application, the properties of the metal and the aimed process window.

Tantalum precursor:
Several precursors are commercially available for Tantalum nitride deposition. Most used for CVD and ALD processes are the **T**ertiary**B**utylimido,**T**ris(**D**i**E**thylamino)**T**antalum (TBTDET), **t**-**A**myl**i**midotris(di**m**ethyl**a**mido)**ta**ntalum and **P**entakis(**D**i**M**ethyl**A**mido)**T**antalum (PDMAT) [18, 49–52].

Table 2.1: *Comparison of TBTDET and PDMAT precursors*

	TBTDET	**PDMAT**
Formula	$Ta(NtBu)(NEt_2)_3$	$Ta(NMe_2)_5$
Molecular Weight	468.46 g.mol^{-1}	401.33 g.mol^{-1}
Boiling point	120°C @ 1 Torr	100°C @ 0.1 Torr
Vapour pressure	$\sim$ 1 Torr @ 120 °C	$\sim$ 1 Torr @ 90 °C
Flash point	46 °C	NA

Due to the different intrinsic properties, it was already proven that TBTDET is more suited for tantalum nitride metal deposition. When using PDMAT and NH_3 it was reported that films with some Ta and N could be grown, but that they contained a great deal of carbon and were non-conducting due to the formation of Ta_3N_5 phase (a nitrogen rich dielectric) [53]. In contrast, when TBTDET was used with NH_3 electrically conducting films of TaN were created with low carbon content and low resistivity [18, 54, 55].
Thus, for MOCVD and ALD the TBTDET molecule was chosen. TBTDET molecule is presented in the diagram figure 2.2.

Two noticeable features of this molecule are: one the lack of tantalum-carbon bonds and second the presence of a double tantalum-nitride bond. These features dictate the stoichiometry of the deposited material.

Titanium precursor:
As for tantalum, few titanium metalorganic precursors are commercially available. Most used precursors for titanium nitride deposition are **T**etrakis(**D**i**E**thyl**A**mido)**T**itanium (TDEAT)

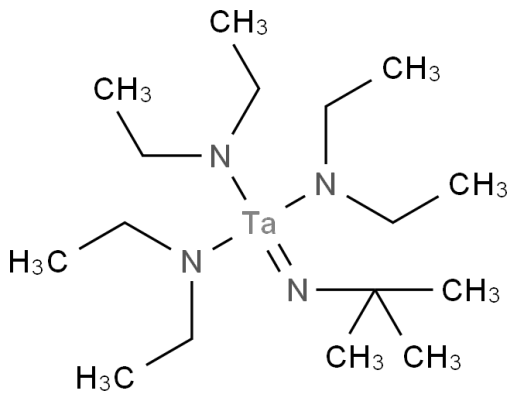

FIGURE 2.2: *Skeletal formula of tantalum TBTDET precursor molecule*

and **T**etrakis(**D**i**M**ethyl**A**mido)**T**itanium (TDMAT) [17, 56–61].

TABLE 2.2: *Comparison of TDEAT and TDMAT precursors*

	TDEAT	**TDMAT**
Formula	$Ti(NEt_2)_4$	$Ti(NMe_2)_4$
Molecular Weight	336.4 $g.mol^{-1}$	224.19 $g.mol^{-1}$
Boiling point	60°C @ 1 Torr	65°C @ 1 Torr
Vapour pressure	1 Torr @ 100 °C	0.0067 Torr @ 25 °C
Flash point	10 °C	NA

Previous investigations showed that, even if TDEAT has a higher temperature process window it is more suited for TiN MOCVD and ALD deposition [59]. Advantages over TDMAT include: better decomposition of the precursor molecule and lower resistivity obtained at the same substrate temperature.
Hence, if the process temperature can be above 250°C then TDEAT precursor is a better choice. Because metal for the gate can be deposited at temperatures up to 400°C without any damageable consequences on the substrate, TDEAT was chosen.

TDEAT molecule is presented in the diagram figure 2.3.

As for tantalum molecule, titanium precursor do not present any carbide bonds, the metal atoms are only bonded with nitrogen atoms.

Finally, to do the doping of tantalum and titanium nitride layers, aluminium was chosen. Aluminium doping was already widely studied in the case of PVD deposition and proved to be efficient for work function shift of the TiN from p-mos to n-mos [62, 63]. However, it was not reported any CVD doping or bi-metal deposition investigation.

Aluminium precursor:
Doping of tantalum and titanium by aluminium arose new problematics and constraints. Yet,

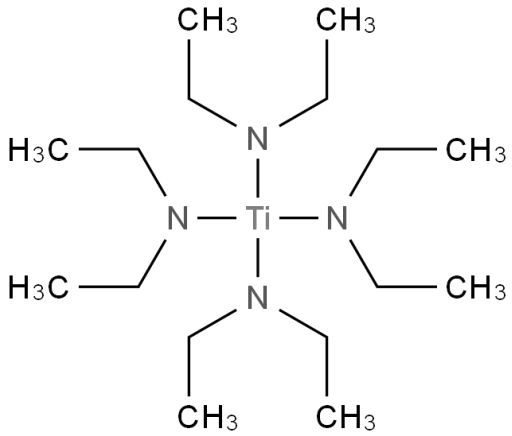

FIGURE 2.3: *Skeletal formula of titanium TDEAT precursor molecule*

only one precursor fitting the deposition module's constraint was commercially available. **T**ri**M**ethyl**A**luminium (TMA) was used to dope the TaN and TiN metals [23].

TABLE 2.3: *TMA characteristics*

	TMA
Formula	$Al(Me)_3$
Molecular Weight	72.1 $g.mol^{-1}$
Boiling point	126°C @ 1 Torr
Vapour pressure	9 Torr @ 20 °C
Flash point	-17 °C

TMA molecule is presented in the diagram figure 2.4.

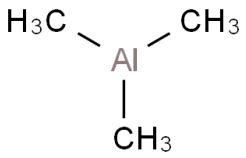

FIGURE 2.4: *Aluminium TMA precursor molecule*

TMA molecules do not contains Al-N bonds to avoid the formation of AlN_x alloys which are insulating, thus highly undesirable as metal gate material.
Many articles in the literature report about the use of TMA molecule. Although, it has been used only for deposition of aluminium oxide [64–68]. Thus all of the work on Al doping will be innovating and new problematics might arise.

2.2.2 (Plasma Enhanced) Metal-Organic Chemical Vapour Deposition

2.2.2.1 MOCVD principle

With the constraints of high conformity and low roughness presented in the Chapter 1 one of the most investigated deposition method for metal gate is the Metal-Organic Chemical Vapour Deposition (MOCVD).

MOCVD is a versatile and flexible method for deposition of thin films [46, 69, 70], with a wide variety of materials available, see Appendix B. It involves a few number of sequential steps, starting from vapour phase delivery to the reactor, progressing through a series of quasi steady-state sub-processes happening at the substrate surface, and concluding with the formation of solid thin film in its final micro-structure.
Sequence of MOCVD deposition is schematically illustrated in figure 2.5 and the individual sub-processes are described below.

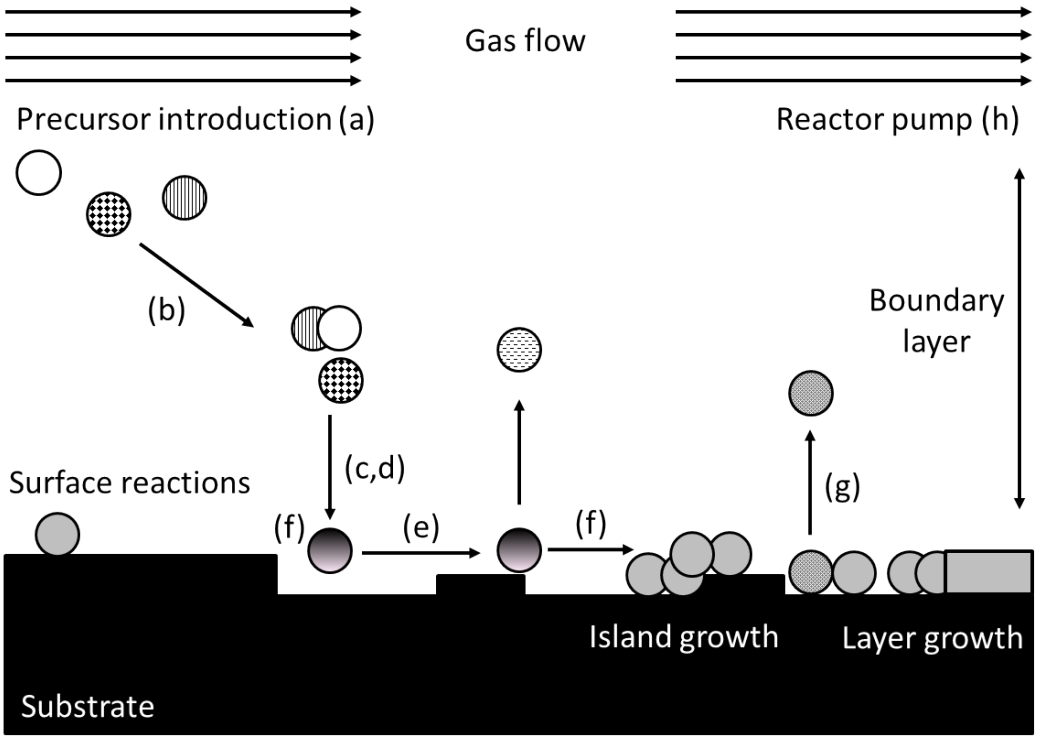

FIGURE 2.5: *MOCVD reaction mechanisms*

a *Precursor introduction:* Precursor is delivered to the reactor in vapour phase. The precursor vapours are transported to the reaction zone by inert gases such as helium or argon.

b *Reactions occurring in the gas-phase:* The precursor molecules present in the reactor may interact with each other or with reactant gas prior to deposition, thereby resulting in heterogeneous nucleation and sometimes even in powder formation. Formation of particles in the gas phase endangers the repeatability, the "cleanness" and the quality of the deposited films and hence gas phase reactions should be avoided.

c *Diffusion of the precursor molecules to the surface:* Transport near to the solid surface is always dominated by diffusion mechanism. When uniformly distributed diluted precursor vapours are forced over the flat substrate, the velocity profile develops averages with no net motion, that is, the velocity is zero when adjacent to the substrate or the reactor walls. The gaseous layer between the substrate and the position where the velocity is maximum, is called the boundary layer (see figure 2.5). Through the boundary layer precursor vapours are not carried by the vector gas but via diffusion through the layer to the substrate surface. The rate of diffusion depends on the total reactor pressure, temperature and the concentration of precursor molecules in the gas phase present above the boundary layer.

d *Adsorption of the precursor molecules at the surface:* the precursor molecules after diffusing through the boundary layer are absorbed on the substrate surface. Usually, the adsorbed reactants are assumed to be in equilibrium with the reactants in the gas phase.

e *Migration (surface diffusion) of the adsorbed species:* the adsorbed species undergo surface diffusion phenomenon and migrate prior to reaction. This migration phenomenon was not proven until today but it is the main hypothesis for island growth explanation [71].

f *Precursor decomposition at the surface and film growth:* the molecules of precursor adsorbed, either react with their neighbouring molecules, with the substrate, or with the molecules present in the gas phase to form a film.

g *Desorption and diffusion of the reaction by-products:* the reaction by-products which are formed as a result of surface reactions, and which do not contribute in film formation, desorb from the surface and diffuse out through the boundary layer. This step is defining the choice of the precursor, so as only volatile by-products are formed during the reaction path. Similarly the unreacted precursor molecules also desorb and diffuse through the stagnant boundary layer.

h *Removal of by-products:* volatile by-products and the unreacted precursor molecules are pushed out from the reactor by bulk gas flowing in the reactor.

Since MOCVD process occurs through a sequence of sub-process, the slowest sub-process is the overall deposition rate determining step.

Generally for a CVD process three different film growth regimes are apparent, they are introduced figure 2.6. From Arrhenius plot (figure 2.6), which is the plot of growth rate versus the inverse of temperature, the three rate determining cases depending on the substrate temperature can be clearly understood.
In other words, growth rate is determined by:

- supply of the precursor to the reactor growth zone. When step **a** or **h**, previously introduced, is the slowest step then the MOCVD process is said to be in the **depletion region**. Mass transport is responsible for precursor supply to the reactor zone and removal of the reaction by-products as well as the unreacted reactants from the reactor.

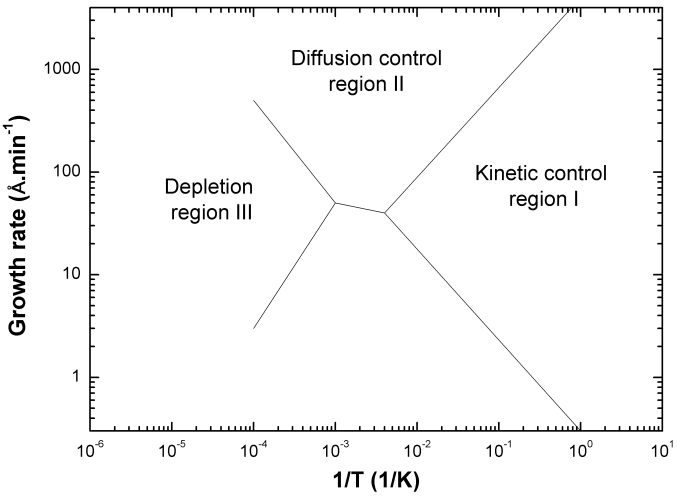

FIGURE 2.6: *Film growth regimes for a CVD process*

- diffusion of the precursor molecules through the boundary layer. When step **c** or **g** is the slowest process, the MOCVD reaction is said to be in the **diffusion control region**. Diffusion rate determining region is generally observed at relatively higher substrate temperatures. This is because at low substrate temperatures, precursor molecules with high rate of diffusion will not decompose quantitatively. Since growth controlled by diffusion begins at high temperatures, where almost all the precursor molecules that touch the substrate surface react to form the film, further increase in the deposition temperature does not show significant effect on the growth rate. Thus diffusion controlled region can be said to be independent of the substrate temperature, however generally non-uniform and rough film surfaces are obtained, due to gas flow dynamics.
- surface phenomenon occurring. When either step **d**, **e** or **f** is the slowest process, the film growth is said to be in a **kinetic control region**. Process such as precursor adsorption, surface reactions and desorption of the by-products are kinetic processes. Growth rate limited by chemical kinetics occurs at low temperatures and the growth increases exponentially with increase in temperature following the Arrhenius equation [72]. Because the reactions are slow compared to the diffusion through the boundary layer, the diffusion length of the precursor molecule is long. This results in a smooth uniform film growth and enables conformal growth over large substrate area.

2.2.2.2 Plasma for MOCVD enhancement or densification

Introduction to plasma

Taking into consideration the energy of the particles, plasma is often defined as the fourth state of matter, apart from solids, liquids and gases [73]. In a more rigorous way, plasma can be defined as a quasi-neutral gas of charged and neutral particles characterised by a collective behaviour (plasma waves and oscillations).

Chemically reactive plasma discharges are often used to modify the surface properties of materials, but plasma can also be used to activate some reaction mechanism, for example by breaking down the precursors molecules, thanks to the extra energy brought [74].

A plasma is defined by a large number of parameters, such as power, frequency, pressure, flow rates, temperatures, type of electrodes and reactor type/geometry. These parameters are often interdependent but interact mutually in determining the material properties.
Once a plasma is stabilised and controlled, it can be characterised by the following basic parameters:

- the density of neutral particles, $n_{neutrals}$.
- the densities of electrons and ions, n_e and n_i. If the quasi-neutral state model of plasma is taken into consideration, then the following relation is true:

$$\sum_{\alpha} q_\alpha n_\alpha = 0 \tag{2.2}$$

  with q_α the charge and n_α the density of the specie α.
- energy distributions for neutral particles, ions and electrons
- temperatures of the different species in the plasma
- degree of ionisation of the plasma

The plasma density, which controls the electron density, is an important parameter in plasma processing because the efficiency of the processes occurring in the plasma depends on the formation of radicals. Indeed chemical bonds of the precursor molecules are broken by electron or energetic ions. A parameter that defines the density of charged particles in the plasma is the degree of ionisation. It specifies the fraction of particles in the plasma phase that are ionised.
For plasma used in this work and sustained at high pressure (more than 1 Torr) the degree of ionisation was calculated to be typically between 10^{-4} and 10^{-1}.

Plasma Enhanced MOCVD

Plasma Enhanced MOCVD (PEMOCVD) is a plasma activated deposition. Deposition of layers by PEMOCVD is the most complex of all plasma surface treatment techniques. In-depth understanding is still limited, and the development of new deposition processes is mostly empirical.
In thermal CVD processes, the surface reactions are usually determined by thermodynamic considerations and controlled by the temperature of the reactor and substrates, as presented earlier. Whereas in PEMOCVD, plasma can induce several chemical reactions, each interacting with the others and can result in unexpected characteristics of the deposited material. Because most radicals react with the surface, the composition of the films deposited by PEMOCVD is determined to a large extent by the relative fluxes of all the species forming the film. New reactions activated by plasma may be considered as an advantage because it allows the formation of new materials, not conceivable thermodynamically, although it may also be a disadvantage as it complicates the study of the parameters of reaction control and reproducibility of the composition.

Plasma densified MOCVD

Plasma densified MOCVD is a thermally activated deposition, including a plasma step for

densification of the deposited layer. In this case the plasma is used to expel the reaction by-products and brings some energy to allow ordering of the atoms which can, for example, facilitate the creation of crystals. Material properties depend on the thickness of the deposited layer at the densification step and on the length of the densification step [16], however densification on thicker layers leads to the creation of a gradient in the material (either of composition, or of density).
This method is quite similar to the Atomic Layer Deposition, which will be presented in details section 2.2.3, especially if only a really thin layer or a monolayer is deposited before densification.

2.2.2.3 MOCVDs tool description

Part of the materials presented in this work were deposited using an AltaCVD Advanced Materials^{TM} reactor produced by AltaTech, France, allowing (PE)MOCVD deposition on 300 mm substrates. The deposition chamber was specifically designed for Liquid Metal-Organic deposition (LIMOCVD) with and without plasma assistance. It also includes the in-situ characterization tools for Optical Emission Spectroscopy (OES) and X-Ray Photoelectron Spectroscopy (XPS). A schematic representation of the deposition chamber and the gases inputted is given figure 2.7.

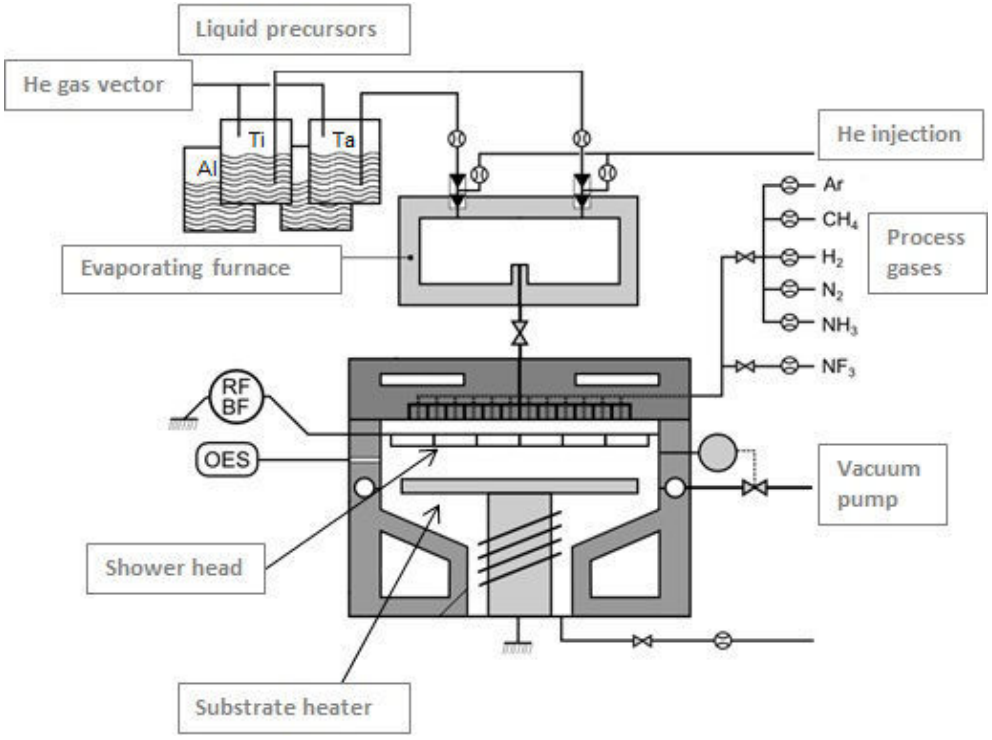

FIGURE 2.7: *Schematic representation of the AltaCVD Advanced Materials^{TM} deposition chamber*

Liquid precursor is pushed by He vector gas and brought to the heated injectors, where the frequency, opened-time of the injector and pressure allow a control over the quantity of liquid

injected.
Injectors are made of three important parts, the liquid injection needle, the gas injection needle and a mixture chamber. After each liquid injection to the mixture chamber He gas is introduced to the mixture chamber so all the liquid can be pushed to the evaporating furnace. The evaporating furnace is at the same pressure as the deposition chamber, a few Torr, which is 10^6 times lower than the injection pressure. As a consequence the liquid/gas mixture is sprayed into the evaporating furnace in droplets of a few nano to micro litres. Heating of the evaporating furnace avoids condensation of these droplets on the walls and allows the transfer of the precursor to the deposition chamber.
To enter the deposition chamber, the precursor mixture is going through a double threaded shower. Half of the openings are dedicated to the precursor while the second half is for the reactant and/or process gas. This separation delays the activation of the reaction between precursor and reactant gas, avoiding the step **b** presented section 2.2.2.1.

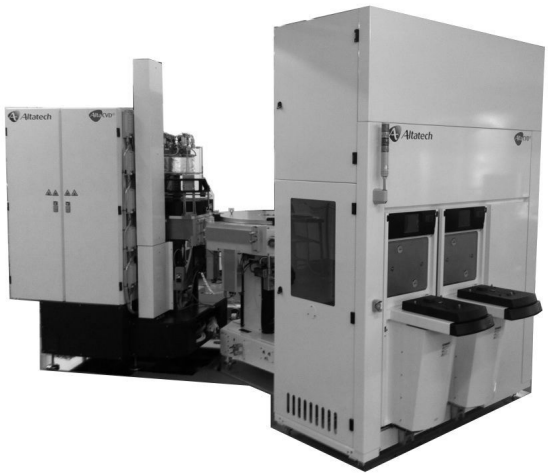

FIGURE 2.8: *Picture of the actual AltaCVD Advanced Materials^{TM} tool*

This tool is a pre-industrial model, with an uniformity comprised between 5 and 10% on 300 mm wafer and less than 50 particles added with a size comprised between 90 nm and 250 nm. These specifications make it suitable for microelectronic industry.

2.2.2.4 Advantages, limitations and constraints

MOCVD has the advantage of being a surface reactant deposition, i.e. deposition is conformal whatever the pattern of the device. Moreover the growth rate of MOCVD can vary from few nanometres up to several microns per minutes depending on the deposited material and the reaction mechanism. In this study due to the thin layers aimed at the lowest deposition rate was preferred in order to have a better control over the deposited thickness.

One of the main advantage of the AltaCVD Advanced Materials^{TM} tool, is the possibility to inject four precursors through the four separated liquid lines. It allows the development

of metallic alloys, but also the stacking of metals without vacuum-break, avoiding oxidation of the metals.

MOCVD has the disadvantage of bringing carbon contamination in the deposited layer, to limit this contamination, importance has to be granted to the efficiency of the deposition reaction and on the exhaust of by-products. The other limitation of MOCVD is that the deposition is dependent on a thermodynamic reaction mechanism, it is a chemistry driven process and thus not every compounds or alloys can be deposited. The use of plasma in PEMOCVD can be a solution to rectify this shortcoming. Another way to successfully do the deposition is to develop new precursors with different reaction mechanism or lower activation temperatures [75].

2.2.3 (Plasma Enhanced) Atomic Layer Deposition

2.2.3.1 Principle

Atomic Layer Deposition (ALD), also called Atomic Layer Chemical Vapour Deposition (ALCVD) is a particular method of the MOCVD group.
The main difference of ALD is that the complete deposition reaction is made by steps. First the precursor, in the gaseous phase, is introduced in the chamber and thermodynamically reacts with the heated substrate to form a monolayer. This reaction of the precursor with the substrate is a limited and self-saturated reaction. In a second step excess of precursor is pumped out of the chamber before the third step: introduction of reactive gas. Reactive gas is used to activate the deposited monolayer, before another introduction of the precursor, by creation of nucleation sites thanks to new surfacing ending. Activation of the layer means to liberate all the possible growth sites on the substrate. In figure 2.9 are presented the succession of steps forming a cycle.
During a cycle, precursor and reactive gas are not present in the deposition chamber at the same time, thus limiting unwanted reactions in the gas phase as introduced section 2.2.2.1. Thanks to the self-saturated reaction the thickness is proportional to the number of cycles, which makes it easy to obtain the aimed thickness by adapting the number of cycles.

Like for CVD, each ALD process has an ideal process "window" in which growth is saturated at a monolayer of film. As presented figure 2.10, this ALD window is temperature and growth rate dependant. If the temperature is too low, the precursor can condensate on the walls of the reactor or the reaction mechanism may not be activated. On the other hand, with a too high temperature, desorption of the precursor from the substrate may happen or it might decompose before the activation step and unwanted reaction may occur.

Several activation step mechanisms are available, i.e. the reactive gas introduction can be replaced by a plasma, for further densification of the film and surface sites activation. This variation of the ALD process is called Plasma Enhanced ALD (PEALD). Plasma has the same advantage as in the PEMOCVD, it allows some non-favourable reaction mechanism

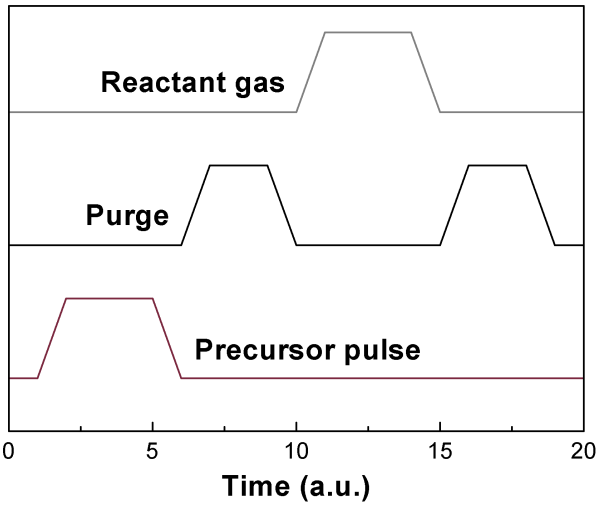

FIGURE 2.9: *Succession of ALD steps to form a layer*

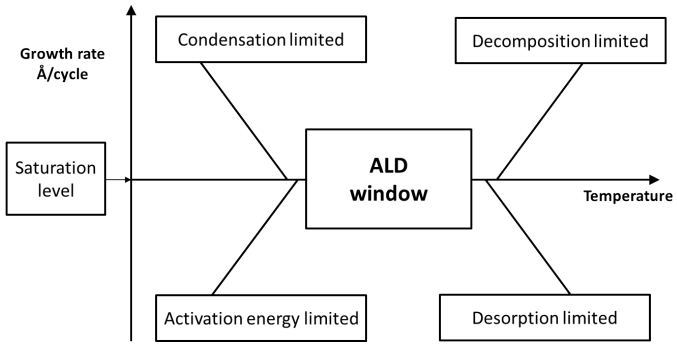

FIGURE 2.10: *ALD process window*

[16]. Moreover, excited radicals created in the plasma can easily form volatile species with the carbonate by-products of deposition reaction, leading to better removal of the by-products and thus lowering contamination levels.

2.2.3.2 Tool description

To have a good control over the entering flow of precursor and reactant gases pulsed valves with high speed actuation have to be chosen for the ALD reactor. Their role is similar to the injectors in the LIMOCVD reactor AltaCVD Advanced Materials^{TM}. Unlike LIMOCVD, precursor is brought from the canister to the substrate in the gas phase. Instead of using a vector gas to push the precursor out of the canister, the vector gas is entered in the liquid precursor to create bubbles and then carry to the deposition chamber the molecules in the vapour phase. In this case the canister is called a bubbler.
Description of the (PE)ALD deposition chamber is given figure 2.11. As seen on this figure, precursor and reactant gas are entering the chamber through the same one-stage shower. This can be done thanks to the alternation of precursor and reactant gas during ALD process. To limit the creation of particles due to some precursor or gas residues in the shower, the purge step has to be carefully tuned to remove any exceeding reactant.

A ring for outgoing gases is used in order to distribute the precursor and reactant gas equally on all the wafer and thus to improve the uniformity of the layer.

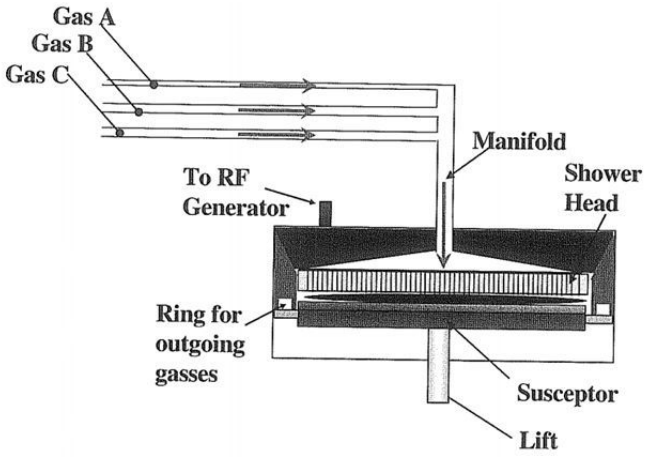

FIGURE 2.11: *Deposition chamber scheme of ALD tool*

This tool is an industrial model, with an uniformity below 5% on 300 mm wafer and less than 50 particles added with a size comprised between 90 nm and 250 nm.

2.2.3.3 Advantages, limitations and constraints

ALD has the advantage of even better conformity than MOCVD, thanks to the self-saturated monolayer deposition, with ultra high aspect ratio > 100:1 proven [48].

As MOCVD, ALD has the advantage of being a gentle deposition process, which can be of use for sensitive dielectrics/substrates. It is due to the fact that the molecules of precursor reach the substrate with no energy and no parasitic reaction is supposed to happen if the precursor is chosen well accordingly to the qualities and weaknesses of the substrate.
However, in some cases the deposition temperature can be an inconvenient. As the deposition reaction is only thermodynamically activated it is not possible to reduce it, thus impacting substrates for example in the case of metal deposition on polymers.
Main limitation of the ALD is the relatively low deposition rate, between 0.5 and 1.5 Å per cycle, with a cycle being about 10 seconds up to one minute long. This low through-put is highly investigated by manufacturers to increase the number of ALD chambers used in industry [35, 44, 48], some of the solutions include batch processing [76].

2.2.4 Physical Vapour Deposition

2.2.4.1 Principle

During Physical Vapour Deposition (PVD) a material is converted to the gas phase in a vacuum system by evaporation or sputtering on an atomic scale. The gas hits the samples to be coated and is deposited there as a nanometre-to-micrometre-thick layer, deposited thickness being directly related to the sputtering time. During the entire deposition process, which is divided in three stages: conversion to the gas phase, movement to the samples and condensation on the surface of the sample; only the aggregate state of the material changes from "solid" to "gaseous" and back to "solid". However, it basically remains the same material in terms of chemistry, on the contrary to CVD.
A key component of the PVD is the vacuum system. It is necessary during the evaporation step to remove the particles present between the source and the substrate. By doing so, evaporated particles have a straight path to the substrate, i.e. the mean-free-path is made long enough for the matter to reach the substrate. The pressure range depends on the deposited material and on the evaporation means but is typically included in a 10^{-2} to 10^{-7} Torr range [77]. Deposition is usually done at 20°C.

Vaporisation of the material can be achieved by several means, including electron bombardment, plasma discharge, electrical heating, laser decomposition and electric arc discharge. In this study a plasma of argon (Ar) was used to create the necessary ion bombardment for sputtering.

Additionally, reactive gas such as nitrogen may be introduced into the vacuum chamber during metal deposition to create metallic compounds. Variation of the reactant gases flows results in a variation of the stoichiometry of the deposited material [20, 77].

2.2.4.2 Advantages, limitations and constraints

PVD has the possibility to create pure metals, which is complicated using MOCVD and ALD, except if chloride or fluoride based precursors are used. Contamination in the deposited layer is dictated by the purity of the vaporised material, which is at least 99.99% and usually 99.999% for microelectronic grade.
As the deposition is controlled by the sputtering, many materials can be used in PVD process, i.e. whatever specie that can be purified and that can form a target. Moreover, deposition by PVD is done at room temperature, no heating of the substrate is needed. This and the low energy of the atoms reaching the substrate allow deposition of many materials on every possible substrate with limited damages.

Moreover compared to MOCVD and ALD, PVD has the advantage of not using liquid precursors which are highly toxic and reactive at the air. That advantage is overcame when the source material is used and a new one has to be installed. For MOCVD and ALD a canister is easily changed when empty, but to replace the PVD target the deposition chamber has to

be opened, a quite long and fastidious maintenance.

Biggest inconvenient of PVD is the non-conformity of the deposited layer. Indeed, due to the low energy of the atoms and the geometry of the deposition chamber, atoms are landing with a perpendicular path to the substrate, which makes it impossible to deposit on the vertical walls of any pattern present.
Finally, due to the inertness of the sputtered atoms, it is not possible with PVD to deposit alloys. Only bi-metals are deposited, meaning that no bonds are created between the two deposited species. Stoichiometry of the layer is then easily controlled by the distance to the substrate or the power used when sputtering of two targets used for the bi-metal or by the stoichiometry of the target when only one target of a bi-material is in use.

2.3 Characterization tools

2.3.1 Four points probe

2.3.1.1 Technique description

A basic property of a conductive material is its electrical conductivity, or opposite the resistivity. The electrical resistivity is determined by the availability of "free electrons" in the material. In turn, the availability of free electrons is determined by the physical binding properties of the material on a molecular level. It implies that the impurities or dopants added to a material will either increase or decrease its resistivity.
Thus measurement of the resistivity is used to both characterise the material and as a process control parameter.
To obtain the resistivity of a material, one must measure the sheet resistance. To do so a current has to pass through the end of a thin conducting sheet, which has to be deposited on an insulating material. The sheet has a length, a width and a thickness. The length/width ratio is determined by the probe used, thus knowing the thickness of the layer it is possible to determine, by Ohms Law equation 2.3a, the resistance of one square, named **Rs** (see equation 2.3c), by sending a current through probes 1 and 4, figure 2.12, and measuring the voltage at the probes 2 and 3 figure 2.12.

$$Rs = V \div I \tag{2.3a}$$

$$Rs = resistivity \times \frac{length}{(thickness \times width)} \tag{2.3b}$$

$$resistivity = Rs \times thickness \tag{2.3c}$$

with R the resistance, V the voltage, I the current, thickness, width and length the dimensions of the conductive sheet.
That way the measured voltage corresponds to the circulating voltage into the sample with

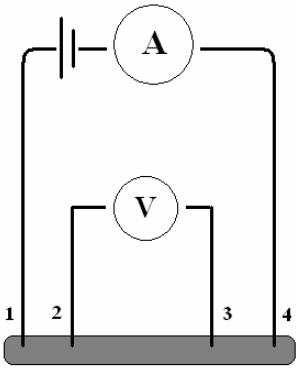

FIGURE 2.12: *Four-points measurement of resistance*

no current.

2.3.1.2 Advantages, limitations and constraints

Resistivity measurement is the easiest way to control a process and survey any deviation of the process. By a fast measurement it is possible to know if there is change in the composition or grain size of the material, when the thickness is known, or to know if there is a change in the thickness when the composition and grain size are known.
Thus, the main disadvantage of resistivity measurement is the need of knowledge of another characteristic of the material to conclude on any variation.

Uniformity of the layer is the only characteristic at reach by a resistivity measurement alone. As the resistivity is given directly from the measure, meaning that there is no need of mathematical calculation, four point probe is widely used for process control and process development. Although, due to the size of the probe about 1 cm of the edge of the wafers can not be measured and as to be taken into consideration as it represents 1/16 of the wafer total area.

To be able to measure the resistivity of a layer few conditions have to be respected. First, as explained previously, deposition has to be done on an insulator material, usually a thick layer (about 100 nm) of SiO_2 is used. Then, the resistivity of the layer has to be in the measurable range of the tool, typically obtained for a layer at least 10 nm thick and with a controlled level of oxidation. For example Al layer can not be measured as a thin (about 3 nm [78]) but highly insulating alumina layer is formed at vacuum break.
The biggest con against resistivity measurement is the fact that it is a destructive measurement. Indeed, when the probes are in contact with the sample, the pressure applied can locally damage the deposited layer. As usually 49 points are measured on a 300 mm wafer the impact is too significant to consider any other measurement on the same sample.

2.3.2 X-Ray Reflectivity

2.3.2.1 Technique description

X-Ray Reflectivity (XRR) is a non-contact, non-destructive, surface-sensitive analytical technique. Analysis of X-Ray reflection intensity curves from grazing incident X-Ray beam[2] is used for determination of thin-film parameters including thickness, density, and surface or interface roughness of a layer or a stack of layers.
When X-Rays are irradiated onto the sample at very low angles there is total reflection of X-rays from the sample surface. As the angle of irradiation is gradually increased beyond a certain angle called critical angle, which is dependent on the material, X-rays are reflected from the interfaces of the sample and give rise to interference fringes. As shown figure 2.13 left, the periodicity of the fringes is proportional to the thickness of the film, the fall of intensity is proportional to the roughness of the film and amplitude of the fringes is proportional to the density of the top and bottom layers, figure 2.13 right.

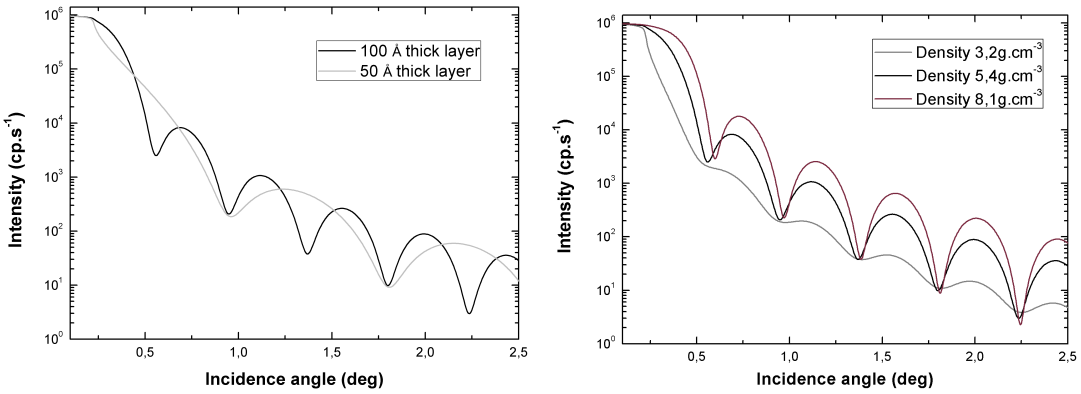

FIGURE 2.13: *Evolution of XRR spectra with thickness and density variation*

2.3.2.2 Advantages, limitations and constraints

Advantage of XRR over different thickness measurements techniques (like ellipsometry), on top of the possibility to measure non transparent samples, is that no properties of the film are required to understand the spectra obtained. On the other hand it is limited to samples with a thickness of maximum 300 nm, due to the absorption of the X-Ray by the material, which is not a constraint in this study.
Reducing the noise/signal ratio for multilayered samples is essential to obtain a spectra which allows interpretation of the interfacial roughness and interactions (such as the creation of an oxide) and can be obtained only by longer signal acquisition.
Compared to other thickness measurement methods, like ellipsometry, XRR is an absolute measure which does not need calibration to access the layers information. This advantage is significant for the new materials development.

[2]See Appendix C for description of X-Ray generation

XRR has one limit, in metal gate application, that cannot be overcome. In fact, this limit is due to the principle of XRR and corresponds to the correlation between the arches size and the thickness of the sample. When measuring samples of 2 nm or less, the arches are so large that they are not visible with the available angle range. To face this problem thicker layers are used for process development and the thickness is adapted only for integration.

2.3.3 X-Ray Diffraction

2.3.3.1 Technique description

XRD is a bulk characterisation technique which is highly sensitive to crystal structure. XRD allows for rapid, non-destructive qualitative and quantitative analysis of ordered materials.

An X-rays wavelength, of a few Å, is comparable to interatomic distances and so, an incident X-ray beam is scattered by individual atoms in all directions. In randomly distributed atoms, such as those in an amorphous material, scattered rays will have a random phase relationship relative to one another and neither full constructive, nor destructive, interference will occur. In a crystal where atoms are arranged periodically on a lattice, scattered beams will have definite phase relationships. These phase relations are such that, in most directions, destructive interference occurs giving almost zero intensity. In a few directions the scattered beams will be completely in phase and so, constructively interfere to form diffracted beams, as represented figure 2.14.

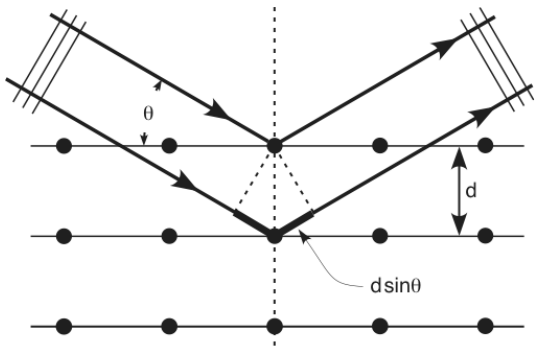

FIGURE 2.14: *Schematic representation of interactions that result as an X-Ray beam hits a sample*

These diffracted beam directions are those that satisfy Bragg's law, equation 2.4. It can be understood by considering entire crystal planes as the scattering entity, rather than the individual scattering centres within the plane. Strong diffraction occurs when:

$$n\lambda = 2dsin\theta \tag{2.4}$$

where n is an integer representing the order of diffraction, λ is the X-Ray wavelength, d is the spacing between atomic planes and 2θ is the scattering angle in the plane of the source

and detector.

The Bragg law is simply a consequence of the periodicity of the lattice and makes no reference to the arrangement of atoms in the basis associated with each lattice point. This way, the Bragg law merely represents the minimum condition for diffraction of X-rays by a set of parallel planes. The amount of radiation reflected, if any, when the Bragg condition is met depends on the structure factor; a mathematical description of how the crystal scatters incident radiation. This essentially determines the scattering at a given angle by multiplying the scattering strength of (i) an electron or nucleus, (ii) an atom, (iii) an unit cell and (iv) the total number of unit cells, all with regard to the direction of scattering and the relative phase of the scattered waves. The phases may add up or cancel, hence some reflections are not seen.

In this study XRD is used to:

- examine the crystallinity of the samples
- find the crystal structure of a material
- determine the preferred orientation of the grains

Finally giving access to the crystal structure of the material, with the preferred crystalline orientation and the lattice length using reference database for comparison [79].

2.3.3.2 Advantages, limitations and constraints

Main limitation of XRD is the obligation to use thick layers to have a visible diffracted signal. Besides, crystallography is influenced by the thickness of the layer, a thin layer can be amorphous and at some thickness there may be enough energy in the system to change towards a crystalline structure. As a consequence, for thin layers if no signal is acquired it does not mean that the layer is amorphous, it may be a limitation from the sensor or acquisition time resulting in a low signal/noise ratio.
With thick layers, XRD is a powerful and rapid (<30 min) tool for identification of the crystal phases in a material. Moreover, identification of the phases is clear with the important database available. Determination of the peaks present in the spectra is relatively straight forward, there is no necessary deconvolution or mathematical fitting.
However, homogeneous and single phase material are best for identification of a material crystallinity. Superposition of peaks can lead to some misinterpretation of the phases really in the layer.
Last but not least, to reduce the signal/noise ratio and acquire a better signal the needed time of measurement is exponential.

2.3.4 Secondary and Transmission Electron Microscopy

2.3.4.1 Technique description

In electron microscopes, samples are imaged by electron beams that are used as "illumination sources".
An electron beam has a wavelength many orders of magnitude shorter than that of light (for example, 100keV electrons have a $\lambda = 3.7$ pm), which gives much higher spatial resolution than what is achieved by optical microscopes. Instead of optical lenses, electron microscopes rely on magnetic and electrostatic fields which act as electron lenses to focus the electron beam and form images.
When a high energy electron beam hits a sample, various interactions between the electrons and the atoms take place, as can be appreciated from the figure 2.15. These interactions give important information about the structure of the matter.

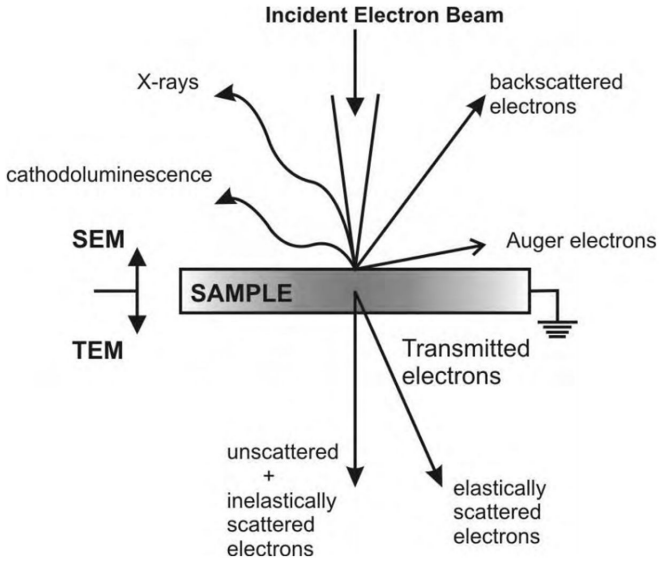

FIGURE 2.15: *Schematic representation of interactions that result from an electron beam hitting a sample*

For surface imaging the secondary electrons are used in a Scanning Electron Microscope (SEM). Indeed, the number of secondary electrons is a function of the angle between the surface and the beam. On a flat surface, the plume of secondary electrons is mostly contained by the sample, but on a tilted surface, the plume is partially exposed and more electrons are emitted. By scanning the sample and detecting the secondary electrons, an image displaying the tilt of the surface is created. The image is obtained by raster scan pattern of the sample, to achieve a maximum resolution of a few nanometre.

For better resolution Transmission Electron Microscopy (TEM) can be used. Figure 2.15 shows that some incident electrons are transmitted for samples thin enough. In a TEM the transmitted electrons are focused into an enlarged image on a sensitive screen. Depending

on the interactions that occur within the specimen the transmitted electrons can be identified in three groups: unscattered, inelastically scattered and elastically scattered electrons. Unscattered electrons go through the sample without any interaction occurring. They do not change either their trajectory or their energy. Inelastically scattered electrons interact with the sample atoms, losing some energy due to the collisions, but the process occurs with very little deviation. Finally elastically scattered electrons interact with the heavy atoms and their trajectory is affected without loosing any, or very little, energy.
The essential specimen requirement for TEM analysis is that the sample must have low electron energy loss, so that a sufficient amount of electrons are transmitted and form an image. Therefore, TEM samples must be thin enough in the travelling direction of the electrons to avoid strong inelastic collisions and electron energy loss. Thin films of the order of 100 nm are usually required for good images acquisition.

2.3.4.2 Advantages, limitations and constraints

Depending on the wanted magnification, SEM is an easy to operate tool with rapid acquisition (less than 5 min).
On the other hand, TEM sample preparation, which includes griding and ion beam polishing, is time-consuming. Once the sample is ready, TEM observation requests an important stabilisation time of the chamber vacuum and sample vibration, which makes it not easy to control and requires long analysis time.

SEM and TEM analysis are done in Ultra-High Vacuum (UHV) to limit the interactions between the electrons and the atmosphere of the chamber. And to pump to UHV faster small acquisition chambers are in use, which makes it necessary to cut the wafers before observation. These two techniques are thus considered as destructive observations.

Thin layers can be difficult to observe by SEM because of a charging effect appearing when the sample is not conductive, or for layer of less than 2 nm due to the small volume of conductive material, especially when deposited on an insulating layer (i.e. metal gate on high-κ dielectric).

Finally whereas SEM can give only some approximation of the dimensions as it is not calibrated, TEM can use the visible crystalline Si lattice for size comparison and precise estimation of layers thicknesses.

2.3.5 Electrical measurements

2.3.5.1 Technique description

To obtain the electrical characteristics of a metal the Capacitance-Voltage (C-V) and Current-Voltage (I-V) measurements are used[3]. These measurements are made on a MOS capacitor, which is basically a MOSFET without source and drain. Electrical measurements offer a lot of information on the metal, the dielectric, the SiO_2 interfacial layer and the interfaces, with an extraction of the equivalent oxide thickness (EOT), flatband voltage (V_{FB}), threshold voltage (V_T) and leakage current (J_g).
Measurements are done using probes to connect the electrical bench with the sample made of a plug, a conductive metal, an insulating dielectric and the semiconductor substrate, as presented in figure 2.16.

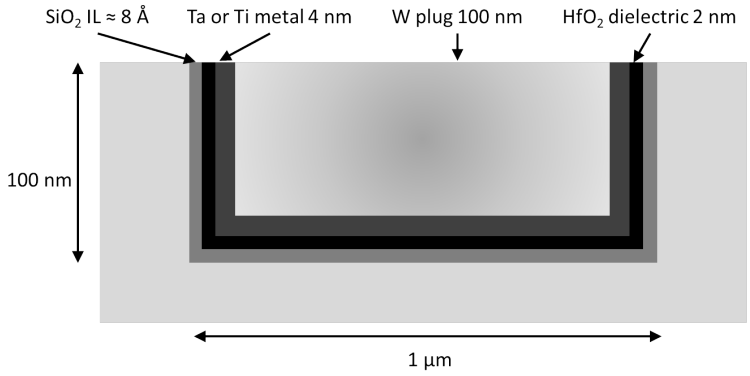

FIGURE 2.16: *Schematic representation of the capacitor used for electrical measurements*

From the hysteresis curve are extracted the EOT, the work function, the amount of default at interface and the current leak. The targeted work function and current leak gain are given in the figure 2.17, left and right respectively.

The current leakage gain compared to SiO_2 at the same thickness is given by the lines with the number of decades gained. HfO_2 which was chosen as dielectric for the metal-gate application is expected to have a current leak gain of 10^4 compared to SiO_2.

2.3.5.2 Advantages, limitations and constraints

Main advantage of the electrical measurement, which can also be considered as a constraint, is the necessity to have a plug for connection between the metal gate and the measurement probe. It is an advantage thanks to the thermal budget used for deposition of the plug, budget also present when the metal is integrated in a device. However, this thermal budget may be a constraint as it can impact the properties of the studied stack.

[3]Capacitance is defined by the amount of charge stored between the electrodes when applying a unit voltage.

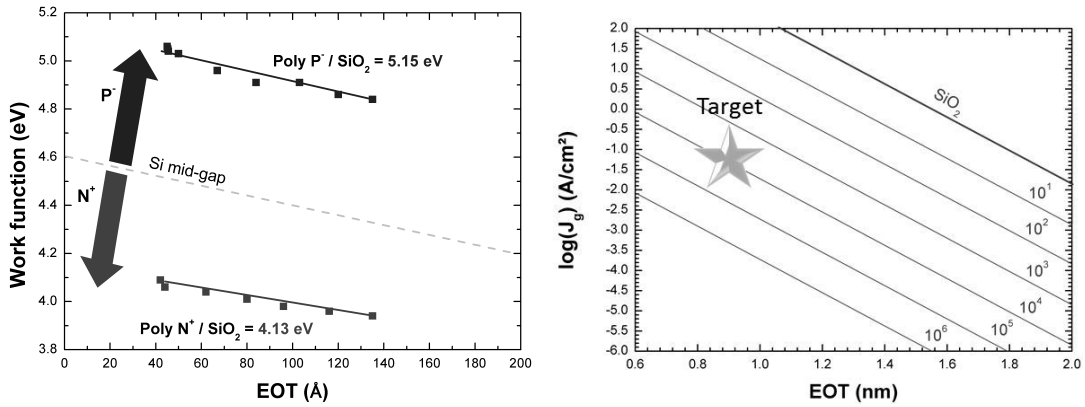

FIGURE 2.17: *Targeted work function for p-mos and n-mos transistors (left) and expected current leakage gain compared to SiO_2 (right) for 14 nm technology node*

Physico-chemical measurements are always done before plug deposition, due to the important thickness of the plug compared to the depth of measurement of XPS for example. Hence, thermal budget of plug deposition has to be taken into account when comparing the physico-chemical measurements and the electrical characteristics of a metal/dielectric stack.

Like every other measurement, electrical characterisation becomes more and more complicated as the thickness of the layers studied shrink. Because of the high leakage current and low EOT the ratio signal/noise is decreasing and extraction of electrical characteristics calls for huge knowledge background of both the electrical properties of materials and the changes that might be brought by process deposition.

2.3.6 X-Ray Photoelectron Spectroscopy

X-Ray Photoelectron Spectroscopy (XPS) or Electron Spectroscopy for Chemical Analysis (ESCA) is an electron spectroscopy method which uses X-Ray to eject electrons from their core level. It is a surface analysis technique (maximum analysed depth is about 10nm) which can be used for every solids, is non-destructive for conductive materials and allows the detection of every elements except hydrogen and helium [80–83]. This technique is quantitative and permits the determination of composition from the analysed sample, bonding environments (also called chemical environments) of each element is also at reach.

2.3.6.1 Principle

The principle of photoelectron spectroscopy is based on the interaction between an electromagnetic wave (X-Rays) and a material (atoms). Since the XPS spectrum directly reflects the electronic structure of a material, it provides information on electron configuration and energy levels within atoms. The process of photoelectron emission from a solid is divided into 3 stages:

a. First, X-Rays are absorbed by atoms, and photoelectrons are emitted (photoelectron emission process);
b. Next, part of the photoelectrons generated within the solid move towards the surface (electron attenuation length (escape depth));
c. Then, the photoelectrons which have reached the surface are emitted into the vacuum (work function).

To limit any interaction between the emitted photoelectrons and the atmosphere of the analysis chamber, an Ultra-High Vacuum (UHV) of minimum 10^{-8} Torr is necessary. Thus, the depth of analysis is defined by the second stage of electron attenuation, as the deeper the photoelectron is emitted in the material the more collisions and energy loss are likely to happen.

Photoelectron emission process and work function

Surface of the sample is irradiated by a beam of X-ray photons. Core levels with lower energy than X-rays energy can be excited and emit an electron by photoelectric effect, at a given energy. Measurement of this kinetic energy informs on the binding energy of the main electronic levels from each elements after the following equation:

$$E_k = hv - E_l - \Phi_{det} \tag{2.5}$$

where E_k is the kinetic energy of the electron entering the sensor (measured), hv the X-ray photons energy (known), E_l the binding energy of the core level electron (referenced in relation with Fermi level of the sample) and Φ_{det} the work function of the spectrometer (constant and known).

XPS analysis gives access, with high precision, to every energy levels for each element present at the surface of the analysed sample. Binding energies are specific to each element and are influenced by the chemical environment, i.e. by chemical bonds of the element with its neighbours.
Thus, XPS gives access to information on:

- *qualitative and quantitative identification* of all elements presents at the surface of the sample;
- *identification of chemical environment* for each element by analysis of electronic levels shifts compared to referenced levels.

But before getting to these two information, three principles have to be introduced.

Electron attenuation length (escape depth)

Photoelectrons generated within a solid interact with other electrons, plasmons, phonons and will gradually lose their energy. Thus, only those photoelectrons that are generated near the top surface of the solid can escape from the sample into the vacuum.
The attenuation length of photoelectrons is defined as the average distance at which the number of electrons escaping without energy loss due to inelastic scattering decreases to $1/e$

(36.8%) [84] of the original value. Attenuation length physically determines the analytical region in depth and ranges from 4 to 10nm in XPS, depending on the material density, conductivity and mass attenuation coefficient.
In practice, attenuation length is the inelastic mean free path empirically obtained by overlayer film method, but the measurement results fluctuate considerably due to the influence of elastic scattering and the difficulty in the experiment. The inelastic mean free path, theoretically calculated from the energy loss function, can also be used instead of attenuation length [84].

XPS spectra composition

Spectra obtained by XPS are composed by:

- *Photoelectrons peaks*: they correspond to the photoelectrons emitted by core level. With high intensity, narrow and generally symmetrical, these peaks are the one used for XPS analysis. They are referenced in literature with energies given depending on their neighbours [81].
- *Auger peaks*: they are a product of Auger electron emission when an electron from upper material takes the place of a core electron ejected by photoemission. Thanks to reference tables they are easily identifiable and can be used for Auger spectroscopy. Their kinetic energy is independent from the source energy.
- *Shake-up and shake-off satellite peaks*: shake-up features occur when additional electron energy level transitions take place during the photoelectron emission process. Shake-off is a sudden change in Coulombic potential as the photo-ejected electron passes through the valence band.
- *Plasmon peaks*: they originate from collective excitations of the valence band. Extrinsic plasmon are excited as the energetic photoelectrons propagates through the solid after the photoelectric process. But intrinsic plasmon correspond to the screening response of the solid to the sudden creation of the core hole in one of its atom.
- *Background*: Electrons emitted within the sample may undergo inelastic collisions thus altering the energy of the electron recorded by the detection system. These energy loss processes result in a background of counts that derives from electronic states other than the characteristic energies for the photoelectric lines, but moreover the shape of the background takes on a character determined by the probability distribution for electrons with a given kinetic energy undergoing some modification to their initial value. Only empirical models can be used to subtract the background in a spectrum [85].

All these features are visible on the Ti*2p* spectra displayed in figure 2.18.

Charging effect

It is noteworthy that XPS analysis of an insulating sample leads to charging effects at the surface. This charging is caused by positives residual charges, originating from photoelectrons emission, which cannot discharge due to the insulating properties of the material. The charges create a surface potential which can slow down the photoelectron and thus move the

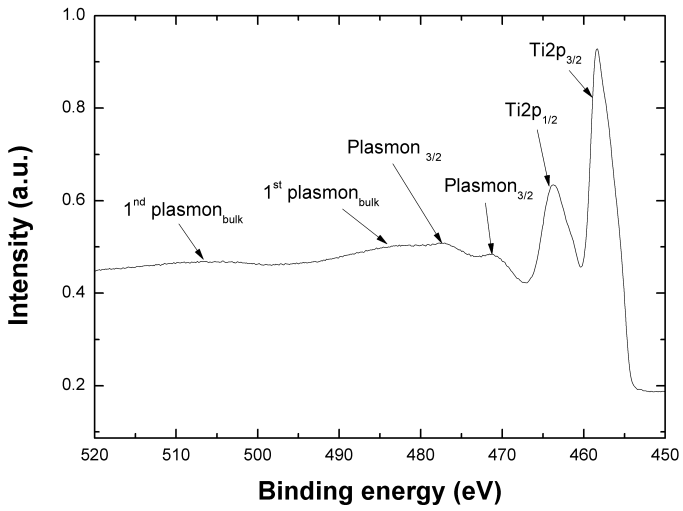

FIGURE 2.18: *XPS spectra composition, example of Ti2p core level*

measured binding energies toward higher energies. It is possible to reduce this effect using a flood gun which neutralises the surface of the sample or by subtracting a charge correction factor from all binding energy using reference peaks [80].

2.3.6.2 Quantitative analysis

Peak intensity in a photoelectron spectrum due to an element is generally determined by three major factors: photoionisation cross section (σ), electron mean free path (λ) and analyser transmission (T). The peak intensity (I_i) of element i in an uniform sample is expressed in the following equation:

$$I_i = C_i\sigma(\sigma_0, \alpha, \beta)\lambda(s, E_i)T(E_i) \tag{2.6}$$

where C_i is the concentration of element i, σ_0 the total photoionisation cross section, α the angle between the directions of photon (X-Ray) incidence and photoelectron emission, β the asymmetry parameter indicating the angle dependence of emitted photoelectron, and E_i the kinetic energy of electrons from element i. The electron mean free path mentioned here is the inelastic mean free path determined by the kinetic energy of the electrons and the nature of the surface. The analyser transmission varies depending on the kinetic energy of the electrons analysed.

There are two major methods for quantitative analysis by XPS; one uses standard samples and the other relative sensitivity factors. Due to the impossibility to use standard sample for new material analysis, relative sensitivity factors were used in this study.
If R_i is the relative sensitivity factor of element i, the concentration C_i is expressed in the following equation:

$$C_i = (I_i/R_i)/\sum_j (I_j/Rj) \tag{2.7}$$

where j runs over all elements present. R_i is given by $R_i = \sigma\lambda(s, E_i)T(E_i)$.

The equation indicates that the relative sensitivity factor method requires the photoionisation cross section and the analyser transmission, in addition to the electron mean free path. Detection sensitivity of XPS, while it varies with the type of elements and sample, is lower than 1 at.%.

Example of evolution of the peak intensity with the concentration increase is presented in figure 2.19. On this figure are presented the Si*2p* peaks for four samples with respectively 7, 13, 18 and 21 Å of SiO_2 on a Si substrate.

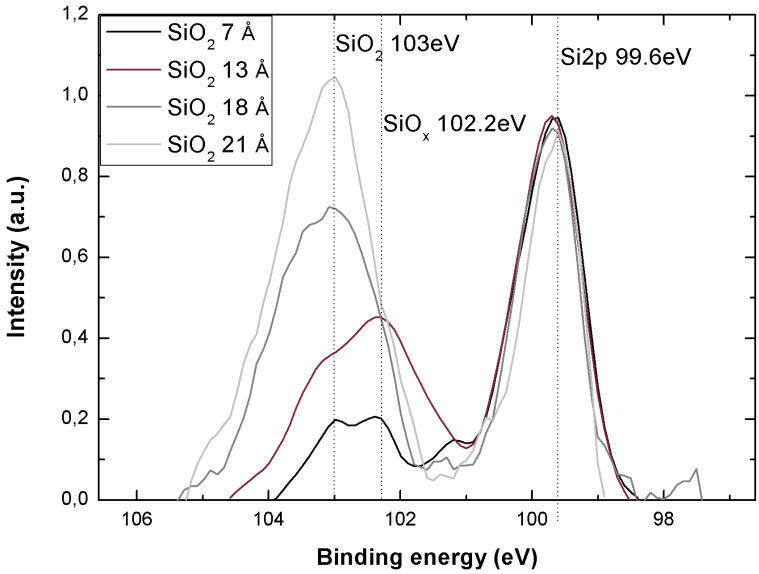

FIGURE 2.19: *Quantitative and qualitative analysis of XPS spectra for samples with variation of SiO_2 thickness*

It appears that the peak area of the Si^{3+} and Si^{4+} environments, corresponding to SiO_x and SiO_2 respectively, is proportional to the thickness of the layer.

2.3.6.3 Qualitative analysis

A more detailed examination of the peak shapes can provide information regarding the chemical environments of the atoms.
Atoms in different chemical environments experience different screening and relaxation effects, and as such present slightly different binding energies. An XPS peak may therefore be viewed as a number of superimposed peaks. An example is shown figure 2.19 with the presence of Si, $SiO_{x,x<2}$ and SiO_2 bonding environments. On this figure, for the thinnest layer, 7 Å the SiO_x binding environment is observed and disappears with the thickness increase to the profit of SiO_2 binding environment.
Each environment creates a peak shape simulating experimental and instrumental broadening of the energy levels. Peak fitting involves attempting to fit the experimentally obtained spectra with a number of these peaks, under suitable constraints. Typically the Full Width

at Half Maximum (FWHM) and the line shapes made of Lorentzian and Gaussian are constant for all peaks, binding energy shifts between peaks are informed by the literature [81] and database [86].

The suitability of a simulated fit may be judged either manually by ensuring the main feature of the spectrum are present or by minimisation of a calculated P^2 figure of merit provided by fitting programs. In practise a mixture of the two is typically used.

2.3.6.4 Angle Resolved XPS (AR-XPS)

The sampling depth of XPS depends upon a number of factors including sample matrix, composition and photoelectron kinetic energy, and is typically in the 4-10 nm range. If the sample is not homogeneous, then XPS analysis will sample a range of compositions and return a weighted average. Ideally, therefore, every XPS analysis should consist in the determination of the complete concentration depth profile within the analysed volume. In many samples, this can be accomplished by means of ion etching. But there are occasions, however, when ion etching is inappropriate, for example in the case of sample, which are thin or contain easily migrating compounds (O or N), and so the sample would undergo chemical degradation. In such cases it is possible to employ angle-resolved XPS (AR-XPS), in which the sample or sensor is tilted so as to vary the angle between the axis of the photoelectron analyser and the normal to the sample surface.

The basis of the angle dependent profiling method can be seen in the cos ϕ dependence of the electron signal. For a given electron energy, varying the take-off angle changes the effective mean escape depth between its full value at $\phi = 0^\circ$ and a minimum at glancing take-off angles. The total probing depth is limited to about three times the inelastic mean free path (typically <10 nm) while the depth resolution is generally limited by the experimental error in the intensity measurement. For the example of a smooth homogeneous layer of element A of thickness d on a substrate B, the normalised intensities are given by:

$$I_A/I_A^0 = 1\text{-}exp(-d/\lambda_{A,A}^0 cos\phi) \tag{2.8}$$

$$I_B/I_B^0 = exp(-d/\lambda_{B,A}^0 cos\phi) \tag{2.9}$$

where $\lambda_{A,A}^0$ is the inelastic mean free path of A electrons in A and $\lambda_{B,A}^0$ is that of B electrons in A.

2.3.6.5 Advantages, limitations and constraints

Because in the experiments presented further eight angles are acquired during AR-XPRS, the signal on each angle corresponds to less than the eighth of the total emitted signal by

the sample. As a consequence, the acquisition time needed to obtain high signal/noise ratio is increased by a factor ten approximately.
Penetration of the X-rays in the material follow a Monte Carlo law, resulting in a non-linear response of the material depending on the depth. Information from the middle of the penetration depth is the most intense. Moreover, the signal from volume material is reduced by absorption of the top layers (cf attenuation length paragraph).
All of this leads to difficult extraction of depth information and make it possible only with the dedicated software.

Chapter 3

Process influence

"Ideas are like rabbits. You get a couple and learn how to handle them, and pretty soon you have a dozen."

John Steinbeck, author

3.1 Introduction

As presented in the Chapter 1, microelectronic requires more and more advanced deposition techniques. The latest challenge is to successfully deposit thin conformal layers of 2 nm or less, on all sides of a 3D pattern, including perpendicular surfaces.
MOCVD and ALD are the most promising techniques for conformal deposition [35, 44], however it is necessary to qualify the process windows and understand the phenomena taking place during deposition to find the best material with a repeatable process.

In order to assess the reaction mechanisms taking place during (PE)MOCVD/ALD deposition, an investigation of the deposition parameters influence on the deposited metals was carried out. Every investigation presented in the following discussion were carried out for both titanium and tantalum materials. To limit repetitions only the results for one of the metals are introduced and discussed in this work. If a different behaviour was found for both metals then the two results are included.

In a MOCVD and ALD process the parameters can be divided into two categories: the parameters influencing the reaction mechanism and influencing the uniformity. The parameters governing the reaction mechanism include substrate temperature, saturation levels of precursors and reactant gas, vapour pressure of the precursor and the bubbler (in the case of ALD) or liquid injectors (in the case of LIMOCVD) temperature [35, 44]. The sticking coefficient of the precursor on the substrate, flow rates, deposition rate, pressure of the chamber, substrate-shower distance and residence time[1] are part of the uniformity parameters.

[1] Residence time (also known as removal time) is the average amount of time that a particle spends in a particular system. Therefore, in the PEMOCVD case it is the time necessary for a precursor to go from the injector to the substrate.

Even though both types of parameters were investigated, only the reaction mechanism parameters influences are introduced thoroughly in this work. Parameters affecting the uniformity of the deposited layer are introduced to only demonstrate their influence and are not discussed in details.

3.2 TaN MOCVD process parameters evaluation

3.2.1 Context

TaN deposition was investigated in depth due to the wide range of properties reachable depending on the deposition method and process parameters. For example the crystalline structure of sputtered TaN_x changes from NaCl-structure to hexagonal when sample temperature goes above 650°C [87]. Besides, change from Ta_3N_5 to TaN composition was observed for ALD deposition with $TaCl_5$ precursor under NH_3 reactant gas when additional zinc reactant gas was introduced [88]. Resistivity of the layer is also reduced by H_2 plasma treatment of the layer [89–91]. Finally, work function of ALD Ta(C)N can be tuned up to 4.9 eV by increasing the amount of (or introducing) carbon present in the layer [50, 92].

Influences of the most significant parameters leading to MOCVD deposition of TaN using TBTDET precursor with NH_3 reactant gas are reported in this part.

3.2.2 Methodology

Liquid Injected MOCVD (LIMOCVD) of TaN was performed on the AltaCVD Advanced Materials^{TM} reaction chamber presented Chapter 2. The precursor used is the TBTDET, stored in a canister kept at ambient temperature. Ar was chosen as inert gas for precursor transportation from the canister to the evaporation furnace (see Chapter 2 for complete description of the tool). Depositions were done on Si (1 0 0) surface without pre-treatment, thus with a native oxide layer, or on wafers with 100 nm SiO_2 thick layer for resistivity measurement.

Thickness and density were extracted after careful fitting of XRR spectra. In the theoretical models a surface oxide layer was added for better matching to experimental spectra, this oxidation of the metal surface was confirmed by XPS analysis of the samples. XPS analysis was performed with a Kα source and a beam spot of 400 μm at 100 eV with a step resolution of 0.1 eV. Bonding environment of Ta, C, N and O are obtained from Ta*4f*, C*1s*, N*1s* and O*1s* core level energies respectively. No cleaning was done before XPS analysis, leading to the presence of atmospheric contamination oxygen and carbon [93]. Finally, resistivity was calculated from four point probe resistance measurement and thickness extracted from XRR.

3.2.3 Substrate temperature

Substrate temperature is an important parameter in MOCVD and ALD deposition techniques, as it is the only parameter which brings the energy requested to activate the decomposition of the precursor and to activate the nucleation sites.
Deposition temperature windows are ruled by the precursor properties and the reactant gas in use. To deposit the material with the best characteristics the temperature has to be carefully chosen to be high enough to activate the deposition mechanism but not too high to avoid the depletion region, as detailed Chapter 2 section 2.2.2.1. Each precursor is developped to favour one reaction mechanism with one particular reactant gas, and thus each precursor has a specific deposition temperature window.

First, an attempt of deposition without a reactant gas was done. Only a monolayer was formed at the surface of the substrate whatever the used temperature, indicating a decomposition of the precursor but no activation of the nucleation sites for further growth. Then, using the same deposition parameters a reactant gas was introduced in the chamber leading to the activation of the nucleation and to the growth of materials. A variation of reactant gas is presented here, before the introduction of plasma for deposition activation, in Chapter 4.

3.2.3.1 Deposition with NH_3 reactant gas

Evolution of TaN deposition rate and density were studied for TBTDET precursor under a NH_3 reductive ambiance, with substrate temperature increase. Results are presented in figure 3.1, with a logarithmic scale of the growth rate depending on the reverse of the temperature expressed in kelvin. This disposition allows to highlight the Arrhenius law (equation 3.1) behaviour of the growth rate [72].

$$k = Ae^{-E_a/k_BT} \tag{3.1}$$

with k the rate constant of the chemical reaction, A a pre-exponential factor, E_a the activation energy, T the temperature in kelvin and k_B the Boltzmann constant.
This evolution of the deposition rate with substrate temperature was explained Chapter 2, in the introduction to MOCVD deposition.
As expected growth rate increases with the temperature and follows the Arrhenius law, indicating a chemically driven deposition. The activation energy[2] of the reaction is given by the slope of the line fitting the evolution between 250°C and 400°C (see figure 3.1). In the case of TaN MOCVD deposition with NH_3 reactant gas, the energy of activation is E_a = 0.46 eV. Values of activation energy from MOCVD reaction, reported in the literature, are included in the 0.9 - 1.1 eV range, corresponding to thermal decomposition of the transition

[2]The activation energy corresponds to "the minimum amount of energy required to initiate the reaction" [72], and consequently a low activation energy connotes a reaction activated at a low temperature, and reciprocally.

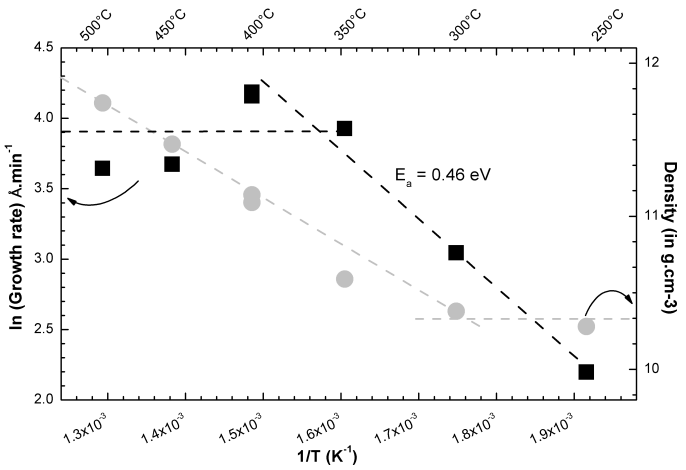

FIGURE 3.1: *TaN growth rate and density plotted as a function of the substrate temperature*

metal metalorganic precursors [58, 94–96]. The lower activation energy calculated here may be associated to the different method of injection used (LIMOCVD) which can facilitate the decomposition of the precursor and thus reduces the activation energy. For instance a reduction by a factor 2.6 of the energy of activation was reported in the case of LICVD copper deposition [97] compared to CVD copper [98].

Growth rate reaches a maximum at 350°C, from where there is no more evolution with further increase of the temperature: a plateau is reached. If the deposition temperature is chosen above or equal to 350°C, then the reaction mechanism is the most efficient. Indeed, for the same quantity of precursor entering the deposition chamber, the thickness of the processed layer is the highest. The two regimes observed here correspond to the kinetic control region (the slope) and the diffusion control region (the plateau). Further increase of the temperature of deposition to reach the depletion regime was not possible due to hardware limitations of the deposition chamber.

An XPS investigation of 4 nm thick TaN layers deposited between 250°C and 400°C revealed that the lowest is the deposition temperature, the highest gets the oxidation of the layer. To avoid any influence of the oxidation rate, time between deposition and XPS analysis was kept constant for all the samples. An ARXPS analysis of both 250°C and 400°C deposited TaN highlighted that the oxidation levels are homogeneous in the volume of both TaN. However, a minimum of oxidation is reached from approximately 300°C. Figure 3.2 presents the Ta-relative atomic percent of N, O and C elements in the layer deposited at temperatures from 250°C to 400°C. In average layers were made of 20 % at of Ta.

An hypothesis explaining the lower oxidation level observed in the figure 3.2, is a higher resistance to oxidation taking place at vacuum break obtained at higher deposition temperature due to the consolidated Ta-N bonds. Indeed, when the temperature is increased, the energy brought for the creation of Ta-N bonds is higher, resulting in more stable bonds

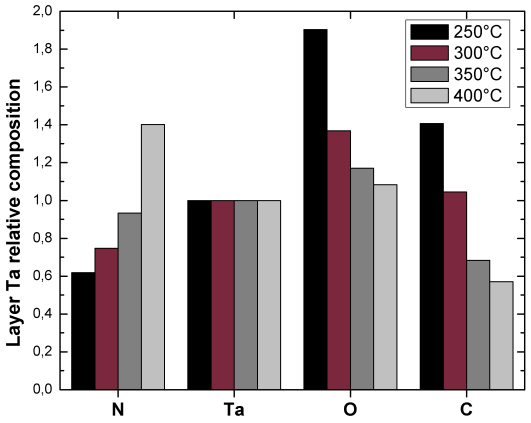

FIGURE 3.2: *TaN layer compositions for different substrate temperature*

which limits the oxidation of the layer at vacuum break, similar oxidation mechanism was already proposed elsewhere [99]. This hypothesis is supported by the evolution of N content evolution, presented in figure 3.2. It is noteworthy that the N*1s* spectra (not shown here) reveal that not all the N observed in TaN layer is bonded to Ta, part of it creates bonds with O or keeps its initial bonds with C.
It also appears, in figure 3.2, that the carbon content of the layer decreases as the deposition temperature increases. The minimum carbon content is obtained at 400°C and corresponds to the atomic percent of carbon added in average from atmospheric contamination at vacuum break [93]. Thus, the higher carbon content observed at lower temperatures is probably due to non-complete decomposition of TBTDET molecule, resulting in the presence of carbonated reaction by-products.

The observed amounts variation of oxygen and nitrogen in the layers, is in good agreement with the increase of the density presented in figure 3.1, left axis. In fact, it is well known that the density of Ta_2O_5 is lower than the density of TaN, at 8.2 g.cm^{-3} and 12.5 g.cm^{-3}, respectively [100]. As for N content in TaN layer, presented in figure 3.2, the density is slowly increasing till 350°C, from where a fast rise is observed, figure 3.1.
Similar densities of TaN were obtained with other deposition methods, such as PVD (10.2 g.cm^{-3}) [101], CVD (9.7 g.cm^{-3}) [101], ALD (7-9.2 g.cm^{-3}) [102] and PEALD (10.5-11.5 g.cm^{-3}) [16]. The relatively high density of the layer obtained here suggests a low carbon contamination and an efficient deposition process.
It was further reported that, in the case of TaN deposition by sputtering, an increase of the deposition temperature favours the crystallisation of the layer [103], leading to a gain in density. Crystallisation increase of materials with temperature and deposition time increase is generally true, example on HfO_2 crystallisation behaviour with both deposition temperature and deposition time was reported in details [104]. Furthermore, higher crystallinity of TaN layer can decrease the oxidation of the metal (i.e. limit the creation of Ta-O bonds) [105].

In summary, 350°C was found to be the minimum substrate temperature required to obtain the most stable TaN layers, with the highest Ta/N ratio, highest density and most efficient deposition reaction mechanism (highest growth rate).

3.2.3.2 Deposition with H_2 and NH_3/H_2 mixed reactant gas

A study of the growth rate evolution was performed regarding the introduction in the chamber of reactant gas H_2 and NH_3/H_2 mixture. Reactant gas flows were calculated to have excess of reactant gas for both NH_3 and H_2 when using single reactant gas and no excess for the mixture of NH_3 and H_2. This methodology allows to separate the effects of each reactant gas and determine the possible reaction path.

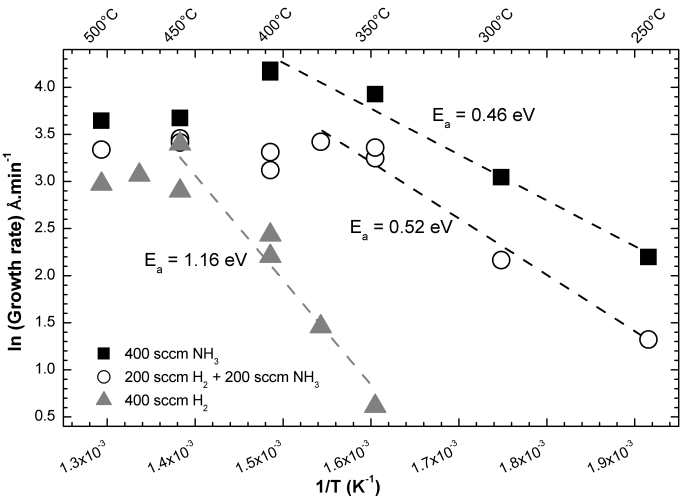

FIGURE 3.3: *Evolution of the growth rate for different reactant gas with variation of the substrate temperature*

Figure 3.3 reveals that the three gases used for deposition have in common an increase of the growth rate with increasing temperature until a plateau is reached at high temperature. The 250 - 500°C temperature window allows to observe both the kinetic control region and the diffusion control region. The energy required to activate the deposition reaction at the substrate surface is not the same for the three environments. If the chamber is saturated by NH_3, as presented earlier the activation energy is about $E_a = 0.46$ eV. Then, if only H_2 is introduced in the chamber during the deposition, the activation energy is going up to $E_a = 1.16$ eV. Finally, in between, when the mixture of NH_3/H_2 is used the activation energy increases from $E_a = 0.48$ eV to $E_a = 0.52$ eV.
This behaviour suggests that NH_3 gas is more reactive than H_2 gas and a shortage of NH_3 reactant gas leads to the increase of the deposition activation energy.

Density of the TaN layers deposited with NH_3, H_2 and the mixture of NH_3/H_2 are displayed figure 3.4.

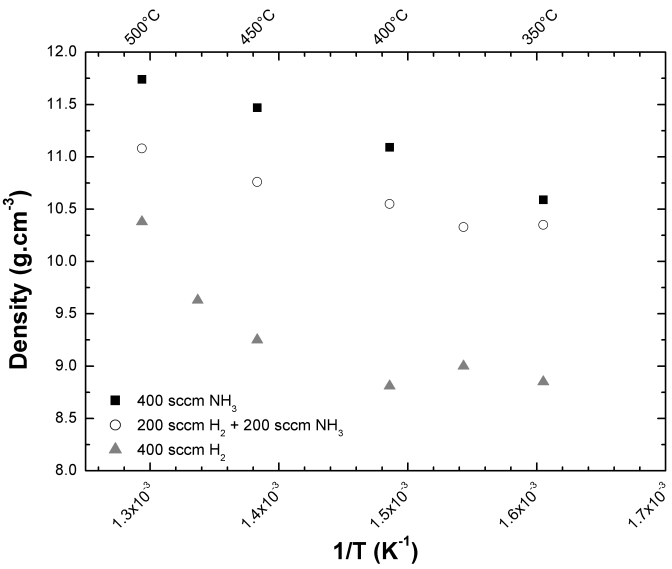

FIGURE 3.4: *Evolution of the film density as a function of the substrate temperature for different reactant gas*

A similar behaviour as for the growth rate is observed for the density evolution of TaN. The maximum being obtained for NH_3 reactant gas at high deposition temperature. H_2 reactant gas leads to the formation of low density layers, with a fast density increase from 450°C. The mixture of NH_3/H_2 results in the formation of a layer with densities comprised between pure NH_3 and pure H_2 deposition.

One notices that depositions done at the lowest temperature (i.e. $\leq$ 300°C with H_2 and $\leq$ 200°C with NH_3) present a monolayer of TaN on the substrate. This monolayer suggests that there was saturation of the substrate surface, where TBTDET molecule stick on initial nucleation sites. But no further nucleation sites, on top of TBTDET saturated surface, are available due to the low activation temperature; therefore, there is no further growth of the layer.
Change of the reactant gas influences the activation energy of the deposition and the maximum growth rate. Indeed, when NH_3 is saturating the chamber atmosphere a growth rate of 1.11 Å.s^{-1} is reached at 400°C. Whereas with H_2 and NH_3 + H_2, maxima of 0.37 and 0.55 Å.s^{-1} are reached at 450°C, respectively, so NH_3 gas reactant results not only in lower activation energy of the deposition reaction but also in a more efficient deposition. This point will be discussed further and a possible reaction mechanism will be proposed later in this chapter, section 3.2.7.

Binding energy, extracted from XPS analysis, of the Ta metal atoms is presented in figure 3.5 (left), with the Ta and N atomic percent, versus the used reactant gas. Comparison of Ta binding energy for TaN deposited with NH_3, NH_3 + H_2 and H_2 at 350°C is given in figure 3.5 (right).

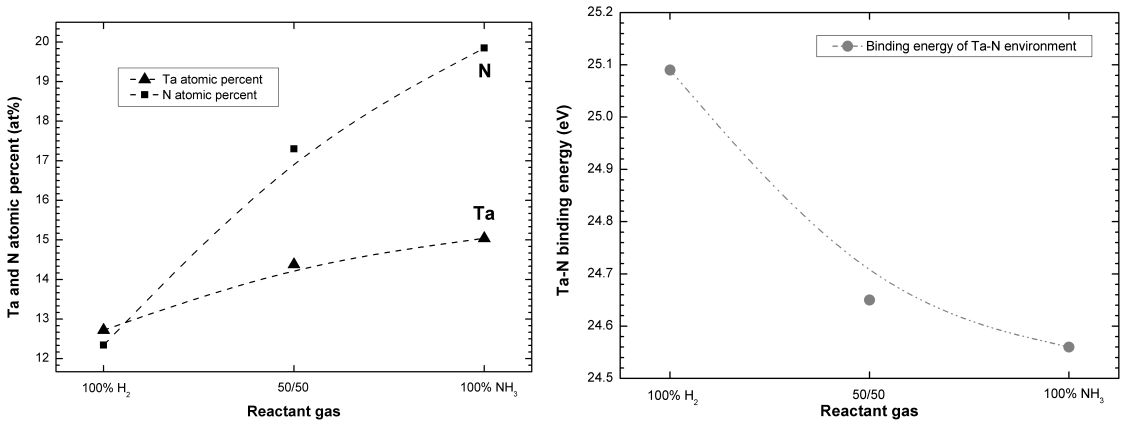

FIGURE 3.5: *Evolution of composition and TaN-Ta4f binding energy as a function of the reactant gas (at 350° C)*

It appears that the N/Ta ratio is 30% higher for NH_3 reactant gas, with a lower oxidation level; both resulting in the decrease of Ta atoms binding energy.
The change of composition depending on the reactant gas, suggests that the deposition reaction by-products include diethylamine groups. Indeed, in the precursor molecule the Ta:N ratio is 1:4, but the deposited layers with H_2 reactant gas have a Ta:N ratio of 1:1 and 3:4 when deposited with NH_3 reactant gas. The double TaN bond present in the molecule is probably the only one kept during the deposition reaction. The lower content of N in the layer deposited with H_2 suggests that during the deposition mechanism not only ethane groups but also diethylamine groups are taken away from the TBTDET molecule and substituted by H endings. A diagram presenting the path introduced here is given later in this chapter, section 3.2.7.

The carbon content of the layer is not presented here due to the absence of change whatever the reactant gas used. Meanwhile, this absence of change, highlights the fact that elimination of carbon from the precursor has the same efficiency no matter the reactant gas used. Consequently, decomposition of the precursor in carbonate by-products and exhaust of these reaction by-products do not seem to be linked to the reactant gas but are mainly linked to the temperature of the substrate, as revealed in figure 3.2.

3.2.4 Liquid injector temperature

In the LIMOCVD (Alta Advanced Materials®) reactor, the evaporating furnace can be heated to ease the vaporisation of the precursor when going through the injectors, see Chapter 2, in figure 2.7 page 23. Once vaporised the precursor enters the deposition chamber to react at the surface of the substrate. However, depending on the temperature of the injectors the precursor can be degraded, which may result into different reaction mechanisms and change the characteristics of the deposited material.

3.2.4.1 Methodology

The best set of parameters leading to deposition of optimal films are chosen from the previous study and kept constant in this section. Hence, TBTDET is introduced in the deposition chamber and reacts with NH_3 gas at 350°C.
Variation of injectors temperature was carried out from 40°C, the lowest possible temperature above which the susceptor heat is not affecting the injectors temperature regulation, to 90°C, the maximum temperature limited by the capabilities of the evaporating furnace.
XRR, four points probe and XPS analyses are carried out with the same parameters as presented earlier in Chapter 3, section 3.2.2.

3.2.4.2 Deposited thickness and resistivity modification

Evolution of TaN deposited thickness and resistivity with liquid injector temperature is given in figure 3.6, all other process parameters were kept constant. As presented in Chapter 2, the thickness variation informs on the efficiency of the reaction mechanism, whereas the resistivity gives an insight on the decomposition of the precursor molecule and on the exhaust of the reaction by-products, due to the influence of C contamination in the film.

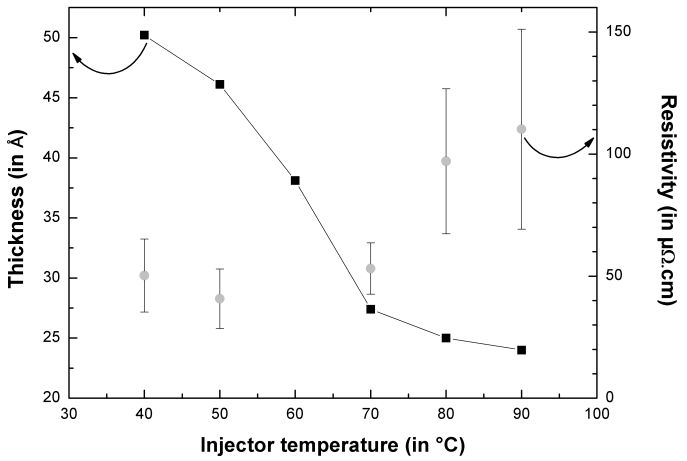

FIGURE 3.6: *Evolution of the MOCVD TaN deposited thickness and resistivity as a function of the injector temperature*

A decrease of the evaporation furnace temperature from 90°C down to 40°C multiplies the deposition rate by a factor 2. Such increase highlights that more material is deposited at lower furnace temperature, thus it is possible to suppose that the precursor is degraded and undergo a pre-decomposition in the furnace at higher temperatures. The vapour pressure of TBTDET is 140°C at 2 Torr, however acceleration of the molecules when getting out of the injector is significant (pressure changes from 2.10^3 to 2 Torr), which can already alter the structure of the precursor, through the supply of kinetic energy.
The density of the layer (not shown here) displays a similar behaviour as the thickness, it increases from 11.06 g.cm^{-3} at 90°C to 12.35 g.cm^{-3} at 40°C. The efficiency of the deposition

reaction is thus much higher for liquid injectors at 40°C, than at 90°C.

Resistivity measurements, presented figure 3.6, reveal two significant properties of the layers. First effect is the decrease of the resistivity by a factor 2.2 as the temperature of the liquid injector is reduced, below the TaN bulk resistivity of 100 μΩ.cm [100]. This reduction can be correlated to the better decomposition of the precursor on the sample and lower by-products in the layer, probably enhanced by the absence of pre-decomposition of the precursor in the evaporation furnace. Second effect is the attenuation of the measured variability on the samples for liquid injector temperature below 70°C. Better uniformity of the resistivity within the wafer may be linked to a more homogeneous reaction, which can also be associated to the absence of precursor pre-decomposition in the furnace.

3.2.4.3 Chemical bonding evolution

These modifications in resistivity with injection temperature go along with some bonding environments changes. Hence, in figure 3.7 are presented the XPS spectra of 4 nm MOCVD TaN deposited with injector temperatures from 50 to 90°C.

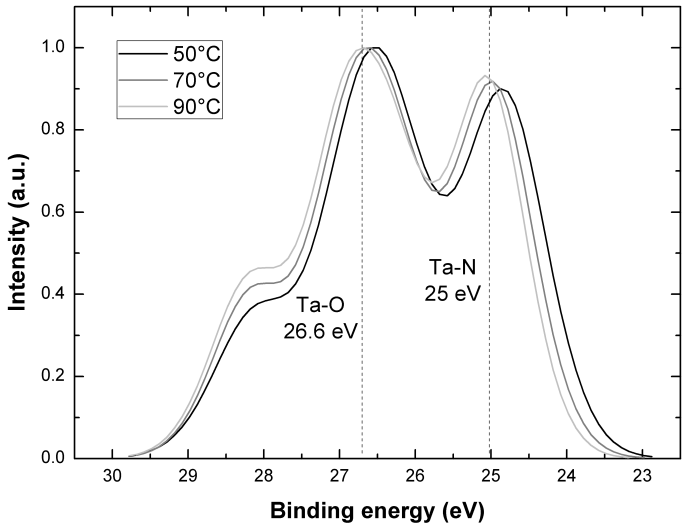

FIGURE 3.7: *Evolution of Ta4f spectra in MOCVD TaN samples for different injector temperatures from 50 to 90°C*

It appears that increase of furnace temperature results in modification of the deposited material. Two important changes of Ta*4f* binding energy are observed: first there is an increase of the oxidation level (Ta-O bonds doublet located at 26.6 eV) with temperature increase. Second, the binding energy of Ta bonded to N (Ta-N bonds doublet located at 25 eV) is shifted to lower energy with furnace temperature decrease. The energy shift of Ta-N peak, at higher deposition temperature, can be explained by a lower oxidation of the layer, thus by more nitrogen bonded to tantalum.

The changes observed in Ta*4f* spectra cannot be seen in N*1s* spectra due to the presence of the Ta*3d* peak at 404 eV, which covers some of the bonding environments of nitrogen [86]. However, the influence of injector temperature is visible on O*1s* and C*1s* spectra, displayed in figure 3.8.

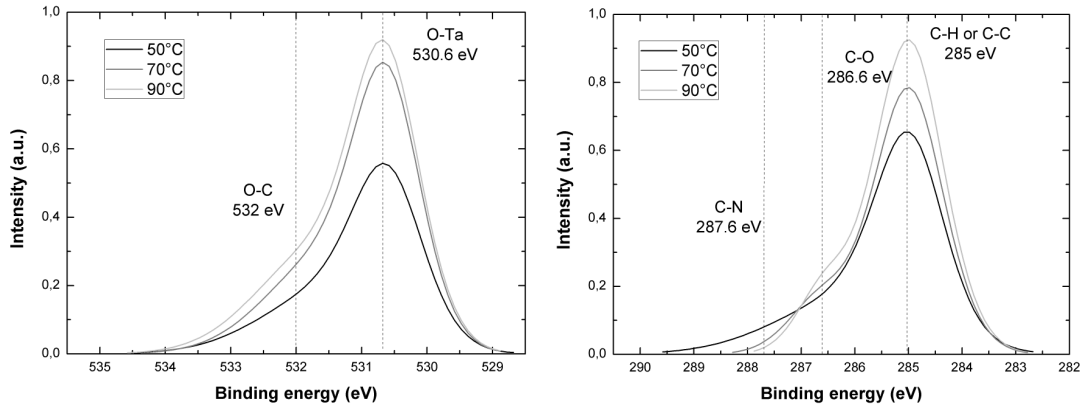

FIGURE 3.8: *Evolution of O1s (left) and C1s (right) spectra in MOCVD TaN for different injector temperatures*

On O*1s* spectra (figure 3.8 left) increase of O bonded with both Ta and C can be observed as the furnace temperature is increased. However, there is no shift in energy of the peaks meaning that whatever the injector temperature, chemical bonds between Ta and O is same. O is bonded to Ta as a first neighbour and not as a second neighbour, indeed if O would bond to TaN (O-N-Ta) and not to Ta (O-Ta) a shift of O*1s* O-Ta peak toward lower energies would be observed.
Contrary to O*1s* spectra, C*1s* spectra presents a new bonding environment when injector temperature is decreased to 50°C. In figure 3.8 right, on C*1s* spectrum of TaN deposited with a furnace temperature of 50°C, a peak corresponding to C-N bond located at 287.6 eV is revealed. This new C-N environment can be assimilated to the diethylamide groups present in the TBTDET molecule. The presence of this environment only in the 50°C injector deposited TaN layer confirms the non-activation of the precursor molecule in the evaporation furnace at 50°C, the precursor reaches the surface of the sample in a non-degraded form.

Evaporation furnace temperature influence on the composition of the layers is reported in atomic percent table 3.1.

TABLE 3.1: *Composition of MOCVD TaN for different injector temperatures*

	50°C	**70°C**	**90°C**
Ta (at%)	28.3	27.1	25.1
N (at%)	29.5	29.3	28.5
C (at%)	8.2	8.5	9.3
O (at%)	34.0	35.2	37.1

As suggested earlier by deconvolution of Ta*4f* spectra, Ta content is higher for the lowest furnace temperature. Nitrogen content has a similar behaviour but with a lower variation. The carbon content of the layer deposited with a furnace temperature of 50°C is low, considering that roughly 8 at% of carbon is brought by atmospheric contamination at vacuum break [93]. Some increase of C content with furnace temperature increase is observed. It is possible that part of the by-products, formed during the pre-decomposition of the precursors in the furnace, are deposited in the TaN layer. Carbon content rise in the layer was supposed earlier to explain the resistivity and measurements variation increase of the layer reported in figure 3.6, this supposition is therefore confirmed here.
Lastly, the oxygen content of the layer significantly increases with injector temperature increase. As introduced earlier the increase of furnace temperature modifies the chemical bonds brought into play during the deposition reaction mechanism. Thus, the Ta present in the layer forms different bonds which appear to be weaker. Weaker bonds resulting in lower stability, in turn resulting in higher oxidation of the layer.

Overall it appears that a decrease of the liquid injector temperature leads to a decrease of the oxygen content and increase of nitrogen content. It confirms that higher temperature result in the degradation of the precursor and creation of N-C_xH_y by-products in the evaporation furnace.
Thanks to the double stage shower, no reactant gas is present in the evaporation furnace, limiting, if not avoiding, deposition of TaN on the walls of the furnace which would happen after the precursor degradation. However, it appeared through different experiments not presented here, that part of the activated precursor is staying in the evaporation furnace and is released during the next deposition process, the evaporation furnace is acting as a buffer. This buffer effect has to be carefully taken into account to avoid cross-contamination of the deposited species when the deposited material campaign is changed (from TaN to TiN and reciprocally).

In conclusion, even if the decomposition of the precursor on the surface of the substrate may not be complete with a furnace temperature of 50°C, it appears that the increase of the furnace temperature results in a pre-decomposition of the precursor which degrades the properties of the deposited layer (higher resistivity, lower uniformity and lower resistance to oxidation). Also, the deposition is twice more efficient at lower furnace temperature, probably thanks to a lower buffer effect of the evaporation furnace.
Following these results, in the rest of this work the furnace temperature will be kept at 40°C to avoid activation of the precursor in the evaporation furnace.

3.2.5 Deposition kinetics

MOCVD deposition is based on a chemical reaction which, as investigated earlier, requires a minimum energy to be activated. Furthermore, a chemical reaction is also defined by a

kinetic parameter; parameter corresponding to the time needed for the reaction to be completed.

Survey of the variation fo the layer thickness with the deposition time is given in the figure 3.9 for TaN deposited at 350°C with NH_3 reactant gas and an injection frequency of 0.1 Hz. The injection frequency was chosen as low as possible in order to have more reactant gas than precursor, i.e. to have a precursor limited reaction, thus revealing the kinetics of the precursor decomposition. Impact of the injection frequency on the growth rate will be introduced later in this chapter, section 3.2.6.

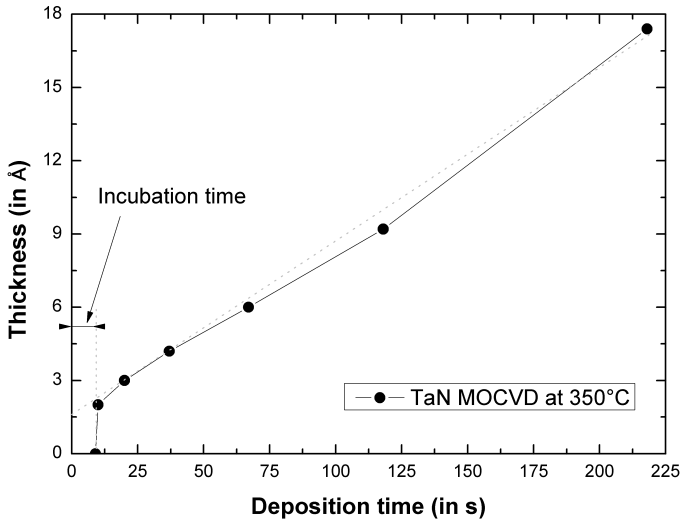

FIGURE 3.9: *Evolution of the TaN deposited thickness as a function of the deposition time*

No deposition was observed for deposition times of less than 10 s; no Ta atoms were detected using XPS. It is possible that the precursor needs up to 10 s to go through the evaporation furnace, and through the shower to reach the substrate. A two regime LIMOCVD growth was reported elsewhere and was assimilated to an irreducible time during which precursor has to be in contact with the injectors. If another deposition is done without cleaning of the chamber and within 10 min, this 10 s delay disappears. It confirms the supposition of injector surface wetting, indeed the injectors are already saturated by the precursor from the previous deposition.

For a deposition time of 10 s the thickness of the layer was too small to be measured by XRR, but an XPS analysis revealed the presence of a thin layer of metal on the substrate. By extrapolation of the Si*2p* peak intensity the thickness was estimated to be about 2 Å of TaN [3], which corresponds to a monolayer of TaN.

[3]The thickness of an homogeneous layer can be calculated using XPS and reference samples by extraction of the substrate main peak intensity. Indeed, if the substrate is covered by a layer the depth of analysis stays the same and the intensity of the substrate main peak is reduced. Reduction of the intensity depends on the thickness of the layer and on the attenuation coefficient of the layer. Due to the size of the XPS beam, this

From figure 3.9 it appears that a linear growth of the layer with time is observed after 25 s of deposition.
For deposition included between 10 s and 25 s, the deposition rate appears to increase, until the final growth rate is reached. This increase can be assimilated to a change of the surface, from substrate native oxide until the creation of the first monolayer of TaN, and thus to the change of nucleation sites.

To conclude, the linear evolution of the deposited thickness proves that the decomposition of the precursor and thus the deposition reaction is not limited by the kinetics of the reaction. In other terms, the deposition rate is not limited by the TBTDET decomposition speed in NH_3 ambiance.

A further investigation of the deposition mechanisms is introduced in the next paragraph, with the study of the injection frequency effect on the deposition.

3.2.6 Effect of the injection frequency

The evolutions of thickness, density and resistivity of the TaN layer were investigated as a function of the injection frequency. The amount of precursor entering the chamber was kept constant by a variation of the deposition time; i.e. from 100 s at 1 Hz to 1000 s at 0.1 Hz. Here again the chamber atmosphere is saturated in NH_3.
Resulting thickness and deposition rate are presented in figure 3.10.

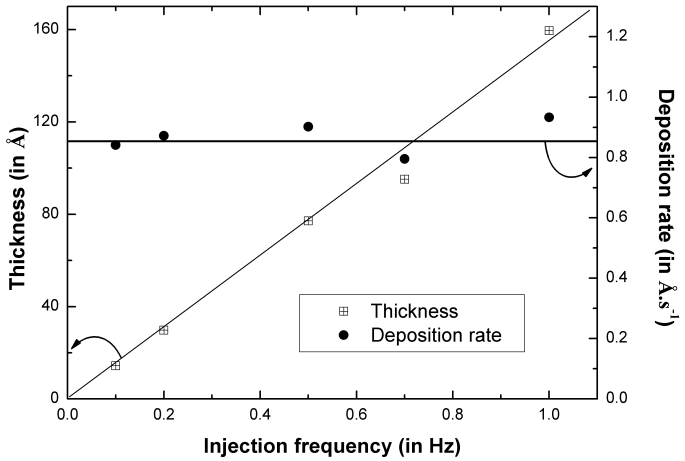

FIGURE 3.10: *Variation of the thickness deposited and deposition rate with injection frequency*

Evolution of the deposition rate with injection frequency increase, presented in figure 3.10, and clearly indicates that there is no dependency between the deposited thickness and the frequency of liquid injectors. It suggests that, no matter what the quantity of precursor

estimation of the layer thickness supposes that the roughness of the layer is low, and that the growth is 2D type.

injected in the chamber, all or a constant part of the precursor is reacting on the substrate. In conclusion, the kinetic coefficient of the reaction is infinite, the reaction is spontaneous at 350°C.
No variation of the density or resistivity was observed neither (not presented here), which confirms that the reaction mechanism is not impacted by the injection frequencies. If the decomposition of the precursor would not have been complete, it would have been pointed out by the deposited thickness decrease and/or density decrease and/or resistivity increase with the injection frequency increase.

In summary, the injection frequency does not impact the deposition mechanism and the deposited material. Hence, in order to have a better control of the deposited thickness at the Ångström level the injection frequency will be kept at 0.1 Hz for both TiN and TaN deposition. Using lower deposition rate also minimises the variability of the deposition by facilitating the exhaust of by-products.

3.2.7 Discussion about TaN deposition reaction path

3.2.7.1 TBTDET with NH_3 reactant gas

The previous parts reveal the importance of temperature as a first order parameter for MOCVD TaN deposition: a higher temperature allowing better exhaust of the carbonates by-products and enhancing the creation of Ta-N bonds.
Taking into consideration these evidences, the reaction path of TBTDET decomposition with NH_3 is proposed in figure 3.11.

The first TaN monolayer is always deposited on some oxide nucleation sites, either on a dielectric layer either on a native silicon oxide. The case of native SiO_2 is depicted here.
Ta-O bonds creation is energetically favourable, due to the lower Ta-O Gibbs Free energy of formation [$\Delta G_{formation}(Ta_2O_5)$ = -1079 kJ/mol (at 325°C and for 1 mole of Ta)] compared to Ta-N formation [$\Delta G_{formation}(TaN)$ = -222 kJ/mol (at 325°C and for 1 mole of Ta)]. SiO_2 substrate was proven to be natively OH terminated [106], so thanks to the thermal budget, TBTDET grafts to the oxygen by Ta-O bonds formation and parts with some diethylamine and ethane groups[4]. The NH_3 reactant gas present in excess in the chamber would complete the hydrogen bonds, resulting in the release of H_2 by-product. Next TBTDET molecule in contact with the metal surface could then substitute H in the Ta-H or Ta-N-H surface endings of the material and growth will continue.
One notices that if part of the Ta atoms are only bonded to H after the deposition, noticeable oxidation would occur at vacuum break, due to the weakness of these hydrogen bonds.

This reaction path is also supported by the evolution of Ta-N binding energy with the reactant gas used. Hence, if more NH_3 is introduced in the deposition chamber then Ta-N Ta*4f* XPS peak binding energy is lowered: evolution of the binding energy being directly related to the

[4]Methane (CH_4) and diethylamide ($NH(C_2H_5)$) groups are part of the precursor molecule

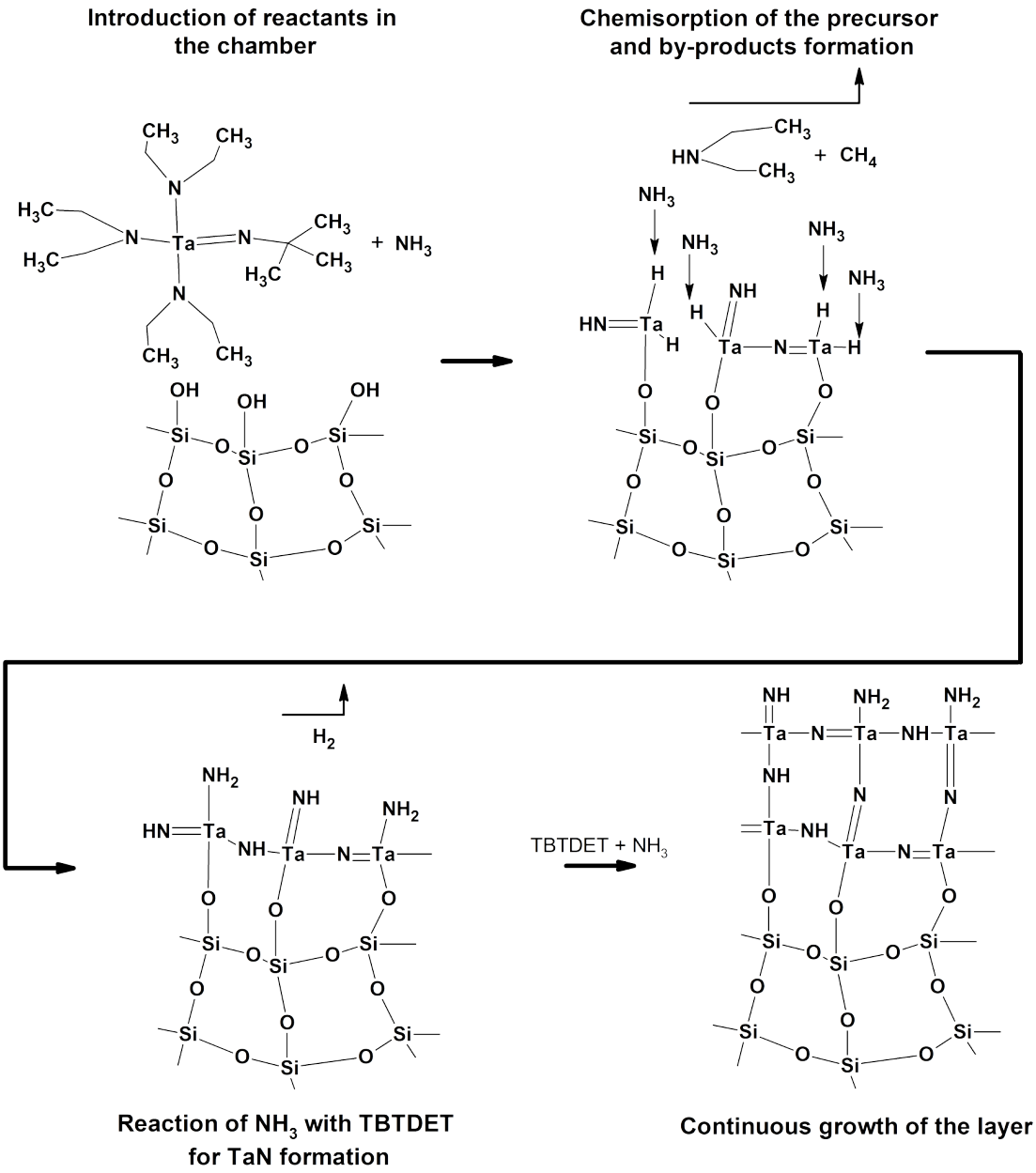

FIGURE 3.11: *Possible reaction mechanism for deposition of TaN with TBTDET and NH_3 reactant gas.*

composition of the layer. Similar evolution of the binding energy of metal peak toward lower binding energy with an increase of the nitrogen content was already presented elsewhere [15].

3.2.7.2 TBTDET with H_2 reactant gas

Substitution of NH_3 reactant gas by H_2 reactant gas led to the increase of the TaN deposition activation energy. In order to understand the different path involved in H_2 ambiance, the decomposition of the reactant gas in the chamber atmosphere has to be taken into consideration. Gibbs free energy calculation of equation 3.2 is used for calculation of the temperature of NH_3 decomposition and is presented in figure 3.12.

$$NH_3(g) \rightarrow N_2(g) + H_2(g) \tag{3.2}$$

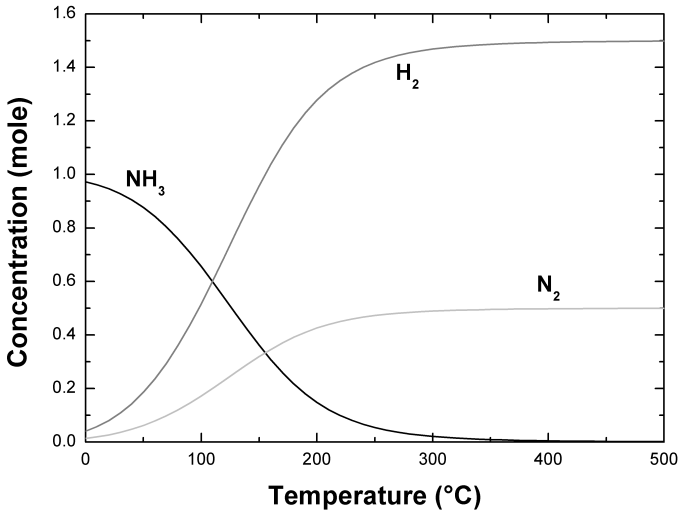

FIGURE 3.12: *Decomposition of NH_3 at a pressure of 2 Torr depending on the temperature*

Decomposition of 1 mole of NH_3 at 350°C leads to the formation of N_2 and H_2 from 100°C. Table 3.2 summarises the amounts of each phases at 350°C.

TABLE 3.2: *Products from decomposition of 1 mole of NH_3 at 325°C*

Phase	H_2	N_2	NH_3	H	NH_2
Equilibrium at 350°C (in mole)	1.4999	0.4999	$4.8x10^{-5}$	$8.0x10^{-15}$	$7.3x10^{-20}$

Other phases, like NH, N_2H_2 or N are also present but in very low amount, therefore are not taken into consideration.

By comparison of NH_3 and H_2 reactant gas decomposition, the influence of each gas on the activation energy can be deduced.
Decomposition of one mole of H_2 reactant gas at 350°C leads to the creation of $4.6x10^{-15}$ mole of H, as for the decomposition of NH_3. So H might not account for the decrease of activation energy.
Then, NH_3 gas flow introduced in the chamber is 200 sccm, which equals to $1.43x10^{-4}$ $mol.s^{-1}$, it is then decomposed at 350°C and only $3x10^{-9}$ $mol.s^{-1}$ of NH_3 are left in the chamber. Considering the growth rate of the TaN layer, 0.5 $Å.s^{-1}$, at a density of 11 $g.cm^{-3}$ and with the hypothesis that 100% of the precursor entering the chamber is deposited on the substrate, calculation of the Ta flow finds $8.5x10^{-7}$ $mol.s^{-1}$. Therefore, there is at least two decades between the amount of NH_3 and of the amount of Ta in the chamber, suggesting that the amount of NH_3 after decomposition (table 3.2) is not significant compared to H_2

and N_2. It is confirmed in the figure 3.12.

To conclude the higher energy activation measured in H_2 ambiance may be correlated to the lack of nitrogen in the deposition chamber. Indeed, from 200°C NH_3 reactant gas decomposes to form N_2.

Following this discussion, a possible reaction path for deposition with H_2 reactant gas is depicted in figures 3.11 and 3.13.

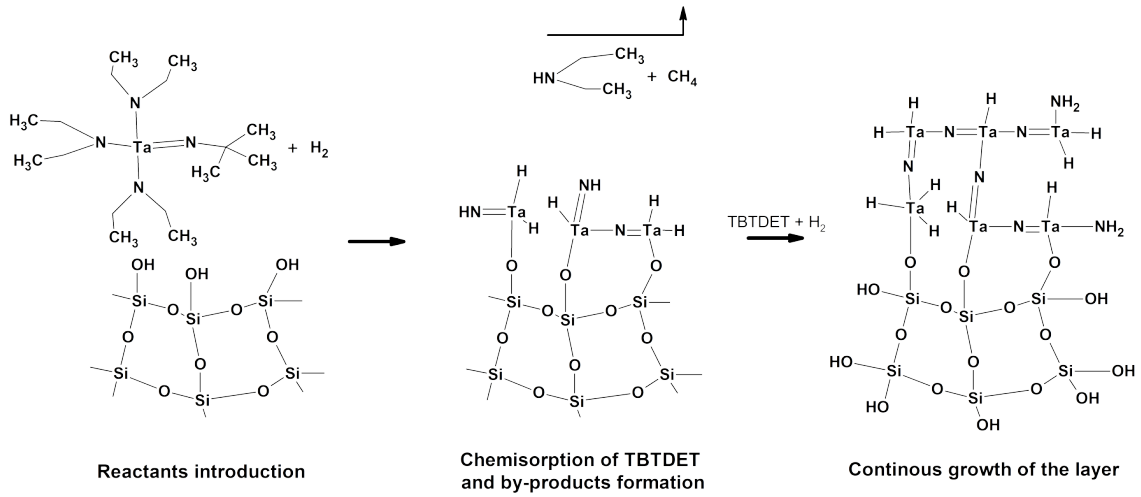

FIGURE 3.13: *Possible reaction mechanism for deposition of TaN with TBTDET and H_2 reactant gas.*

Deposition mechanisms with both NH_3 and H_2 are activated the same way: temperature brings the necessary energy to decompose the precursor and allows deposition on the substrate. Thanks to their high volatility, the elimination of ethane and diethylamine groups is rapid and carbon contamination low.
Then, Ta is forming bonds with H for H_2 reactant gas. As Ta-Ta metal bonds (located below 22 eV) were never observed by XPS, even with transfer under vacuum from deposition chamber to XPS chamber, it is reasonable to suppose that the energy brought to the system is not sufficient to create these bonds.

Hypothesis to explain the change in oxidation level was first mentioned in section 3.2.3 page 47. Basically, depending on the bonds formed during deposition, the oxidation resistance of the layer is changed, weaker bonds allowing higher oxidation of tantalum at vacuum break, thanks to the low Gibbs energy of formation of tantalum oxide ($\Delta_{formation}(Ta_2O_5) = -1079 kJ.mol^{-1}$ at 325°C). So it can be assumed that deposition with H_2 reactant gas results in creation of Ta-H bonds, weaker than the Ta-N created with NH_3. Moreover, O_2 affinity with H is high and leads to the formation of OH. Thus, upon vacuum break the weak bonds in TaN are replaced by Ta-O bonds resulting in the higher oxidation level of the layer.

3.2.8 Conclusion

Estimation of the carbon content present in the layers highlighted that the reactant gases do not take part in the evacuation of the reaction by-products. However, that is not the only role of the reactant gas, and H_2 reactant gas appears to not bring the nitrogen necessary to avoid the oxidation of the tantalum, as does NH_3 reactant gas. As already implied by figure 3.3 the highest Ta/N ratio, corresponding to the highest density (see figure 3.4), is obtained with NH_3 reactant gas for deposition temperature of 350°C or more.

3.3 TiN MOCVD process parameters evaluation

3.3.1 Substrate temperature

Investigation of the process window for MOCVD deposition of titanium nitride with TDEAT precursor and NH_3 reactant gas is presented in this paragraph.
Experimental calculation of activation energy of TiN MOCVD reaction mechanism, using Arrhenius law (equation 3.1, page 47), is reported in the figure 3.14.

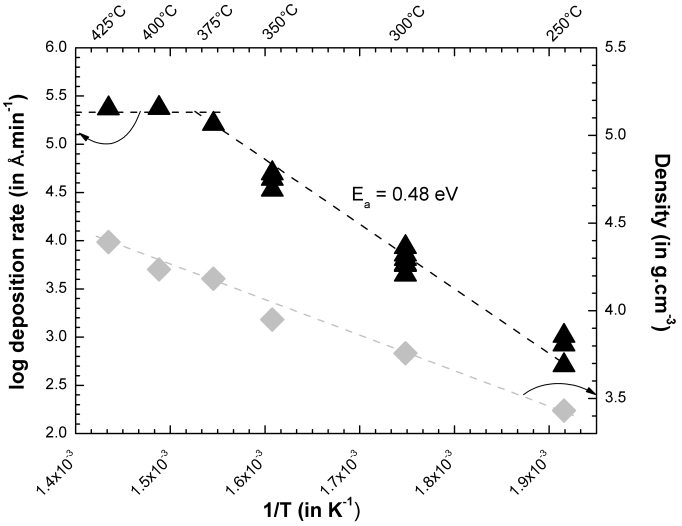

FIGURE 3.14: *Evolution of TiN growth rate and density with variation of the substrate temperature*

The growth rate evolution of TiN deposition is similar to the one of TaN deposition, with a clear increase from 200°C up to 350°C, from where a plateau is reached. Although, density has a different behaviour: contrary to TaN density, figure 3.1, no stabilisation of TiN density can be reached when the substrate temperature increases.
The theoretical density of stoichiometric and crystalline TiN is 5.22 g.cm^{-3} [100]. The maximum density obtained by MOCVD deposition is 4.39 g.cm^{-3} at 425°C. As for TaCN deposition, the lower density can be partly explained by the presence of titanium oxide (TiO_2 = 4.23 g.cm^{-3} [100]). Moreover, TiN theoretical density is given for crystalline structure which is not the case here as the layer is amorphous (confirmed by XRD measurements and

TEM observation, not presented here).
The N:Ti ratio of the material deposited at 425°C is 0.93:1, meaning that the TiN is slightly sub-stoichiometric.
Literature reports similar densities for stoichiometric TiN deposited by sputtering (4.3-5.2 g.cm^{-3}) [107] and ALD (3.2-3.4 g.cm^{-3}) [108]. Again, the lower density of chemically based deposition is linked to the amorphous phase of the layers.

Experimental determination of TiN MOCVD activation energy in NH_3 ambiance gives an energy of $E_a = 0.48$ eV, 5% higher than TBTDET in NH_3.
Similar activation energy for TaN and TiN MOCVD suggests that, if TaN and TiN would be injected together in the chamber then the same amount of TaN and TiN would be deposited.

Following these investigations and the results obtained, hereafter the temperature of the substrate was kept at 350°C (except if specified).

3.3.2 Deposition kinetic

Survey of the layer thickness depending on the deposition time is given figure 3.15 for TiN deposited at 350°C in NH_3 ambiance and an injection frequency of 0.1 Hz. The injection frequency was chosen as low as possible in order to have more reactant gas than precursor, i.e. to have a precursor limited reaction, thus revealing the kinetics of the deposition.

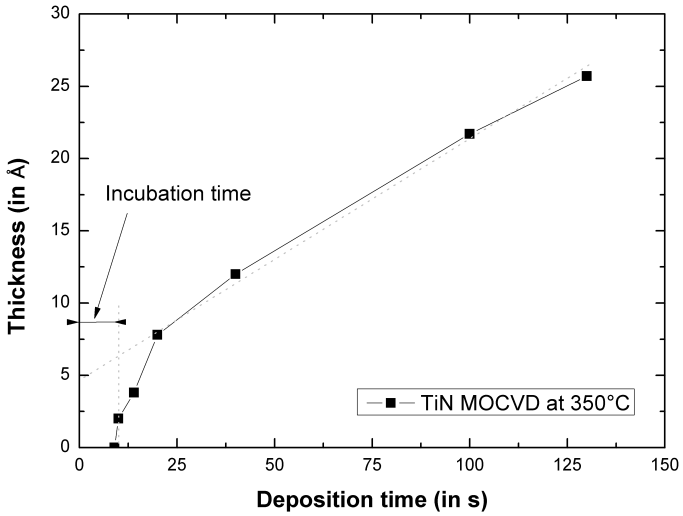

FIGURE 3.15: *Evolution of the TiN deposited thickness with increase of the deposition time, with TDEAT and NH_3 reactants*

No deposition was observed for deposition times of less than 10 s; no Ti atoms were detected using XPS. At 10 s of deposition the thickness of the layer could not be measured by XRR, however an XPS analysis revealed the presence of a thin layer of metal on the substrate.
There is an increase of the growth rate from 10 s of deposition until the final deposition regime is reached after 25 s. This growth rate increase may be related to the presence of an

incubation time [5] associated to a change of substrate, from oxide to metal.
Overall the same three steps with deposition rate changes, as for TBTDET deposition with NH_3 are observed. First, no deposition until the precursor reaches the substrate, second the covering of oxide nucleation sites and finally the cruising deposition rate reached after 25 s for TBTDET and 38 s for TDEAT.

3.3.3 Discussion about TiN deposition reaction path

A possible reaction path of TiN deposited on SiO_2 using TDEAT and NH_3 reactants is proposed figure 3.16.

The TDEAT introduced in the deposition chamber will react with -OH terminated substrate and creates Ti-O bonds. The substrate temperature allows a decomposition of the precursor molecule, creating diethylamine, ethane and hydrogen by-products. Ti grafted at the surface of the substrate would then bond with N from NH_3 reactant gas. And new precursor reaching on the substrate surface can then react with the new -NH terminated surface, resulting in the growth of the layer.

3.4 Parameters influencing the uniformity

The parameters which were found to impact the thickness but not the physico-chemical properties of the deposited layer are introduced and briefly discussed in this part, for the case of titanium deposition with TDEAT and NH_3 at 350 °C.

3.4.1 Injection frequency

If the material characteristics are not impacted by the variation of injection frequency, as already reported in the case of TBTDET precursor in section 3.2.6, the thickness uniformity is impacted. A lower frequency allows a better uniformity over the surface of the wafer. At 1 Hz, the centre of the substrate has a higher thickness than the edge of the substrate. It tends to indicate that the flow in the chamber is not high enough, leading to the decomposition of the precursor mainly at the centre of the substrate, before it reaches the edge of the substrate.
An increase of the vector gas flow in the injector results in the improvement of the thickness uniformity, which confirms the hypothesis that at higher injection frequencies there is not enough flow to carry all the precursor to the edges of the substrate. However, due to limitations of the deposition tool, the uniformity obtained at 1 Hz with the highest vector gas flow is not as good as the uniformity of the layer deposited at 0.1 Hz.

[5] The incubation time is defined as the time from the beginning of TiN deposition to the appearance of Ti layer.

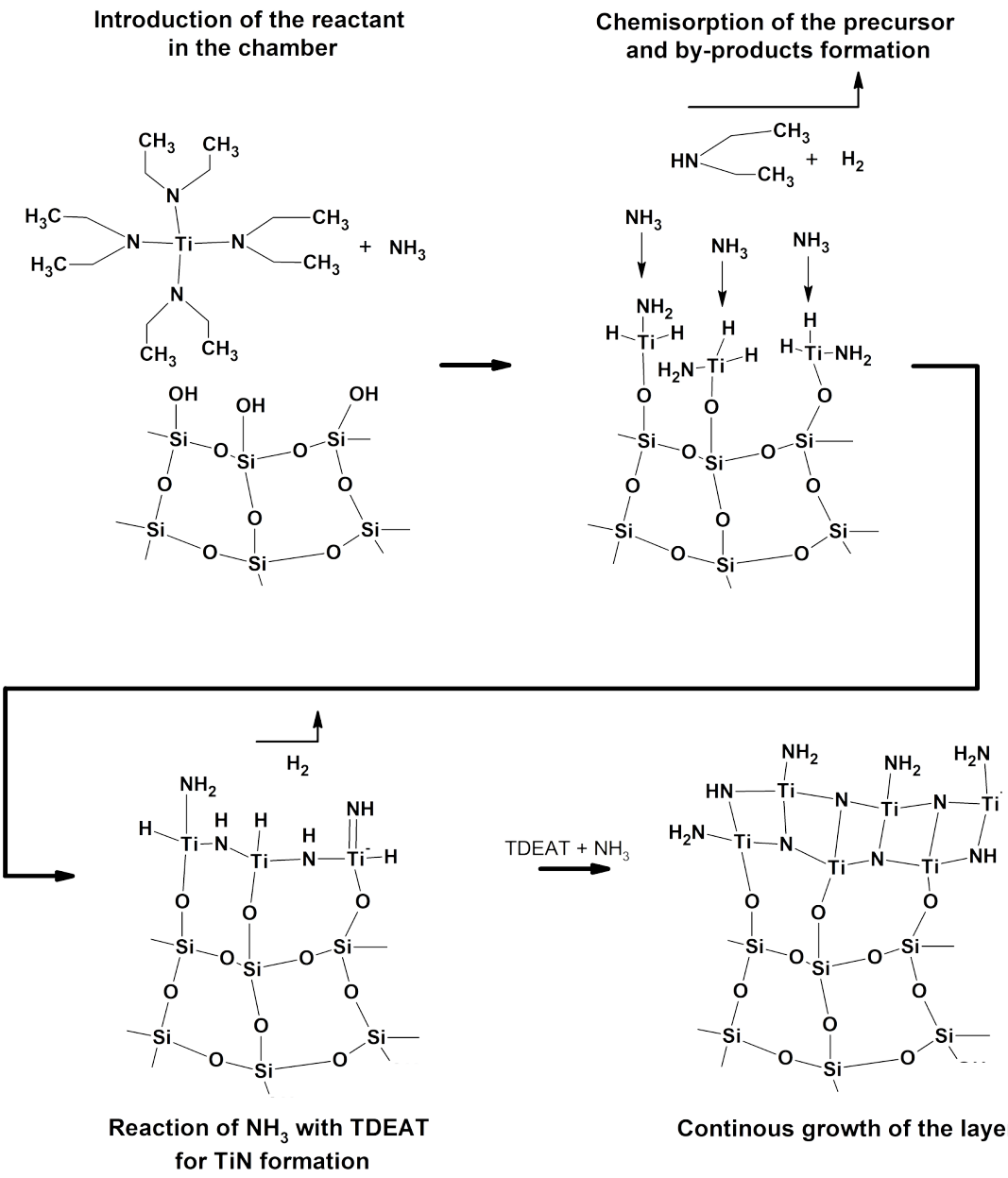

FIGURE 3.16: *Possible reaction mechanism for deposition of TiN with TDEAT and NH_3 reactant gas.*

3.4.2 Distance shower to substrate

Thickness uniformity of the deposited layer can be improved by an increase of the distance between the substrate and the shower, as presented in figure 3.17. For this study only the distance from the substrate to the shower was changed, all other experimental conditions were kept constant. The deposited thickness was measured by XRR on 49 points with a 10 mm edge exclusion. The thickness given in figure 3.17 corresponds to the average calculated from these 49 points. Variance is also included in figure 3.17 and is defined by :

$$Var(X) = \frac{1}{n}\sum_{i=1}^{n}(x_i - \mu)^2 \tag{3.3}$$

with μ the average thickness, x_i the thickness on the point i and n the number of points measured. The variance is expressed in $Å^2$.

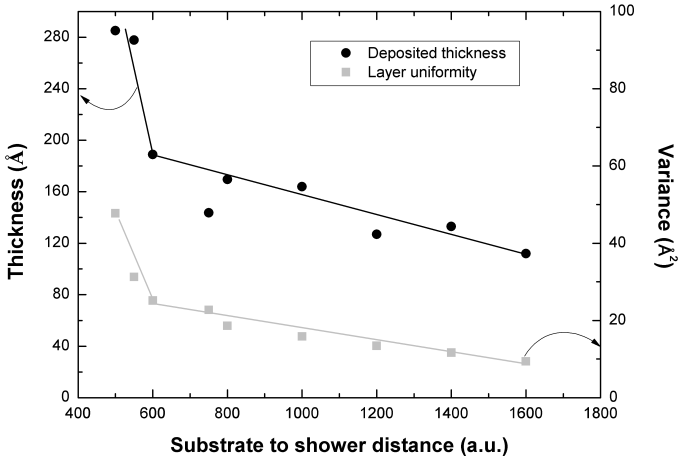

FIGURE 3.17: *Variation of layer uniformity on 300 mm with distance substrate-shower increase*

The first unexpected effect of distance increase from substrate to shower is the reduction of the deposited thickness. It seems that only the thickness is affected, not the deposition reaction as the resistivity, density or composition of the layer remain unchanged (not shown here). One possible explanation, is that part of the precursor is pumped to the exhaust before reaching the substrate (i.e. the wafer is out of the flow isolines). In other words, flow isolines seem concentrated a the shower centre and increase of shower to substrate gap induces a better distribution of the flow lines over the wafer surface.
Uniformity is greatly improved when the distance increases, this improvement can be explained if first it is supposed that the shower does not properly distribute properly the precursor and gas reactant. In particular, if more precursor is going through the centre of the shower, increasing the distance from substrate to shower permits to spread the precursor at the wafer surface thanks to the pumping effect.

As a result increasing the distance from the substrate to the shower allows to improve the uniformity of the deposited layer, but it also results in lower deposited thickness, since part of the precursor molecules are directly pumped out without touching the surface of the wafer.

3.4.3 Vector gas flow

Argon vector gas can be introduced in the chamber from two different locations, first for transport of precursor molecules from the injectors and through the furnace, second for reactant gas transport from the dual channel shower.

To increase the flow of precursor vector gas entering the deposition chamber the vector gas injector opening time has to be raised, see Chapter 2 for detailed presentation of the AltaCVD tool. No influence on the deposition or uniformity was observed when longer opening time of the gas injector was used. It is presumably due to the buffer action of the evaporation furnace which regulates the flow entering the deposition chamber.

On the other hand, change in the flow of reactant vector gas resulted in different deposition rate and subtle uniformity improvement, as introduced in figure 3.18.

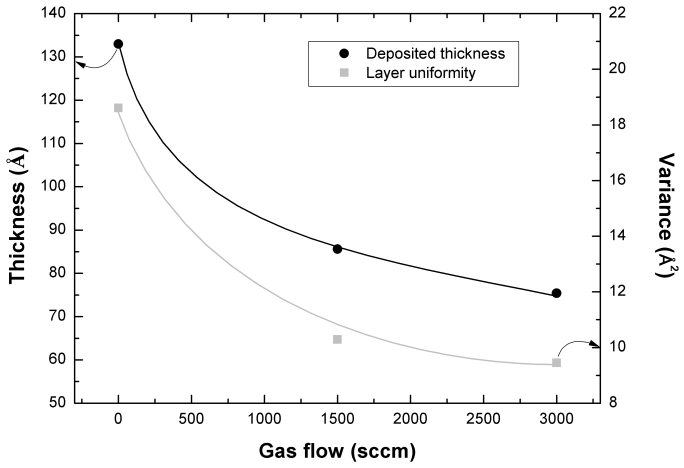

FIGURE 3.18: *Variation of layer uniformity with reactant gas flow increase*

Modification of the vector gas flow going through the dual channel shower has a direct influence on the residence time of the deposition reactants (precursor molecules and reactant gas). Indeed, by increasing the vector gas flow, the reactants are remaining during a shorter time in the chamber, thus they have less time to react and to deposit on the surface of the substrate. It is clearly visible on the figure 3.18, where the addition of the vector gas flow results in a decrease of the deposited thickness.

Nevertheless, increase of reactant vector gas allows a better dispersion of the reactant gas in the chamber and thus, similarly to the increase of the substrate to shower gap, an improvement of the thickness uniformity with vector gas flow increase, vector gas introduced with the reactant gas, is observed.

Thickness profiles through the wafer diameter, of the layers deposited with 0, 1500 and 3000 sccm of Ar gas flow are plotted on the figure 3.19.

The deposition has a shape referred to as "doughnut" shape, the highest thickness being located close to the half radius. When the vector gas flow is increased a clear reduction of this profile is observed. There is a better dispersion of the precursor on the substrate with high gas flow.

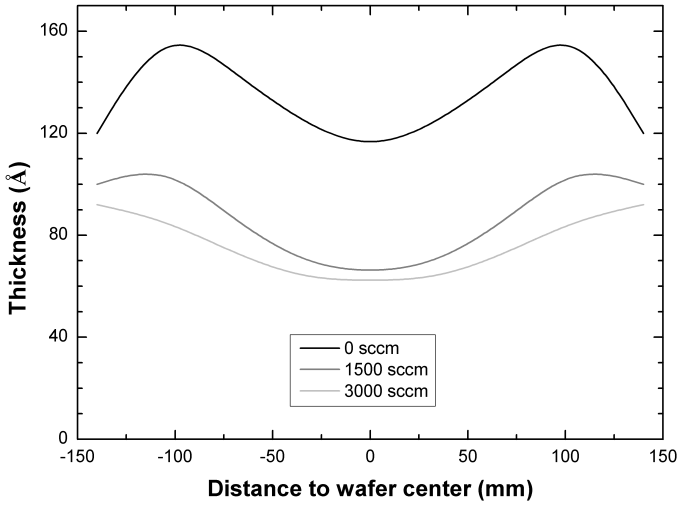

FIGURE 3.19: *Variation of layer thickness on the diameter of 300 mm wafer with reactant gas flow increase*

Another significant information visible in figure 3.19, is the perfectly symmetric profile obtained. The symmetry is kept whatever the chosen diameter. This information points out that the atmosphere in the deposition chamber is homogeneous, i.e. there are no perturbations of the flows in the chamber or in the pumping area. The speed of the matter in the atmosphere of the chamber in flow isolines is constant with a centred axe of symmetry.

By adjusting the vector gas flow the behaviour of the uniformity is changed. So with a 3000 sccm vector gas flow, the new best distance was found to be 700 a.u., resulting in an uniformity as low as 7%.

3.4.4 Deposition chamber pressure

As introduced earlier, the residence time of the precursor molecules in the chamber is decreased by the increase of the vector gas flow. A decrease of the chamber pressure also results in a reduction of the residence time due to a more important pumping flow in order to obtain the requested pressure in the chamber.
A direct consequence is that the uniformity of the layer is also impacted by the pressure of the deposition chamber. Pressure variation from 0.5 to 8 Torr was investigated and as expected, a higher pressure allowing longer residence time and results in a better uniformity of the deposited layer.

With the best parameters possible, the thickness uniformity was lowered to 5%, similar to the specifications of an industrial tools.

3.5 MOCVD conformity control

3.5.1 Methodology

To validate the hypothesis of conformal deposition using the MOCVD method a 4 nm TaN MOCVD layer was deposited on a 15 nm wide and 15 nm high Si Fin line patterned on SiO_2 substrate. The process parameters were chosen as follow:

- substrate temperature: 350°C
- chamber pressure: 2 Torr
- liquid injector temperature: 40°C
- reactant gas/precursor ratio: >1000
- deposition rate: 0.2 Å.s^{-1}
- spacing substrate-shower: 0.7 cm

3.5.2 SEM conformity observation

Pictures from the SEM observation are presented figure 3.20, (left secondary electrons and right back-scattered electrons).

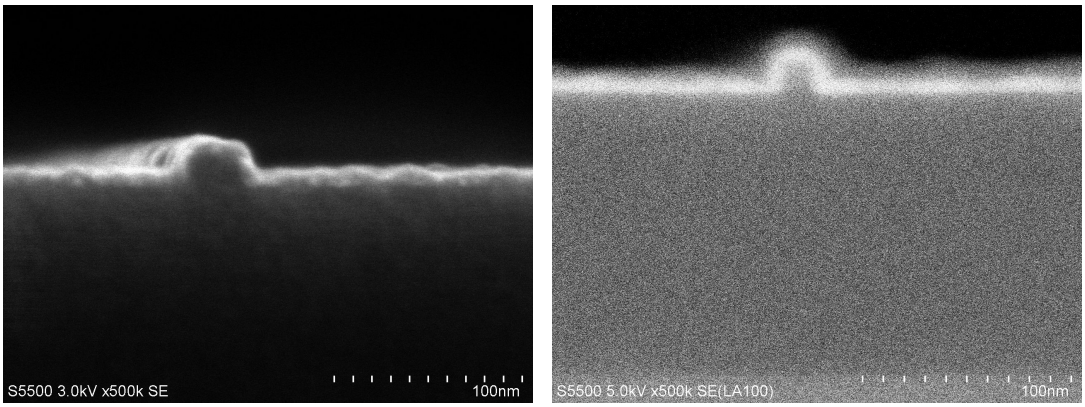

FIGURE 3.20: *SEM secondary electron (left) and back-scattered (right) observation of MOCVD deposited TaN on 15 nm Si Fin*

The secondary electron picture has a better resolution because of the high number of emitted electrons, however since only a small quantity of conductive material was deposited on SiO_2 insulator a charging effect of the sample is observed. This charging led to the destruction of the layer and the degradation of image resolution, which induces difficulties to observe interfaces.
Hence, to have a better separation of the TaN and SiO_2 layers a picture was taken in back-scattered mode, which is more sensitive to materials densities and conductivities. This picture reveals a net and clear interface with no voids between TaN and the substrate. Also, the thickness of the layer on the vertical surfaces is the same as on the horizontal surfaces. A software estimation of the deposited thickness on both vertical and horizontal surfaces revealed a ratio of 1:1. Therefore, the conformity of MOCVD deposition on small 3D patterns

is validated.

3.5.3 Roughness observation

Using SEM it is also possible to observe the surface roughness. Picture of TaN surface deposited by MOCVD on Fin structures is shown in figure 3.21.

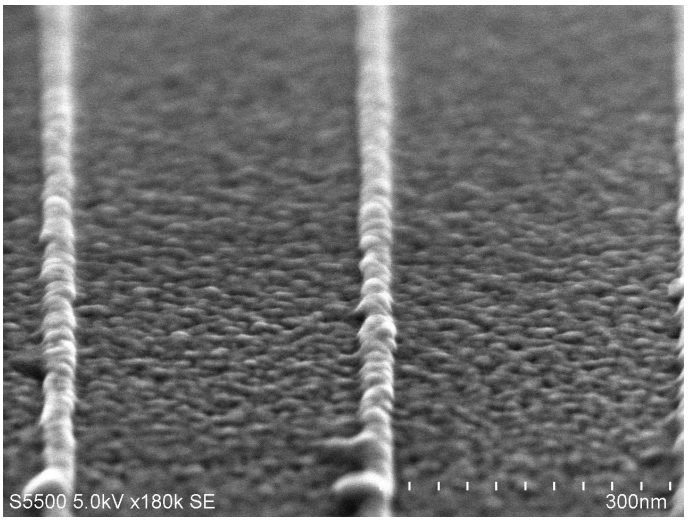

FIGURE 3.21: *Surface roughness of MOCVD deposited TaN on 15 nm Fin*

The roughness/granularity observed is linked to the well known TaN island growth regime where important crystallinity of TaN is usually expected. In this case, the 4 nm thick TaN deposited leads to the formation of a close film (i.e. no voids are observed between the grains), and the presence of local bumps may be source of electrical variability (such as transistor V_t shift) as already reported for advanced technology nodes [109].

3.5.4 Conclusion

This first observation of MOCVD TaN layer confirms that MOCVD technique is conformal on patterns of a few nanometres. With the ratio 1:1 estimated on vertical:horizontal surfaces, MOCVD is suitable for advanced CMOS technologies. In Chapter 5, electrical measurements of the MOCVD layers will give an insight into the influence of the grains on the threshold voltage variability.

3.6 Conclusion to the Chapter 3

Deposition of TaN and TiN by MOCVD appears to follow a complex chemical reaction path influenced by different parameters.

The first and most important parameter is the substrate temperature. As shown in figure 3.1 and 3.14, complete reaction is obtained from 350°C for TaN and TiN. Further increase of the temperature does not enhance the deposition rate but favours densification of the material and so limits the oxidation observed at vacuum break.
Then it appeared that in a LIMOCVD tool, the temperature of the liquid injector has a strong influence on the deposited material. Indeed, an increase of the evaporator and furnace evaporation temperature results in a degradation of the properties of the layer, correlated to an activation and pre-decomposition of the precursor molecule in the evaporating furnace.
Also, even if the material growth is only activated thermally, physical properties modifications of the metals (thickness, density, resistivity to oxidation...) were observed with a variation of the reactant gas. These modifications confirmed the diethylamine by-products creation due to the clear evolution of nitrogen content in the TaN layer. Using NH_3 reactant gas allowed to increase the N/Ta ratio, contrary to H_2 reactant gas. Furthermore, oxidation of the metallic layer is directly correlated to the stoichiometry of the layer. Main hypothesis is that Ta vacant bonds and hydrogen bonds are replaced by oxygen bonds at vacuum break.
Besides, it was shown that other parameters have no influence on the physico-chemical properties of the film but impact the deposition efficiency and thickness uniformity.
Finally, the conformity of MOCVD deposition technique was proven on small patterns of 15 nm, with great success.

In summary, the investigations presented in this chapter reveal the process parameter windows in which the best material can be obtained, together with the highest reaction efficiency. Yet, some parameters, inherent to the deposition chamber characteristics (buffer effect of the evaporation furnace for example) could not be tuned.
Possible deposition reaction path were proposed in accordance to the evolution of stoichiometry and bonding environments of the species present in the deposited layer.

Chapter 4

Plasma influence

"The science of today is the technology of tomorrow"
Edward Teller, physicist

4.1 Introduction

Plasma deposited metalorganic films have been used for applications from diffusion barriers [110], superconductors [111], to catalytic support materials [112]. Recently, thanks to a better control over the growth rate, PEMOCVD started to be considered for applications requiring thin layers, including metal gate [19, 22, 90].
Main advantage of the plasma addition to MOCVD is to reduce the substrate temperature necessary to obtain the same reactions. Thus, PEMOCVD is a promising method for deposition of metals on High-κ dielectrics for non-planar devices such as FinFet or Trigate. Lower temperature of deposition garantees the quality of the High-κ dielectric, as HfO_2 for example.

Plasma energy can also be used as treatment of the deposited layer for densification and/or activation of the nucleation sites [16, 53, 90, 113]. Plasma Densified MOCVD (PDMOCVD) and by extension Plasma Enhanced ALD (PEALD) are both using plasma steps during the deposition process.
Previous works [61, 114] reported that nitrogen, hydrogen or N_2/H_2 plasma treatment of a TiN material leads to the densification of the layer and highly reduces the amount of contaminants (C, H, O,...) inserted in the layer during the pyrolysis of the metalorganic precursor. The plasma also modifies the initial preferred growth orientation of the crystals from (100) to (110). Knowing that the atomic density evolves with the preferred orientation of the layer and that the work function increases with the density of the referential planes [115], plasma may be used for the fine tuning of the metal work function.

Due to the complexity of the plasma reactions, there is no clear understanding of the deposition mechanisms taking place during metalorganic deposition. So in this chapter, emphasis will be put on the understanding of the phenomena taking place during plasma activation of the precursor (for PEMOCVD) or plasma treatment of the surface (for PEALD).
First, the influence of each parameter for PEMOCVD deposition of Ta(C)N and Ti(C)N is introduced and compared with MOCVD results from Chapter 3. A decorrelation between

plasma and thermal activation of the reaction mechanisms is investigated. The advantages of higher plasma power for decomposition of the precursor are discussed and linked with the physical properties of the deposited material. An innovative work investigating the effects of plasma frequency modification on the decomposition of the precursor and the resulting transformation of the deposited metal is presented. Then, the effects of plasma used for surface treatment are studied by a comparison of PEALD and ALD deposited metals. Finally, the conformity of the PEMOCVD deposition is characterised on small dimension patterns.

4.2 Influence of plasma in PEMOCVD

During PEMOCVD, part of the deposition reaction path is activated by the plasma. The decomposition of the precursor molecule is partly achieved in the volume of the plasma by bond breaking from the excited species.
In this first section, variation of the process parameters and the corresponding influences on the properties of the deposited material are reported.

4.2.1 PEMOCVD standard parameters

First, a short and rapid overview of the common parameters (such as temperature, reactant gas, ...) is given, in regards to the MOCVD process introduced in Chapter 3.

Substrate temperature
Deposition was done at temperatures ranging from 150°C to 400°C and only a decrease of the carbon contamination was observed. Therefore, the substrate temperature does not impact the growth rate of the layers.
It is important to notice that the carbon present in the layer was not bonded with the metal, only C-H and C-N bonds were found by XPS analysis. The fact that no Ti-C nor Ta-C bonds were observed confirms that the carbon is brought from reaction by-products only. This carbon content increase at low temperature deposition can be associated to a difficult elimination of the reaction by-products, mainly methane and diethylamine groups or similar.

Liquid injector temperature
Because the precursors are going in the plasma after passing through the evaporation furnace, the precursor pre-decomposition with high furnace temperature revealed in the MOCVD deposition, in Chapter 3 section 3.2.4, has no impact on the deposited material. Actually, the buffer effect encountered with the furnace temperature increase is kept and the deposited thickness with high temperature furnace is lower than the thickness obtained with low temperature furnace.

Effect of injection frequency
Increasing the injection frequency of precursor during PEMOCVD did not change the deposited thickness for the same quantity of precursor injected or the physical characteristics

of the deposited material. But to reduce the plasma damages on sub-layer higher injection frequency have to be preferred, since the damages are proportional to the plasma budget (plasma power x plasma duration). Therefore, to limit as much as possible the deposition time and thus the damages brought by the plasma, the injection frequency is kept at 1 Hz, higher limit until which the uniformity of the layer is acceptable.

Reactant gas

In the investigated process window, a change of the reactant gas was not possible due to the non-stability of the plasma when NH_3 or N_2 reactants were used instead of H_2. The non-stability of the plasma was visible by OES as an important variation of the plasma intensity and resulted in a non-repeatable deposition process.

Deposition chamber pressure

As for MOCVD process, the pressure of the chamber during deposition has an impact on the residence time of the precursor. The higher the pressure, the longer the residence time. Uniformity of the deposition is affected, like in MOCVD mode, but no change of material characteristics was seen, in the pressure range of 0.5 to 8 Torr.

Moreover, increasing the pressure during precursor plasma activation leads to a reduction of the plasma sheath[1] thickness. Indeed, it was shown that a power law relationship, equation 4.1, exists between the pressure of the reactive gas and the sheath thickness [113, 116].

$$p^n S = constant \quad or \quad S = S_0 p^{-n} \tag{4.1}$$

with p the plasma pressure (in mTorr), S the plasma sheath (in cm) and S_0 a constant defined by the initial state of the sheath. n exponent is included between 0 and 1 and depends on the reactive gas in the plasma.

In general, in Capacitively Coupled Plasma (CCP) chambers, an increase of the plasma density is going along with the pressure increase [117].

So overall, smaller plasma sheath increases the gap between the plasma and the substrate, resulting in lower damages but limiting the interest of a higher plasma density as the active species are further from the substrate. However in the chosen process conditions, if the pressure is too high the plasma cannot stabilise.

Finally, the absence of change in the characteristics of the deposited material can be explained by the fact that higher plasma density is going along with a shorter residence time of the precursor molecule. Thus, the plasma might be more efficient but the precursor is going through the plasma during a shorter time.

[1]The plasma sheath is a layer in the plasma which has a greater density of positive ions, and hence an overall excess positive charge, that balances an opposite negative charge on the surface of a material with which it is in contact.

4.2.2 PEMOCVD plasma power variation

The most important parameter in a PEMOCVD process is the plasma power, as the energy brought for decomposition of the precursor depends strongly on this first order parameter. By increasing the plasma power more energy is brought for the decomposition of the precursor and for the activation of nucleation sites.

In the following paragraph, PEMOCVD deposition of TiN with TDEAT and H_2 reactants is discussed. The lowest temperature to thermally decompose TDEAT, with an NH_3 ambiance, on Si-substrate was reported previously to be about 200°C, Chapter 3 section 3.2.3 figure 3.1. Moreover, H_2 reactant gas appeared to increase the lowest temperature required for deposition. Therefore, in the current work, the substrate temperature was kept constant at 150°C to avoid any competition between plasma deposition and thermal deposition.
First, it appeared that the effect of plasma power increase, from 80 to 300 W, is negligible on XRR extracted thickness and density during PEMOCVD deposition. A slight densification was observed with plasma power increase, but the variation was within the measurement error and so will not be discussed here.
Bonding environments of Ti and N evolve with plasma power, as presented figure 4.1.

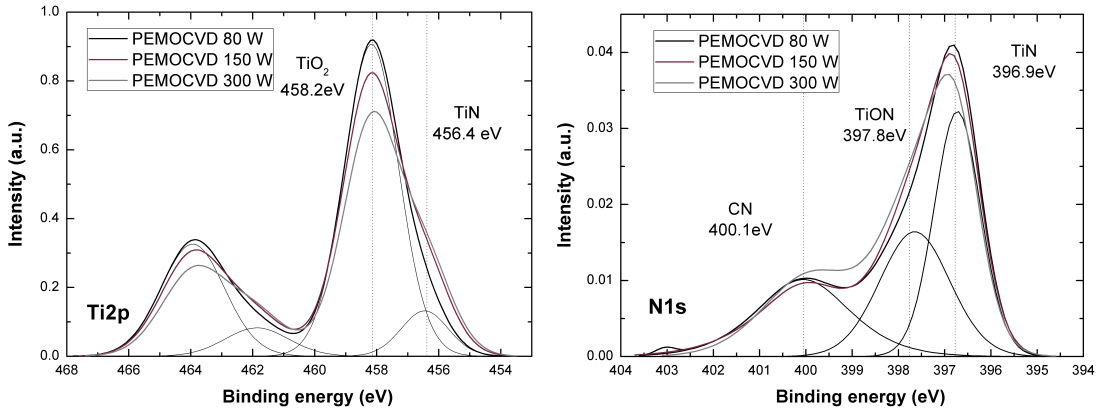

FIGURE 4.1: *Evolution of Ti2p (left) and N1s (right) TiN PEMOCVD XPS spectra with plasma power increase*

Hence, in figure 4.1 left a clear variation of TiN oxidation state with a plasma power increase is revealed. Indeed, both Ti-N bond (456 eV) and Ti-O bond (458.6 eV) are affected by the plasma power used for deposition. One must recall that the oxygen element is not present in the chamber or in the TDEAT molecule, and that there should not be any remaining oxygen contamination in the reactor chamber during the process. The absence of oxygen was further supported by OES investigation of the plasma. From 80 W to 300 W, Ti-O component decreases, revealing a higher oxidation resistance of the layer at vacuum break. At the same time Ti-N environment intensity increases with a shift towards lower energies, confirming the lower oxidation state of Ti.
Ti-N modifications can also be observed on N*1s* spectra presented in figure 4.1 (right). On this spectra three main environments are observed: N-Ti (396.9 eV [81]), N-Ti-O (398.1 eV

[81]) and N-C (400.1 eV [81]). First observation is the increase of Ti-N bonds with plasma power increase, in good correlation with Ti*2p* spectra figure 4.1 (left). Second fact is the decrease of N-Ti-O environment, matching with the oxidation decrease seen on Ti*2p* spectra figure 4.1 (left). Finally, N-C environment coincides with the diethylamine groups from the precursor. Their presence can be explained by the low temperature of the PEMOCVD deposition (150°C) and the absence of change with plasma power variation implies that the exhaust of diethylamine group is not affected by the plasma.

In summary, plasma power increase appears to improve the N stability in TiN layer, in turns limiting the oxidation of the layer at vacuum break. Because no nitrogen other than the one already present in the precursor is introduced in the chamber during PEMOCVD deposition (H_2 plasma is used in this study), it is possible to suppose that higher plasma power allows to break more diethylamine groups creating N* and CH_4. Free nitrogen are then reacting with Ti and results in the higher TiN bonds created at higher plasma power.

However, as highlighted by the composition of the layers in table 4.1, the exhaust of deposition reaction by-products is not complete and high level of carbon is found in the layer.

TABLE 4.1: *Ti relative composition of PEMOCVD TiN depending on plasma power*

	80 W	**150 W**	**300 W**
Ti	1	1	1
N (N at.% \ Ti at.%)	1.27	1.29	1.34
O (O at.% \ Ti at.%)	1.53	1.44	1.35
C (C at.% \ Ti at.%)	2.37	2.75	3.35

The composition of the layer is consistent with the observations and suppositions done from figure 4.1.
Plasma power increase permits a slight increase of N ratio together with a higher resistance against oxidation but increases the C content. Most of the carbon found in the material has a binding energy of 285 eV, characteristic of hydrocarbons bonds, such as CH_x. And as supposed earlier, the important carbon content in the layers can be associated to the low substrate temperature which does not enhance the volatility of the carbonates reaction by-products. The C content increase with the plasma power increase highlights that the dissociation of the precursor molecule is done in the plasma atmosphere. Increase of plasma energy allows different dissociation and results in higher C-H groups formation.
If temperature of substrate is rose to 350°C, whatever the plasma power used, the carbon content decreases from 38 at.% down to 8.2 at.%, characteristic of the carbon brought by atmosphere contamination also found on MOCVD and ALD layers.
Also it appears that oxydation of the layer decreases with the plasma power increase. This evolution can be linked to the densification of the layer, reducing the solubility of O in TiN.

The resistivity evolution of 10 nm TiN layer deposited with several plasma powers was investigated at a substrate temperature of 350°C, to limit the influence of carbon on the

resistivity, and is presented in figure 4.2.

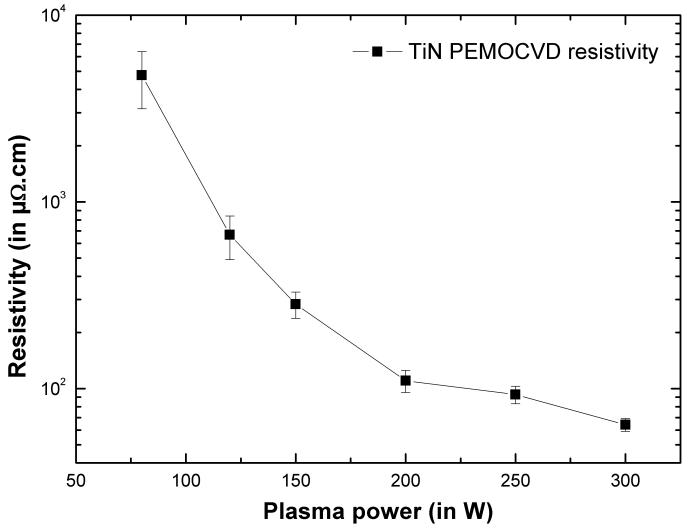

FIGURE 4.2: *Evolution of the resistivity with plasma power increase*

By increasing the plasma power from 80 W up to 300 W the resistivity decreases from 4 000 µΩ.cm down to 60 µΩ.cm. Resistivity is first rocketing down, from 80 W to 200 W, and stabilises above 200 W at values lower than 100 µΩ.cm. TiN resistivities reported in the literature are included in the 50 - 200 µΩ.cm range for PVD [11, 17] and 100 - 500 µΩ.cm range for (PE)CVD [60, 118].

Uniformity of resistivity measurements is also given in figure 4.2, with higher reproducibility for higher plasma power, going along with a resistivity decrease. Lower oxidation of the layer may explain the lower variation; higher oxidation may create some localised insulator influencing the resistivity measurement.

4.2.3 Conclusion on PEMOCVD

The differences of deposition reaction mechanism between MOCVD and PEMOCVD were highlighted in this chapter. Whereas MOCVD is a deposition based on a chemical surface reactions, PEMOCVD is a reaction activated within the volume of the plasma and resulting in the deposition of a layer.

Two fundamental points must be reminded from these investigations: first, even if precursor dissociation and deposition activation are provided by the plasma, the substrate needs to be heated to allow a better exhaust of the reaction by-products. Low temperature substrate (lower than 300°C) will result in highly carbonated layers. Such carbon embedded in the layer does not create bonds with the metal and thus induces an increase of the film resistivity. The second point concerns the plasma power used during deposition. Even when the reactants amount which enters the deposition chamber is kept constant, by increasing the plasma power the stoichiometry of the layer is changed. More precisely, higher plasma power

results in higher resistance against oxidation and leads to better quality film.

Finally, the plasma frequency, can be tuned in the way to improve precursor decomposition in the plasma. It can be achieved by adding LF waves simultaneously with well known RF waves. Hence, a complete investigation of the plasma modifications after addition of low frequency plasma to radio frequency plasma and the resulting changes of the deposited material is now presented.

4.3 Influence of LF plasma power addition for PEMOCVD

4.3.1 Introduction

As introduced earlier, in PEMOCVD deposition mode, dissociation of the precursor affects the chemical, physical and electrical properties of the deposited film as well as the growth rate of the resulting film. In a CCP reactor, with a fixed RF frequency, the electron density is known to increase with the plasma power and the electron temperature is known to vary with the pressure. Thus, if one wants to modify the dissociation rate of a given precursor, pressure and power have to be carefully tuned. Another parameter often not taken into account, but that should be considered is the plasma frequency. Flam, in 1986, studied the plasma frequency effect in low pressure plasma etching [119]. He showed that frequency alters many plasma parameters such as the spatial distribution of species, the energies and concentrations as a function of time, and energies of ions impinging the substrate. In their simulation paper, Surenda and Graves predicted that higher RF frequencies would produce higher plasma densities for the same voltage [120]. Also, faster plasma etching can be obtained by increasing the traditional 13.56 MHz RF frequency. Goto *et al* proposed a mix of low and high frequency to have both high density and highly energetic ions [121]. Following this work, dual-frequency (DF) reactors have been developed as fine etching tool for microelectronic manufacturing. In that case, the CCP is driven by a HF and a LF source attached to either one electrode or two electrodes. One frequency is chosen to be much higher than the other in order to achieve an independent control of ion bombardment and electron density (i.e. ion flux). More details can be found in the review of Bi *et al* concerning DF capacitive discharges [122].

Many groups have created models and simulated the effect of LF addition on plasma density. Depending on the model assumptions and on the pressure, it was reported that the plasma density may be reduced due to sheath width variation, and that it may also be increased due to highly energetic secondary electrons [123–132]. Both *et al* showed that if plasma negative ion density is included in the simulation then it can strongly modify the effect of adding LF to HF. They found that a mixture of the 27 and 2 MHz RF powers have significant effects on plasma density in Ar/O_2 mixture, whereas the 2 MHz power weakly increases the electron density when the 27 MHz power is low in a $Ar/C_4F_8/O_2$ plasma [130]. Donko *et al* also showed how the γ-coefficient of the secondary electrons may be used to interpret papers published with contradictory results [131], and they concluded that there is only a

small pressure process window for which the effect of secondary electrons on the ionisation compensates the frequency coupling effect.

Compared to etching tools, only few papers report the effect LF addition to an HF source for high-pressure plasma used in deposition processes. The effect of frequency has mainly been studied for the deposition of silicon-based materials such as SiO_2, SiO_xN_y, Si_3N_4 and SiC, with the idea of controlling the stress by modifying the ion bombardment of chemical bonds in the film [132–134]. Most of the reported experiments are not really DF processes since they are using a very high frequency source for the plasma generation with additional RF bias at the substrate holder [135]. As an example, in case of silicon oxynitride deposition, it was reported that thin films deposited with a RF/microwave DF source have a higher surface potential and improved charge retention in comparison to films obtained in an RF mode [136]. Bieder *et al* also studied the MW/RF dual excitation for SiO_2 deposition [110] while L. Yang *et al* used this dual mode for diamond-like Deposition [137]. In their case, this mode was mainly used to control the energies of hydrogen ions and the induced stress in the film, not to improve the dissociation rate of the precursor. Recently, Jin *et al* have studied the effect of DF plasma on SiO_x deposition by adding an ultra-high frequency (320 MHz) source to a 13.56 MHz source [138].

The impact of RF frequency on precursor deposition and PECVD process optimisation was discussed in depth by Moisan *et al*, who compared the MW PECVD to the RF PECVD and the parameters determining the optimum frequency of operation [139]. Bieder *et al* have also compared two RF frequencies for SiO_2 deposition [110]. In both case no LF frequency was used and the RF frequency (ω) was always higher than the ion plasma frequency (ω_{pi}) of the precursor and/or ions from the precursor decomposition. Since the excitation frequency has profound effects on the spatial distribution of species and their concentrations, the dissociation of the precursor can strongly be increased by crossing the discharge excitation frequency to the basic ion plasma frequency, ω_{pi}, as suggested by Flamm [119]. Manolache *et al* investigated the chlorine contents of 40 KHz and 13.56 MHz silicon tetrachloride and dichlorosilane plasmas in the 100-500 mTorr range by OES [140]. They found the concentration of free chlorine in the dichlorosilane plasma to be much higher at the low RF range and drew conclusions about potential routes that can be developed for frequency-controlled molecular fragmentation. This route is considered here, with comparison and discussion over the improvements brought by DF LF/RF plasma in TiN deposition thanks to the modification of the precursor's decomposition reaction. For this study, a 300 mm industrial PECVD tool from Altatech Semiconductor was used. It is a capacitive plasma chamber with a DF source: 13.56 MHz and 350 kHz. The LF was chosen in order to be lower than the ion plasma frequency of the precursor. The impact of LF addition on plasma density and precursor dissociation are discussed thanks to OES monitoring of the plasma during the process.

4.3.2 Experiments

Samples depositions were made with the AltaCVD Advanced Materials^{TM}, 300mm pulsed PEMOCVD chamber presented earlier in figure 2.7. The pressure in the chamber is kept constant at 2 Torr, resulting in a narrow sheath, far from the substrate. Two independently controlled generators are used with frequencies of 13.56 MHz and 350 kHz, for RF and LF plasma, respectively. Both generators deliver the power at the shower head, substrate heater being grounded. For discussion of the experimental results, the plasma power given here corresponds to the input plasma power minus the reflected power.

PEMOCVD allows deposition of carbo-nitride alloys of metals [141], with a variation of the composition depending on the plasma power. In PEMOCVD process, first the chamber is filled with Ar and He inert carrier and H_2 reactant gases, before plasma activation. Then precursors in a vapour phase are introduced in the chamber and have to go through the plasma to reach the substrate. Plasma energy allows an activation of the first reactions leading to the decomposition of the molecules; second reactions are taking place at the substrate surface, i.e. at 350°C. All depositions were done on 300mm silicon (1 0 0) prime wafers.

Plasma emission was monitored by OES, with a signal acquisition from 200 nm to 800 nm at a frequency of one spectrum per second, and gives an insight into the plasma chemistry. The thickness, density and roughness of the deposited films were obtained by careful fitting of XRR experimental spectra; resistivity is measured with a four point probe; chemical composition and chemical bonding were analysed by XPS.
XPS acquisition was done with a quasi-*in situ* tool, which limits TiN oxidation and carbon contamination introduced at vacuum break [93], thus no oxygen nor carbon removal was performed before analysis. Carbon C*1s*, situated at 285 eV, was used to remove any possible binding energy shift from the charging sample. Bonding environments of Ti, C, N and O were analysed using the Ti*2p*, C*1s*, N*1s* and O*1s* core level energy regions respectively. XPS deconvolution was done using the following constraints for Ti*2p*: Ti$2p^{5/2}$ and Ti$2p^{3/2}$ are separated by a shift in bonding energy of $\Delta E = 5.54$ eV and an area ratio of 0.5.

4.3.3 Plasma modification

In order to discuss the plasma modification induced by LF power and added to RF power, three plasmas were analysed: pure argon plasma, Ar + H_2 plasma and Ar + H_2 + precursor plasma. Hydrogen in the plasma deposition was used for the removal and control of the carbon content in the TiN films. All the plasmas' emission intensities were recorded by OES as a function of RF power (from 0 to 500 W) and as a function of LF power (from 0 to 100 W) added to 200 W RF power.

4.3.3.1 Impact of LF addition on pure Ar plasma

As introduced before, LF addition to RF can enhance the precursor decomposition in the plasma thanks to the modification of the electronic density or electronic temperature. The LF field can also penetrate into the plasma volume resulting in an increased heating of heavy ions (from precursor dissociation). Therefore, the influence of LF addition on pure Ar plasma was monitored in order to discuss the role of LF addition on electron density or temperature modification. The 200-800 nm optical emission spectra were recorded as a function of RF and RF + LF powers. The evolutions of two emitted peaks are mainly discussed here: the Ar* emission line at 419.8 nm, which corresponds to the transition from $Ar(3p_5)$ to $Ar(1s_4)$, and Ar^{+}* emission line at 432.8 nm. The Ar* line has already been found to be a good probe to determine the plasma density in CCP sources as a function of driving frequency [142].
For pure Argon plasma, the optical emission of Ar originates from the direct electron impact excitation of the Ar atom, and the emission process of Ar* [$3p^5 5p(3p_5) \rightarrow 3p^5 4s(1s_4)$] by the electron impact is:

$$e + Ar\ [3p^6(^1S_0)] \xrightarrow{E>14.57eV} Ar\ [3p^5 5p(^3p_5)] + e \rightarrow Ar\ [3p^5 4s(^1s_4)] + hv\ (419.8\ nm) \quad (4.2)$$

Therefore, the light emission intensity is proportional to the density of Ar species in the electronically excited state: $I_{Ar*}(419\text{ nm}) = k[\text{Ar*}]$ and the density of excited states [Ar*] is proportional to the density of Ar ground state species times the efficiency of the plasma η_F: $[\text{Ar*}] = \eta_F[\text{Ar}]$. Finally, $I_{Ar*}(419\text{ nm}) = k\eta_F[\text{Ar}]$. The efficiency of the plasma to excite species depends on the electron density and energy distribution (temperature, T_e). In these experimental conditions, for pure Ar plasma as a function of plasma RF power, if electron temperature variation is neglected, then the Ar* intensity can be directly correlated to the electron density. When LF is added to RF, the electron temperature can be modified due to different mechanisms for sustaining the discharge (secondary electrons versus an electron reflected by an oscillating sheath, see the discussion hereafter). Unfortunately, at the moment it is not possible to measure the effect of LF addition on T_e, so that the Ar* intensity variations will be correlated here to electronic density variations.
The impact of RF and LF power on Ar spectra is illustrated in figure 4.3, from 410 to 440 nm. In this figure, one can compare the evolution of the intensity of the OES bands when going from 200 W RF to 300 W RF and from 200 W RF to 200 W RF + 60 W LF. In both cases, an increase of the intensity was observed when increasing the power injected in the plasma. But it appears that higher intensities were obtained with LF added to RF. A simple explanation is that higher plasma densities are obtained with LF addition instead of RF addition to the 200 RF power. In this case, the assumption that electron temperature is not modified when adding LF was made. This should be verified in a complementary study.

Figure 4.4a shows the evolution of the Ar* (419.8 nm) emission line as a function of RF power and RF (200 W) + LF power. Figure 4.4b shows the evolution of Ar^{+}* (434.8 nm). In figure 4.4a, with RF power only, the relation between plasma power and plasma intensity is of a square root type. Before 30 W, there is not enough energy to switch on the plasma; above 50 W one can see a quite linear relation. Such a relation between plasma power and intensity

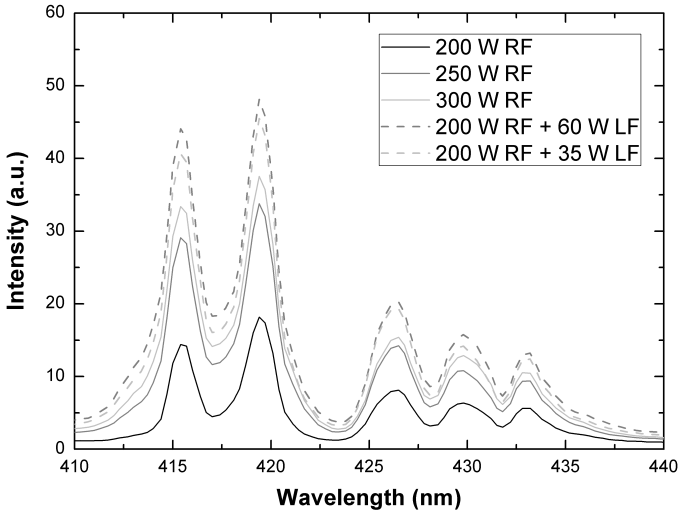

FIGURE 4.3: *OES of the ALTACVD Ar plasma in the 410-440 spectral range*

is characteristic of CCP reactors. Godyak and Piejak have shown that a CCP discharge is dominated by Ohmic heating at high pressure (versus stochastic at low pressure) [143]. In this case, the plasma density, n_0, can be correlated to the RF frequency, ω, and the applied RF voltage, V_0, by the following equation (see reference [144] for more details on RF plasma):

$$n_0 \propto \omega^2 V_0^{1/2} \tag{4.3}$$

The same evolution is observed for the $Ar^{+}*$ emission line as a function of RF power in figure 4.4b. When LF power was added to 200 W RF power, strong modifications were observed. As an example, the ratio I (419.8 nm - 300 W RF) / I (419.8 nm - 200 W RF) is equal to 1.37, while the ratio I (419.8 nm - 200 W RF + 100 W LF) / I (419.8 nm - 200 W RF) is equal to 2.17. The same evolution is obtained with the $Ar^{+}*$ emission, going from a value of 1.48 to 2.27.

As mentioned in the introduction, some authors have reported that the addition of LF to RF power may increase the plasma density due to highly energetic secondary electrons. Thus the discharge is not dominated by Ohmic heating. The transition in CCP RF source towards a regime dominated by secondary electrons (also called "γ-regime") has been studied in the past [120, 145–148]. As an example, Belenguer and Boeuf have studied the case of Helium (3 Torr) plasma, and they clearly showed that two different regimes may exist [149]. The transition from one regime to the other depends on the energy obtained by the electrons in the sheath and their ability to ionise. It means that large sheath (thus high power) and high pressure help to shift the plasma in the direction of γ-regime. Godyak *et al* were able in their plasma to have a γ-regime transition when increasing the voltage to values higher than 400 V in pure Helium plasma at 3 Torr [150]. Belenger and Boeuf were able to fit the experimental curves when the effects of secondary electrons were taken into consideration, with an emission coefficient, γ, of 0.08 [149].

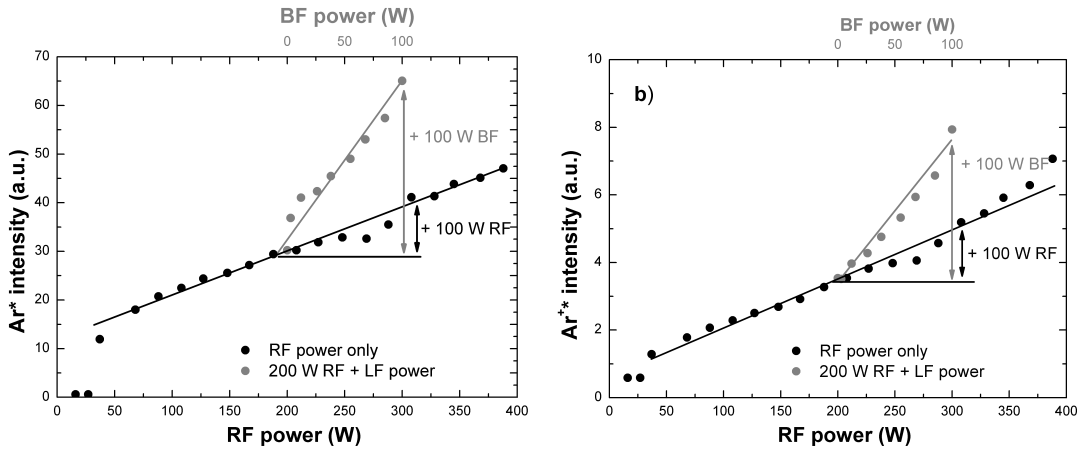

FIGURE 4.4: *Evolution of the Ar* (a) and Ar^{+}* (b) emission lines as a function of RF power and 200 W RF + LF power*

In this experiments, the high-pressure regime may help to obtain the γ-regime. Moreover, LF addition may have increased the sheath width, which is also in favour of the γ-regime. In order to confirm that Ar* intensity enhancement can be linked to the transition to a γ-regime when LF is added; OES measurements were performed at higher RF power. As seen figure 4.5, for RF power higher than 400 W, a modification of the Ar* intensity variation was observed, with again a fast increase of the Ar* intensity. This can be interpreted as a transition to γ-regime in single RF plasma when power is higher than 400 W. A power of 400W seems to be the threshold above which the discharge is sustained by secondary electrons. At these higher RF power, the Ar* intensity now follows the same law as the one obtained with LF addition. Therefore, in these experimental conditions, the plasma density increases by LF addition thanks to secondary electrons. This behaviour is contrary to what was obtained by numerical models at low pressure (see reference [125] for example). However, this result is in good agreement with recent papers from Ahn *et al* [151], Xiang-Mei *et al* [152], and Schulze *et al* [146].

4.3.3.2 Impact of LF addition on Ar+H_2 plasma

Contrary to pure Ar plasma, when adding LF to RF in an Ar + H_2 plasma, the intensity of the Ar* emission lines decreased with LF addition (easily observed for the 750 nm Ar* emission line; see figure 4.7d for example). This may indicate a decrease of electron density or electron temperature with LF addition, which is contradictory with what was observed in pure Ar plasma; this point will be discussed later. The H_2 continuum from the primary system in the 300 - 500 nm range (see figure 4.6) also decreased with LF power. New emission peaks were also observed with LF power addition, some are highlighted by an arrow in figures 4.7a and 4.7b. In the 400-500 nm range, the new peaks observed can be attributed to the H_2 secondary system ($G^1\Sigma_g^+ - B^1\Sigma_u^+$) [153]. The H_α emission peak from Balmer lines at 656.3 nm also increased with LF power indicating an increase of H atomic species in the plasma. This increase can be correlated to the intensity decrease of the Ar* emission line and may

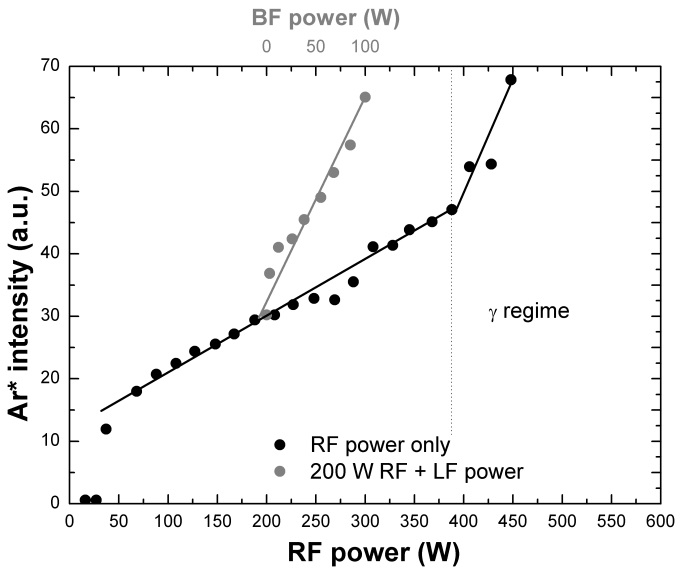

FIGURE 4.5: *Evidence of a γ-mode transition at 400 W for pure Ar plasma with singe RF power*

finally be the consequence of the high level of excited argon activating the dissociation of H_2 in these experimental conditions. Therefore the opposite behaviour of Ar* at 750 nm and H* by the H_2 dissociation can be explained from collisions with Ar* following the reaction proposed by [154]:

$$Ar(^2P_1) + H_2 \rightarrow Ar(^1S_0) + 2H \tag{4.4}$$

And in a more general way, the reaction rate that may occur in the Ar/H_2 plasma can be written as follows for Ar* excited species and Ar_m metastable species [155–157]:

$$Ar^* + H_2 \rightarrow Ar + 2H \tag{4.5}$$

$$Ar_m + H_2 \rightarrow Ar + 2H \tag{4.6}$$

This increase of H density in the plasma may be of importance for the PECVD process since H atoms might break different bonds in the precursor molecule than in pure RF plasma conditions.

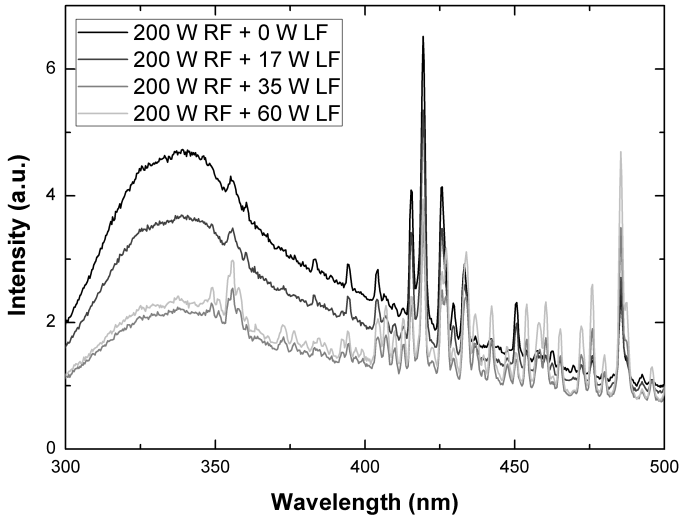

FIGURE 4.6: *Impact of LF addition in Ar+H_2 OES in the 300 - 500 nm range*

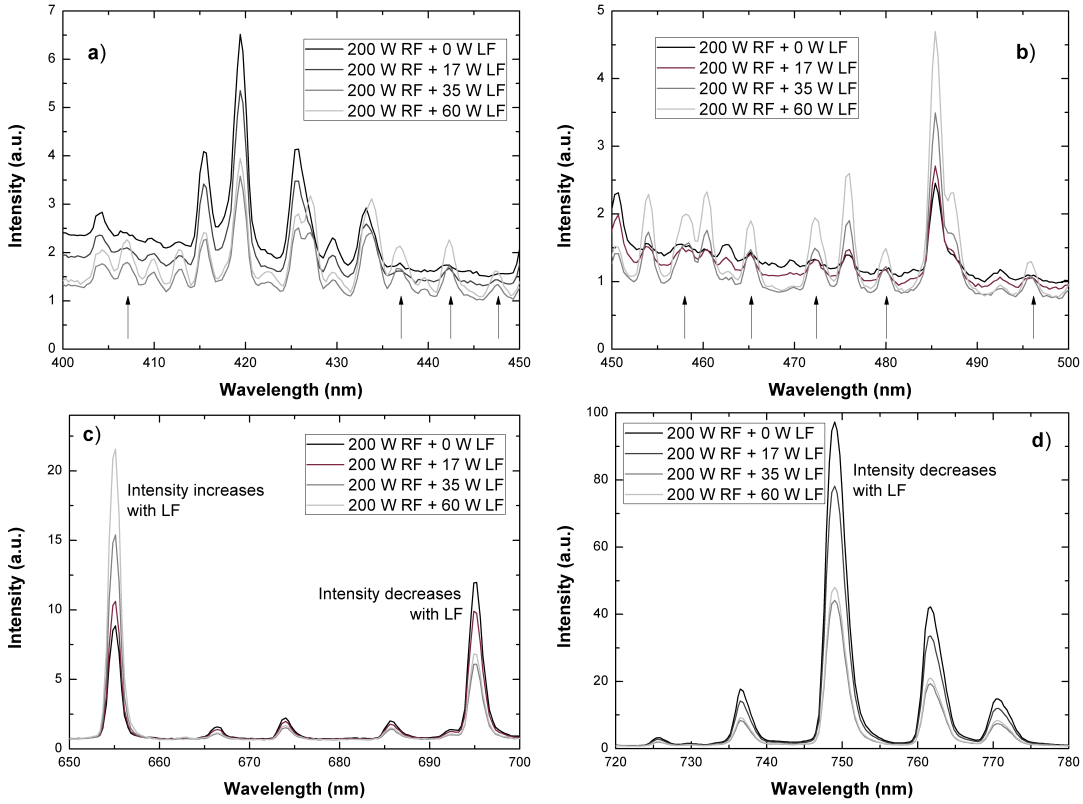

FIGURE 4.7: *Impact of LF addition in Ar+H_2 OES in 4 spectral ranges: a: 400-450 nm; b: 450-500 nm; c: 650 -700 nm; d: 720-780 nm. Arrows in the figures indicate new emission peaks*

4.3.3.3 Modification of OES for Ar+H_2+Ti precursor

Figure 4.8 shows the modification in the OES when adding Ti precursor in the gas phase. Figure 4.8a is a comparison between 200 W RF plasmas with and without a precursor. The OES spectrum in the 300 - 500 nm range shows that a new emission peak could now be observed at 386 nm (indicated by an arrow in figure 4.8a). This peak corresponds to the

CN* emission band from the violet band system [153]. This is not surprising since CN bonds are present in the Ti precursor. No Ti* emission line is observed at 363.5 nm, indicating that the precursor is probably not completely dissociated in the plasma phase, this result being in contradiction with what was reported by Rie *et al* [158]. The intensity of H* atomic species was observed to decrease when adding Ti in the gas phase. This can be seen in figure 4.8a with the decrease of H_β emission line from the Balmer lines at 486.1 nm and the H_α line at 656.3 nm (figure 4.9d). It is not surprising since the H atoms were expected to react with carbon-based radicals from the precursor in order to limit the C, H and reaction by-product content in the growing film.

The same spectral range for a 200 W RF + 60 W LF plasma, with and without Ti precursor added to Ar +H_2 plasma, is presented figure 4.8b. A new CN* emission band clearly appears at 386 nm. Another new weak emission peak is observed at 336 nm and can be attributed to a weak emission from NH* band [153], indicating that the precursor dissociation is modified when adding LF to RF. The comparison in all the spectral ranges shows new weak peaks at 402 nm, 446 nm (see figure 4.9a, arrows), 491 nm, and 586 nm. These peaks are due to He* emission such as He ($3d^3D/2p^3P_0$) at 587.6 nm. Helium was used in the process as a gas carrier for the liquid injection of the Ti precursor. As of today, no explanation for the presence of emitted He* in the DF mode and not the RF mode has been found. However, as for pure argon plasma, it shows that the plasma is strongly modified by LF addition.

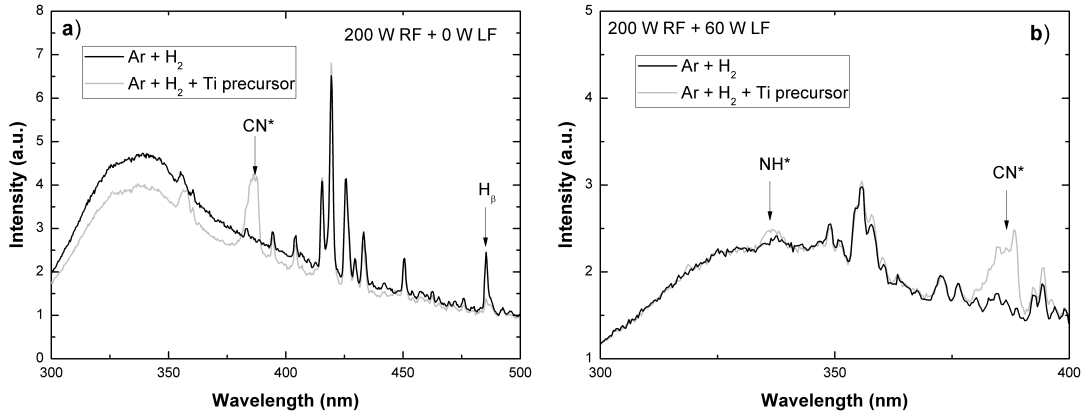

FIGURE 4.8: *a: is a comparison for a 200 W RF plasma with and without Ti precursor; b: shows the impact of Ti precursor for 200 W RF + 60 W LF plasma*

Figure 4.10 shows the evolution of the OES spectra in the 300-400 nm range as a function of LF power added to RF power. Some of the new peaks are correlated to new emission from the H_2 plasma as previously observed, and the only two new peaks which come into view with the introduction of the precursor are NH* at 336 nm and CN* at 386 nm.

In summary, it was showed that LF addition to RF increases the Ar plasma density. This can be interpreted by a transition to the γ-mode due to secondary electrons' heating. In Ar/H_2 plasma, the LF addition helped to increase the H density in the plasma by H_2 dissociative collision with excited Ar or metastable Ar. Finally, the TiN precursor was not completely dissociated in this discharge and in the dual mode, but new excited species were observed,

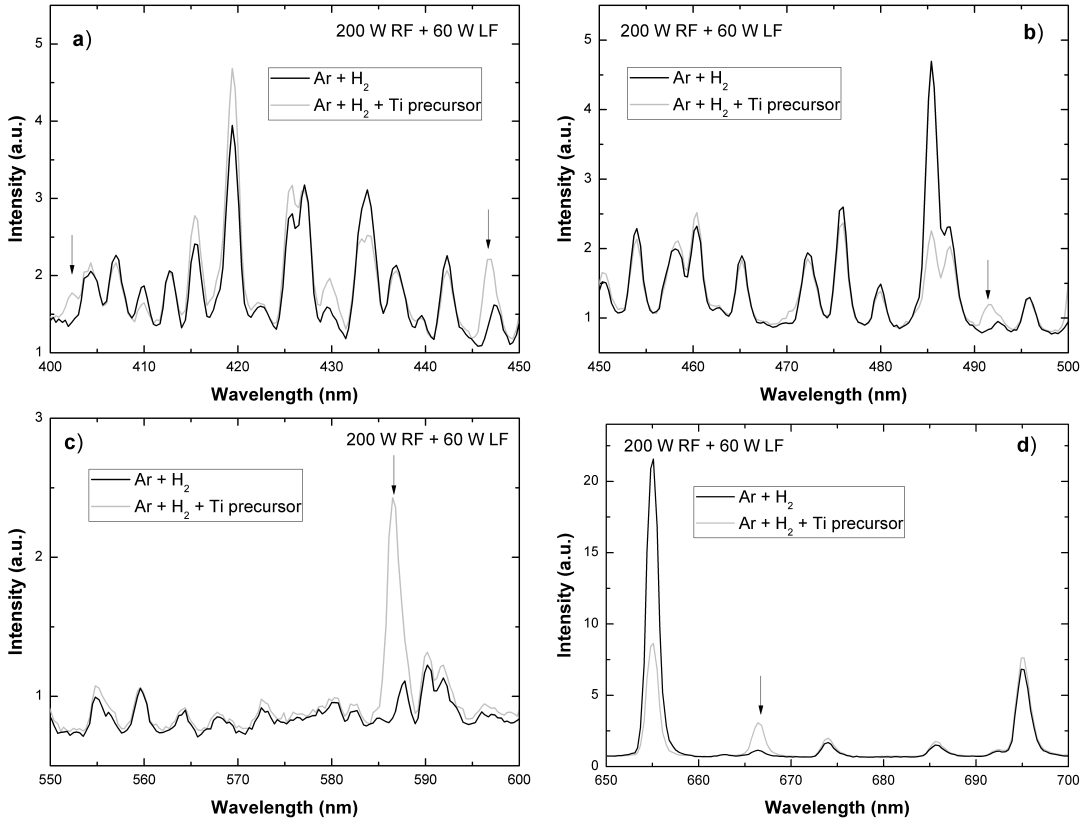

FIGURE 4.9: *Effect of Ti precursor addition in the OES of the 200 W RF + 60 W LF plasma : a: 400 - 450 nm range; b: 450 - 500 nm range; c: 550 - 600 nm range ; d: 650 - 700 nm range*

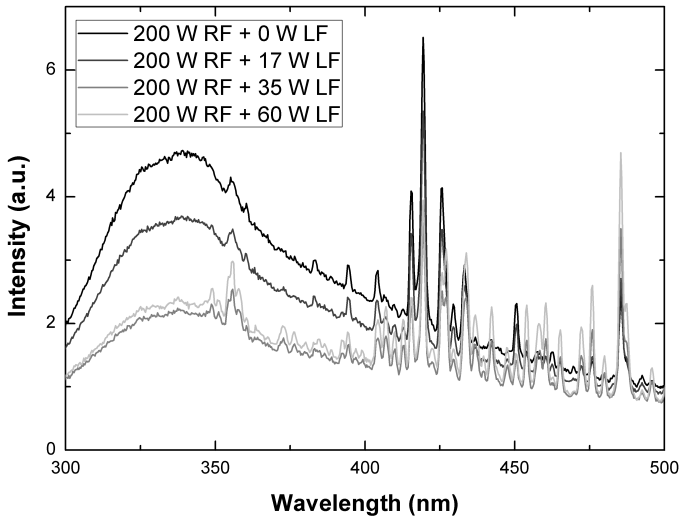

FIGURE 4.10: *Evolution of the OES of Ar+H_2+Ti precursor plasma with LF power*

indicating a different fragmentation of the precursor. The effect of the LF addition on the TiN film properties will now be examined.

4.3.4 Thin TiN film analysis

As for OES analyses, the properties of thin TiN films deposited in the pure RF mode are first discussed. Then, properties of TiN films obtained in the Dual Mode will be analysed and compared to the RF ones.

4.3.4.1 Impact of RF power on thin film properties

In table 4.2 are given the deposition rate, density, roughness and resistivity of TiN layers obtained for RF plasma power between 200 and 300 W.

TABLE 4.2: *Evolution of thickness, density and resistivity with increase of RF plasma power*

RF Power (W)	**Deposition rate** (Å.s^{-1})	**Density** (g.cm^{-3})	**Roughness** (Å)	**Resistivity** (mΩ.cm)
200	1.03	3.38	26.2	110
250	1.25	3.34	27.1	93
300	1.60	3.35	27.4	64

As usually observed in PECVD, increasing the RF power improves the dissociation of the precursor and increases the deposition rate [158]. The growth rate increased by a factor 1.55 from 200 to 300 W, quite similar to the plasma density evolution (Ar* line) of 1.37. In parallel to the growth rate evolution, the resistivity decreased when the RF power increased: its value was reduced from 110 mΩ.cm to 64 mΩ.cm. Roughness of the thin TiN films is only slightly modified by RF power, with a little variation (from 26.2 to 27.4 Å). Finally, increasing the plasma power does not affect density, which is low compared to the theoretical density of TiN: 5.40g.cm^{-3} [100]. A high level of oxidation has to be taken into account for density calculation, as it reduces the density (TiO_2: 4.23g.cm^{-3} [100]) and can partly explain the low density measured. Moreover, theoretical densities are calculated for a perfectly crystalline material, whereas the obtained TiN is amorphous (confirmed by XRD analysis and TEM observation, not shown here) with a lower density.
Hence, a possible hypothesis to explain the improvements observed is that the increase in plasma power may improve the by-products' removal during deposition leading to the easier nucleation of the layer and to a reduction of resistivity. Indeed, the presence of carbon from reaction by-products in the layer decreases the conductivity of the layer.
The XPS analysis of TiN RF 200 W, 250 W and 300 W layers is discussed later in comparison with LF deposition results.

4.3.4.2 Impact of LF addition to RF plasma on thin film properties

To evaluate the impact of LF addition to RF plasma on TiN material deposition and to be able to compare it with the increase of RF plasma power, all deposition parameters were unchanged, and only LF power was added to 200 W of RF power. Figure 4.11 shows the deposition rate obtained with and without LF addition. Figure 4.12 shows the impact of the DF mode on resistivity while figure 4.13 illustrates the beneficial role of LF addition on thin films' density. The fitting error from XRR spectra is at maximum 10%, thus is not significant and is not reported in figures 4.11 and 4.13. The error bars in figure 4.12 correspond to the resistivity uniformity measured with 1 cm edge exclusion.

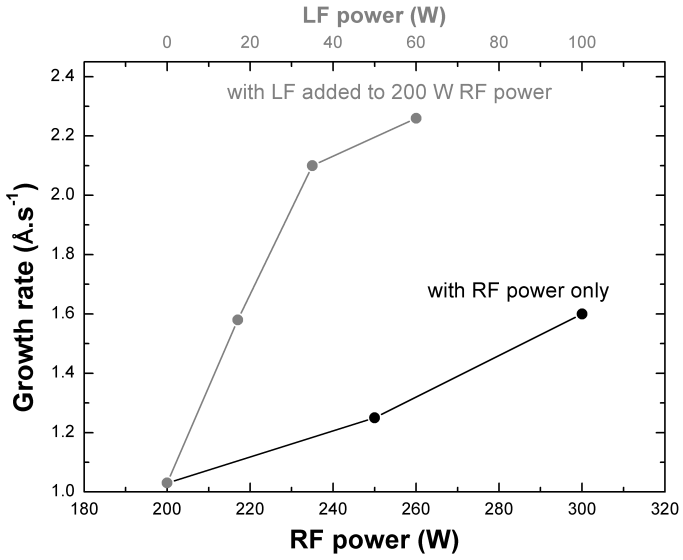

FIGURE 4.11: *TiN deposition rate in RF mode and Dual Frequency mode with LF addition*

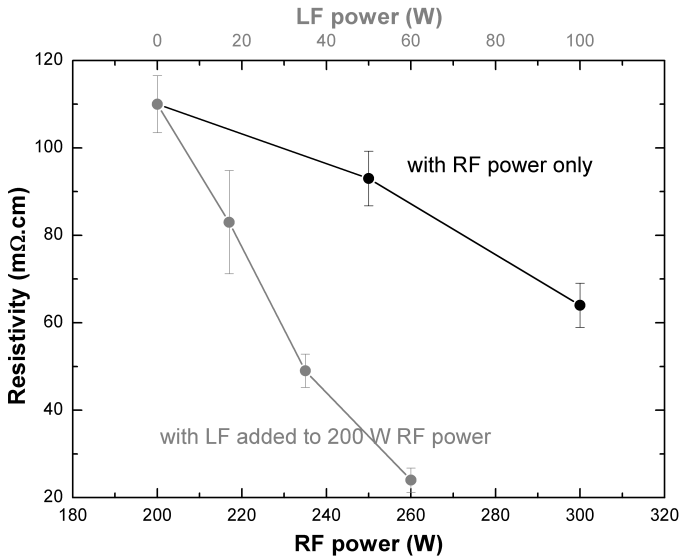

FIGURE 4.12: *TiN resistivity in RF mode and Dual Frequency mode with LF addition*

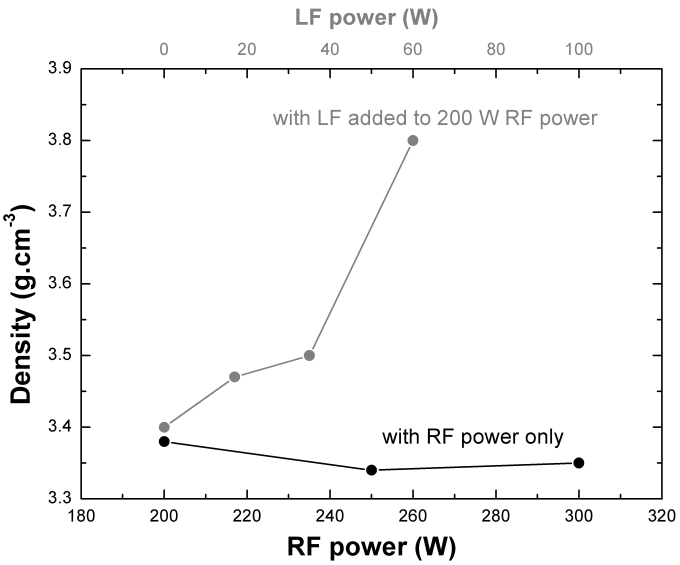

FIGURE 4.13: *TiN density in RF mode and Dual Frequency mode with LF addition*

It is clear from figures 4.11-4.13 that strong modifications are obtained with LF addition. Again the higher deposition rate in the DF mode can be correlated to the higher electron density of the plasma. In the single RF mode with addition of 100 W RF (from 200 to 300 W), the deposition rate increases by 60%, but with only 60 W LF added, deposition rate is increased by 126%. And whereas an increase of RF power from 200 W to 300 W leads to an increase of deposition rate only, adding LF power in plasma allows to increase both the deposition rate and the density of the layer, as shown in figure 4.13. An increase of both deposition rate and density indicates that the reaction mechanism is more efficient, i.e. more material is deposited on the substrate. However, above 35 W of added LF plasma power, the deposition rate and density do not have a linear growth with the plasma power increase. There is a change in the slope for all the characteristics of the material after 35 W of added LF, towards lower augmentation of the deposition rate and resistivity but higher density.
The addition of LF plasma also has an important effect on sheet resistivity. Indeed, increase of RF plasma power from 200 W to 300 W reduces the resistivity by a factor two. Such a reduction is obtained with only 35 W of LF plasma power, and adding 60 W of LF plasma power reduces the resistivity by a factor five. This decrease of resistivity is partly linked to the density of the layer; a material has its optimum conductivity when it is the closest to the theoretical density.

4.3.4.3 Impact of LF addition to RF plasma reaction mechanism

The impact of LF on chemical composition was studied by XPS on TiN materials. Figure 4.14 presents the Ti*2p* spectra of samples deposited with 200 W RF, 300 W RF, and 200 W RF + 35 W LF.

Bonding environments corresponding to each peak are noted on figure 4.14. TiO_2, TiON, TiN and TiC are located at 458.6 eV, 458 eV, 456 eV and 454.9 eV respectively [81].

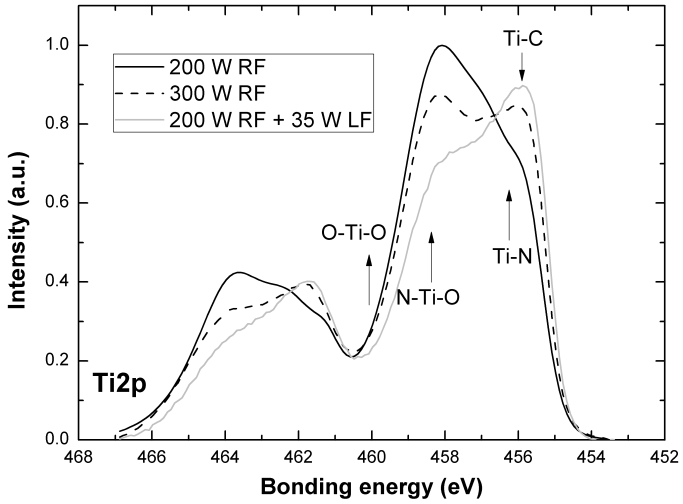

FIGURE 4.14: *XPS Ti2p spectra of TiN samples*

In figure 4.14, it appears that an RF power increase from 200 to 300 W favours the creation of TiN, resulting in lower TiON formation. Then, LF plasma power addition also reveals important changes. First the Ti-N bonds increase and the TiON bonds are reduced. If the LF sample is compared to the sample with 300 W RF power it appears that the TiN creation is similar; however, an additional 100 W of RF are used, compared with the 35W of LF. The second important change is the shift of the TiN peak maximum towards lower energies, when RF is increased or LF plasma is added. This shift may correspond to the creation of the TiC bonding environment. However, due to the low number of bonds created, the new environment TiC is not observed as a new peak.
XPS measurements were also performed a second time, after a several hours' vacuum break, to compare the oxidation uptake of each sample. The spectra are not presented here, as no significant difference between the samples was observed. Thus, oxygen uptake is similar no matter what plasma was used for deposition.

The Ti*2p* modifications previously observed are compared with the evolution of the C*1s* XPS spectrum with LF power increase, presented figure 4.15a. Evolution of the C-Ti peak area, which corresponds to the amount of carbon atoms bonded with titanium, is given figure 4.15b.

The C*1s* spectra in figure 4.15a clearly highlight the formation of TiC bonds when using LF plasma, with a C-Ti environment at 282 eV [81]. The intensity of the Ti-C peak confirms the supposition of low TiC content in the layer and the impossibility of observing the TiC peak in the Ti*2p* spectrum. Moreover, an increase of the LF plasma power leads to a higher TiC peak, as seen on the evolution of the peak area of C bonded with Ti, shown figure 4.15b. Changes on N*1s* spectra, not shown here, are not as visible; only a shift towards lower energy of N-Ti bonds is apparent. This shift corresponds to the increase of TiN bonds and to the decrease of TiO environments, as seen on Ti*2p* spectra figure 4.14.
Two explanations can support the presence of new TiC bonds in the materials. First, this

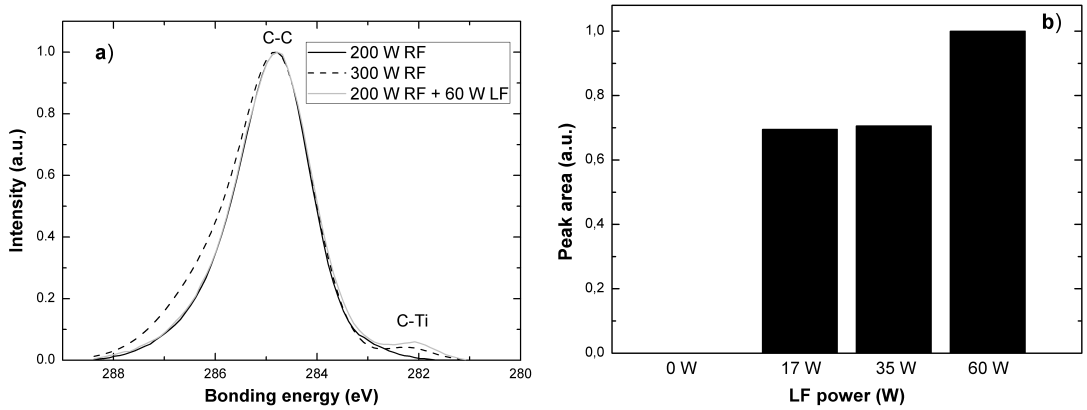

FIGURE 4.15: *C1s XPS spectra a: and evolution of the area of the Ti-C bonding environment b:*

can be due to the modification of the Ti precursor dissociation in the plasma phase (as observed by OES with new emission peaks) and so modifications of elastic and inelastic collisions in the plasma phase thanks to electronic density and temperature modifications with LF addition. Moreover, the ion plasma frequency (f_{pi}) of the precursor, and heavy ions coming from the precursor dissociation, is a few MHz. Thus the LF field can penetrate into the plasma volume causing increased heating of heavy ions and increased dissociation. This is in agreement with papers from Flamm [119] and Manolach *et al* [140]. The second mechanism can entail heterogeneous reactions, i.e. reactions at the surface of the growing film. Hence, the TiC formation can be due to the activation of a transposition mechanism, from the metalorganic titanium precursor, following the equation [17]:

$$TiN + CH_4(g) \rightarrow TiC + 1/2N_2(g) + 2H_2(g) \tag{4.7}$$

Since the deposition is done at 350°C and at 2 Torr, it is possible to determine the Gibbs energy of the reaction 4.7 to be +75 kJ.mol^{-1}. This reaction is not spontaneous, but TiC formation is favoured at higher temperatures, as shown in figure 4.16. The calculations indicate that transposition reaction 4.7 threshold is 970°C. Such a high temperature is not supposed to be reached at the surface of the sample, even when the energy brought by the hydrogen plasma is taken into consideration.

Consequently, the hypothesis of surface heating by plasma leading to a transposition reaction is not realistic. The creation of TiC bonds in the plasma phase has to be preferred.
Also, an increase of RF plasma power from 200 W to 300 W does show the creation of TiC bonds, whereas an addition of 17 W of LF plasma power to 200 W RF is sufficient to create TiC bonds, as shown figure 4.15a. As a consequence, the hypothesis of higher efficiency of the decomposition of the precursor's molecules in a DF mode, with a LF source lower than the f_{pi} of the precursor, can be made.
This reduction of the plasma power needed to create material with lower resistivity is welcome for some of the applications, i.e. plasma was proven to be the source of damage on the dielectric, resulting in poor electrical characteristics when used for CMOS technologies [19].

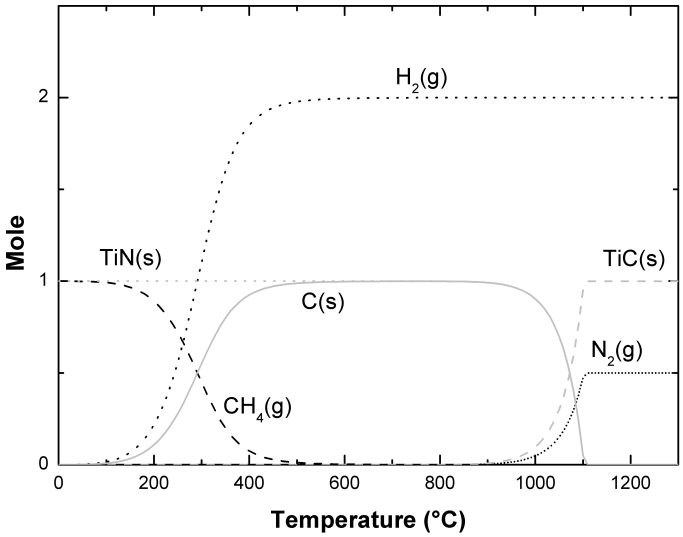

FIGURE 4.16: *Evolution of the Gibbs energy of the products from the equation 4.7*

4.3.5 Conclusion

In the PEMOCVD mode, it has been shown that using a dual-frequency instead of a single RF is a very good method to enhance the deposition rate and film properties, such as density and resistivity. It has been shown that modification of the properties of a TiN metal are obvious with the DF mode: the film is deposited faster and it has a higher density and lower resistivity. In the case of pure argon plasma, the optical emission spectroscopy of the plasmas has shown that the DF mode increases the plasma density. This is explained by a transition to a γ-mode in the CCP discharge thanks to secondary electrons. The H atoms' density is also higher in the DF mode. Finally, new emitted peaks are observed. These can be correlated to a modification of the Ti precursor dissociation in the DF mode. As a consequence, new bonds are also observed in the growing film.

As introduced Chapter 2, activation of nucleation sites in ALD process can be achieved by plasma treatment of the substrate. In that case plasma does not have an action in the volume but only on the surface. Study of the plasma power modification during PEALD deposition is then reported in the next section.

4.4 Influence of plasma power in PEALD

4.4.1 Introduction

ALD, as MOCVD, is a thermally ruled deposition. However, the activation of nucleation sites in ALD process is done by the reactant after the surface saturation of the substrate with the precursor (report to Chapter 2, section 2.2.3 for a complete description of ALD). Main ALD parameters and their influences are:

- **Substrate temperature**: monolayer deposition of the precursor is happening in a precise temperature range. The surface saturation allows a linear growth rate, whatever the substrate used.
- **Precursor injection quantity**: the quantity of precursor injected to the chamber has to be carefully chosen to allow surface saturation of the substrate and to avoid important wasting of the excess precursor.
- **Purging time**: the purging step of ALD allows for precursor excess removal. After this step precursor is only found on the substrate, not in the atmosphere of the deposition chamber.
- **Reactant gas flow**: as for precursor injection, reactant gas flow has to be adapted to have complete reaction of the precursor, any excess will be pumped to exhaust.
- **Other parameters**: the rest of the parameters are reactor dependant and can affect the uniformity of the deposition or the amount of particles formed on the substrate during the process.

The activation step of ALD, step based on reactant gas activating nucleation sites at the surface of the substrate, can be replaced by a plasma activation step. In this case, the deposition method is called Plasma Enhanced ALD (PEALD).
If many articles report the influence of ALD parameters (such as temperature [51, 54, 159, 160], precursor chemistry [54, 161], reactant gas [51], or other parameters [52, 160]), the influence of the plasma step used in PEALD process for densification of the layer is not complete [89, 90].

So in this part of the work, a focus is done on the importance of the plasma step during PEALD deposition, highlighting the material modifications obtained. Modifications which would not be possible without the energy brought by the plasma activation step.

4.4.2 Experimental methods

The following experiment is presented for the case of tantalum deposition by PEALD, but similar behaviour and reaction mechanism has been observed for tantalum deposition by plasma densified MOCVD and with lower extent for titanium plasma densified MOCVD deposition.

4.4.2.1 Samples preparation

All depositions were done in the ASM EmerALD® 3000 chamber, on 300 mm silicon (1 0 0) substrate with a silicon thermal oxide of 100 nm for resistivity 4-points probe measurements. TBTDET precursor was used for deposition. It is of importance to remember that as presented in Chapter 2 figure 2.2, in TBTDET molecule the tantalum atom is bonded directly only with nitrogen, and that one of the bounds is double; there is no direct bond between tantalum and carbon.
Process steps of PEALD deposition are presented figure 4.17. The process can be decomposed

as follow: introduction of precursor in the deposition chamber until the surface saturation is reached, purging excess of precursor, activating H_2/Ar plasma and purging before new surface saturation with precursor. Number of cycles is chosen depending on the targeted thickness, as the deposition rate is linear from the first cycles. In the current study, the number of cycles was fixed to 320, which leads to a film thickness ranging from 9 to 12 nm.
Constant plasma time and constant plasma budget are compared here. A first set of three

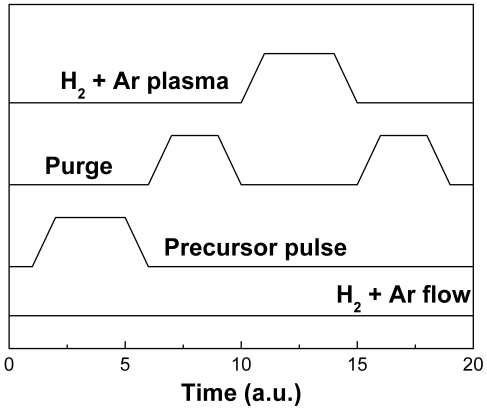

FIGURE 4.17: *PEALD purges and pulses steps*

films, S1, S2 and S3, was deposited at constant plasma time t1 and variable plasma power: low power (LP), middle power (MP) and high power (HP). Three additional films, S4, S5 and S6, were processed at LP, MP and HP plasma power condition but with adapted plasma time t_3, t_2 and t_1 respectively, ($t_3 > t_2 > t_1$), in order to obtain a fixed product of plasma power by time, called plasma budget. Identical plasma budget results in the following relation:

$$P_{LP} \times t_3 = P_{MP} \times t_2 = P_{HP} \times t_1 \tag{4.8}$$

with P_{LP}, P_{MP} and P_{HP} the plasma power of samples S_4, S_5 and S_6 respectively.
These two sets of experiments allow a comparison of the influence of instant plasma power vs. total plasma budget on the TaCN film. The sample with the higher plasma power condition and a chosen plasma time t_1 was done twice (S_3 and S_6) in order to confirm process repeatability. Used plasma powers and times are summarised in the table 4.3, with in line the constant plasma time and in diagonal the constant plasma budget.

TABLE 4.3: *Samples time and power of plasma step*

	Low Power	**Middle Power**	**High Power**
$\mathbf{t_1}$	Sample 1	Sample 2	Sample 3 and 6
$\mathbf{t_2}$		Sample 5	
$\mathbf{t_3}$	Sample 4		

4.4.2.2 Characterisations

Transfer from the deposition chamber to other characterisation equipments required vacuum break, leading to surface oxidation of the films. To limit the variation of the oxide growth, a minimum of one hour vacuum break was observed between deposition and characterisation, in order to insure stabilisation of the oxide before analysis [162]. Thickness, density and roughness were measured by X-Ray Reflection (XRR), in 43 points with $2\theta = [0; 3.5°]$, and 4 points probe technique was used to measure the films resistivity in 49 points. Average from all the points measured is presented here, the error bars on the figures correspond to the measured variability. Crystallography of the samples was obtained by X-Ray Diffraction (XRD) on a $2\theta = [30; 80°]$ range, compositions and chemical bonding were measured by X-Ray Photoelectron Spectroscopy (XPS) using a Al - Kα (1486.6 eV) source and a spot size of 400 µm with a passing energy of 100 eV.

4.4.3 Results

4.4.3.1 Thickness and density

In figure 4.18 are given the XRR average thicknesses and densities versus plasma power, over the 43 measured points extracted by careful spectra fitting. To obtain satisfying fit between the spectra and the model, 15 Å tantalum oxide layer was added on top of the TaCN layer, indicating a clear surface oxidation of the film. Besides, layer roughness did not change with plasma modification.

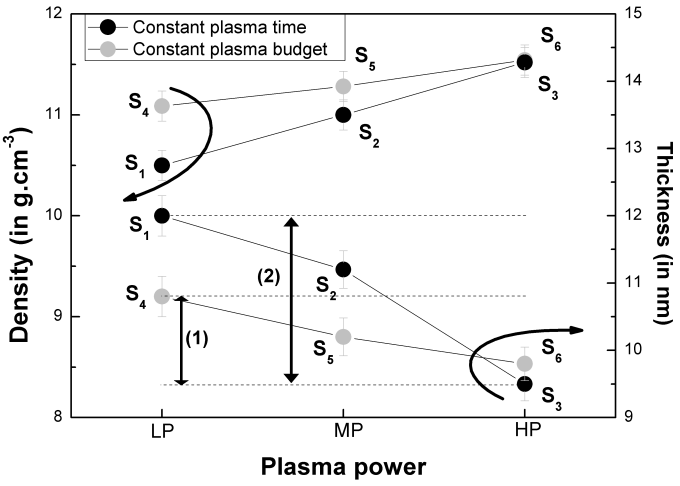

FIGURE 4.18: *TaCN evolution with plasma power increase*

It appears that the two samples S_3 and S_6 generated at HP present a similar variation of thickness and density included in the measurement error margin. This similarity was confirmed with resistivity measurements. Thus process is considered to be stable.
First, for constant plasma time experiments, thickness decrease (left axis) and density increase (right axis) are observed at higher plasma power, which indicates a densification of the material (see (2) on figure 4.18). Measured density, 10.5 g.cm^{-3} for LP and 11.5 g.cm^{-3} for

HP, has to be compared with theoretical density of TaN: 13.7 g.cm^{-3} and TaC: 14.5 g.cm^{-3} [100]. Difference between theoretical and experimental density values could be related to TaCN surface oxidation.
Second, for the constant plasma budget experiments, a decrease of thickness and increase of density with longer plasma time at both LP and HP conditions are observed. At constant plasma budget a significant variation of density and thickness can be observed between S_4 LP and S_6 HP (see (1) on figure 4.18). Therefore by comparison of the two sets of experiments it appears that plasma time increase is leading to lower changes in the material than plasma power increase. Higher plasma power seems to be more efficient to break down the precursor molecule and enable formation of new bonds.

Resistivity of the layers, in figure 4.19, exhibits similar behaviour as the thickness presented previously.

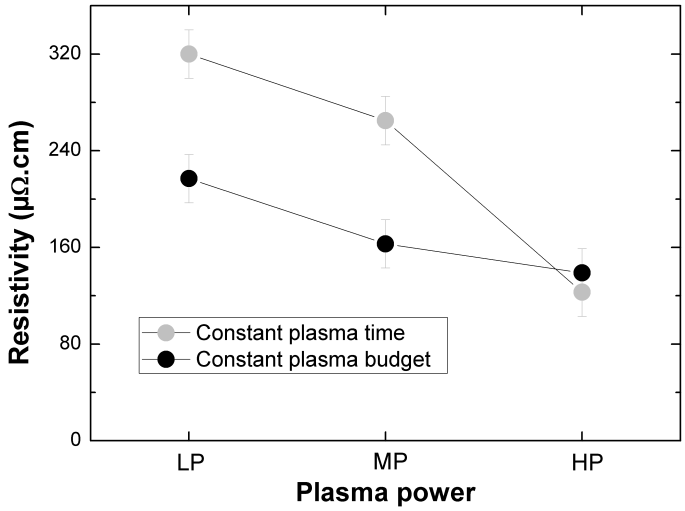

FIGURE 4.19: *Evolution of TaCN resistivity with plasma power*

Constant plasma time experiment shows a decrease of resistivity by a factor 3 from LP to HP samples. From literature, it is known that cubic-TaN (150 μΩ.cm) is more resistive than cubic-TaC (30 μΩ.cm) [100] for highly crystalline samples. Therefore, it suggests that plasma power increase changes the materials properties from TaN-like to TaC-like film. Obtained resistivity is comparable with resistivity of films deposited by MOCVD [18, 163, 164] and reactive sputtering [165, 166] techniques, as it is ranging from 200 to 1000 μΩ.cm depending on process conditions.
In line with the previous XRR study, it appears that LP and HP samples in the constant plasma budget experiment show a decrease of resistivity. Effect of plasma time increase on resistivity is obvious (see figure 4.19 S_1, S_4 at LP and S_2, S_5 at MP) but not as efficient as a plasma power increase (HP values). Here again, one can conclude that higher plasma power is more efficient to decompose the precursor than longer plasma time.

In the rest of the discussions, focus will be done on constant plasma time experiments, S_1,

S_2 and S_3 samples, which represent extreme cases (i.e. the other samples are expected to present intermediate properties).

4.4.3.2 Crystallography

Crystallographic spectra, obtained by 1° incident angle XRD, of LP and HP samples are presented in figure 4.20, along with the theoretic peaks of cubic-TaN and cubic-TaC [79]. Spectrum from MP sample is not displayed to allow a better view of LP and HP differences.

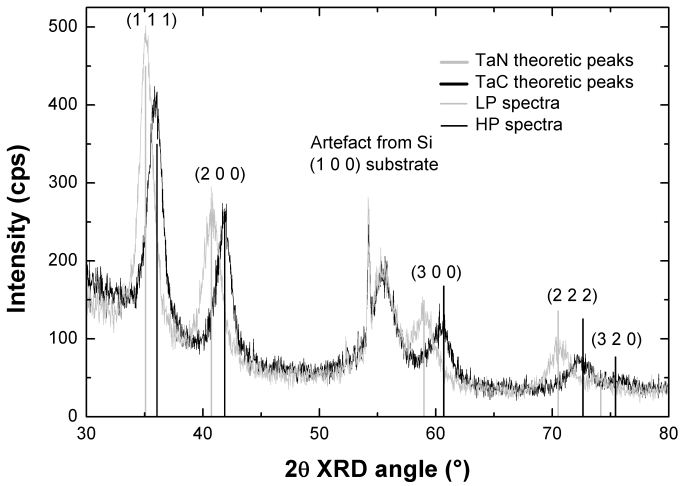

FIGURE 4.20: *Evolution of TaCN crystallography with plasma power*

Five Miller indexes are visible in the analysed window. These indexes confirm that both LP and HP samples have a cubic structure. Moreover, matching between experimental spectra and theoretical peaks shows that the increase of plasma power is changing the crystallography of the films from cubic-TaN to cubic-TaC, this evolution is clearly visible for all the indexes.

The shift of the crystallographic peaks is related to a modification of the lattice parameter of the layer, from 4.32 Å at LP to 4.42 Å at HP. These two values perfectly match with reported cubic-TaN and cubic-TaC lattice parameter [79].

In addition, the artefact from substrate silicon (1 0 0) at 2θ =57°, visible for both LP and HP samples, shows that the shift in peaks location is not due to measurement error but corresponds to a change in the deposited material.

Although, spectrum of the intermediate power sample (MP) is not presented here, it appears that the five indexes peaks of MP sample are all located in between LP and HP peaks. Full width at half maximum (FWHM) and intensity of the peaks are similar for the three samples, which shows that it exists only one kind of lattice within the layer. If MP layer would be made from a mixture of TaN and TaC poly-crystals an enlargement of the peaks together with a decrease of intensity would have been observed. Thus modification of lattice size is gradual with plasma power increase.

The high intensity and low FWHM of the peaks in the spectra confirms the high crystallinity of the material. So the lower density observed in the figure 4.18 cannot be explained by a

low crystallinity of the layer.

4.4.3.3 Chemical environments

The chemical environment of the species in LP and HP layers was deduced from XPS analysis. Ta*4f*, C*1s* and N*1s* spectra acquired on LP samples are presented in figure 4.21 and 4.22, HP sample Ta*4f*, C*1s* and N*1s* are presented in figure 4.23 and 4.24.

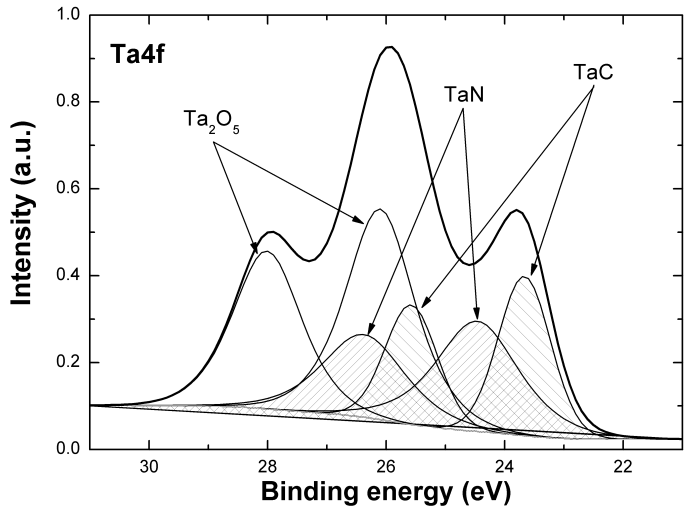

FIGURE 4.21: *Ta4f chemical environments of TaCN-LP sample*

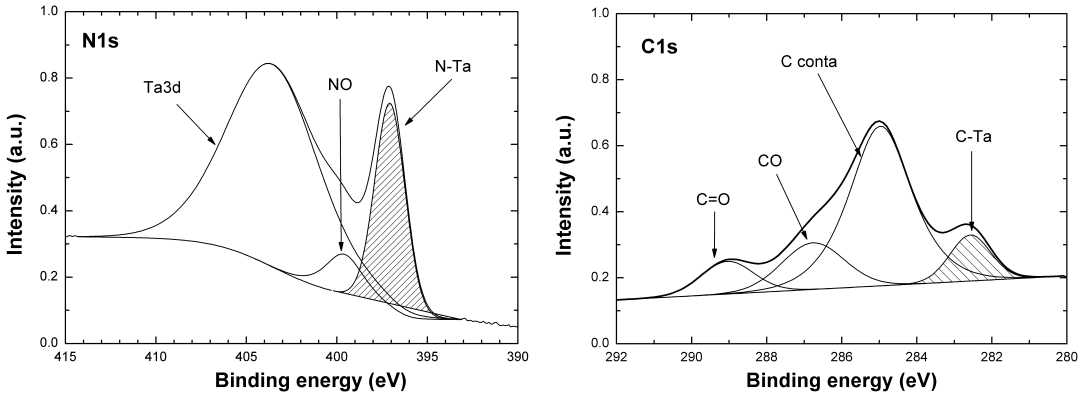

FIGURE 4.22: *N1s and C1s chemical environments of TaCN-LP sample*

Ta*4f* spectra from LP sample, in figure 4.21, and HP sample, in figure 4.23, exhibit three environments; Ta-O (i.e. Ta bonded with oxygen), Ta-N and Ta-C located at 26 eV, 24.5 eV and 23.5 eV respectively [81]. Because of the three overlaid bonding environments, analysis of the spectra is quite difficult. In order to have more information on the material bonds, environments of carbon and nitrogen were studied, with C*1s* and N*1s* respectively. Spectra are presented figure 4.22 for LP sample and figure 4.24 for HP sample. Environment changes of C*1s* and N*1s* are clearly highlighted from these spectra. In figures 4.22 and 4.24, the C*1s* peak present at 283 eV (on the right of the spectra) correspond to C-Ta bonds. Figures 4.22

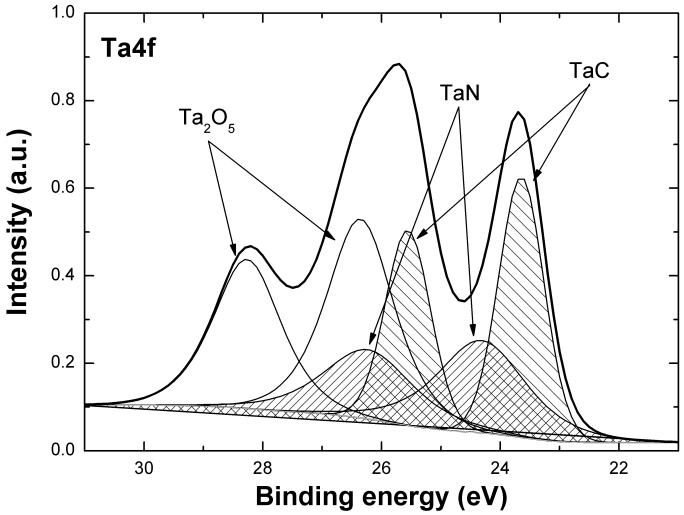

FIGURE 4.23: *Chemical environments of TaCN-HP sample*

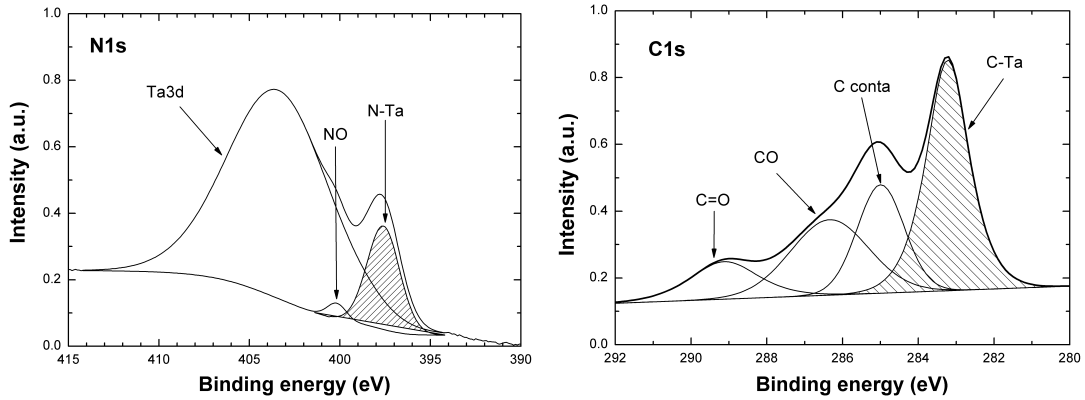

FIGURE 4.24: *N1s and C1s chemical environments of TaCN-HP sample*

and 4.24, the N*1s* peaks present at 397 eV (on the right of the spectra) correspond to N-Ta bonds. Evolution of carbon and nitrogen bonds is consistent with the hypothesis expressed above: plasma power increase allows a better precursor's molecule bonds separation which changes the material from TaN-like to TaC-like.
Quantification of the species present in the films can be extracted from the current XPS spectra, leading to the composition of the layers. Indeed, area under the curve is proportional to the number of bonds present in the analysed volume. Films compositions are given in figure 4.25. This estimation only includes C-Ta (obtained in C*1s*), N-Ta (obtained in N*1s*) and Ta-C, Ta-N bonds (obtained in Ta*4f*).

Layers compositions reveal that the number of carbons in C-Ta bonds is increasing with higher plasma power, whereas nitrogen in N-Ta bonds is decreasing. This observation further confirms modification of the material from TaN-like to TaC-like, keeping a TaC_xN_{1-x} composition.
Representation of Ta atoms and their bonds for LP and HP are given figure 4.25a and 4.25b, it reflects the composition changes of the deposited layers from $TaC_{0.19}N_{0.86}$ at LP to $TaC_{0.56}N_{0.49}$ at HP.

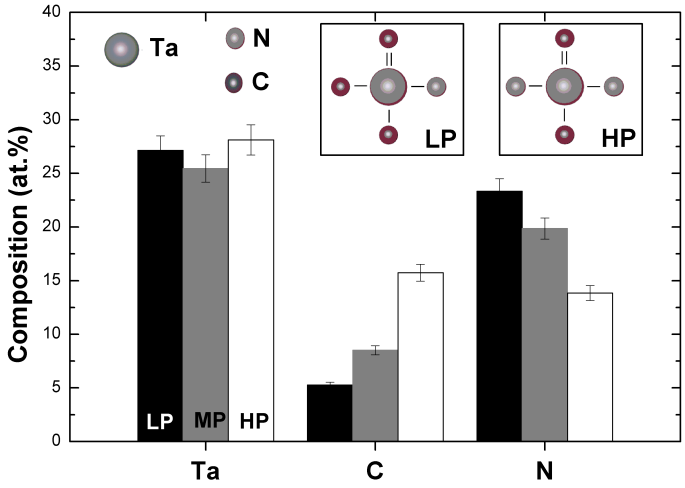

FIGURE 4.25: *Chemical composition of TaCN-LP, TaCN and TaCN-HP samples*

4.4.4 Discussion

4.4.4.1 Composition

Overall, characterisations done in this study proved the evolution of TaCN metal properties from a TaN-like to a TaC-like material. This evolution was linked to the increase of plasma power which allows to break chemical bond between Ta and N in the TBTDET molecule, resulting in an increase of tantalum bonded with carbon in the deposited material. Also due to the original chemical structure of TBTDET molecule, nitrogen concentration in the layers is greater than carbon concentration. Complete replacement of nitrogen by carbon has not been seen, even with higher plasma power than presented here. This observation can be associated to the presence of a double bond between Ta and N, the plasma energy required to break this bond is more important.
On the XPS spectra presented figures 4.21, 4.22, 4.23 and 4.24 no C-N, N-N nor Ta-Ta bonds were observed, whatever the plasma parameters. Therefore it appears that all C and N coming from the precursor molecule either react with Ta to form Ta-C or Ta-N bonds or is pumped away from the sample surface as a deposition by-product. No residues, such as $N(CH_3)_x$ or CH_x are detected in the film. The absence of carbon impurities in the film and the presence of Ta-C explain the low resistivity of the layers, indeed carbon impurities increase the resistivity of the films [167], whereas carbides decrease it.

4.4.4.2 Film density

Crystallographic analysis of the samples, in figure 4.20, showed a high crystallinity of the films, suggesting that experimental density should be similar to theoretical one. Using Angle Resolved XPS, the surface oxidation was determined to be thinner than 2 nm. Knowing that Ta_2O_5 density is 8.2 g.cm^{-3} [100], a stack of 2nm of Ta_2O_5 and 10nm of TaN or TaC has an total density of 12.5 or 13.3 g.cm^{-3} respectively. Thus, not only surface oxides account for

the low density measured. Another hypothesis to explain the density shift is the oxidation of the first deposited nanometres by interaction with the substrate. It has been shown that ALD deposited TaN is creating only Ta-O bonds in the early steps of the process [168]. Thus it can be supposed that there is oxidation of TaCN, located at the TaCN/SiO_2 interface, but because of TaCN surface oxidation it is not possible to locate the Ta-O bond at the interface by XPS. A 1 nm tantalum oxide at the substrate interface would decrease the density from 12.5 to 11.9 g.cm^{-3} and 13.3 g.cm^{-3} to 12.7 g.cm^{-3} for TaN and TaC respectively. On top of that the XRR fitting error has to be taken into consideration. This error which can be evaluated to 10%, leading to a measured density of TaN or TaC matching to the theoretical densities of crystalline material.

4.4.4.3 Film formation

TBTDET metalorganic precursor has similar behaviour to other metalorganic precursors, such as TDEAT, as metal is only bonded to nitrogen. Thus deposition of TBTDET can be resolved by three different reactions [17]: transamination exchange with the formation of diethylamine and methane (4.9), amine elimination (4.10, 4.11) and possible transposition reaction resulting in the formation of ammonia and hydrogen (4.12) or nitrogen and hydrogen (4.13).

$$Ta[N(C_2H_5)_2]_3[=NC(CH_3)_3] + 8H_2(g) \rightarrow [NH_2]_2Ta[N(C_2H_5)_2][=NC(CH_3)_3] + 8CH_4(g) \quad (4.9)$$

$$N_2Ta[N(CH_2CH_3)_2][=NC(CH_3)_3] + H_{plasma} \rightarrow N_2TaH_2 + 2N(CH_3)_3(g) + 5CH_4(g) \quad (4.10)$$

$$N_2Ta[N(CH_2CH_3)_2][=NC(CH_3)_3] + H_{plasma} \rightarrow N_2Ta(NH_2)_2 + 8CH_4(g) \quad (4.11)$$

$$TaN + CH_4(g) \rightarrow TaC + NH_3(g) + 1/2H_2(g) \quad (4.12)$$

$$TaN + CH_4(g) \rightarrow TaC + 1/2N_2(g) + 2H_2(g) \quad (4.13)$$

To explain the formation of TaC with plasma power increase the Gibbs energy of the transposition reaction was calculated. Considering that in this experiment deposition is done at 325°C and under 1 Torr the Gibbs energy of reaction (4.13) can be determined to be +77

kJ/mol, thus the reaction is not spontaneous. But a temperature increase will lead to the enhancement of TaC formation, as shown in figure 4.26.

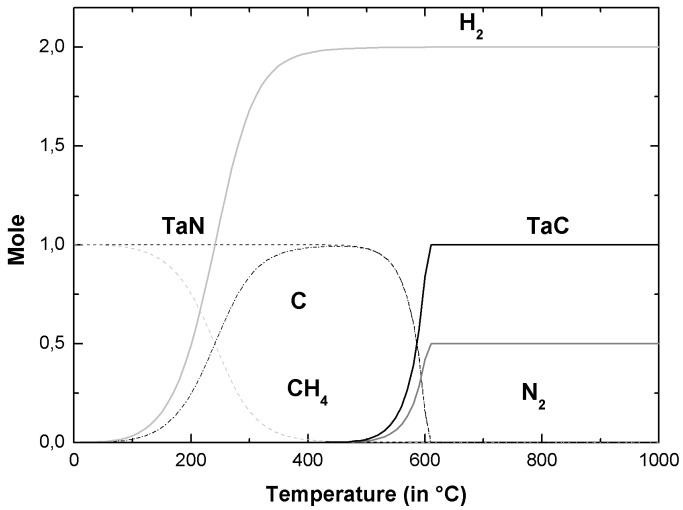

FIGURE 4.26: *Gibbs energy calculation of TaC formation*

Calculation reports that transposition reactions (4.12) and (4.13) appear from 550°C, such temperature can be reached locally at the sample surface thanks to hydrogen plasma. As a result increase of H_2 plasma power is leading to an increase of the local temperature and will promote the transposition reaction, leading to creation of TaC.
XRD measurements, figure 4.20, showed a gradual change of the lattice parameter from cubic-TaN to cubic-TaC but composition analysis, figure 4.25, confirmed that the material always contains nitrogen and carbon. Thus, it appears that increase of plasma power is leading to introduction of carbon atoms in TaN lattice, progressively affecting the lattice parameter of the material towards a TaC lattice. One can suppose that this carbon nitrogen exchange and evolution of the lattice parameter may lead to high internal stress of the material.

4.4.5 Conclusion

In this part, the influence of plasma power on TaCN films deposited by PEALD was evaluated. XRR and four points probe measurements showed that using higher plasma power lower resistivity and higher density films are obtained. These changes were compared with theoretical data of TaN and TaC material to highlight the similarities and it appears that increase of plasma power is shifting the material from a TaN-like to a TaC-like material. Increasing plasma time to have same plasma budget at all plasma power (the product of plasma power and plasma time being constant) leads to a decrease of the observed variations between low and high plasma power, but differences are still significant. XRD analyses support the TaN-like and TaC-like hypothesis with really good fitting of the experimental and theoretical Miller indexes. Then, a correlation was done with XPS measurement, proving the hypotheses of TaN-like and TaC-like materials thanks to chemical bonding and film

composition. XPS analysis also showed a significant O contamination due to post-deposition oxidation of TaCN films in ambient atmosphere. Finally, a reaction mechanism was proposed to explain the formation of TaC from the TaN bond initially present in the TBTDET molecule.

4.5 PEMOCVD conformity control

To validate the hypothesis of conformal deposition using the PEMOCVD method, a 4 nm TaN PEMOCVD layer was deposited on a 15 nm wide and 15 nm Si high Fin-like structure, patterned on SiO_2 substrate. To compare the conformity of PEMOCVD deposition vs. MOCVD, introduced Chapter 3 section 3.5.1, the patterns from the same wafer were used for deposition with the following parameters:

- substrate temperature: 350°C
- chamber pressure: 2 Torr
- liquid injector temperature: 40°C
- plasma power: 100 W
- deposition rate: 0.2 Å.s^{-1} (similar to MOCVD deposition for better comparison)

As for MOCVD deposition the substrate is made of SiO_2 and the quantity of metal deposited is not sufficient to avoid any charging effect. Meanwhile, secondary and back scattered electron images were acquired and are presented in figure 4.27. To ease the comparison the same magnification was used in figure 4.28 as in figure 3.21 of MOCVD layer presented in Chapter 3, section 3.5.1.

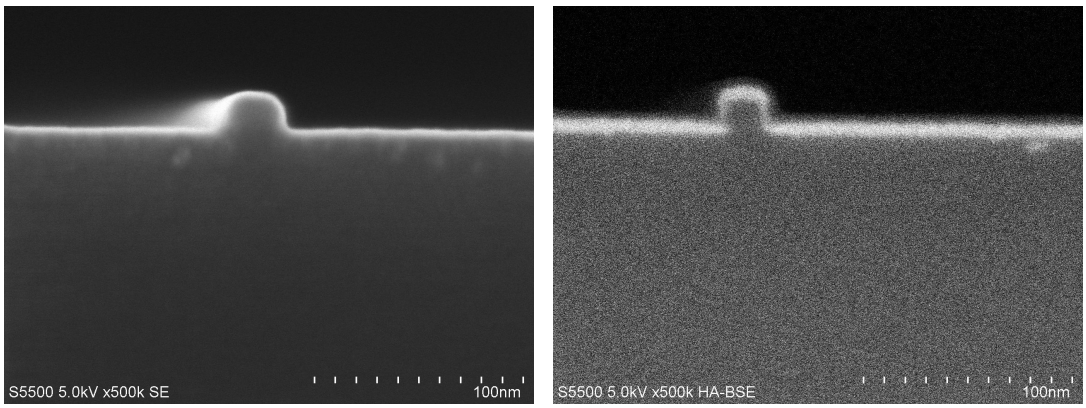

FIGURE 4.27: *SEM observation of PEMOCVD deposited TaN on 15 nm Fin*

Conformity appears to be lower than what was obtained with MOCVD deposition. In fact, the thickness deposited on horizontal surfaces appears to be higher than the thickness on the side walls of the Fin structure. A rough estimation of the thickness gives a ratio 1.2:1 for surface:wall deposited thicknesses. This observation is in good correlation with the fact that PEMOCVD is not a process induced by surface reaction, contrary to MOCVD, but is

affected by the directionality of the active species.

It also appears, figure 4.28, that the roughness is lower than when MOCVD is used.

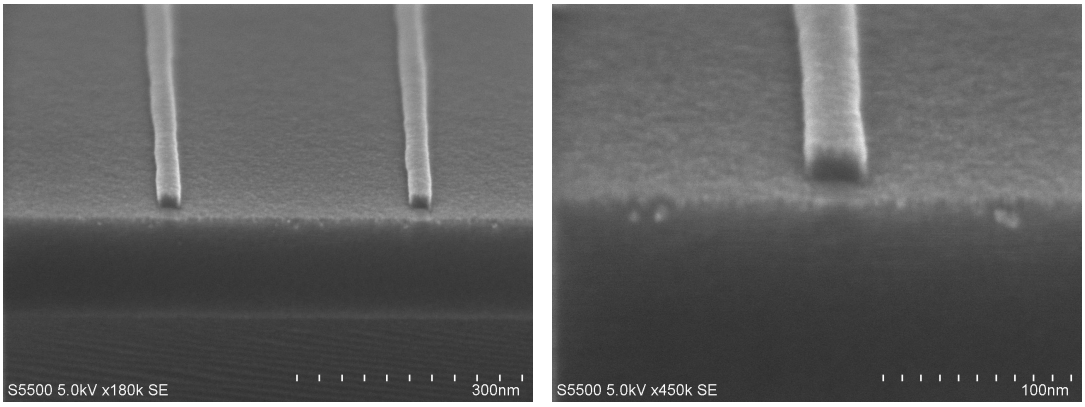

FIGURE 4.28: *SEM observation of PEMOCVD deposited TaN on 15 nm Fin*

Hence, at x180k magnification no grains are visible on the PEMOCVD layer (left), and only some small grains are observed with higher magnification (x500k figure 4.28 right). This difference highlights the variation of reaction mechanism between MOCVD and PEMOCVD depositions. Whereas MOCVD has an island based growth, resulting in large grains, PEMOCVD deposition reaction activation is done in the volume of the plasma, resulting in the formation of small grains or even amorphous layers.

4.6 Conclusion to the Chapter 4

In this chapter, the importance of plasma either for decomposition of the precursor (PEMOCVD) or activation of nucleation sites (PEALD) was highlighted.
First, it was shown that parameters which proved to impact the deposited material during MOCVD have a limited effects on the PEMOCVD deposition. Indeed, the reaction mechanism and decomposition of the precursor are mainly activated by the plasma, in its volume away from the substrate surface. Only the substrate temperature influences the deposition, higher temperature allowing lower carbon contamination due to better exhaust of the reaction by-products.
It also appears that plasma has a strong influence on the deposited material. Lower resistivity, higher growth rate and density can be achieved by increasing the plasma power. This evolution confirms the activation of the deposition reaction mechanism in the volume of the plasma.
On top of plasma power, another parameter is influencing the decomposition of the precursor: the plasma frequency. Addition of a low frequency source to a radio frequency source modifies the characteristics of the plasma applied to TiN-PEMOCVD, such as plasma density and excited species, resulting in a better decomposition of the precursor. New metal-carbon (Ti-C) bonds are created and it is demonstrated that these bonds would be produced by

MOCVD exclusively by an increase of the temperature up to 970°C.
Later on, in an ALD deposition chamber, investigation of plasma surface treatment for nucleation sites activation and densification of the layer was completed. Increase of the plasma power applied to TaN-PEALD resulted in an increase of the density, crystallinity and decrease of the resistivity and thickness. A careful XPS investigation revealed that new metal-carbon (Ta-C) bonds are formed and it is also demonstrated that these bonds would be produced by MOCVD only if an increase of the temperature to 550°C would be used.

To conclude, in this chapter the importance of plasma power and plasma frequency were demonstrated. It was shown that plasma helps to trigger reaction paths that would be possible only with considerable temperature increase when using thermally activated reaction.

In the next chapter these different metals and processes are integrated in a metal gate stack and interactions with substrate material (dielectric or other metal) are discussed.

Chapter 5

Interactions with sub-layer during metal integration

"The most exciting phrase to hear in science, the one that heralds the most discoveries, is not 'Eureka!' (I found it!) but 'That's funny...' !"

Isaac Asimov, biochemist

5.1 Introduction

In the previous chapter the importance of process tuning was demonstrated and a range of materials with different properties were produced. The materials created were characterised as bulk materials, without paying attention to the surface or interface reactions/interactions. However, from volume study of bulk materials, there is a necessary evolution towards surface/interface investigations, linked to the thickness reduction of the layers as mentioned in the Chapter 1, figure 2.1.

Also, as already mentioned in the Chapter 1, for advanced technology nodes the surface/interface has grown in importance on the definition of the general device behaviour. It is now well known that continuous reduction of layers thickness arises new challenges although the same thickness reduction offers new possibilities. Thus, it is necessary to fully understand and control the modifications taking place during the integration of the material. For example, the affinity of TiN with oxygen is now used for SiO_2 interfacial layer reduction by scavenging of the oxygen [169, 170]. This is made possible by the easy migration of species through the thin HfO_2 layer. In fine, the layers are so thin that some of the interactions might be related to layers which are not in contact.
Chemical modifications of the metal or dielectric have direct influence on the determination of the device physical and electrical properties [19, 22, 90, 171–174]. Thus by carefully adapting the deposition process to limit or to enhance some of the interactions it is possible to aim different characteristics suitable for the p-MOS or n-MOS devices.

Therefore, this chapter will focus on the interactions of materials or processes with the substrate. The first part will investigate the tuning of PEALD Ta(C)N deposition process parameters and link it to the modifications brought to the substrate, in particular when

plasma is involved. Plasma provides more energy to the system through the formation of radicals [73, 113, 175], which can penetrate deep in the matter and interact with the substrate, thus modifying it. In a second part, the interactions observed during the deposition of Ta(C)N on HfO_2 will be used to improve another metal, here a PVD deposited TiN. Oxidation decrease and nitridation increase are the result of Ta(C)N interactions. TiN may also be used in that configuration as a protective film to reduce the impact of plasma and limit the damages on the dielectric.

5.2 Impact of plasma on dielectric under-layer

5.2.1 Context

Advanced 22 nm node devices, based on 3D architecture, such as FinFET, induce new challenges for gate metal deposition. Such technologies require very thin dielectric/metal gate films with good conformity and low leakage current. ALD-deposited hafnium oxide is currently used in the advanced CMOS transistors fabrication [176, 177] and allows to lower the Equivalent Oxide Thickness (EOT) below a nanometre while maintaining acceptable current gate leakages. Tantalum-based metal gates have been widely studied as an alternative to the well-known standard Titanium nitride [30]. In particular, Tantalum carbo-nitride alloys (TaCN) can range from TaN to TaC, including TaCN. Tantalum alloys, not only have good thermal stability, chemical inertness and compatibility with current technologies [14], but also have a wide range of possible characteristics; i.e. Work Function (WF) changes from near mid-gap TaN, 4.55 eV [92], to n-type TaC metal 4.2 eV [178, 179]. Moreover, tantalum alloys are known to be good chemical etch barriers, which can be convenient for integration to current process flows. It also acts as chemical barrier against oxygen diffusion which can limit the regrowth of SiO_2 interfacial layer between dielectric and Si substrate [180, 181]. Thanks to its low roughness and good conformity (Plasma Enhanced) Atomic Layer Deposition ((PE)ALD), is a good candidate for metal deposition in advanced nodes [44, 182]. In a previous study, this deposition technique has been used for TaCN deposition and it has been shown that power of hydrogen plasma has a direct influence on TaCN properties, by modulating the formation of Ta-C bonds as presented in the Chapter 4. However, the dielectric underneath can be severely affected during the plasma steps of PEALD metal deposition by electrons, excited and hot ionised species from the plasma, such as H^+, NH^+ and other radicals formed by precursor's decomposition [19]. In plasma ambient, ions and electrons are collected by the metal electrode which serves as an antenna [175], a steady-state voltage may appear in the metal due to charge collection and resulting on electrical stress which can affect underlying gate oxide [175, 183–187]. The two main phenomena inducing dioxide degradation are: first, the oxide breakdown due to a conduction path formed from the anode to the cathode [184, 185], second the weakening of the oxide by charge trapping correlated to the formation of defects in the oxide [186, 187].
Thus, the aim of this investigation is to first understand the reactions taking place at the metal/high-κ interface and then evaluate the plasma damages on high-κ layer, in order to

obtain the best TaCN properties with the lowest impact on the HfO_2. First, X-ray photoelectron spectroscopy (XPS) is used to highlight the interactions of TaCN with HfO_2. Then depth composition by Angle-resolved XPS (AR-XPS) is used to evaluate reactions at the interface and species (O, N) exchanges between TaCN and HfO_2. Finally electrical characteristics of TaCN/HfO_2/SiO_2/Si are discussed with regards to the metal deposition parameters and chemical environments obtained by XPS analysis.

5.2.2 Experimental methods

Material characterisations were carried out on Si (1 0 0) blanket wafers. To measure the variation of EOT simple MOS stacks with TaCN/HfO_2/SiO_2/Si were realised in oxide cavities on p-type silicon substrate (5-10 Ω.cm). Both blanket and CMOS wafers were cleaned by an initial HF bath to remove native oxide, followed by a 8 Å chemical oxide formation. This oxide was formed by a wet oxidation and acts as an interfacial oxide layer and nucleation surface for 2 nm thick HfO_2. HfO_2 was deposited at 350°C by atomic layer deposition using alternation of H_2 and $HfCl_4$ precursors at 133 Pa. HfO_2 was then annealed under N_2 atmosphere at 650°C during 2 min for by-products exhaust. To avoid regrowth of SiO_2, HfO_2 deposition was performed within 2 hours after chemical SiO_2 formation. Before metal deposition, a 3 min degassing at 325°C was performed to allow surface moisture removal from HfO_2 surface. 4 nm TaCN metal was then deposited by PEALD with Tris(diethylamino)(tert-butylimido)tantalum (TBTDET) precursor and H_2 plasma. PEALD deposition principle was already detailed in the Chapter 2. Finally, to allow electrical measurements on MOS stacks, contact plug based on 5 nm TiN / 150 nm W was CVD-deposited at back-end temperatures on top of TaCN.
Plasma power influence was studied at different conditions: 175 W, 250 W and 325 W plasma power, respectively named PEALD-LP, PEALD and PEALD-HP, all other deposition parameters are kept constant. To allow complete understanding of chemical interactions, samples with SiO_2/Si only, HfO_2/SiO_2/Si and TaCN/SiO_2/Si were also prepared on blanket wafers. Physical Vapor Deposition (PVD) TiN and Ion Beam Deposition (IBD) TaN metals were also deposited on HfO_2 as references for electrical measurements.

XPS measurements were performed with a Theta 300 XPS tool from Thermo Scientific. A high resolution monochromatic Al Kα X-Ray source (1486.6 eV photons) with a pass energy of 100 eV and a resolution of 0.1 eV. No carbon nor oxide removal was performed on the samples before XPS characterization, thus due to oxidation and atmospheric contamination high levels of C and O were observed at the extreme surface of the samples. Carbon C*1s*, located at 285 eV [81] was used to remove any possible shift in the binding energy due to sample charging. Observation of Ta, Hf, Si, C, N, and O chemical environments were extracted from the Ta*4f*, Hf*4f*, Si*2p*, C*1s*, N*1s* and O*1s* core level energy regions, respectively. Using a numerical procedure, spectral fitting was performed to extract the peak contributions in the acquired energy regions. Individual line shapes were simulated with a

combination of Lorentzian and Gaussian functions using the commercial software Advantage. The background subtraction was performed using a Shirley function calculated from a numerical iterative method. AR-XPS measurements used the same parameters as XPS, with the simultaneous acquisition of eight angles, in the range 23° to 76°, without physical tilt of the sample, which allows the formation of an accurate depth resolved profile. Based on intensity evolution of the Ta*4f*, Hf*4f* and Si*2p* line shapes, it is possible to build a depth composition profile of the sample. As a result of this analysis the variation of intensity (in arbitrary unit) is plotted through the depth of the sample. It is noteworthy that only the variation of composition should be taken into account: the higher intensity of an element cannot be interpreted as a higher concentration of this element in the sample.
XPS spectra fitting was done using the following constraints: Hf$4f_{5/2}$ was defined with a shift in energy of $\Delta E = 1.71$ eV and an area ratio of 0.75 compared to Hf$4f_{7/2}$ [81]. A shift in energy of $\Delta E = 1.91$ eV was taken for Ta$4f_{7/2}$ and Ta$4f_{5/2}$ doublets separation, with also an area ratio of 0.75.
Thanks to the identical Si*2p* line shapes obtained with SiO_2/Si, HfO_2/SiO_2/Si and TaCN/SiO_2/Si (not shown here), Si can be considered as not interacting with the HfO_2 and TaCN materials. Thus Hf*4f* and Ta*4f* peaks from HfO_2/SiO_2/Si and TaCN/SiO_2/Si samples are used as individual references for TaCN/HfO_2/SiO_2/Si stack peaks fitting and interpretation.

5.2.3 Results

5.2.3.1 Chemical interactions

XPS Hf*4f* spectra of HfO_2 before and after TaCN low plasma power deposition are presented figure 5.1.

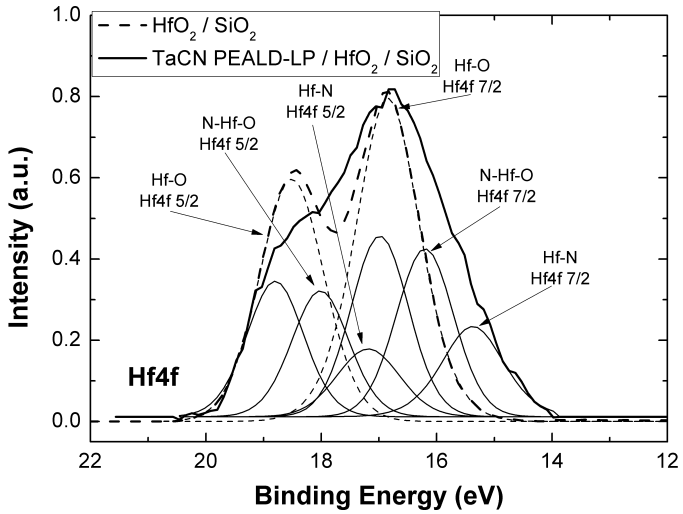

FIGURE 5.1: *Comparison Hf4f XPS environment from HfO_2/SiO_2/Si and PEALD-LP-TaCN/HfO_2/SiO_2/Si*

Fitting of HfO_2/SiO_2 reference can be achieved using only one doublet, standing for Hf-O environment and located at 16.8 eV. Deposition of PEALD-LP-TaCN on top of HfO_2 is

leading to the formation of new chemical environments in Hf*4f* region. Hence, PEALD-LP-TaCN/HfO_2/SiO_2/Si spectrum is noticeably broadened, thus indicating at least two additional bonding environments. The first one, adjusted at 15.3 eV is attributed to the formation of Hf-N bonds [81] in HfO_2 layer. The second environment doublet at 16.2 eV corresponds to the presence of O-Hf-N-like bonds. From O-Hf-N peak it is not possible to discern if N is placed as a first of second neighbour of the Hf.
Because of the important amount of oxygen in HfO_2 layer and oxidation of TaCN layer, no significant evolution of O bonds was observed in O*1s* spectra, therefore O*1s* region is not presented here.

To complete the understanding of TaCN interactions with HfO_2, Ta*4f* spectra from TaCN low power deposited on HfO_2/SiO_2/Si and on SiO_2/Si are now compared in figure 5.2.

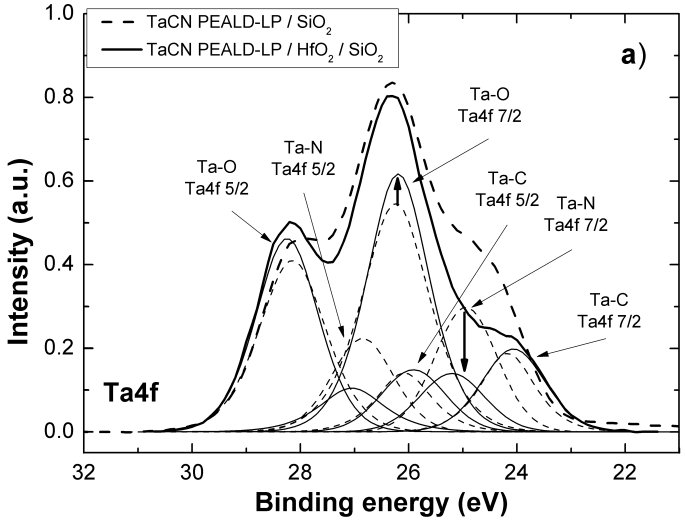

FIGURE 5.2: *Comparison Ta4f XPS environment from PEALD-LP-TaCN/SiO_2/Si and PEALD-LP-TaCN/HfO_2/SiO_2/Si*

Although the same TaCN deposition is achieved, Ta*4f* spectra are different when deposited on both dielectrics and three modifications are noticed: i: the first one concerns Ta-O bonding environment, located at 26.2 eV. While no shift in binding energy is observed, Ta-O peak relative intensity increases when TaCN is deposited on HfO_2; ii: the second effect is the significant decrease of Ta-N peak intensity, meaning lower Ta-N bonds when deposited on HfO_2, and biding energy shift from 25.2 eV to 25 eV; iii: the third change deals with Ta-C environment, at 24.2 eV, which is shifted to lower energy. Creation of Ta-C bonds can only be the result of the deposition process through a well-known transposition reaction [17], as in the TBTDET molecule tantalum atoms are bonded only to nitrogen, i.e. there are no direct bonds between tantalum and carbon. The evolution of TaCN from TaN-like toward TaC-like deposition by plasma power increase was demonstrated in the Chapter 4, the presence of carbides validated by the C*1s* spectra are presented there.

N*1s* spectra from TaCN deposited on HfO_2/SiO_2 and on SiO_2 are compared figure 5.3.

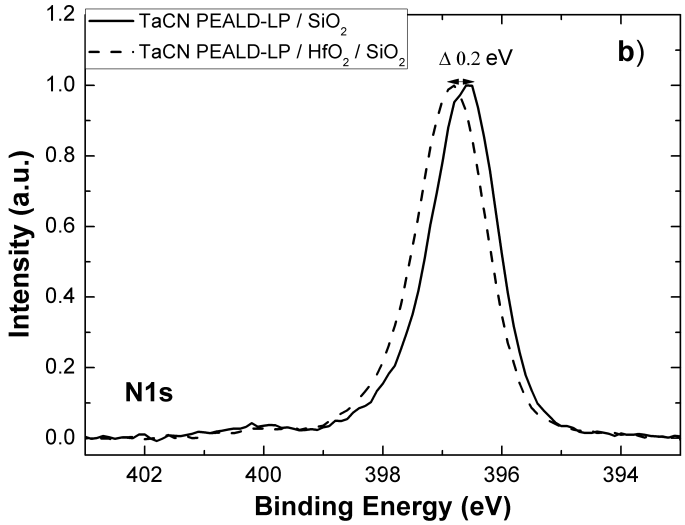

FIGURE 5.3: *Comparison N1s XPS environment from PEALD-LP-TaCN/SiO_2/Si and PEALD-LP-TaCN/HfO_2/SiO_2/Si*

Unfortunately, it is not possible to separate the environments composing the spectra. Meanwhile a shift is observed of the maximum intensity of 0.2 eV towards lower binding energy (from 396.8 eV to 396.6 eV) when deposited on HfO_2/SiO_2/Si. This shift can be related to the formation of Hf-N bonds.

At last, SiO_2 and Si environments were observed on Si*2p* peak (not presented here) and no Si-N bonds appeared after deposition of TaCN either at low or high power on HfO_2/SiO_2 neither on SiO_2. It also appears that the area ratio of SiO_2 and Si features does not evolve, suggesting that SiO_2 interface layer (IL) was not impacted by TaCN deposition and did not regrow.

5.2.3.2 Composition profile

Using AR-XPS it is possible to build a depth composition profile of the sample, based on intensity evolution of the peaks. Results from this analysis are displayed in a graph with the variation of intensity (in arbitrary unit) across the depth of the sample. It is noteworthy that only the variation of composition should be taken into account, the higher intensity of one element cannot be interpreted as a higher concentration of this element in the sample. Figures 5.4a and b bring into comparison the depth profiles from sample TaCN low and high power deposited on HfO_2/SiO_2/Si.

Both figures reveal that the TaCN surface is highly oxidised, due to the vacuum break before XPS analyses; oxidation of TaCN at TaCN/HfO_2 interface is also unveiled. This oxidation, at TaCN/HfO_2 interface, highlights the chemical interactions between the metal and the dielectric. The oxygen profile is similar on both low and high power materials, with a clear increase

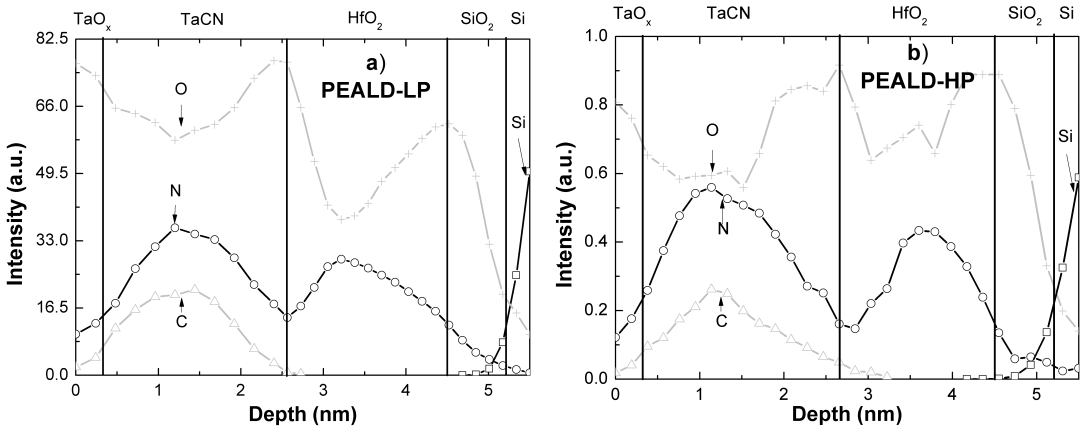

FIGURE 5.4: *Depth profile reconstruction from ARXPS of a: PEALD-LP-TaCN/HfO_2/SiO_2/Si and b: PEALD-HP-TaCN/HfO_2/SiO_2/Si*

of O content at top and bottom interfaces of TaCN layer. Low and high power TaCN samples also exhibit a carbon content confined to the TaCN layer, with a maximum localised at the centre of the layer in concordance with the evolution of Ta-O bonds contribution both at the surface and HfO_2 interface. Nitrogen content follows the same profile within TaCN layer for low and high plasma power samples, but N is not only limited to TaCN layer: as seen on Hf*4f* XPS spectra, N is also located in HfO_2 layer. Nitrogen content in HfO_2 layer presents a Gaussian shape, which can be explained by N migration into HfO_2 activated by H_2 plasma used during TaCN deposition. High plasma power (figure 5.4b) presents a more important gap between extrema compared to low power plasma. This difference implies that plasma power increase promotes N exchange from TaCN to HfO_2. Finally, as mentioned earlier, no SiO_2 thickness change is observed if low and high power plasmas are compared, and the 0.7 nm thickness of SiO_2 IL is confirmed, indicating that H_2 plasma does not impact SiO_2 IL.

5.2.3.3 Electrical results

Φ_m(eff) extracted from MOS capacitors are presented figure 5.5.

Starting from the PVD TiN reference, with a p-type Φ_m(eff) = 4.9 eV and an EOT of 0.92 nm, it appears that IBD TaN as a similar EOT but a lower work function localised at mid-gap as the Si, Φ_m(eff) = 4.6 eV. PEALD-TaCN clearly shows that this reduction of the work function from PVD TiN to IBD TaN is not linked only to the metal but also to the process. Indeed, PEALD-LP-TaCN has a work function of 4.8 eV with an EOT reduced down to 0.89 nm. Increase of plasma power, with PEALD-TaCN leads to a gain in Φ_m(eff) up to 5.1 eV. But higher plasma power, PEALD-HP-TaCN sample, does not increase to the Φ_m(eff) further, a Φ_m(eff) plateau seems to be reached.

In figure 5.6 are presented the variation of log(J_g) with regards to EOT.

PVD TiN has a current leakage gain of 10^4 A.cm^{-2}, while IBD TaN has the same EOT but

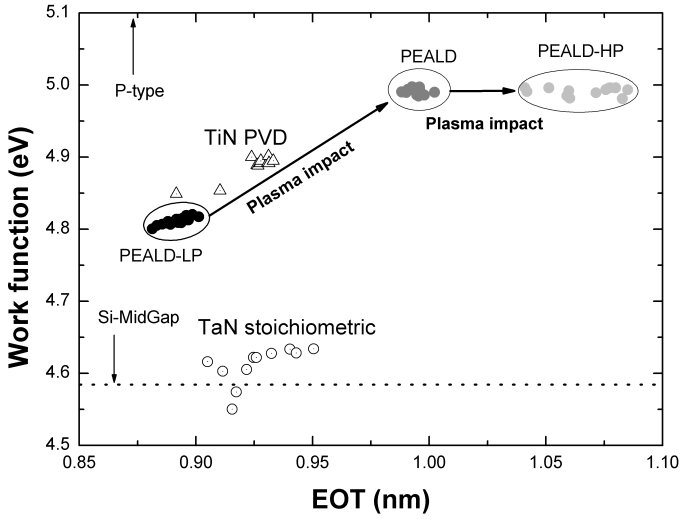

FIGURE 5.5: *Φm(eff) variation with TaCN plasma power increase*

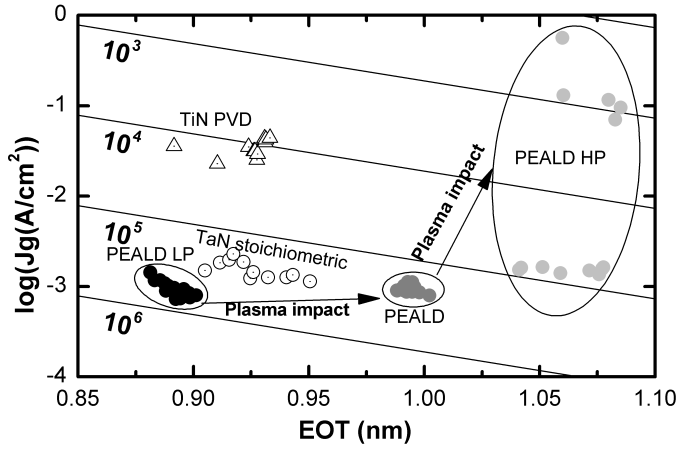

FIGURE 5.6: *Variation of log(J_g) with TaCN plasma power increase*

with an improved current leakage gain up to 2 x 10^5 A.cm^{-2}. Deposition of low power TaCN results in a current leakage gain of 8 x 10^5 A.cm^{-2} combined with a lower EOT. Increasing plasma power during TaCN deposition induces a noticeable dispersion of current leakage (see PEALD-HP case for example), as well as a significant degradation of the EOT, from 0.89 nm to 1.05 nm in the case of PEALD-LP-TaCN and PEALD-HP-TaCN respectively.

5.2.4 Discussion

5.2.4.1 Chemical interactions and formation free enthalpy

Plasma step in PEALD is used to activate the nucleation sites and as reported in Chapter 4, plasma brings enough energy during the densification step to break some Ta-N bonds originally present in the precursor and allow the formation of Ta-C bonds. Although, plasma also promotes the formation of Hf-N and O-Hf-N bonds when TaCN is deposited on HfO_2, as highlighted in figure 5.1. Intensity of these new bonding environments (position shift and intensities changes) are strongly linked to the plasma power used during deposition, as

recorded in figure 5.4a and b. Figure 5.2 reveals that formation of TaO and TaN bonding environments depends on the dielectric used as substrate (HfO_2 or SiO_2). In fact, no exchange between TaCN and SiO_2 was observed, contrary to deposition on HfO_2. Consequently, an exchange of N and O elements between TaCN and HfO_2 layers is implied by this comparison.

In order to explain HfN formation and subsequent extension of nitrogen into HfO_2 with plasma power increase, equation 5.1 gives the simplest possible reaction path which does not include H_2 plasma contribution.

$$TaN + HfO_2 + 1/4O_2 \rightarrow 1/2Ta_2O_5 + HfN \qquad \Delta G(_{formation}) = +1106kJ.mol^{-1} \quad (5.1)$$

Calculation of the Gibbs free energy was done for one mole of Ta and since it is highly positive, the reaction is unlikely to happen. Then, if one considers H_2 plasma interactions, by the mean of H atoms and H excited species (H*), formation of the HfON and/or HfN can be partly explained using the following intermediate reaction mechanisms (equations 5.2, 5.3 and 5.4):

$$HfO_2 + 4H_{plasma} \rightarrow Hf + 2H_2O \qquad \Delta G(_{formation}) = -143kJ.mol^{-1} \quad (5.2)$$

$$TaN + 3/2H_2O + 1/2O_2 \rightarrow 1/2Ta_2O_5 + NH_3 \qquad \Delta G(_{formation}) = -392kJ.mol^{-1} \quad (5.3)$$

$$Hf + NH_3 \rightarrow HfN + 3/2H_2 \qquad \Delta G(_{formation}) = -671kJ.mol^{-1} \quad (5.4)$$

This reaction path is possibly activated by the energy of the plasma used during deposition. H and H* are known to easily diffuse in materials, such as in forming gas, one of the most known example. Thus, if H penetrates in the HfO_2 layer, it can lead to reduction of the dielectric (for instance through O vacancies formation) with the creation of volatile OH^- or H_2O. H_2O is then absorbed by the TaCN deposited on HfO_2 (equation 5.3), resulting in N release which in turn reacts with O vacancies inducing Hf-N and/or O-Hf-N bonds (equation 5.4).

5.2.4.2 EOT variation

Evolution of EOT will now be discussed in correlation with the phenomena introduced earlier. First, EOT is defined by the following equation 5.5:

$$EOT = t_{SiO_2} + \Sigma_i \frac{\varepsilon_{SiO_2}}{\varepsilon_{High-\kappa_i} \times t_{\varepsilon_{High-\kappa}}} \quad (5.5)$$

With t_{SiO_2} and $t_{High-\kappa}$ the physical thicknesses of SiO_2 interfacial layer (IL) and of High-κ, ε_{SiO_2} and $\varepsilon_{High-\kappa}$ the dielectric constant of SiO_2 IL and High-K materials respectively. An increase of $\varepsilon_{High-\kappa}$ reduces $\varepsilon_{SiO_2}/\varepsilon_{High-\kappa}$ ratio, which results in the decrease of the measured EOT. In addition, increase of $\varepsilon_{High-\kappa}$ due to HfON formation has already been reported [172–174].
The high-k dielectric constant increase gives a first insight on the observed reduction of EOT for PEALD-LP compared to TiN or TaN references. Meanwhile, it does not give an explanation to the increasing EOT with plasma power. As already noticed from figure 5.4a and b, TaO_x formation is enhanced at $TaCN/HfO_2$ interface when plasma power is increased. This observation is in good agreement with the proposed reaction mechanisms equations 5.2, 5.3 and 5.4. Furthermore, equation 5.5 also indicates that the addition of a new dielectric in the existing dielectric stack results in the increase of the total EOT.
Hypothesis of TaO_x formation at the interface is also supported by the significant difference in the Gibbs free energy of formation between Ta_2O_5 [$\Delta G_{formation}(Ta_2O_5)$ = -1079 kJ/mol (at 325°C)] and TaN [$\Delta G_{formation}(TaN)$ = -222 kJ/mol (at 325°C)]. Furthermore, tantalum oxide formation in the first cycles of ALD TaCN deposition on oxides was already reported elsewhere [168].
Amorphous Ta_2O_5 has a dielectric constant which is in the 22-25 range, thus taking for hypothesis that a 1 nm Ta_2O_5 oxide is formed on top of HfO_2 with an $\varepsilon_{High-\kappa}$ of 22, it represents an EOT increase of 0.15 Å. This estimation is in line with the measured EOT regrowth from 0.89, sample PEALD-LP-TaCN, to 1.04 nm, in the case PEALD-HP-TaCN. Nevertheless, the dielectric constants of TaO_x oxides are lower than the one of amorphous Ta_2O_5, the difference is counterbalanced by further N migrating to HfO_2 resulting in $\varepsilon_{High-\kappa}$ rise when plasma power is increased.

5.2.4.3 Leakage current evolution

Formation of HfON was already linked with the reduction of current leakage [188], and consequently can account for the improvement, by a factor 3, of the current leakage observed between IBD-TaN and PEALD-LP-TaCN in figure 5.5. Thanks to AR-XPS depth profile reconstruction (figure 5.4), it comes into view that N is present in HfO_2 layer with a gradient which can be assimilated to a diffusion phenomenon. N migration into HfO_2 is expected to be initiated by reactive H or H* species during plasma steps (see equations 5.2, 5.3 and 5.4), with the migration depth of nitrogen limited by the energy level supplied from plasma. And since the energy distribution of reactive species in plasma corresponds to a Gaussian law [189], the N concentration also presents a Gaussian profile (figure 5.4a and b). Increasing plasma power affects the N gradient found in HfO_2 layer, as seen on depth profile of PEALD-HP-TaCN figure 5.4b, nitrogen is going deeper in the layer and the maximum concentration is pushed further. Nitrogen presence at the HfO_2/SiO_2 interface is creating defects which can explain part of the current leakage scattering measured (figure 5.6). Leakage current and dispersion increase, observed for PEALD-HP-TaCN, also indicates that plasma affects

the dielectric and/or the interlayer. These plasma damages include the effect of electrons, ions, neutral species and UV radiation; yet separate impact of each component of the plasma would require further investigation and thus will not be discussed here.
Another phenomenon enhancing the degradation of current leakage is the important O removal from the HfO_2 dielectric and the creation of vacancies [190]. Consequently, TaO_x, HfON and HfN creation are in accordance with both leakage current degradation and EOT regrowth.

5.2.4.4 Φm(eff) modification

PVD TiN is currently a standard in advanced microelectronic recommendations by ITRS [30], and as such it is a reference for electrical specifications of metal layer. IBD TaN is used to give some information on TaN material and influence of deposition technique on electrical characteristics of the device.
In Chapter 4, it was reported that plasma power has a direct influence on the composition of the deposited TaCN, a higher plasma power leading to a clear increase of Ta-C bonds; i.e. high plasma power induces non-spontaneous Ta-N to Ta-C transposition, thanks to local increase of the temperature. Elsewhere, it was reported [92] that TaC is a p-type material, with Φm(eff) at 4.9-5.0 eV on HfO_2. In this experiment, the PEALD-LP-TaCN has a Φm(eff) = 4.8 eV, close to TiN-PVD. With higher plasma power, PEALD-TaCN sample, the Φm(eff) gains 0.2 eV to Φm(eff) = 5 eV, thus getting at the same values of TaC metal. Hence, TaC formation can be correlated to Φm(eff) increase.
Further increase of the plasma power, for PEALD-HP-TaCN sample, does not influence the Φm(eff), a plateau is reached with PEALD-TaCN, even that the composition changes toward a more TaC-like material, c.f. Chapter 3.
Incorporation of N in HfO_2 film was proven to be responsible for a shift of the Φm(eff) to lower values [184], indicating that N may introduce positive fixed charges. In this study such a phenomenon has not been encountered, possibly due to the chemical bonding of N in HfO_2 which is not seen with nitridation, indeed N is only in interstitial sites.

In summary, the plasma used for densification of the TaCN layer was found to enhance the interactions taking place at the TaCN/HfO_2 interface. A possible mechanism is first, due to the ease of penetration of H_2 species in material inducing some oxide removal from the HfO_2 layer, then H_2 species also interact with TaCN layer by N removal. Oxygen is brought to the surface where it reacts with the TaCN deposited, oxidising the tantalum layer, while N is migrating in HfO_2 layer and form Hf-N bonds. This mechanism is represented in figure 5.7, HfO_2 layer is amorphous but for clarity a crystalline structure was used.

5.2.5 Conclusion

In this study, XPS analysis was used to highlight interactions between PEALD TaCN and HfO_2, formation of TaO_x, HfN and HfON was demonstrated. Possible reaction mechanism,

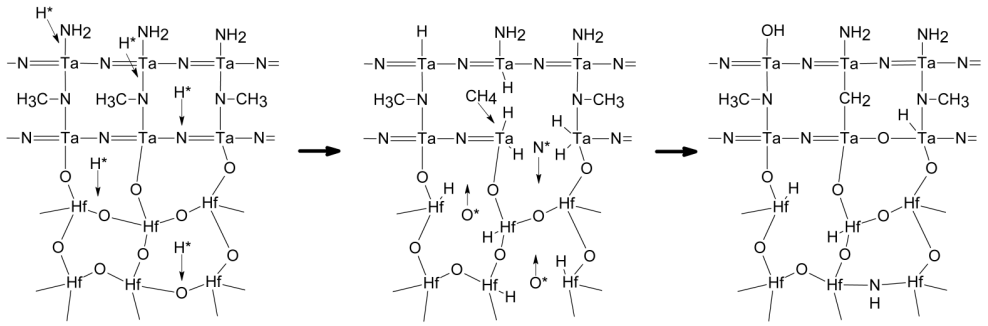

FIGURE 5.7: *Possible reaction mechanism of Hf-N and Ta-O creation*

with their Gibbs free energy, are proposed and linked to the dielectric constant increase, which results in the reduction of the measured EOT, down to 0.89 nm. Current leakage improvement, up to 8 x 10^5 times better than SiO_2, was also attributed to HfN creation. Furthermore, an increase of plasma power, used for TaCN densification and TaC formation in PEALD process, leads to degradation of the stack by an increase of the EOT due to TaO_x formation at TaCN/HfO_2 interface, degradation of the gain in leakage current because of HfO_2 oxygen removal and finally a scattering of the electrical values assimilated to the creation of defects at HfO_2/SiO_2 interface. Overall, TaCN was successfully used for high-κ/metal gate application with low EOT and low leakage current and importance of plasma tuning to limit its impact on electrical characteristics was demonstrated. Thus, in the current deposition conditions and in the used deposition chamber, it appears that low plasma power has to be preferred to limit the damages brought to the dielectric.

5.3 Using TaCN reactivity for PVD-TiN electrical properties improvement

5.3.1 Context

New technology nodes in CMOS industry require improvement of the materials used to obtain the similar or better properties with thinner layers, compared to the previous generation. However, reduction of the dimensions has significant drawbacks connected to the rising surface/volume ratio, e.g. in a 2 nm layer about 30% of the atoms are at the surface/interface. With such ratios, interfacial reactions have a higher impact on the overall behaviour of the layer and the metals are relatively highly oxidised. Titanium nitride deposited by Physical Vapour Deposition (PVD-TiN) is now widely employed as a metal-gate material on the HfO_2 high-κ dielectrics for CMOS transistors. Extended investigation was carried on the influence of the deposition process on the properties of the metal, in order to reduce the resistivity to the 50-200 $\mu\Omega$.cm range [11, 17], increase the work function up to 4.9 eV [20, 191] and limit the oxidation of the metal [192]. PVD-TiN is also proposed as a sacrificial scavenging material, for oxide reduction of the Interfacial Layer (IL), thanks to its high affinity for oxygen [169, 170]. But until now no solution with a low thermal budget has been found to avoid or remove oxidation of TiN after vacuum break.

Besides, new metals are investigated for replacement of TiN metal gate. Tantalum alloys are some of the most researched in current literature, thanks to their barrier properties and p-type work function [14, 50, 89]. However, when plasma is used for densification of tantalum nitride during plasma enhanced atomic layer deposition (PEALD) interactions with the dielectric are activated leading to deterioration of the film's electrical characteristics if plasma is not well tuned, as presented previously.
Hence, in this work an alternative solution is presented for the improvement of PVD-TiN electrical characteristics, with the aim to increase scavenging of oxygen from the SiO_2 Interface Layer (IL), together with a reduction of the plasma damages linked to plasma densification. ALD tantalum carbo-nitride (TaCN) was deposited on top of PVD-TiN/HfO_2 stack, with or without plasma densification ((PE)ALD). Interactions at the metal-metal and metal-dielectric interfaces were surveyed by X-Ray Reflectivity (XRR) and X-ray Photoelectron Spectroscopy (XPS).
Using quasi in-situ XPS to avoid vacuum break between tantalum deposition and analysis, it appeared that tantalum draws out oxygen from PVD-TiN. Separation of (PE)ALD steps allowed to assess the reaction mechanisms taking place at the metal/metal interface.
Finally, equivalent oxide thickness and leakage current of TaCN/TiN/HfO_2/SiO_2/Si stacks are introduced, discussed and correlated with the corresponding physical and chemical properties observed by XRR and XPS.

5.3.2 Experimental methods

All material characterisations were carried on prime Si (1 0 0) 300 mm wafers. Simple MOS, as presented in section 5.2.2, are used with the same fabrication process as previously. Also, a CVD-TiN / CVD-W plug was deposited on top of the stack for electrical characterisation, process conditions were introduced section 5.2.2.
TiN metal was deposited by Physical Vapour Deposition (PVD) by sputtering of a pure Ti target with N_2 flow, N_2 flow was tuned to obtain a stoichiometric TiN. TaCN metal was deposited by (PE)ALD with TBTDET precursor and NH_3 flow (ALD) or H_2 plasma (PEALD), for activation steps. Two PEALD-TaCN samples were made, one with low plasma power, the other with high plasma power and are referred to as PEALD-TaCN and PEALD-HP-TaCN (High-Power) respectively, in the rest of the section. (PE)ALD-TaCN deposition technique, plasma power modifications consequences and electrical results were already presented in Chapter 2, Chapter 3 and in the previous section.
XRR and XPS are used for full-sheet characterisation, parameters are not changed compared to what was used in the section 5.2.2. In addition, electronic density of the samples was calculated from the XRR spectra.

Considering XPS analysis, no carbon or oxide removal was performed before characterization, hence due to oxidation and atmospheric contamination high levels of C and O were observed at the extreme surface of the samples. Carbon C*1s*, situated at 285 eV [81] was used to remove any possible shift in the binding energy due to sample charging.

XPS deconvolution was done using the following constraints: Hf$4f_{5/2}$ was defined with a shift in energy of ΔE=1.71 eV and an area ratio of 0.75 compared to Hf$4f_{7/2}$ [81]. Parameters for Ta$4f$ peaks are: Ta$4f_{7/2}$ and Ta$4f_{5/2}$ are separated by ΔE=1.91 eV [81], also with an area ratio of 0.75. Finally, Ti$2p_{5/2}$ and Ti$2p_{3/2}$ are constraint by a shift in binding energy of ΔE=5.54eV [81] and an area ratio of 0.5. However, as reported by Strydom [193] and Jeager [85] Ti$2p$ core-level photoelectrons can undergo shake-up events which creates discrete energy loss resulting in a difficult interpretation of the spectra and the impossibility to constraint the Ti$2p$ 3/2 and 1/2 binding environments components. Thus, these environments are integrated in the TiON environment and evolution/modifications of this environment will not be discussed later on.

5.3.3 TiN and TaCN interactions analysis

XRR spectra of ALD-TaCN/TiN/HfO_2/SiO_2/Si, PEALD-TaCN/TiN/HfO_2/SiO_2/Si and PEALD-HP-TaCN/TiN/HfO_2/SiO_2/Si are presented figure 5.8a. The corresponding electronic density extraction is also given figure 5.8b, together with the electronic density extraction of TiN/HfO_2/SiO_2/Si.

All three TaCN processes were tuned on SiO_2 to obtain 2 nm thick layers.

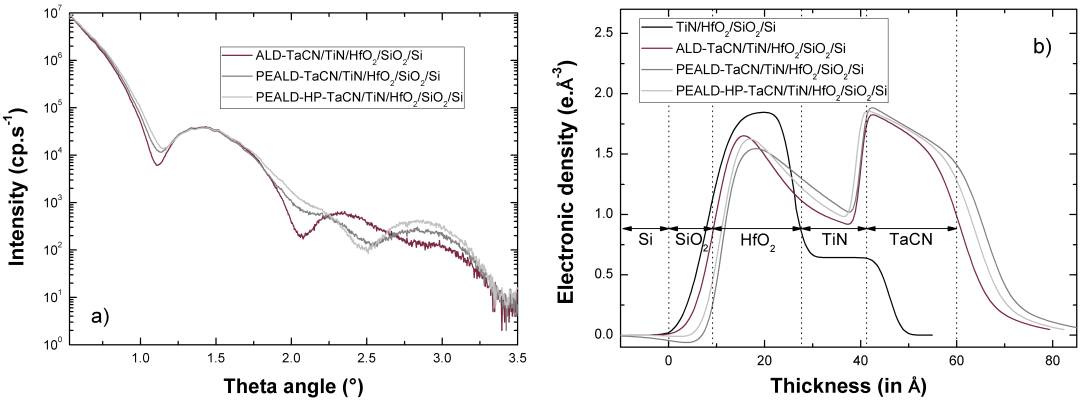

FIGURE 5.8: *a: XRR spectra and b: electronic density extraction of ALD-TaCN/TiN/HfO_2/SiO_2/Si, PEALD TaCN/TiN/HfO_2/SiO_2/Si and PEALD HP TaCN/TiN/HfO_2/SiO_2/Si*

On figure 5.8a, a clear distinction can be made between ALD and PEALD processes. Sample with ALD-TaCN presents a different length of the arches, meaning that the deposited layer is thinner than for PEALD-TaCN and PEALD-HP-TaCN samples. It also appears that interfaces are impacted by the plasma step with a reduction of minimum intensity reached at the angle of 1°. Electronic density extraction, figure 5.8b, amplifies the differences between the samples and eases the interpretation of the XRR spectra. From left to right it comes into view that HfO_2/SiO_2 interface is sharper for ALD process, together with a decrease of HfO_2 electronic density while the plasma power increases. Then, one can observe that in the metal films/layers, TiN electronic density increases with the plasma power increase, and that TaN has a higher density when plasma densification is used. Finally, the thickness of

TaCN increases from ALD to PEALD-HP-TaCN.

If TaCN deposition modifies the TiN properties the opposite is also true: TaCN is influenced by the TiN. Whereas the three processes, ALD, PEALD and PEALD-HP, were finely tuned on SiO_2 substrate to obtain the 2 nm thickness layers, it appears in figure 5.8b, that the thickness of TaCN layers varies when deposited on TiN. Measured thickness of ALD-TaCN is 1.8 nm, PEALD-TaCN is 2.1 nm and it goes up to 2.2 nm PEALD-HP-TaCN. Therefore, plasma step in PEALD eases the nucleation of TaCN on TiN substrate compared to SiO_2 substrate, contrary to ALD which has lower growth rate on TiN substrate compared to SiO_2 substrate.

Thickness of the layers was confirmed by TEM observations. A picture of the PEALD-TaCN/HfO_2/SiO_2/Si stack is presented figure 5.9.

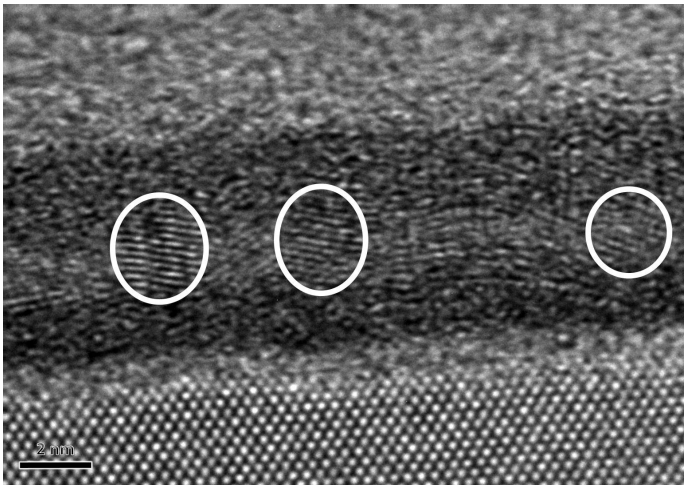

FIGURE 5.9: *TEM observation of PEALD-TaCN/TiN/HfO_2/SiO_2/Si stack*

Software measurement of the thicknesses was performed on twelve locations and average values were extracted. The PEALD-TaCN layer thickness is 2.15 nm ($\pm$ 0.12 nm), PVD-TiN 1.85 nm ($\pm$ 0.14 nm) and HfO_2 1.9 nm ($\pm$ 0.08 nm). These values are in good agreement with the XRR measurement, they confirm both the higher thickness of TaCN than the one measured on SiO_2 (2 nm) and the TiN and HfO_2 thickness reduction after PEALD-TaCN deposition.
This TEM observation also reveals an important information about the crystallography of the layers. Whereas PVD-TiN layers of less than 10 nm are amorphous as deposited, crystals are seen here and circled figure 5.9. It seems that the crystals start in the TaCN layer, which is highly crystalline c.f. Chapter 4, and propagate through TiN. These crystals are not visible at the TaCN surface, where the most tantalum oxide is supposed to be present, and they do not show a preferential direction.
In conclusion, TaCN deposition leads to the formation of crystals in the PVD-TiN layer, which is initially amorphous. To explain the presence of these grains, it is also possible to suppose that the oxygen removed by TaCN deposition reduces the necessary energy for the

crystallisation of PVD-TiN to occur.

The thickness and density variations, observed by XRR, will be discussed later, in section 5.3.5, in regard to the chemical interactions that will be presented in the next section.

In the figure 5.10 are presented the Ta*4f* XPS spectra of TaCN ALD, PEALD and PEALD-HP deposited on SiO_2/Si (left) and TiN/HfO_2/SiO_2/Si (right).

Peak fitting of the Ta*4f* spectra was achieved using three environments: Ta_2O_5, TaN and

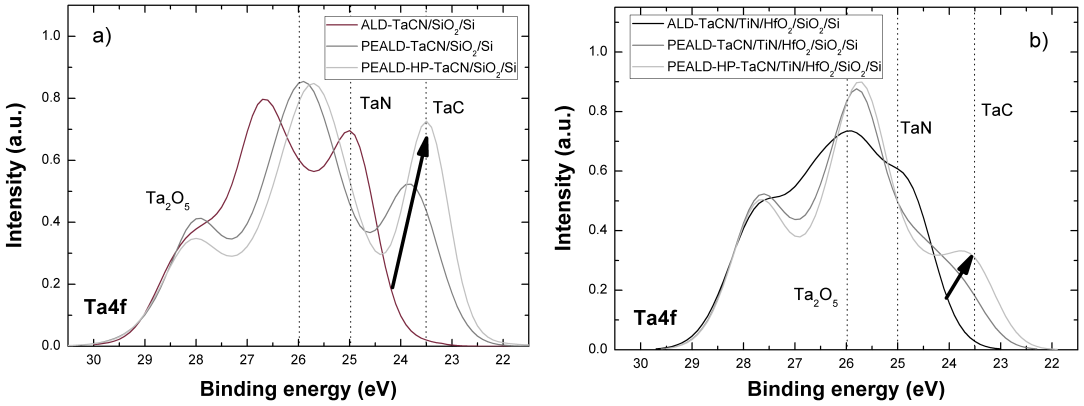

FIGURE 5.10: *Ta4f XPS spectra of ALD-TaCN, PEALD-TaCN and PEALD-HP-TaCN deposited on a: SiO_2/Si and on b: TiN/HfO_2/SiO_2/Si*

TaC, located at 26 eV, 25 eV and 23.5 eV, respectively (but not included in the figure to ease its readability) [81]. Strong evolution of the TaN and TaC peaks is observed in figure 5.10a, as the process changes from ALD to PEALD and PEALD-HP.

By comparison of the bonding peaks between TaCN deposited on SiO_2/Si (figure 5.10a) and on TiN/HfO_2/SiO_2/Si (figure 5.10b) three changes come into view. First, Ta_2O_5/TaN ratio is inverted when TaCN is deposited on TiN/HfO_2/SiO_2/Si. In particular, the separation of Ta_2O_5 and TaN environments with ALD-TaCN is more difficult due to the presence of TaON environment, situated in between. Secondly, it appears that the Ta_2O_5 intensity variation between PEALD and PEALD-HP on SiO_2 substrate is reduced when TaCN is deposited on TiN/HfO_2/SiO_2/Si. Finally, TaN and TaC bonding environments located at 25 eV and 23.5 eV, are strongly reduced on TiN/HfO_2/SiO_2/Si from high plasma case in PEALD-HP to no plasma in ALD.

Comparison of Ti*2p* XPS spectra from TiN as-deposited, with ALD-TaCN, PEALD-TaCN and PEALD-HP-TaCN is given figure 5.11 (left). Doublets from TiO_2 (459.5 eV), TiON (457.2 eV) and TiN (455.5 eV) chemical environments are inserted to ease the graphic interpretation in the two extremes conditions, i.e. TiN as deposited and under 2 nm PEALD-HP-TaCN, in figure 5.11 (right).

It appears, in figure 5.11 (left), that whatever the TaCN deposition conditions used a clear decrease of TiO_2 environment is observed. Oxygen removal from TiN is more efficient when a H_2 plasma activation step is used during PEALD-TaCN deposition instead of the NH_3 only in ALD case. Meanwhile, NH_3 appears to be enough reactive with oxygen to remove some of

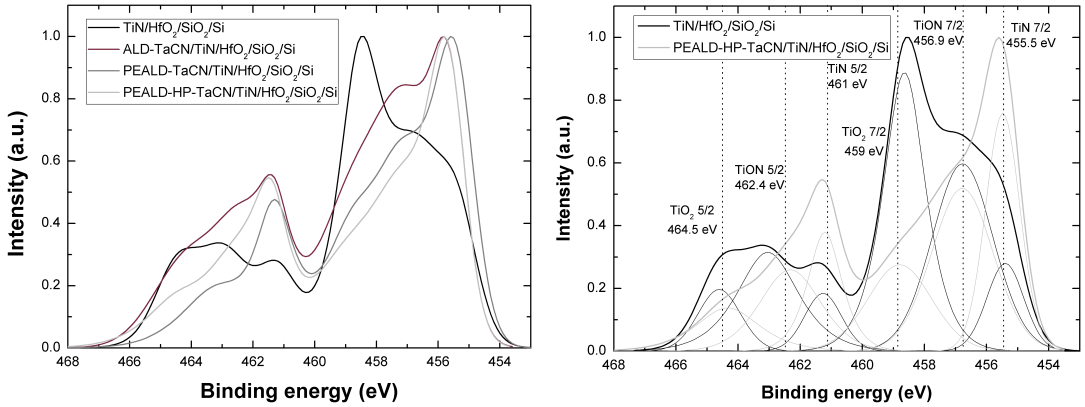

FIGURE 5.11: *XPS Ti2p spectra of TiN/HfO_2/SiO_2/Si (black), ALD-TaCN/TiN/HfO_2/SiO_2/Si (dark grey), PEALD-TaCN/TiN/HfO_2/SiO_2/Si (grey) and PEALD-HP-TaCN/TiN/HfO_2/SiO_2/Si (light grey)*

the oxygen [194]. In the case of H_2 plasma, it is well known that such reducing ambiance is efficient for surface oxidation removal [195, 196], thanks to the creation of volatile OH^- and H_2O molecules. This is even more pronounced when plasma power increases with noticeable decrease of TiO contribution between PEALD and PEALD-HP TaCN.

Increase of TiN environment after TaCN deposition is also observed, through the slight shift towards lower energies of TiN bonding environment which is associated to the higher N/Ti ratio, as reported elsewhere [15, 81].

Also, an indirect result concerning Ta alloys oxygen barrier property is confirmed in this experiment. Indeed, after TaCN deposition and before XPS analysis there was a vacuum break and the observed oxygen removal from TiN layer is conserved. If TaCN would not be a barrier to oxygen diffusion there would be an oxygen uptake of the TiN layer, back to the oxidation levels seen before TaCN deposition. Therefore, a 2 nm layer of (PE)ALD-TaCN appears to be sufficient to protect TiN from re-oxidation; i.e. TaCN acts as a barrier to diffusion of oxygen.

Hf*4f* core level energies are shown in figure 5.12, for PVD-TiN, and after (PE)ALD-TaCN deposition on TiN. HfO_2 control sample, without a metal layer on top of it, is also added for comparison.

HfO_2 spectrum of the control sample was fitted with one doublet. After TiN deposition a new environment on the Hf*4f* peak appears at low energy. This new bonding environment can be associated to the formation of Hf-N [81, 86]. The reaction path leading to the formation of HfN bonds was first introduced in section 5.2.3.1. After ALD-TaCN deposition an increase of HfN feature is observed. When plasma is used for PEALD-TaCN and PEALD-HP-TaCN deposition a further increase of Hf-N bonds is observed, influence of plasma on TaCN/HfO_2 interactions was also introduced in the section 5.2.3.1.

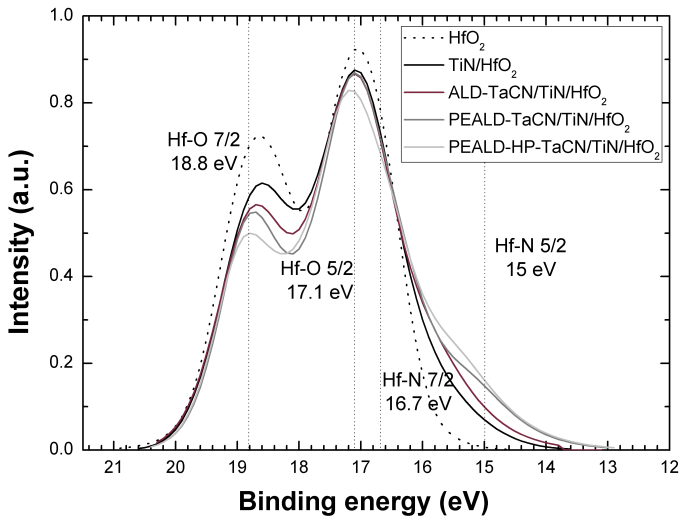

FIGURE 5.12: *Hf4f spectra evolution with PVD-TiN, ALD-TaCN, PEALD-TaCN and PEALD-HP-TaCN deposition*

5.3.4 (PE)ALD-TaCN steps influence on PVD-TiN oxidation

To simulate (PE)ALD-TaCN deposition, activation steps were performed on PVD-TiN-/HfO_2/SiO_2/Si samples in the deposition reactor and transferred to the XPS module without vacuum break, this methodology is also called quasi-*in situ* XPS. Transfer from reaction chamber to analysis chamber was done under a 10^2 mTorr vacuum and it was already proven that such a transfer avoids carbon contamination and limits the oxidation of the layers [93].

ALD deposition comprises three steps, they are: 325°C substrate heating, NH_3 flow and TBTDET precursor introduction. In the PEALD process the NH_3 flow is replaced by a H_2 plasma after TBTDET precursor introduction.
A comparison of Ti*2p* core levels of as-deposited TiN and 325°C annealed case, together with the impact of reactive steps with NH_3 flow at 325°C and H_2 plasma at 325°C is given figure 5.13. The reactants gas flows, chamber pressure, plasma power and process time copied from the (PE)ALD-TaCN deposition recipes.

Figure 5.13 shows that annealing under vacuum of TiN has little impact on Ti*2p* environments, only a slight increase of TiO_2 and TiN contributions together with TiON feature decrease is observed. The absence of oxygen release or up-take is also confirmed in O*1s* peak intensity (not presented here), were no evolution was recorded. Addition of NH_3 flow during annealing leads to a limited increase of the TiN peak. However, H_2 plasma clearly shows a decrease of TiO_2 and TiON environments in Ti*2p* spectrum, with no change observed on Ti-N feature.

Evolution of equivalent oxide thickness (EOT) with leakage current gain for the three TaCN processes is presented figure 5.14, together with the previous results obtained with (PE)ALD-TaCN/HfO_2 and PVD-TiN/HfO_2 as control stacks.

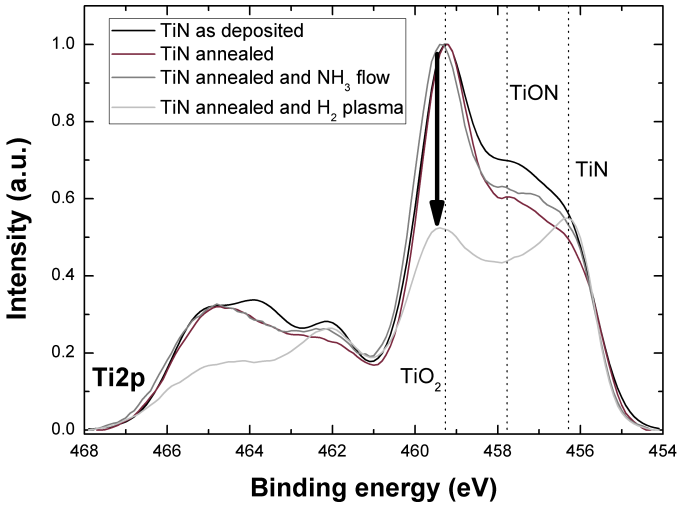

FIGURE 5.13: *Ti2p XPS spectra of TiN as-deposited, after 325°C anneal, 325°C anneal with NH_3 flow, 325°C anneal with H_2 plasma*

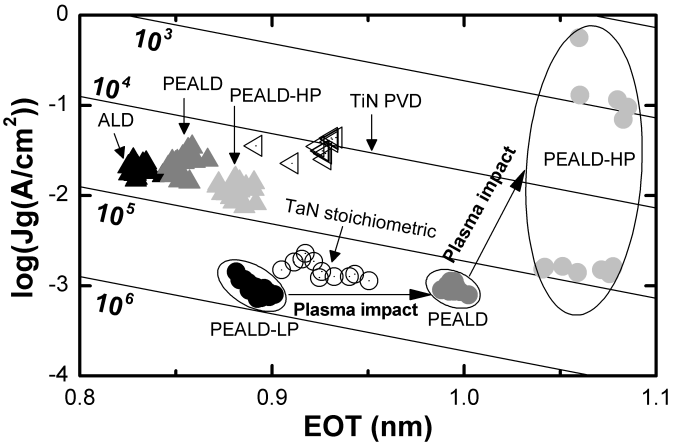

FIGURE 5.14: *Evolution of Jg versus EOT of (PE)ALD-TaCN/TiN/HfO_2/SiO_2/Si, (PE)ALD-TaCN/HfO_2/SiO_2/Si and PVD-TiN/HfO_2/SiO_2/Si stacks*

Compared to PVD-TiN control sample, a reduction of the EOT is observed with the addition of (PE)ALD-TaCN on top of PVD-TiN with a factor 5 gain in the current leak. The power increase, used for the creation of TaC bonds in PEALD-TaCN, results in the increase of the measured EOT, with no change on the current leak. Similar behaviour is observed for (PE)ALD-TaCN/HfO_2/SiO_2/Si.

Φ_m of PVD-TiN, (PE)ALD-TaCN, PVD-TaN and (PE)ALD-TaCN/PVD-TiN metals on HfO_2 are presented figure 5.15.

PVD-TiN is adapted to p-MOS specifications with a p-type Φ_m of 4.9 eV. Located at the bottom of the figure, with a Φ_m of 4.6 eV, there is the PVD-TaN which is mid-gap. Evolution of the Φ_m of PEALD-LP-TaCN, PEALD-TaCN and PEALD-HP-TaCN was presented in the first part of this chapter. If PVD-TiN is inserted between (PE)ALD-TaCN and HfO_2 the devices keep the Φ_m of the TiN at 4.85 eV. TiN prevents the Φ_m increase measured when

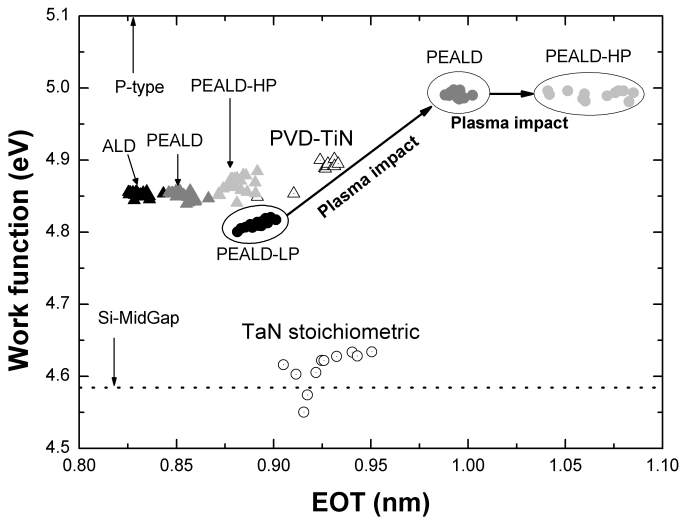

FIGURE 5.15: *Evolution of work function versus EOT of (PE)ALD-TaCN/TiN/HfO_2/SiO_2/Si, (PE)ALD-TaCN/HfO_2/SiO_2/Si and PVD-TiN/HfO_2/SiO_2/Si stacks*

plasma power is increased, in PEALD-TaCN/HfO_2/SiO_2/Si stack.

5.3.5 TiN layer modifications and oxide removal reaction mechanism

XRR measurement of ALD-TaCN/TiN/HfO_2/SiO_2/Si, figure 5.8, suggest a strong interaction between the TaCN and TiN metals. It is visible on the increase of TiN density and on the reduction of TiN thickness. These interactions are enhanced when using H_2 plasma step in PEALD mode, further supported by the plasma power increase. Data presented in figure 5.11 demonstrate that the density increase of PVD-TiN corresponds to the replacement of some of the oxygen trapped/located in the TiN film by nitrogen. The oxide removal is improved when H_2 plasma is used during PEALD-TaCN deposition compared to ALD-TaCN deposition, but nitrogen content in Ti*2p* reaches the same level.

Based on these results reaction mechanism path with the corresponding Gibbs energies calculated at 325°C and 2 Torr pressure is now discussed.
First, one has to take into consideration that affinity of TBTDET molecule with oxygen is used for the deposition of ALD Ta_2O_5 [197], indeed Ta_2O_5 formation has a low Gibbs free energy of formation ($\Delta G_{formation}(Ta_2O_5)$ = -1079 kJ/mol at 325°C).
Three reactions leading to the oxide removal from TiN layer have to be considered, one has for reactant TaN (equation 5.6), second NH_3 gas (equation 5.7) and third the H_2 radicals from the plasma (equation 5.8). All three reactions result in the formation of H_2O by-product then interacting with TaN to form Ta_2O_5 (equation 5.9). Once nitrogen is released by TaCN it can form new TiN bonds (equation 5.10).

$$TiO_2 + TaN + 1/4O_2 \rightarrow TiN + 1/2Ta_2O_5 \qquad \Delta G = -137kJ \tag{5.6}$$

$$TiO_2 + NH_3 \rightarrow TiN + H_2O + OH^- \qquad \Delta G = +325kJ \tag{5.7}$$

$$TiO_2 + 4H_{plasma} \rightarrow Ti + 2H_2O \qquad \Delta G = -286kJ \tag{5.8}$$

$$TaN + 5/2H_2O \rightarrow 1/2Ta_2O_5 + NH_3 + H_2 \qquad \Delta G = -126kJ \tag{5.9}$$

$$Ti + NH_3 \rightarrow TiN + 3/2H_2 \qquad \Delta G = -311kJ \tag{5.10}$$

The oxygen brought as reactant in the equation 5.6 is coming from interstitial sites in the TiN layer [198, 199]. The negative Gibbs free energy indicates that this reaction is possible. Yet, other sub-mechanisms of reaction are possible. For example as supposed from ALD steps separation, figure 5.11, NH_3 gas does not influence TiO_2 layer, supported by the positive Gibbs energy of the reaction 5.7. On the other hand, as it was shown figure 5.11 the H_2 plasma is reducing the oxygen content of TiN layer, confirmed by the negative Gibbs energy of the reaction equation 5.8. Once H_2O by-product is created it can react with the TaN deposited on top, forming Ta_2O_5 and nitride by-products. Finally, the nitrides are going in the titanium layer now un-oxidised and form TiN. When plasma power is increased the reaction equation 5.8 is favoured, thus more oxygen is taken from TiN layer and more nitrogen is released from TaCN layer. This effect can be correlated to the nitrogen increase in HfO_2 observed figure 5.12.

Furthermore, the oxygen removed from PVD-TiN appears to be present in the TaCN layer, as suggested in figure 5.10. The change of substrate, from SiO_2 in figure 5.10a, to TiN in figure 5.10b, implies that the deposition reaction mechanism is greatly impacted by the substrate. Less TaC bonds, located at 23.5 eV, are formed when TaCN is deposited on PVD-TiN. Creation of TaC bonds by transamination reaction thanks to plasma activation was introduced in Chapter 4 and was linked to the energy brought by the plasma, higher energy leading to higher TaC content in TaCN. However, when deposited on TiN, plasma power increase does not enhance the transamination reaction but appears to favour the oxide removal from TiN. Thus resulting in a reduction of TaC peak intensity, figure 5.10b, and increase of Ta_2O_5 peak intensity.

5.3.6 Particular impact of ALD and PEALD activation steps

TiON mixture evolution and possible separation of TiN and TiO_2 under annealing was already described elsewhere [200]. Decrease of TiON Ti*2p* XPS peak was highlighted and regrowth of TiO_2 surface layer was supported by the increase of TiO_2 Ti*2p* XPS peak. Similar behaviour is observed in figure 5.13 after annealing at 325°C under vacuum: TiN and TiON peaks intensity decrease. When NH_3 gas flow is added a small but significant increase of TiN peak is observed, however this increase is far smaller than what is observed after TaCN deposition. As introduced earlier, the reactivity of NH_3 with TiO_2 is not sufficient

to allow the oxygen removal. Finally, the plasma H_2 results in the important decrease of TiO_2 and TiON and increase of TiN peaks. Oxygen removal by H_2 plasma is confirmed here again, also plasma power increase (not shown here) leads to further reduction of TiO_2 peak as seen figure 5.11. However, the TiN peak intensity does not reach the levels obtained with TaCN ALD or PEALD deposition. Therefore, the last step of TaCN deposition, which was not reproduced due to a hardware limitation, is responsible for both some removal of oxygen from TiN and addition of nitrogen to TiN.
To conclude, improvement of TiN after ALD-TaCN results from the chemical affinity of TaCN with oxygen, whereas improvement of TiN after PEALD-TaCN results from both the chemical affinity of TaCN with oxygen and from the action of H_2 plasma.

5.3.7 Correlation with electrical results

TiN oxygen scavenging properties were already reported [170] and are used for SiO_2 IL reduction [169]. Similar phenomenon can be observed here, with the increase of the scavenging effect by TaCN capping of TiN. By comparison of TiN/HfO_2/SiO_2/Si and ALD-TaCN/TiN/HfO_2/SiO_2/Si electrical results, figure 5.14, a decrease of the EOT is revealed when ALD-TaCN capping is added. This EOT reduction is going along an improvement of the leakage current gain. These two modifications, as reported elsewhere [171, 173, 188], are to be linked with the creation of hafnium-nitrogen bonds and $\varepsilon_{High-\kappa}$ increase, confirmed figure 5.12.
By addition of plasma densification step to TaCN deposition an increase of the EOT is seen. It was demonstrated, with AR-XPS analysis, that this increase corresponds to the creation of Ta_2O_5 dielectric after oxygen release. In this case the increase is lower than what is observed if no TiN layer is placed between TaCN and HfO_2, plasma impact figure 5.14. Even if the EOT increases the leakage current gain is stable, H_2 plasma does not degrade the HfO_2 as observed without TiN and presented earlier in this chapter. Plasma power rise confirms the supposition by an enhancement of the EOT growth previously introduced.

5.3.7.1 Role of TiN layer in the stack

When TaCN is deposited directly on HfO_2, plasma impact leads to a degradation of the measured EOT and a scattering of the leakage current values due to oxide removal from the HfO_2 dielectric. Mechanism of oxide removal was proposed and linked to the energy brought by H radicals from plasma. Including a 2 nm PVD-TiN layer between PEALD-TaCN and HfO_2 permits to avoid most of the degradation previously linked to the plasma step. Yet, the EOT increase observed figure 5.14 suggests that the TiN layer reduces the amount of radicals reaching the dielectric but does not block all the radicals.
The protection brought by TiN also has some drawbacks, indeed the gain in V_{FB} observed when plasma power is increased for TaCN deposition, and associated to TaC creation, is not perceived. Hence it is possible to suppose that only the first two nanometres of metal, or

less, dictate the work function of the stack.

5.3.8 Conclusion

Using XPS analysis it was possible to demonstrate the metal-metal interactions first seen using XRR, when (PE)ALD-TaCN is deposited on PVD-TiN. Different composition of TaCN layer is observed when deposited on TiN, compared to deposited on SiO_2, with lower carbon content and higher oxidation. At the same time, oxygen removal from TiN layer and nitrogen addition is revealed. Penetration of nitrogen is observed down to HfO_2 layer, with the creation of HfN bonds. These chemical modifications of the layers induce changes on the electrical characteristics of the metal/metal/dielectric stack. Reduction of the EOT is correlated to the $\varepsilon_{High-\kappa}$ increase, while the addition of plasma for TaCN deposition results in the increase of the EOT which may be due to Ta_2O_5, formation. Finally, by comparison of PEALD-TaCN/TiN/HfO_2 and PEALD-TaCN/HfO_2 the importance of TiN as protection layer against plasma damages is proven.

5.4 Conclusion to the Chapter 5

In this chapter the advantages and difficulties connected with the integration of the processes studied in Chapter 4 were developped.
At first a metal-dielectric interaction between TaCN and HfO_2 was revealed. TaCN is scavenging some of the oxygen present in HfO_2 layer, creating a new dielectric, Ta_2O_5, at the TaCN/HfO_2 interface. In the meanwhile nitrogen from TaCN is migrating in HfO_2 layer and creates HfN bonds, which result in an increase of the $\varepsilon_{High-\kappa}$, as confirmed by electrical measurements. Using ALD deposition the leakage current gain is even improved, highlighting the fact that the amount of oxygen removed from HfO_2 does not significantly degrade the properties of the dielectric. However, for densification of TaCN layer during PEALD deposition is activated by a plasma and opposite phenomena are observed, both EOT and leakage current are degraded possibly due to penetration of H radical in the HfO_2. By increasing the plasma power, thus increasing the radicals and hot species density, a scattering of the electrical properties appears which confirms that electrical degradations are linked with the plasma activity.
Next several effects induced by TaCN deposition were investigated when deposited on TiN; oxygen removal by TaCN scavenging, TaCN barrier property to oxygen and nitrogen migration to TaCN underlayer. It appears that all the phenomenons of oxygen scavenging and nitrogen migration observed after TaCN deposition on HfO_2 were also monitored on TiN. Moreover, the oxygen concentration in TiN kept lower levels thus corroborating the barrier property of TaCN. Lastly, the plasma impact with degradation of the electrical properties detected on HfO_2 is minimised with the addition of TiN. So TiN acts as a protection layer against plasma radicals, however it also prevents the ΔV_{FB} increase when TaC is created.

The pro and cons of ALD, PEALD-LP, PEALD and PEALD-HP are presented in the table 5.1.

TABLE 5.1: *Advantages and limitations of the PEALD TaCN with different plasma power (NA means not-available)*

Property	**ALD**	**PEALD-LP**	**PEALD**	**PEALD-HP**
Density	low	medium	high	high
Resistivity	medium	medium	low	very low
Oxgyen removal	moderate	NA	significant	important
Nitrogen migration	moderate	NA	significant	important
Equivalent Oxyde Thickness	lower than PVD-TiN	NA	higher than PVD-TiN	important regrowth
Work function	p-type	NA	strong p-type	strong p-type
Leakage current	low	NA	controlled	unacceptable

So overall, it appears that depending on the application plasma densification of the TaCN layer might not be an advantage. Thus for advanced CMOS, the lower EOT obtained with ALD-TaCN can be preferred to the higher work function of the PEALD-TaCN. On the other hand, for relaxed devices the strong p-type characteristic of PEALD-TaCN is an advantage over the low EOT of ALD-TaCN. Anyhow, the damages brought by PEALD-HP-TaCN on the dielectric appear to be too high to consider its integration in an high-κ/metal gate stack.

To conclude, TaCN integration on HfO_2 dielectric and on TiN metal appeared to have some benefits and hindrances. By a careful separation of thermal and plasma effects the reaction mechanisms happening at TaCN deposition could be deduced in order to limit the interactions and obtain the best properties on the metal without damaging the dielectric.
Now that understanding of (PE)MOCVD and (PE)ALD reaction mechanism and the possible interactions with the substrates was achieved, doping by Al of these materials will be examined in the next chapter and the effect of Al addition will be decorrelated from the rest.

Chapter 6

Aluminium doping

"If we knew what it was we were doing, it would not be called research, would it?"
Albert Einstein, theoretical physicist

6.1 Introduction

As introduced in the Chapter 1, scaling of CMOS devices requires to lower the gate resistance for good device performance. To reduce the resistivity of the metals development of new metals for TiN replacement is one way, and was presented in the previous chapters. Another one is to use dopant inserted in a metal matrix. Addition of Al dopant has been investigated and reported in the literature. Al alloys show a high oxidation resistance and a good thermal stability [62].

TiAlN is a good candidate for advanced CMOS nodes [201–203]. TiAlN deposited by ALD was found to have a resistivity lower than 400 μΩ.cm [23], which is similar to the resistivity of thin TiN layers (report to Section 4.2.2). Main advantage of TiAlN is to show the appropriate work function values for dual metal gate application, as by controlling the amount of N and Al. For example, very low $\Phi_m = 4.36$ eV was demonstrated by alloying TiN and Al [62]. Al dopant allows a work function variation due to its low intrinsic work function of 4.08 eV [204].
Another phenomenon brought by the addition of Al in the metal is the formation of a surface oxide barrier which limits the diffusion of O. This oxygen barrier consists of an Al_2O_3 layer formed at the extreme surface of the deposited material.

Besides, use of Al in the Ti metals induces O scavenging from SiO_2 interfacial layer, leading to the reduction of the EOT of the stack [205, 206]. Scavenging of O from the SiO_2 is an important phenomenon which allows to reduce the EOT, and is made possible by the high affinity and reactivity of Al with O.

PVD-TaN doping with Al has also been reviewed in the literature, but with much lower extent than the TiAlN compounds. In this chapter, the focus will be done on the Al doping of TaN, and modifications of the electrical properties will be discussed in relation with the

modifications of physico-chemical properties.

First, in order to comprehend the phenomena and behaviour of aluminium when used as doping element, an investigation of PVD-Ta and PVD-TaN doping is presented. Influence of the aluminium content in the layer is linked to the evolution of physico-chemical properties of the material and correlated to the electrical properties evolution.
Then, aluminium and aluminium nitride deposition were investigated in order to understand the reaction mechanism taking place during the formation of the Al or AlN materials. The key phenomena observed are used for an investigation of MOCVD-TaN Al doping and understand the interactions between the metal and the dopant. Then, in order to limit the amount of AlN created in the layer, a process of MOCVD-TaN and PEMOCVD-Al monolayers stacking is introduced and the obtained characteristics compared to the MOCVD-TaAlN. Finally, electrical results from MOCVD-TaN doped with Al and TaN/Al stacking are discussed and the evolutions linked to the results of the physico-chemical characterisations. Moreover, part of the doping behaviour is correlated to the evolutions observed with PVD-TaAl materials.

6.2 Aluminium doping in Physical Vapour Deposition

6.2.1 Context

PVD technique was chosen for reference, because until the 40 nm node it was the most used deposition technique for the gate metal. Besides, PVD-deposited materials are well known and often used as reference for development of solutions addressing new technology nodes.

Doping of the PVD-deposited metals is possible using two targets and by adapting the sputtering power of each target depending on the targeted composition [77]. However, due to the principle of PVD technique, i.e. the species reach the substrate with low energy, no metal-dopant bonding can be expected. Thus, deposition of TaAl or TaAlN using two targets results more in a bi-metal material than in an metal-metal alloy.
Moreover, PVD is a directional deposition and thus is not suitable for advanced nodes including small size 3D patterns.

6.2.2 Physico-chemical characteristics of Al-doped PVD-Ta and PVD-TaN

6.2.2.1 Deposition conditions

Deposition was achieved by PVD co-sputtering of Ta and Al-Ti (Ti 1 at.%) targets. Ti in the Al target is used to decrease the roughness of the deposited layer and is supposed to have little or no effect on the bulk properties of the deposited film. Deposition is performed on a substrate cooled down to ambient temperature. For bulk characterisation of the different alloys, 10 nm thick layers were deposited.
In order to obtain a good composition uniformity the substrate is shifting at high speed from

one target to the other, while rotating. Indeed, the two targets are not placed right above the substrate. The term of nano-laminates can thus describe the obtained materials.
Four TaAl samples were deposited with Al doping concentrations of 0%, 30%, 50% and 70%. Then, by addition of N_2 reactant gas three TaAlN samples were produced with 0%, 30% and 50% of Al. No TaAlN samples were processed with an higher Al content due to the expected formation of insulating AlN.

Material characterisations were carried out on Si (1 0 0) blanket wafers. Deposition was performed on a 100 nm thick layer of insulating SiO_2 layer for resistivity measurement.
XRR spectra extractions confirmed the thickness of the layers and gave access to the density. Four points probe measurement on 49 points was used to extract the resistivity. Crystallography was characterised by XRD, with $2\theta \in [25; 80°]$. Finally chemical environment and binding energy were analysed using XPS, Al-Kα beam with an energy of 100 eV, a spot size of 400 µm and a resolution of 0.1 eV.

6.2.2.2 Characterisation of PVD-TaAl layers

Samples composition was extracted from XPS analysis and composition of each sample is given table 6.1, in atomic percent.

TABLE 6.1: *XPS extraction of TaAl samples composition*

Aimed Al content	**Ta (at.%)**	**Al (at.%)**	**O (at.%)**	**C (at.%)**	$\frac{Al}{Al+Ta}$ **(%)**
0%	22.1	10.8	48.9	18.2	33
30%	18.7	15.2	52.0	14.1	45
50%	15.1	18.2	51.9	14.8	55
70%	4.4	31.5	51.3	12.9	88

This analysis reveals that in the case of 0% Al, the sample contains a significant amount of Al (about 10 at.%). This level of aluminium cannot be explained at the moment [1], and one should be aware of this amount for the rest of the analyses.
Anyway, the amount of Ta and Al are respectively increasing and decreasing, with a Ta+Al sum included in the 35 - 38% range. Samples are highly oxidised, with a low variation of oxygen levels. A noticeable amount of carbon is detected at the samples surface, with about 8 to 10% brought by the vacuum break before XPS analysis [93]. No reason was found to explain the surplus, or the concentration decrease with Al content increase.

In the rest of this section the XPS estimation of Al content will be used instead of the targeted Al concentrations.

[1] Possible cross-contamination of the Ta and Al targets can be considered, it might also be linked to the presence of Al on the walls of the chamber

Density measurement, from XRR spectra fitting, are displayed figure 6.1, with the Ta and Al atomic percent.

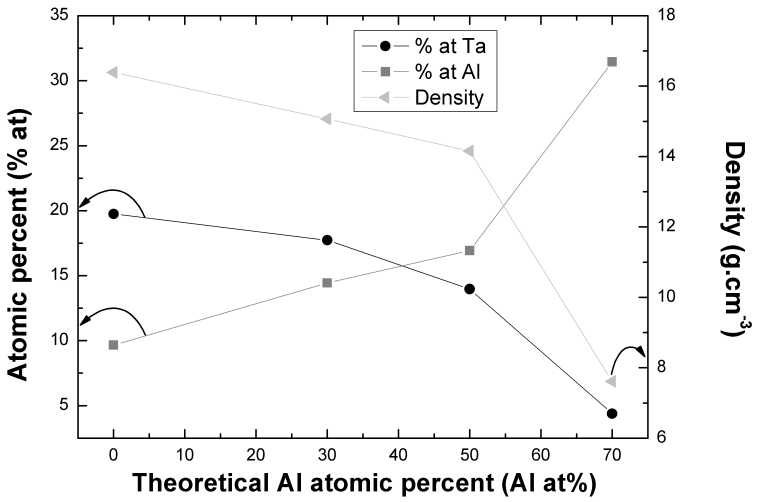

FIGURE 6.1: *Density of TaAl layer depending on the Al content*

Evolution of the density clearly follows the composition of the sample: more Al leads to lower density. Rapid decrease of the density can be explained by the considerable difference between Ta and Al densities (Ta = 16.69 g.cm^{-3} and Al = 2.70 g.cm^{-3} [100]).

The resistivity evolution with Al concentration is presented in figure 6.2. Al ratios (Al)/(Al + Ta), introduced in table 6.1, are also given above each points on the figure.

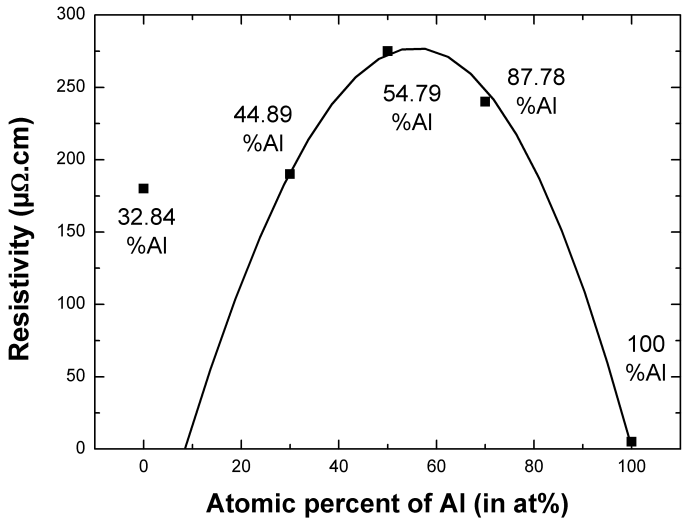

FIGURE 6.2: *Resistivity of TaAl layer depending on the Al content*

The moderate change in resistivity between samples with Al 0% and 30% confirms the similar Al content measured, which is far from the 0% expected.
The bell-shaped curve observed here was already reported for resistivity evolution of TaAl bi-metals deposited by PVD. It starts from the Ta resistivity around 50 µΩ.cm [100] going

up to 280 μΩ.cm for a 50% Al mixture and finally down to pure Al resistivity, at 10 μΩ.cm or less [100].

XRD analysis was completed for every sample and is presented figure 6.3. The theoretical peaks of cubic centred face Ta crystals are also included [79].

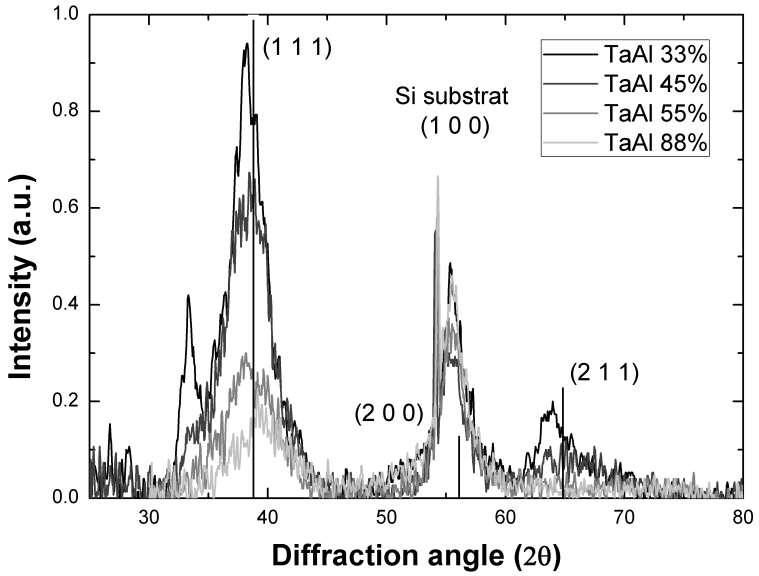

FIGURE 6.3: *Crystallography of TaAl layer depending on the Al content*

The peak positioned at $2\theta = 56°$ originates from the Si substrate.
Three peaks of the Ta cubic crystalline structure are included in the analysed window: Ta (1 1 1), Ta (2 1 1) and Ta (2 0 0), in order of intensity. A parasitic peak from Si (1 0 0) structure is located at the place angle as the Ta (2,0,0) peak, making the interpretation difficult. Another peak is seen at 33° but does not correspond to any Ta cubic centred face peak, neither to another crystalline structure of Ta.
Considering the 10 nm thickness of the samples and the well defined peaks collected, it appears that the layers are highly crystalline. A clear trend of peaks maximum reduction is observed when the amount of Al increases in the layers. It indicates that the addition of Al in the layers restrain the crystallisation of the material. No shift of the peaks position is detected together with the intensity reduction, so Al may not create a crystalline phase with Ta, and Ta keeps the same crystalline structure, i.e. there is no change of the lattice parameters and no constraints added to the crystal.

Phase diagram of Al-Ta is presented in figure 6.4.

From this diagram, it appears that a 30% Al doping in Ta leads to the formation of a TaAl phase. The presence of TaAl crystals in the PVD-TaAl layer could explain the formation of the crystalline peak observed on XRD spectrum at 33°. Yet, it is important to remind of that the diagram presented here is obtained from cooling down TaAl mixtures which were

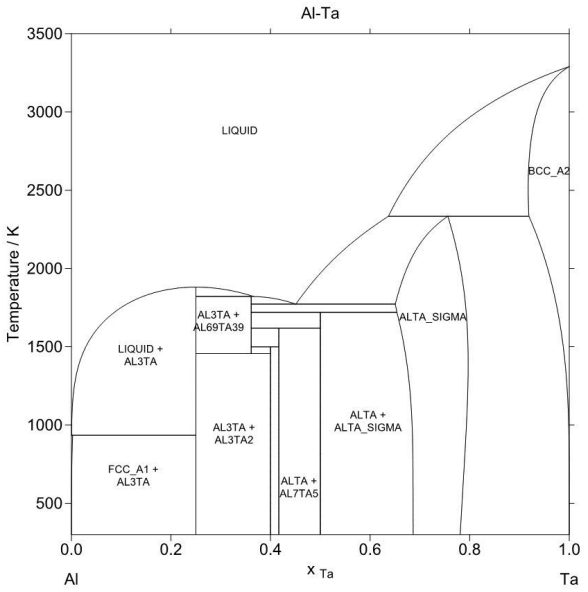

FIGURE 6.4: *Phase diagramm of Ta and Al mixture*

heated up to 3000°C, far from the PVD deposition conditions.

XPS spectra of Ta*4f*, Al*2p* and O*1s* from TaAl samples are shown in figure 6.5 a, b and c, respectively.

Two different Ta*4f* bonding environments appear, figure 6.5a, whatever the Al content. Ta-Ta peak is located at low binding energy, 21 eV [81], while Ta_2O_5 is located at 26 eV [81]. An increase of Al ratio leads to the decrease of Ta_2O_5 environment, until it completely disappears on TaAl sample with 88 % Al ratio.
Al*2p* shows three peaks, the two main peaks are Al_2O_3 located at 74.5 eV [81] and Al-Al at 71.2 eV [81]. A third peak is present between the two first, at 72.4 eV and is attributed to the Ta*5s* feature [81, 86]. At low Al content (33%) mainly the Ta*5s* and Al feature is observed, while increasing Al from 33% to 43% in the layer the Al_2O_3 environment appears and becomes the most prominent contribution. From 43 to 55 % Al-Al peak grows, suggesting that the oxygen cannot migrate in the volume of the layer. Finally, from 55 to 87 % the total acquired signal increases and there is a separation of Al-Al and Al_2O_3 environments. The presence of the Ta*5s* peak at the same energy as the Al*2p* peak highly increases the error margin of Al content quantification. Moreover, due to the presence of Ta*5s* it is not possible to discuss on the presence, or not, of AlO_x environment.
Oxygen O*1s* XPS spectrum, figure 6.5, consists of two peaks. One for Ta_2O_5 at 530.6 eV [81] and the second for Al_2O_3 at 532.3 eV [81]. Here again a clear trend is distinguished with the addition of Al in the layer, more Al in the layer results in the increase of Al_2O_3 peak until the disappearance of Ta_2O_5 for Al 70% sample.
Finally, overall these three spectra show that, contrary to the resistivity evolution which was suggesting a similarity between the Al 33% and 45% doping, the chemistry is highly different between the Al 33% and 45% doping, Al 45% being closer to Al 55% doping.

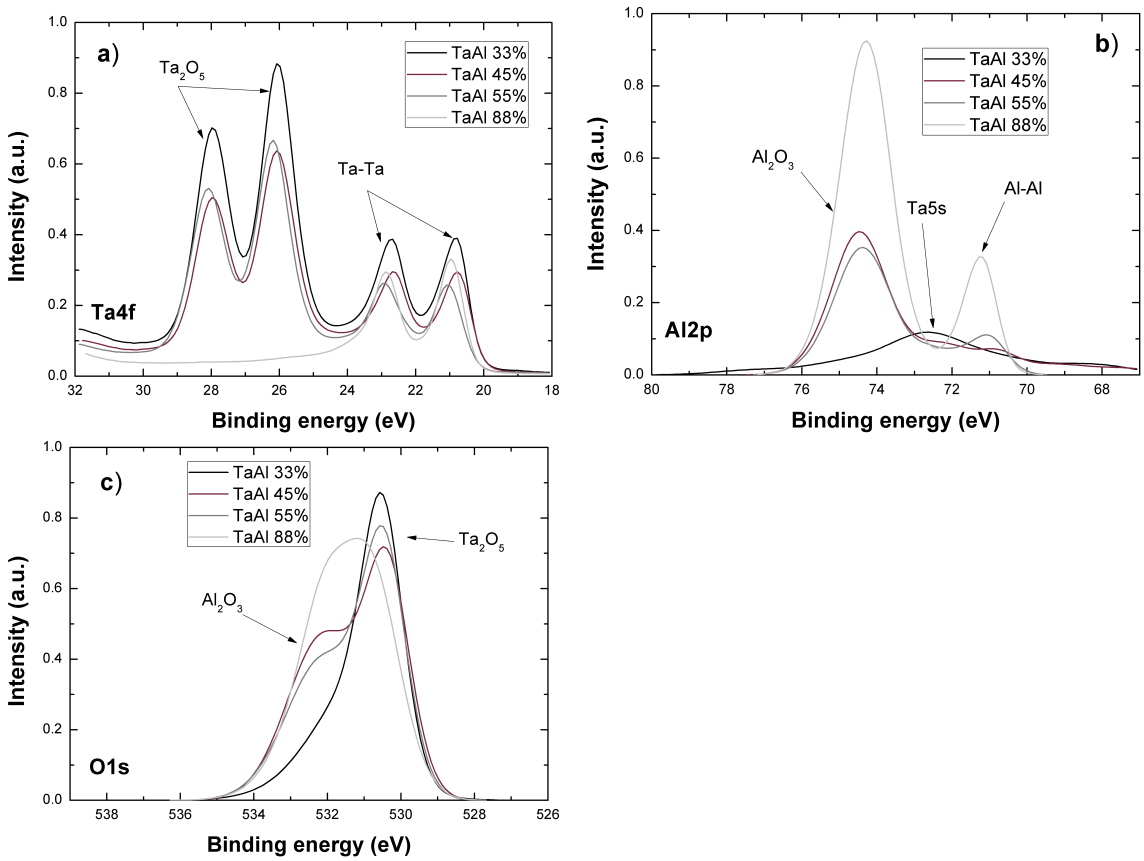

FIGURE 6.5: *Chemical environment of TaAl depending on Al content with XPS spectra a: Ta4f; b: Al2p and c: O1s*

6.2.2.3 Characterisation of PVD-TaAlN layers

Co-sputtering in N_2 reactive ambiance leads to the formation of TaAlN. Samples compositions were extracted from XPS analysis is given table 6.2, in atomic percent.

TABLE 6.2: *XPS extraction of TaAlN samples composition*

Aimed Al content	**Ta (at.%)**	**Al (at.%)**	**N (at.%)**	**O (at.%)**	**C (at.%)**	$\frac{Al}{Al+Ta}$ **(%)**
0%	20.5	12.9	18.2	33.8	14.5	39
30%	17.9	15.5	18.7	32.3	15.5	46
50%	14.4	18.7	18.2	30.4	18.3	57

Here again, the composition analysis reveals that the samples targeted at 0% (i.e. Al free TaN) contains a significant amount of bulk Al (about 12.9 at.%).
Meanwhile, the amount of Ta and Al are respectively increasing and decreasing, with a Ta+Al sum included in the 33 - 33.5 at.% range. No matter the Al content of the layers N at.% is roughly constant, about 18.5 at.%. Samples are also highly oxidised, with a low variation of oxygen levels. A noticeable amount of carbon is detected at the samples surface.

As for PVD-TaAl samples, about 8 to 10% of it is brought by the vacuum break before XPS analysis [93] and no reason was found to explain the surplus.

Density measurement, from XRR spectra fitting, are displayed in figure 6.6, with the targeted Ta and Al atomic percent.

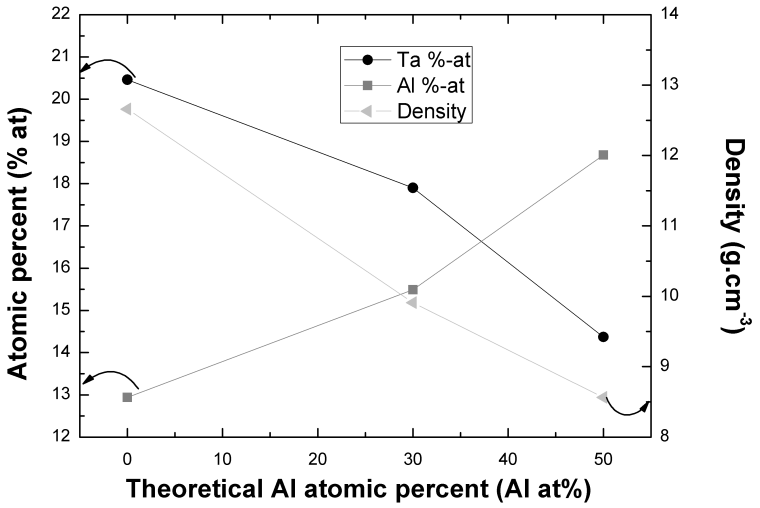

FIGURE 6.6: *Density of TaAlN layer depending on the Al content*

Evolution of the density clearly follows the composition of the sample: more Al leads to lower density. Here again, rapid decrease of the density can be explained by the considerable difference between Ta and Al densities (TaN = 14.3 g.cm^{-3} and AlN = 3.26 g.cm^{-3} [100]).

The resistivity evolution with Al concentration is presented in figure 6.7. Al ratio Al/(Al + Ta) measured by XPS are also given for comparison on the figure.

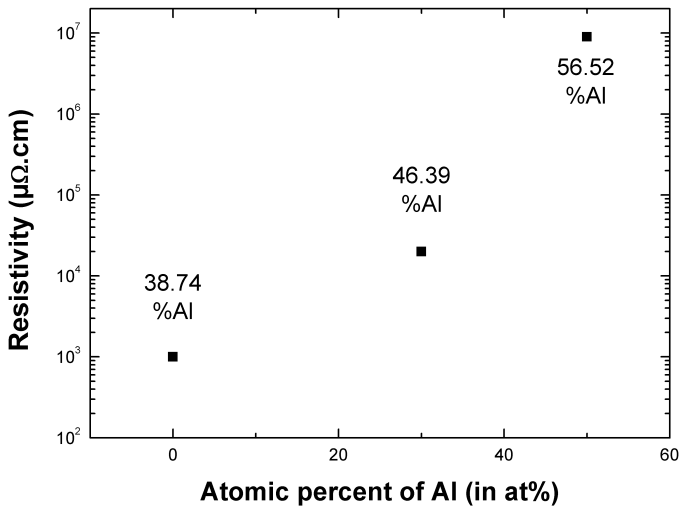

FIGURE 6.7: *Resistivity of TaAlN layer depending on the Al content*

Resistivity of TaAlN samples is higher than expected. The sample with 0% of Al is far above

the nominal TaN resistivity, at 100 μΩ.cm (see Chapter 4, section 4.4.3.1) [18, 100, 163–166]. This observation confirms the presence of Al in the layer with the formation of AlN resulting in a highly resistive film. Finally, AlN formation is confirmed by the increase of the resistivity, up 10 Ω.cm measured at 57% Al content, this value can be compared to the reported resistivity of AlN: about 10^{14} Ω.cm [100].
In the rest of this section, the measured Al content will be used instead of the targeted one.

XRD analysis was performed and is presented figure 6.8. The theoretical peaks of cubic centred face TaN and AlN crystals are also included as reference [79].

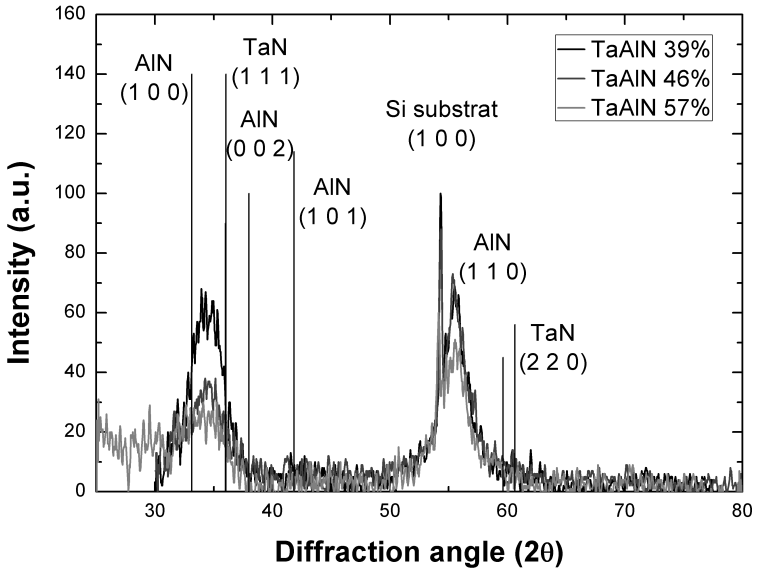

FIGURE 6.8: *Crystallography of TaAlN layer depending on the Al content*

TaAlN show one peak at $2\theta = 34.9°$, corresponding approximately to TaN (1 1 1) orientation. The (2 0 0) and (2 2 0) peaks which should be observed at 41.60 and 60.41°, respectively, in the case of pure TaN, are not observed here. The peak observed at 34.9° is also close to the position of (1 0 0) AlN peak, however if the film would be containing both TaN and AlN crystals a widening of the crystalline peaks would be observed, not a shift.
As for TaAl, an increase of the Al content in the layer decreases the crystallinity of the layer. Hence, with 58% of Al added in TaN induces a reduction of (1 1 1) peak, which becomes almost not visible in the background noise.

Although a clear FCC based structure was observed in TaAl alloy, in the core of TaAlN it seems that the alloy does not share the TaN-based FCC structure.

XPS spectra of Ta*4f*, Al*2p*, O*1s* and N*1s* from TaAlN samples are shown figure 6.9 a, b, c and d respectively.

Ta*4f* XPS spectra, in figure 6.9a, are characteristic of oxidised TaN material, report to the similar spectra which were obtained in the previous chapters, in figure 3.7 chapter 3, for

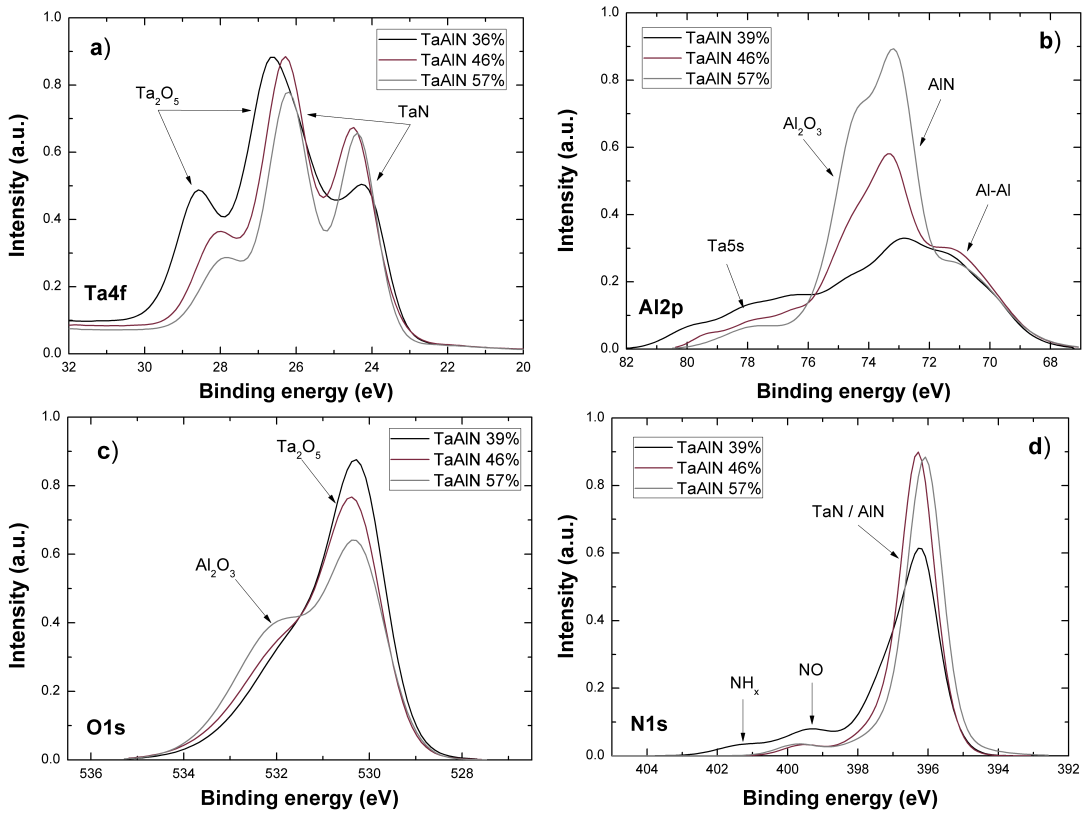

FIGURE 6.9: *Chemical environment of TaAlN depending on Al content with XPS spectra a: Ta4f; b: Al2p; c: O1s and d: N1s*

example. The addition of Al in the layer results in the decrease of the amount of oxygen bonded to Ta, i.e. Ta_2O_5 peak located at 26 eV [81], with a decrease and shift towards lower energy. Consequently the TaN contribution, located at 24 eV, grows when Al is added to the layer.

Al*2p* spectrum, in figure 6.9b, is constituted by at least three peaks and by the Ta*5s* feature. Ranked from high to low binding energy, the extracted peaks are: Al_2O_3 at 74.5 eV, AlN at 73 eV and Al-Al at 71 eV. Increase of Al content favours both Al_2O_3 and AlN environments, while Al-Al appears to be stable.

Oxygen O*1s* XPS spectrum, in figure 6.9 c, consists of two peaks. One is attributed to Ta_2O_5 contribution, at 530.4 eV [81], and a second for Al_2O_3 at 532.3 eV [81]. A clear trend is observed with the addition of Al in the layer, more Al in the layer resulting in the increase of Al_2O_3 peak, while reduction of Ta-O contribution is observed.

Finally, N*1s* spectrum, figure 6.9d, presents four peaks corresponding to TaN or AlN at 396.2 eV, $TaN_{x<1}$ at 397.5 eV (only visible at the lowest Al content), N-O at 399.7eV and NH_x at 401.3 eV.

6.2.2.4 Discussion on Ta and TaN materials doping with Al

In TaAl samples, the oxygen content reported in table 6.1, appears to be roughly stable whatever the Al/(Ta + Al) ratio. Whereas, in TaAlN samples, table 6.2, the oxygen content

appears to decrease, with the increase of Al content in TaAlN (also visible in figure 6.9c). For both TaAl and TaAlN samples, O*1s* spectra figures 6.5c and 6.9c confirm that addition of Al decreases Ta-O environment, located at 530.5 eV, in favour of Al-O environment, at 532 eV. With 70% of Al in TaAl, the TaO_x feature of Ta*4f* XPS spectrum even disappears, in figure 6.5a.
Therefore, formation of an Al_2O_3 passivation layer at sample surface can be assumed. This layer limits the oxygen migration deeper in the volume of the film. This Al oxidation layer is confirmed by Ta oxidation decrease with Al content increase in the films, in figures 6.5a and 6.9a. Moreover, Al_2O_3 formation ($\Delta G_{formation}(Al_2O_3)$ = -1488 kJ/mol^{-1} at 25°C) is thermodynamically more favourable than Ta_2O_5 formation ($\Delta G_{formation}(Ta_2O_5)$ = -1079 kJ/mol^{-1} at 25°C).
Hence, this behaviour suggests that addition of Al in PVD-Ta leads to the formation of a passivation layer at the surface of the film. Whereas in the case of PVD-TaN the oxygen can diffuse in the volume of the film thanks to the presence of nitrogen.

XPS estimation of the layers composition reveals a higher content of Al than targeted, in both TaAl and TaAlN samples. However, an ARXPS analysis (not shown here) suggests that mainly Al_2O_3 is found at the surface of the samples. A separation of the Ta and Al-based phases seems to occur at vacuum break with the formation of Al oxide. The Al quantification by XPS does not follow the density measurement. Indeed, the TaAlN layer with 0% Al appears to have a density of 12 g.cm^{-3} which is close to TaN theoretical density (14.3 g.cm^{-3}) and is not in line with 38% Al estimated by XPS, which would lead to a theoretical density of 9 g.cm^{-3}. The same is observed in the TaAl case.
The difference between XPS quantification and possible Al content need to be confirmed by another characterisation technique. Yet, it can be explained by an important amount of Al at the surface which reduces the signal from species staying under this oxide and resulting in an *overvaluation* of the composition by XPS.

Addition of Al in Ta and TaN layers also leads to the decrease of crystallography, as visible in figure 6.3 and 6.8. On the four TaAl samples and three TaAlN samples an increase of Al content results in the decrease of the crystalline peaks intensity. No other change, like widening or shift of the peaks, is observed when Al is added. Thus, Al present in the layer may not participate in the crystal structure of Ta or TaN and tends to limit Ta and TaN crystallisation.
Even if the crystallisation of the layers is affected by Al addition, no Ta-Al appear to be formed, as suggested by both Ta*4f* and Al*2p* XPS spectra, figures 6.5 and 6.9. This observation further support the hypothesis of Al separation from Ta to form a surface oxide layer at vacuum break.
The absence of Ta-Al metal-dopant bonding is not unexpected due to the relatively low energy provided during the TaAlN deposition. After sputtering of the species off the target, the atoms are reaching the substrate with very low kinetic energy (typically lower than 10 eV). Moreover the deposition is done at room temperature, no energy is provided for the formation of metal-dopant bonds.

Addition of Al in Ta material has a limited impact on the resistivity of the layer. However, by adding Al to the TaN material, AlN is formed and as it is an insulating material the resistivity increases. If Al would not be bonded to N then the resistivity of TaAlN would decrease due to the low resistivity of pure Al = 10 μΩ.cm [100], as confirmed in figure 6.2. AlN formation is further confirmed by Al*2p* XPS spectra in figure 6.9b. However, increasing the amount of Al in the layer also increases the oxidised state of aluminium. The amount of N present in the layer is stable whatever the Al content (see table 6.2), as the amount of N in the deposition chamber is constant for all three depositions it seems that all N_2 is reacting during the deposition process, and is present in Al-N, Ta-N and N-O bonds.
Addition of Al in PVD-Ta and PVD-TaN leads to a passivation of the layer, through the formation of Al_2O_3. This passivation can limit the oxygen migration in the layer and thus stop the EOT regrowth when additional thermal budget is brought during the plug deposition or at annealing.

6.2.3 Electrical results from Al doping of PVD Ta and TaN

Modifications of the electrical results depending on the amount of Al added to the PVD-Ta layers are given figure 6.10.

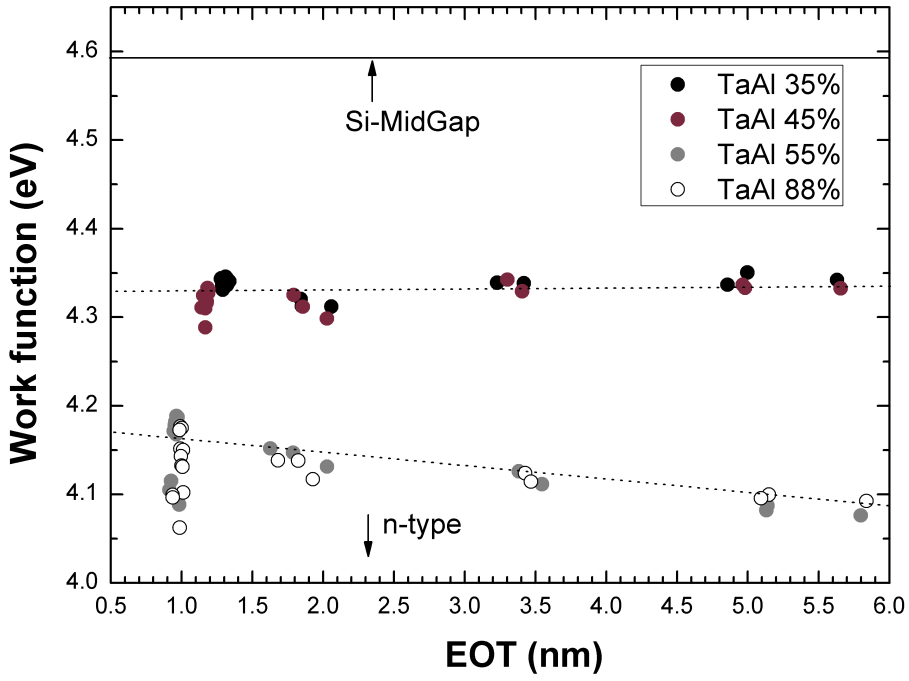

FIGURE 6.10: *Evolution of PVD-Ta work function vs EOT depending on the doping amount*

Whereas ALD-Ta(C)N had a p-type work function, 4.8 eV to 5.0 eV reported in Chapter 5 section 5.3.4, PVD-Ta appears to be n-type with a work function of 4.33 eV.

Addition of 30% Al dopant in PVD-Ta does not change the work function of the transistors. Above 50% of Al added to the PVD-Ta metal, the work function is shifted to lower value, at 4.17 eV, toward the work function of Al. Adding 70% of Al results in the same shift of the work function as when adding 50%, no further decrease is observed.

6.2.4 Conclusion to PVD-Ta and PVD-TaN doping

Al doping of Ta and TaN films results in a decrease of the density and crystallinity but does not result in the formation of Ta-Al bonds. A separation of Al from Ta or TaN is supposed, with an important oxidation of Al leading to the formation of an oxygen barrier.

Addition of Al in TaN layer results in the formation of AlN material, which has insulating properties and is thus not advantageous for metal gate application. Exponential increase of resistivity with Al content increase and Al XPS spectra confirmed the formation of AlN during the deposition process.

Modification of the Φ_m, towards n-type work function when more than 50% of Al are added to PVD-TaAl confirmed the interest of Al doping.

To ease the interpretation of XPS peaks in the doping of metals by MOCVD, the table 6.3 presents the binding energy found on PVD-Ta and PVD-TaN doped with Al.

TABLE 6.3: *Binding energy, in eV, of the different bonds possible in TaAlN layer*

	Ta	**Al**	**N**	**O**
Ta	21	-	24.2	26
Al	-	71	73	74.5

6.3 Aluminium deposition by (PE)MOCVD

6.3.1 Context

As a reminder the TMA molecule, introduced in the Chapter 2, is displayed in the figure 6.11 below. It is formed of three methyl groups sharing covalent electron with 2p3 aluminium orbitals.

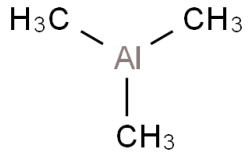

FIGURE 6.11: *Aluminium TMA precursor molecule*

In the literature TMA precursor is mainly used for Al_2O_3 deposition by CVD or ALD with O_2 or H_2O reactant gas [207–209]. TMA precursor reacts with the oxides reactant gases with an activation energy reported to be about 0.2 eV [210], indicating an highly favourable deposition reaction. Few studies report on the AlN deposition by MOCVD or ALD [211–213] but none about metallic Al deposition from metalorganic precursors.

Thus, before using Al or AlN as a dopant in Ti(C)N and Ta(C)N (PE)MOCVD metals few questions needed to be answered. For example Al and AlN deposition activation energy, growth rate and quantity of precursor injected in the deposition chamber have to be known.

6.3.2 Experimental methods

Al and AlN deposition parameters were chosen as close as possible as the best parameters found for TaN and TiN (PE)MOCVD processes. Indeed, the objective here is to use Al as dopant, so deposition parameters have to be compatible with the already existing TaN and TiN processes.
Process parameters of MOCVD-Al are:

- substrate temperature: from 200 to 400°C
- chamber pressure: 2 Torr
- liquid injector temperature: 40°C
- injector frequency: 0.1 Hz
- liquid injector opening time: 1 ms
- nitrogen or hydrogen flow: 200 sccm

Liquid injector frequency and opening time correspond to the lower limit of the tool, the lowest possible deposition rate is required, due to the doping purpose.
Nitrogen flow was chosen sufficiently high to ensure saturation of the chamber, thus the equation 6.1 is not limited by the NH_3 content.

$$Al + NH_3 \rightarrow AlN + \frac{3}{2}H_2 \qquad \Delta G = -271kJ \tag{6.1}$$

To ease the comparison between AlN and Al deposition with NH_3 and H_2, respectively, H_2 chamber saturation at 200 sccm was also chosen.

Using TMA with H_2 to deposit Al layer, by thermal decomposition, leads to the formation of a monolayer, without bulk growth. Surface saturation of the sample is obtained but H_2 is not reactive enough to create new nucleation sites so the growth cannot carry on.

Successful deposition of Al was achieved using plasma decomposition of H_2. The following parameters were chosen:

- substrate temperature: 350°C

- chamber pressure: 2 Torr
- liquid injector temperature: 40°C
- plasma power: 100 W
- injectors frequency: 0.1 Hz

As for MOCVD, process parameters are chosen to ease integration of Al doping in the already existing TaN or TiN processes.
Furthermore, as reported in Chapter 4, temperature does not influence the deposition mechanism in PEMOCVD but helps the exhaust of reaction by-products. Thus, the chosen substrate temperature is 350°C.

Finally, NH_3 plasma assisted deposition of Al with TMA could not be achieved due to the instability of the plasma in the available process window.

Characterisation of the layers was completed using XRR, four points probe, XPS to access density and thickness, resistivity and chemical environments respectively. Description of the tools is given Chapter 2 and the characterisation parameters Chapters 4 and 5.

6.3.3 Thermal decomposition of TMA with NH_3

Because NH_3 plasma assisted deposition is not possible, thermal MOCVD-AlN films were deposited at temperatures ranging from 200 to 400°C and measured by XRR, extracted deposition rates and densities are presented in figure 6.12.

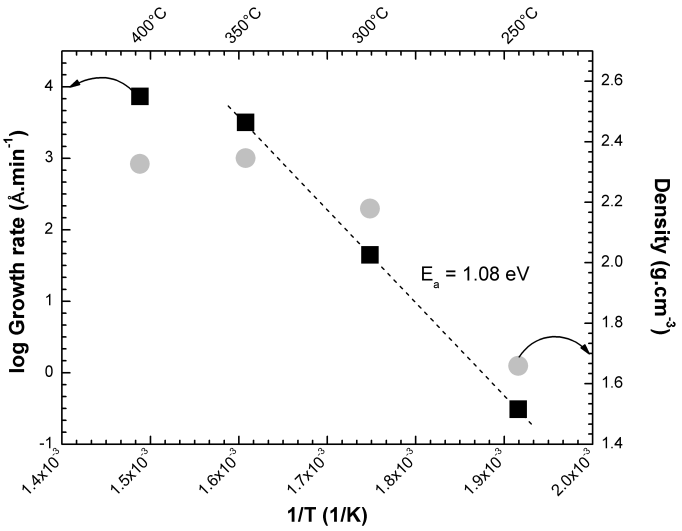

FIGURE 6.12: *Evolution of AlN thickness deposition and density with temperature increase*

Deposition at 200°C leads to the formation of a monolayer, without further growth.
Deposition of AlN with TMA precursor and NH_3 reactant gas from 250 to 350°C follows an Arrhenius law. Fit of the linear increase gives an activation energy of $E_a = 1.08$ eV. Growth

rate appears to stabilise at 350°C, with 0.6 Å.s^1.
Density of the layer has a similar behaviour as deposition rate: a significant increase from 250 to 350°C where it stabilises at 2.37 g.cm^{-3} is observed. The measured density is lower than theoretic density, AlN = 3.26 g.cm^{-3} [100], and closer to Al density, Al = 2.70 g.cm^{-3} [100].

XPS analysis of a 4 nm AlN layer deposited at 350°C with TMA and NH_3 is presented in figure 6.13.

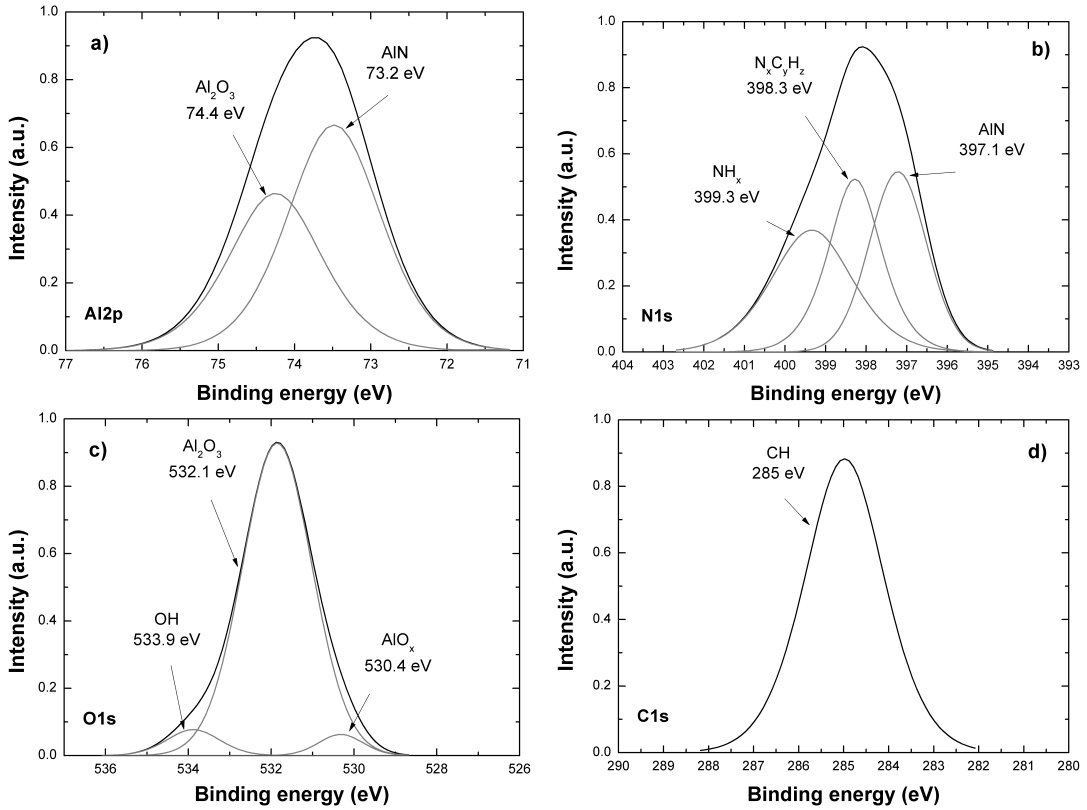

FIGURE 6.13: *a: Al2p, b: N1s, c: O1s and d: C1s XPS spectra of MOCVD-AlN*

In figure 6.13a, two environments are discerned in Al*2p* spectrum, at 74.4 and 73.2 eV, corresponding to Al_2O_3 and AlN bonding environments respectively. No Al-Al bonding environment is recorded.
N*1s* XPS spectrum, in figure 6.13b, is made of three environments: AlN at 397.1 eV, $N_xC_yH_z$ at 398.3 eV and NH_x at 399.3 eV.
On O*1s* XPS spectrum, in figure 6.13c, three bonding environments can be distinguished, from 530.4 to 533.9 eV and are attributed to AlO_x, Al_2O_3 and OH bonding.
Finally, C*1s* spectrum, in figure 6.13d, presents only one environment correlated to carbon contamination at 285 eV.

XPS estimation of the MOCVD-AlN sample composition is given in table 6.4.

TABLE 6.4: *XPS extraction of MOCVD-AlN sample composition*

Al (at.%)	**C (at.%)**	**N (at.%)**	**O (at.%)**
27.4	5.9	12.5	54.5

A ratio of 1:3 for N:Al and 2:1 for O:Al are observed.
Carbon from contamination is below 6 at.%, whereas TMA precursor mainly contains carbon (see figure 6.11). Thus the deposition reaction appears to be complete, the precursor is fully decomposed and reaction by-products well eliminated from the deposited material.

Resistivity measurement was not possible due to the upper limit of the measurement tool. AlN resistivity was out of the measurement range.

6.3.4 H_2 plasma decomposition of TMA

Decomposition of TMA with H_2 plasma was achieved with the aim at depositing pure Al, without nitrogen and limited amount of carbon.

Four points probes measurements were carried out on several samples of Al with thicknesses ranging from 2 nm up to 15 nm without success. Resistivity of the layers was always too high for the tool to measure it. It is supposed that at vacuum break a few nanometres thick Al_2O_3 resistive layer is formed on the deposited Al and prevents resistivity measures.

XPS spectra of Al, N, O and C elements in a 4 nm Al layer deposited by PEMOCVD at 350°C with TMA and H_2 plasma are presented figure 6.14a, b, c and d, respectively.
Al*2p* XPS spectrum, in figure 6.14a, is constituted by three environments. They correspond to Al_2O_3 at 74.5 eV, AlO_x and/or AlC at 73.6 eV and AlC bonding at 72.4 eV.
N*1s* spectrum, figure 6.14b is made of two peaks at 397.1 eV for AlN bonds and 398.3 eV for $N_xC_yH_z$. The presence of AlN is explained by the absence of cleaning before the PEMOCVD-Al deposition, resulting in cross-contamination by species from previous depositions.
Oxygen XPS peaks, in figure 6.14c, located at 532.1 and 530.4 eV, correspond to Al_2O_3 and AlO_x bonding environments respectively.
Finally, two environments corresponding to carbon-metal bonding, AlC and AlC in Al_2O_3, are present at 281.5 and 282.8 eV in figure 6.14d.

In summary, the deposited film is not pure Al as expected, but is formed of AlC. Thus, in the rest of this chapter it will be referred to as PEMOCVD-AlC.

XPS estimation of the PEMOCVD-AlC sample composition is given in table 6.5.

It appears that the nitrogen content in the layer is low, whereas carbon content is much higher than what was obtained with MOCVD-AlN deposition. Also, the Al:O ratio is quite

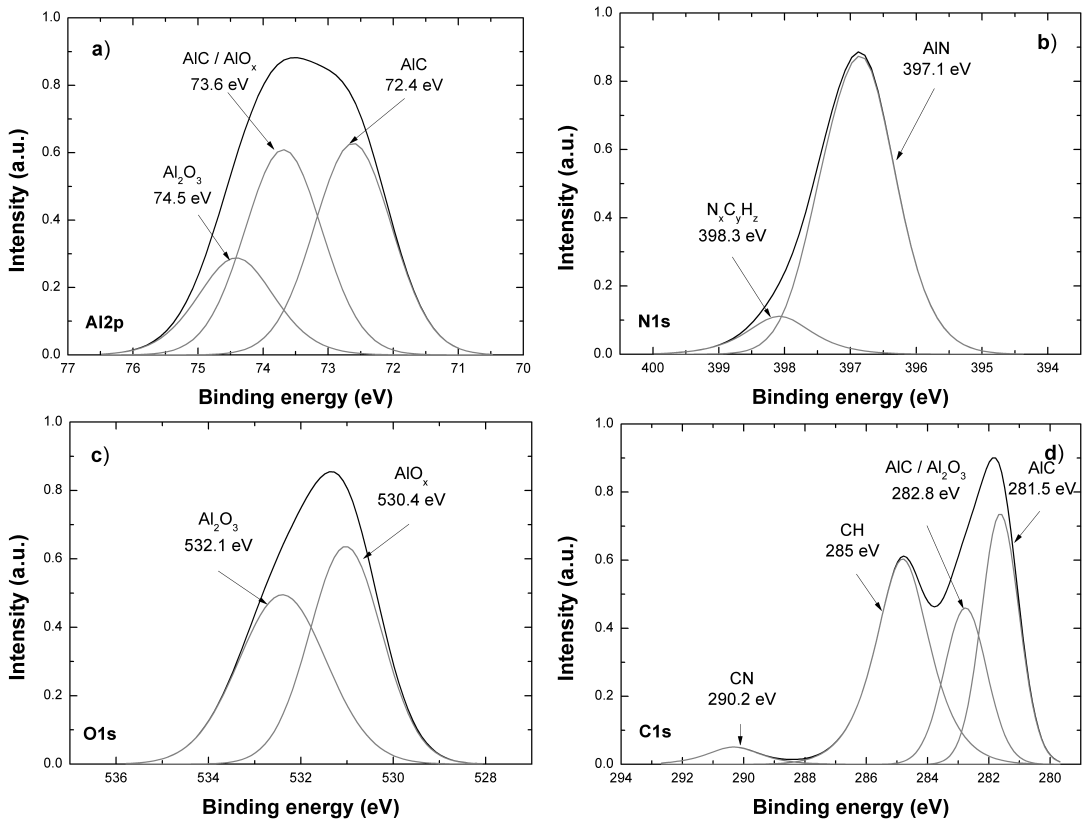

FIGURE 6.14: *a: Al2p, b: N1s, c: O1s and d: C1s XPS spectra of PEMOCVD-AlC*

TABLE 6.5: *XPS extraction of PEMOCVD-AlC sample composition*

Al (at.%)	**C (at.%)**	**N (at.%)**	**O (at.%)**
32.7	17.4	5.5	44.4

low compared to MOCVD-AlN, at 3:4.

Due to the use of H_2 plasma for Al deposition by PEMOCVD, an impact was observed on the Si substrate. The Si*2p* XPS spectrum after PEMOCVD-AlC deposition is presented figure 6.15.

This spectrum reveals the removal of oxygen from SiO_2 when PEMOCVD-AlC is deposited on native SiO_2/Si substrate. Two environments appear at 100 and 101.5 eV and correspond to Si^{3+} and Si^{2+}.

The oxygen removal of a material by H_2 plasma was already shown and discussed in the Chapter 5.

6.3.5 Interpretation of MOCVD-AlN and PEMOCVD-AlC deposition

Using MOCVD and PEMOCVD techniques, deposition of AlN and AlC materials was successfully achieved.

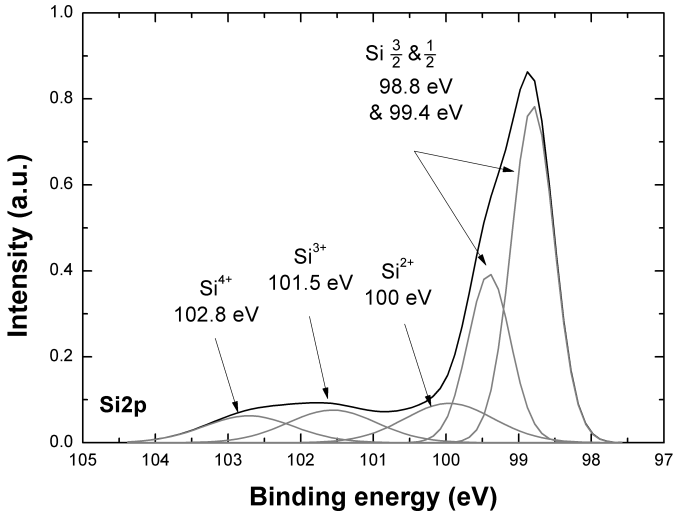

FIGURE 6.15: *Si Si2p spectrum after PEMOCVD-AlC deposition*

TMA reaction with NH_3 reactant gas appears to be complete from 350°C, with low carbon contamination, which also confirms the high efficiency of reaction by-products exhaust. The activation energy of the deposition reaction was calculated to be 1.08 eV, in line with the 0.78 to 0.95 eV reported in the literature [211, 214].
This activation energy is also twice higher than the activation energy of TaN or TiN deposition calculated in Chapter 3, respectively 0.46 and 0.48 eV. This higher activation energy suggests that depositions of TaN or TiN require less energy than AlN deposition.

AlN material is oxidised at vacuum break, the Gibbs free energy of AlN oxidation was calculated at 25°C and for one mole of AlN, from equation 6.2.

$$2AlN + \frac{3}{2}O_2 \rightarrow Al_2O_3 + N_2 \qquad \Delta G = -1008kJ.mol^{-1} \tag{6.2}$$

As the Gibbs free energy of AlN oxidation is highly negative, the reaction is spontaneous, which confirms the formation of aluminium oxide at the sample surface.

TMA deposition is not activated by H_2 reactant gas. Only a monolayer of Al is obtained and suggests that surface saturation of the substrate is reached but the nucleation sites are not activated for further growth of the layer. A different approach is required to activate the nucleation sites using H_2 reactant gas with plasma enhancement, it is the PEMOCVD technique.
TMA activation using H_2 plasma led to the deposition of AlC material. Decomposition of the precursors molecule with a 100 W plasma power is not complete and some carbon, in carbon-metal bond, is found in the deposited layer.

AlC deposition in PEMOCVD mode affects the substrate and leads to the reduction of oxygen from SiO_2 native oxide initially present on the substrate. This oxide removal by H_2 plasma was already observed and discussed in the Chapter 5. One expects that such plasma

conditions on HfO_2 would damage the dielectric and consequently would degrade the electrical properties of the stack.

As for AlN deposition, Al is highly reactive with oxygen, resulting in the formation of Al_2O_3 at the sample surface after vacuum break. Gibbs formation free energy of Al_2O_3 is given equation 6.3.

$$\Delta G_{formation}(Al_2O_3) = -1488kJ.mol^{-1} \qquad at\ 25°C \tag{6.3}$$

The low Gibbs energy of Al_2O_3 formation confirms the high affinity of Al with oxygen. Al_2O_3 oxide level appears to be higher in the case of MOCVD-AlN where it represents two thirds of the layer compared to half of the layer for PEMOCVD-Al. As suggests earlier and in PVD-TaAlN case, nitrogen allowed the oxygen to diffuse in the layer even if an Al_2O_3 passivation is formed at the surface of the film. In the case of PEMOCVD-AlC, diffusion of oxygen appears to be limited, as for PVD-TaAl, which hints on the presence of Al-Al bonds in the volume of the film. An estimated 2 to 3 nm layer of Al_2O_3 is formed at the surface of the samples, in agreement with the thickness reported in the literature [215].

6.3.6 Conclusion

Feasibility of MOCVD-AlN and PEMOCVD-AlC depositions was proven by this experiment and the chemical environments of both AlN and AlC materials are reported.

An important point revealed is that even if the chosen precursor does not contains nitrogen bond it is difficult to avoid AlN creation. Nitrogen present in the deposition chamber from previous deposition process is reacting with the introduced TMA and forms AlN within the Al layer. In fact, N is known to be difficult to pump-out under vacuum. It tends to remain in the chamber and advanced pumping steps are required to insure a satisfying removal of nitrogen.

Processes of PEMOCVD-AlC is applied now for doping of MOCVD deposited TaN metal.

6.4 Al doping of MOCVD-TaN

Complete description of MOCVD-TaN process was given in the Chapter 3 with a detailed explanation of the possible Ta precursors molecule decomposition paths. Influence of the deposition parameters was investigated and discussed in regards to the obtained results. In this part, attempts to insert Al in MOCVD-TaN using TMA precursor are presented.

Doping of the PEMOCVD-TaN process, presented Chapter 4, was also studied, however as it is the last experiment done in this thesis the results are not presented due to the lack of perspective.

6.4.1 MOCVD-TaN doping characterisation

6.4.1.1 Doping of TaN metal

In order to evaluate the possible doping of MOCVD-TaN, TMA precursor was injected together with TBTDET precursor.
Despite the several experiments carried out with variations of the substrate temperature, reactant gas or injected Ta:Al ratio, via injector frequency and injector opening time modulations, no trend allowing an adequate control of doping levels was found. Al content of the layers, quantified by XPS, was greatly higher than the Ta content no matter the chosen process parameters. Therefore, instead of Al doping of TaN, it is more correct to name the films obtained as Al(Ta)N alloying.

Moreover, the buffer/memory effect of the evaporation furnace, already mentioned in the Chapter 3, appeared to be stronger in the case of Al precursor compared to Ti or Ta precursors. It led to the deposition of layer containing significant levels of Al without injection of TMA in the deposition chamber. This cross-contamination made the development of Al doping processes even more difficult.

So far, the recipe with lowest Al content obtained is:

- 350°C substrate
- 2 Torr deposition pressure
- NH_3 saturated ambiance
- injectors temperature of 40°C
- 0.1 Hz injection frequency
- Ta:al injection ratio of 10:1

This recipe is later referred to as MOCVD-TaAlN process.

XPS characterisation of the obtained TaAlN layer is presented in the following section.

6.4.1.2 Chemical environments of MOCVD-TaAlN

XPS spectra from MOCVD-TaAlN, deposited with the previously introduced recipe are presented figure 6.16.

Compared to the Ta*4f* environments presented in the previous chapters (see figure 6.9, page 142 for reference), the Ta*4f* spectrum of MOCVD-TaAlN figure 6.16a has a low oxide feature characterised by a non symmetric trident. Ta is mainly bonded to nitrogen. This observation is similar to the auto-passivation discussed in the case of addition of Al in PVD-Ta and PVD-TaN.
Al*2p* XPS spectrum of MOCVD-TaAlN is shown in figure 6.16b. Al presents three different bonding environments standing for Al_2O_3 at 74.5 eV, AlN at 72 eV and Al-Al at 70.5 eV.
On the N*1s* spectra, figure 6.9d, it is not possible to distinguish AlN from TaN. A Ta*3d* peak is observed and makes the deconvolution of the N1s peaks even more difficult.

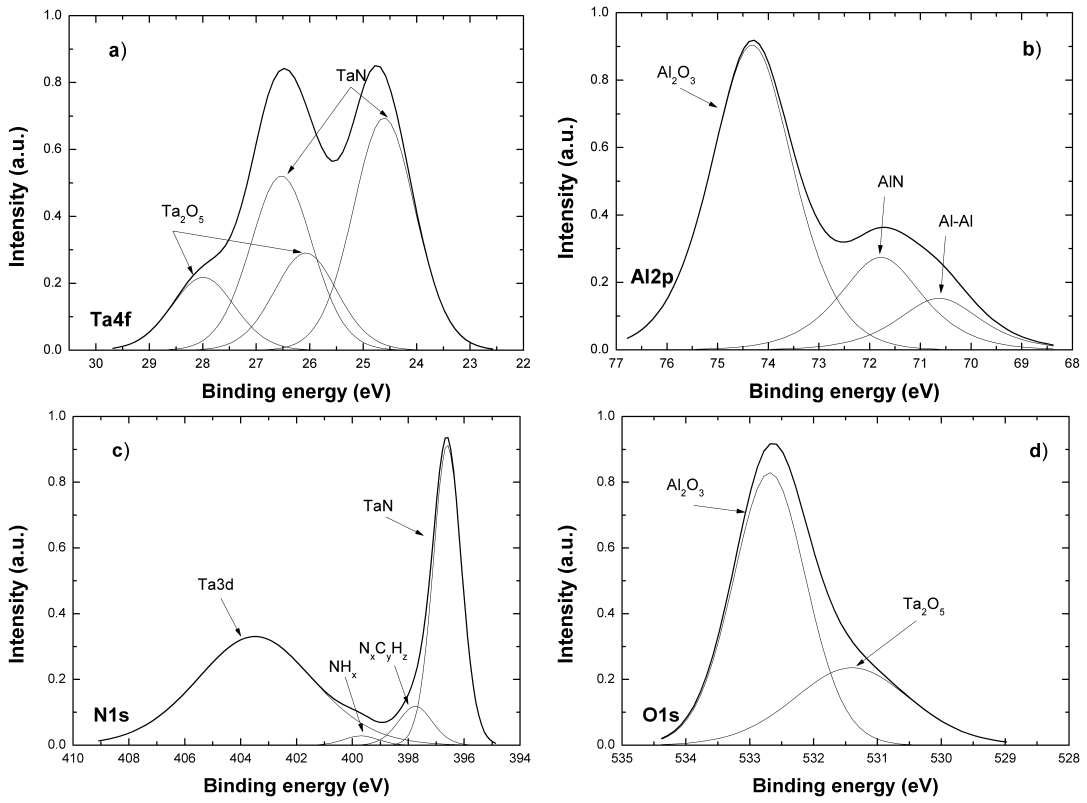

FIGURE 6.16: *a: Ta4f, b: Al2p, c: N1s, d: O1s XPS spectra of MOCVD-TaAlN Ta:Al 10:1 injection ratio*

Finally, O*1s* spectra, figure 6.16d, feature two environments, at 530.6 eV and 532 eV respectively standing for Al_2O_3 and Ta_2O_5. Compared to Ta_2O_5, Al_2O_3 peak has an higher intensity and confirms the low level of tantalum oxide in the layer, i.e. aluminium oxide is preferably formed.

Composition of the MOCVD-TaAlN film was extracted from XPS analysis and is presented in table 6.6.

It results that the Al/(Al + Ta) ratio is 75.9%. The carbon content of the layer is higher

TABLE 6.6: *XPS extraction of MOCVD-TaAlN sample composition*

Injected Ta:Al ratio	**Ta (at.%)**	**Al (at.%)**	**C (at.%)**	**N (at.%)**	**O (at.%)**
10:1	4.9	15.4	15.4	10.1	54.2

than what was obtained for MOCVD-TaN or MOCVD-AlN, which tends to suggest that the decomposition path is affected by the presence of both precursors in the deposition chamber. Else an important oxidation of the layer is also observed.

6.4.1.3 Localisation of Al in the layer

Angle Resolved XPS, presented Chapter 2.3.6.4, was used for a localisation of Al in the MOCVD-TaAlN layer. Resulting Al*2p* and Ta*4f* spectra are given in the figures 6.17 and 6.18 below, depending on the analysis angle, from volume to extreme surface.

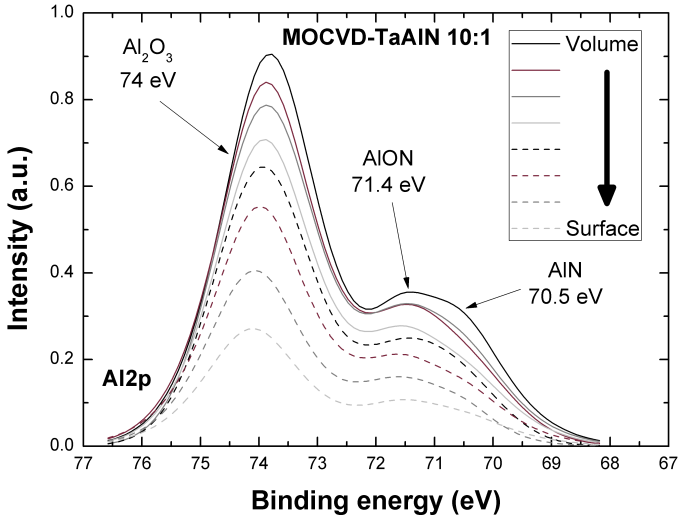

FIGURE 6.17: *Evolution of Al chemical bonding from volume to extreme surface*

Peak intensity evolution suggests that Al-Al is localised in the bulk of the layer, i.e. not only at the surface. However, the bonding environments change from surface to volume. At the extreme surface, more Al_2O_3 is seen while in the volume AlN and Al environments are increasing.

The Ta*4f* spectra evolution from surface to volume of MOCVD-TaAlN sample is presented in figure 6.18a. Same analysis was achieved for MOCVD-TaN, deposited at equivalent process parameters, and is presented figure 6.18b.

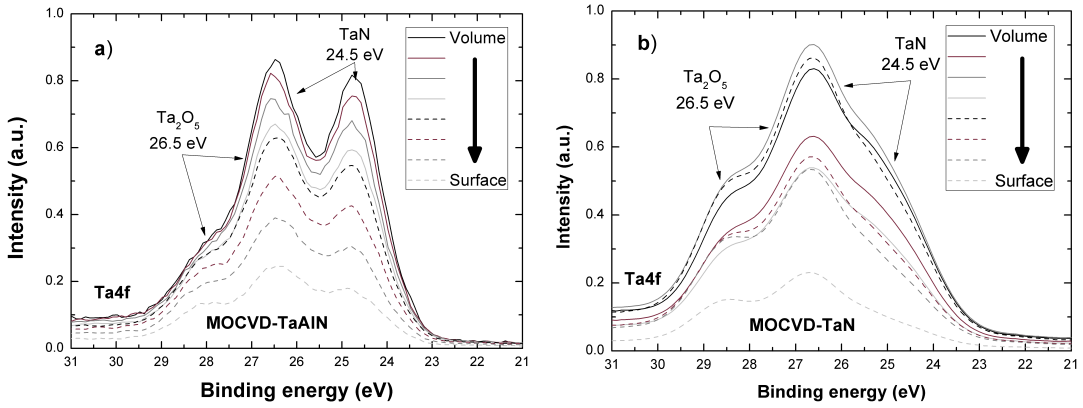

FIGURE 6.18: *Evolution of Ta chemical bonding from volume to extreme surface in MOCVD-TaAlN and MOCVD-TaN*

In the Ta*4f* spectra acquired with TaAlN, in figure 6.18a, the evolution of Ta-O binding from surface to volume is not growing as much as Ta-N feature, indicating an higher oxidation level at the surface of the sample than in the volume.
In comparison, MOCVD-TaN spectra, in figure 6.18, presents the same two features of Ta-O and Ta-N, however the evolution of both is similar from volume to surface, suggesting an homogeneous oxidation of the material in the volume of the layer.

This analysis suggests a separation of Al from the TaAlN material in order to create an oxide layer at the extreme surface of the layer. Moreover, the Al_2O_3 layer protects the volume of the layer from further oxidation, it acts as a barrier to oxygen diffusion. There is a passivation of the layer at the surface of the film. Furthermore, addition of Al in the TaN film leads to the decrease of O solubility.
The separation of Al and Ta might occur through two distinct phenomena. First, Al oxide formation is favoured at the surface of the sample, which tends to "pull" the Al atoms towards the surface of the sample. Second, due to the limited solubility of O in the TaAl mixture, TaN is pushed back from the surface at the oxygen uptake. Altogether, an aluminium oxide film is formed at the surface of the sample and in the volume of the film TaN is found with a limited amount of O.
In summary, the Al oxidation behaviour hinted from PVD-Ta and PVD-TaN doping is confirmed in MOCVD-TaAlN.

6.4.2 Conclusion

The first investigation of the process parameters influence on the deposition of MOCVD-TaAlN did not allow to define a reaction path or understand the phenomena observed. No significant difference, between the process-wise differently doped materials, could be determined and linked to the process conditions.
Thus, only one recipe was qualified for TaAlN deposition by MOCVD. And the repeatability of this process was confirmed, despite the buffer effect of the evaporation furnace.
However, to estimate the influence of Al doping on the MOCVD-deposited TaN metals, several materials are necessary for a comparison. So, new processes were developped and include stacking of MOCVD-TaN with MOCVD-AlN and PEMOCVD-Al. Development of both Al and AlN materials is presented in the following section.

Finally, an ARXPS study of the MOCVD-TaAlN shown that a separation of Al from Ta occurs in the volume of the layer. This phenomenon was already highlighted by the modification of the XPS spectra with Al content increase in PVD-Ta and PVD-TaN. The important oxidation of Al at the surface of the material generate an oxygen barrier, protecting the Ta in volume from oxidation.

6.5 TaN and AlC multistacks formation by cycled (PE)MOCVD

6.5.1 Context

To bypass the limitations previously described and the difficulty to control the Al dopant concentration in TaN layers, multistacks or stacked layers were developped. These stacks range from the superposition of monolayers to the stacking of thick layers, each resulting in different physico-chemical characteristics.

To ease the discussion only two of the developped materials/stacks are presented here:

- 4 nm MOCVD-TaAlN deposited with a Ta:Al injection ratio of 10:1. Already reported in section 6.4.1.
- 4 nm cycled MOCVD-TaN / PEMOCVD-AlC mono-layers repeated five times and covered by a mono-layer of MOCVD-TaN. The last MOCVD-TaN layer is used to limit the oxidation of the aluminium present in the volume of the film. This stack is later referred to as (TaN / Al)x5 and can be associated to the "supercycle" approach used for doping of ALD deposited oxides [207].

6.5.2 Tools and methods

The deposition parameters of the layers used here were already introduced earlier, MOCVD-TaAlN in Chapter 6 section 6.4.1 page 153, MOCVD-TaN in Chapter 3 section 3.5.1 page 70 and PEMOCVD-AlC in Chapter 6 section 6.3.2 page 146.
The same tools are used for resistivity measurement, thickness confirmation and chemical bonding analysis. On the first place XPS was used for the quantification of each species concentration in the layers. However, as stated earlier, XPS is a surface analysis technique, the signal from the species present at the bottom of the stack is lowered by the species from the top of the stack. Thus, the stack composition obtained by XPS does not correspond to the material, when inhomogeneous stacks are investigated an overvaluation of the surface species content is observed.
Therefore, to asses the composition of the multistack, Wavelength Dispersive X-Ray Fluorescence (WDXRF) was used to count the number of aluminium atoms present in the volume of the material. WDRXF is a volume analysis (several microns in depth) and therefore is not affected by the localisation of each specie, a complete description of this technique can be found in [216].

6.5.3 Characterisation of TaAlN multistacks

In table 6.7 are presented the estimated Al% obtained by WDXRF and XPS. The error margin was evaluated to be 20% on the WDXRF quantification and 10% by XPS.

The comparison of XPS and WDXRF confirms the hypotheses about Al separation and formation of an oxide layer at the surface of the sample, resulting in a overvaluation of the Al content in the layers by XPS. XPS which is a surface analysis, is highly impacted by this

TABLE 6.7: *XPS and WDXRF extraction of TaAlN samples Al content*

Al ratio in Ta:Al (in %)	**TaAlN**	**(TaN / Al) x5**
XPS estimation	75.9	92.7
WDXRF estimation	19.0	25.2

localisation of Al, whereas WDXRF, which is a volume analysis, returns a more satisfying estimation of the Al content.
This difference between XPS and WDXRF does not change the trends observed and discussed in the previous sections, i.e. for PVD-TaAl and PVD-TaAlN doping.

Considering that Al and Ta have a density of 3.3 g.cm^{-3} and 12 g.cm^{-3}, that Al and Ta have an atomic weight of 181 g.mol^{-1} and 27 g.mol^{-1}, and that mono-layers of TaN and Al are 0.4 nm thick, the calculated Al of (TaN / Al)x5 film content is close to 50%. The lower Al content obtained with WDXRF measurement may underline a different growth rate of PEMOCVD-AlC when deposited on Si substrate than when deposited on MOCVD-TaN. Some of the interactions between the two metals are not yet fully understood and further investigation are still on-going.

6.5.3.1 Evolution of chemical bonding depending on the process

XPS measurements of the Ta*4f*, Al*2p*, O*1s* and N*1s* core level of MOCVD-TaAlN and (TaN / Al)x5 are presented in figure 6.19.
Spectra of Ta*4f* are presented in figure 6.19a, the spectrum of MOCVD-TaAlN control sample was already introduced and discussed in section 6.4.1.2. The essential information was that Al does not interact with Ta to create metal-dopant bonds, however a layer of Al_2O_3 is formed at the sample surface and protects Ta from oxidation thanks to the important affinity of Al with O. In the case of (TaN / Al)x5 superposition, the spectrum shows two new environments at 23.6 and 22.3 eV corresponding respectively to $TaN_{x<1}$ and TaAl or Ta-Ta. The environment located at 23.6 eV can also be associated to a N-Ta-Al bonding.

Al*2p* spectra of the two layers, in figure 6.19b, present some important variations and do not feature the same bonding environments. (TaN / Al)x5 layer is constituted of two environments, Al_2O_3 and AlON, located at 74.5 eV and 73.5 eV, respectively. The absence of TaAl environment, in (TaN / Al)x5, goes against the TaAl peaks viewed on Ta*4f* spectrum. One possible explanation supposes that the high level of Al_2O_3 results in a peak with a higher intensity than the other environments, resulting in a difficult observation of the peaks with lower intensity. Another explanation is that the feature observed on Ta*4f* peak do not correspond to Ta-Al but to Ta-Ta.

On figure 6.19c are displayed the N*1s* spectra of the layers. TaAlN and (TaN / Al)x5 present the two same main features of N bonded to a metal and in an $N_xC_yH_z$ environment. $N_xC_yH_z$ originates from the precursor molecule, as highlighted Chapter 3.

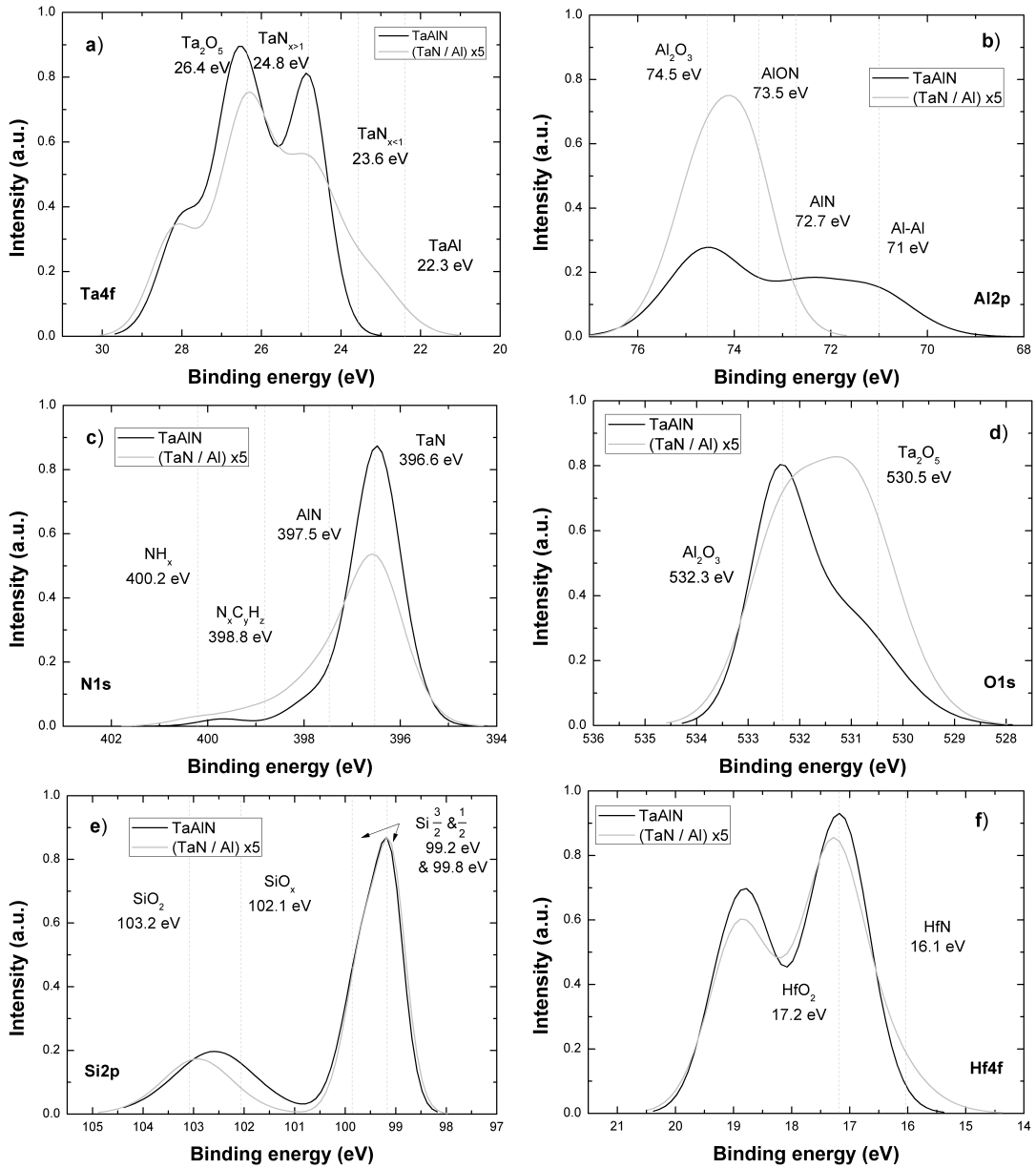

FIGURE 6.19: *Chemical environment of TaN layer doped with Al a: Ta4f; b: Al2p; c: O1s and d: N1s*

O*1s* peaks, in figure 6.19d, display two environments at 532.3 eV and 530.5 eV, which correspond to Al_2O_3 and Ta_2O_5 oxides. On MOCVD-TaAlN the higher intensity of the Al_2O_3 feature compared to the Ta_2O_5 feature supports the hypothesis of Al_2O_3 formation at the surface of the layer, oxide which protects the oxygen from migrating/diffusing in the volume. In opposition to this observation, (TaN / Al)x5 does not show any preferential oxidation of the metals.

Si*2p* environments, figure 6.19e, suggest that (TaN / Al)x5 removes some of the oxygen from the SiO_2 interfacial layer, leading to the formation of SiO_x. This oxide removal was already observed for PEMOCVD-AlC deposition in the section 6.3.4.

Hf*4f* spectra, figure 6.19f, presents a variation for the (TaN / Al)x5 layer compared to the control sample, indeed an HfN bonding environment is observed at 16.1 eV.

In summary, the two processes developped for doping of MOCVD-TaN show important variations in their chemical bonding, and can be easily differentiated from MOCVD-TaN without Al doping.

6.5.3.2 Crystallography

XRD measurements of the MOCVD-TaAlN and (TaN / Al)x5 samples are presented figure 6.20. In addition, the XRD spectra of MOCVD-TaN is displayed for reference.
Where the MOCVD-TaN appeared to be highly crystalline, no peaks are detected by XRD

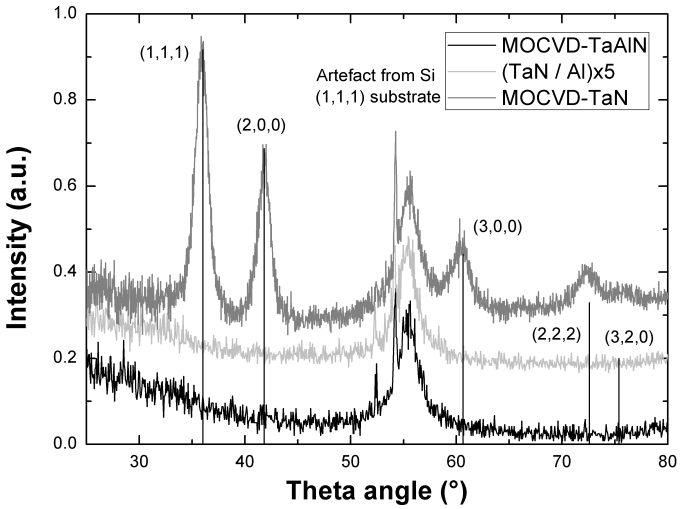

FIGURE 6.20: *Crystallography of the Ta(Al)N materials deposited by (PE)MOCVD*

measurement for MOCVD-TaAlN or (TaN / Al)x5. Only the Si (1 0 0) peak from the substrate appears at θ 55°, and confirms that the same acquisition parameters were used.
The non-crystallinity of the layers may be due to the Al dopant. Indeed, a reduction of the crystallinity was already observed for PVD-Ta and PVD-TaN doping, section 6.2.

Electrical characterisation of these layers are presented in the coming section and compared with the doping of PVD layers.

6.5.4 Electrical characteristics of Al doped metals

6.5.4.1 Transistors fabrication and electrical measurements

In this part of the study electrical characteristics of PVD-Ta(Al), described in the section 6.2, and (PE)MOCVD-Ta(Al)N, introduced in the section 6.5 are compared and discussed. In order to limit the damages of plasma on the dielectric, effects discussed in the Chapter 5, a third sample was added to the two MOCVD samples presented section 6.5. It consists

in the same (TaN / Al)x5 but with an additional MOCVD-TaN "protection" layer inserted between the metal and the dielectric.
Relaxed CMOS capacitors with high-κ/metal stack are used for measurement of the electrical properties of the layers. Description of the devices preparation was introduced in the Chapter 5, section 5.2.2.

It is important to notice that, due to the reduced time available for the integration of the Al doping in capacitors, deposition was done on 200 mm wafers. The only change between 200 and 300 mm wafers concerns the interfacial chemical oxide, which is known to be of better quality and better controlled over the thickness at 0.8 nm for 300 mm wafers, compared to 1 nm for 200 mm wafers.
Moreover, a weaker oxide removal than required was used for native SiO_2 removal and chemical SiO_2 formation, thus the EOT of the capacitors is higher than expected and a variation is observed from wafer to wafer.
So, in this chapter the EOT of the capacitors will not be discussed. Only the work function variations will be taken into account.

6.5.4.2 Evolution of the work function of MOCVD deposited TaAlN

Variation of the work function depending on the EOT and the deposited material is given figure 6.21.

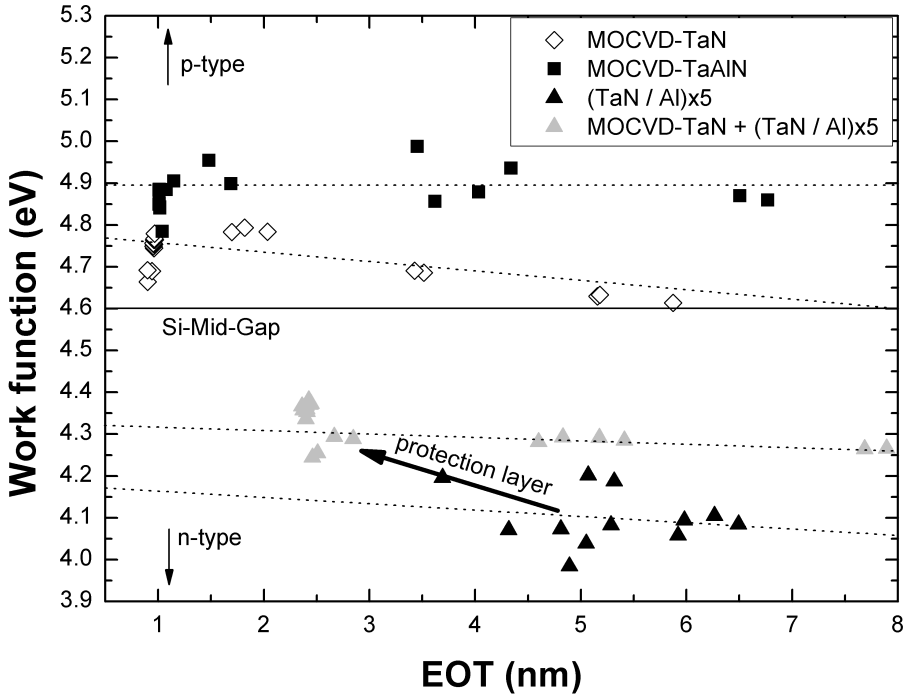

FIGURE 6.21: *Evolution of the work function vs EOT depending on the doping and the deposition technique*

As mentioned earlier, EOT variation cannot be correlated to the metal deposition between different processes, due to the incomplete removal of the oxide. Thus, the evolution of the EOT depending on the processes will be commented only for the (TaN + Al)x5 without and with a 1 nm TaN-MOCVD protection layer.

Comparing (TaN / Al)x5 and TaN + (TaN / Al)x5 clearly shows that protecting the dielectric from the plasma allows to reduce the degradation of the EOT. This degradation is characterised by the EOT regrowth and a dispersion of the measured values. In this case, a 1 nm layer of MOCVD-TaN appears to be enough to protect the dielectric from the plasma active species. However, the introduction of this layer between the dielectric and the (TaN / Al)x5 also reduces the n-type behaviour of the metal stack, from an average work function of 4.1 eV to 4.3 eV. This modification is in agreement with the p-type behaviour of the MOCVD-TaN used for protection of the dielectric, located at 5.0 eV.
Presence of Al not bonded to nitrogen, both in PVD and supposedly in MOCVD metals, allows to reach a n-type work function, i.e. PVD-TaAl and (TaN / Al)x5 materials are located below Si mid-gap line. The low work function of (TaN / Al)x5 tends to confirm the presence of Al metal-metal bonded in the layer.

Finally, the presence of Al in MOCVD-TaAlN appears to have a limited impact on the work function of the transistor, indeed only a -0.1 eV shift of the work function is observed from MOCVD-TaN to MOCVD-TaAlN. Similar behaviour was previously observed for low level of Al doping in PVD-Ta and PVD-TaN, which had the same work function as non doped PVD-Ta and PVD-TaN.

6.5.5 Conclusion and perspectives

Using the AltaCVD deposition chamber, successful doping of MOCVD-TaN was achieved by mean of layers superposition. Some interactions are observed between TaN and Al layers and suggest that the doping is efficient; more than a bi-metal layer is obtained. However, the experiments and results presented in this chapter do not allow to fully comprehend the deposition or interaction mechanisms taking place when doping (PE)MOCVD-TaN metals with aluminium.

Some of the difficulties encountered during the development of the layers are not reported here, for example when a thick (about 2 nm) layer of PEMOCVD-AlC is deposited on the substrate, the growth of MOCVD-TaN on it is not possible. It is possible that the nucleation sites present at the surface of PEMOCVD-AlC are not compatible with the growth of a MOCVD-TaN layer. More time and experiments would be necessary to fully understand and master the doping of Ta with Al in the MOCVD technique.

MOCVD is a chemically driven deposition, thus limited by the chemistry of the reactants. If one of the precursor has a higher affinity than the other with the reactant gas, then the

deposited material will be mainly made of this compound (i.e. precursor + reactant).
One notices that one property of the precursors can favour the deposition of Al in MOCVD-TaAlN, it is the vapour pressure. Vapour pressure of TMA is 9 Torr at 20°C and about 2 Torr at 0°C, whereas for TBTDET it is 1 Torr at 120°C and about 2 Torr at 140°C. In the process conditions used for the MOCVD deposition of TaAlN, 40°C and 2 Torr, the TMA is easily vaporised contrary to TBTDET. This difference might lead to earlier decomposition/activation of TMA than TBTDET precursor, resulting in more Al deposited than Ta.
Other aluminium precursors might be more suitable for LIMOCVD technique in the process conditions used on the AltaCVD tool, Tris(diethylamino)Aluminium (TDEAA) for example as a vapour pressure of 0.2 Torr at 100°C, which is similar to TBTDET precursor. However, the choice of TMA precursor was determined by: first the absence of Al-N bonds in the molecule to avoid the deposition of an AlN insulating material, which is not the case of TDEAA, second point was the availability of the precursor.

To adapt the AltaCVD system to the chosen precursors, a separation of the precursor injection lines and the absence of the evaporation furnace would be necessary and would allow a better control of the injected quantities. Also, heating of each line could be adapted to the characteristics of the precursors.

Nonetheless, the doping of MOCVD-TaN by layers superposition, presented in this section appears to be repeatable and uniform on 300 mm wafers. The repeatability of the process and the chemical modifications described, make the development of these layers promising.
Interest of MOCVD technique is also supported by the fact that, using the same deposition chamber, it is possible from MOCVD-TaN p-type metal with a work function of 4.75 eV to obtain n-type layers with a work function lower than 4.4 eV with the addition of PEMOCVD-AlC. The gap between these p-type and n-type work function match with the requirements made in the ITRS road map to address the sub-20 nm technology nodes [30].

6.6 Conclusion to the Chapter 6

An in depth investigation of PVD-Ta and PVD-TaN doping allowed to comprehend some of the phenomena taking place when increasing amount of Al is added to the Ta and TaN metals. The different oxidation of Ta and TaN highlighted the influence of the aluminium on oxygen diffusion in the layer and on its solubility in the volume of the material. Addition of aluminium clearly resulted in the formation of a passivation layer at the surface of the layer in PVD-Ta case, whereas, in PVD-TaN case aluminium addition led to the passivation in the volume with a reduction of the oxygen content but did not create an efficient barrier against oxygen diffusion.
Electrical characterisation of PVD-Ta, with varying level of Al doping, revealed that a significant level of Al ($\geq 50\%$) is required to obtain a shift, towards the n-type, of the work function. This shift is correlated to the intrinsic work function of Al (4.08 eV).

Before a doping of the MOCVD-TaN layer, deposition of MOCVD-AlN and PEMOCVD-AlC was investigated. Deposition of AlN from TMA precursor and NH_3 reactant gas appears to have a twice higher activation energy than what was calculated for MOCVD-TaN. This result suggests that TaN formation is more favourable than AlN, in the chosen process conditions. Then, to reduce the amount of N in the layer and limit the formation of insulating AlN, PEMOCVD with H_2 plasma is used. The deposited material appears to be an AlC, with low content of nitrogen and low level of oxidation, compared to MOCVD-AlN.
Using the previously developped layers two doping of TaN metals are compared. First, MOCVD-TaAlN is deposited by introduction of both TBTDET and TMA precursors in the chamber, leading to the deposition of a material similar to PVD-TaAlN. Secondly, Al-type doping in achieved by the multistacking of MOCVD-TaN and PEMOCVD-AlC monolayers. The characteristics of this multistacking are close to PVD-TaAl material. XPS analysis of these two doping was facilitate by the knowledge acquired with PVD layers and some of the interactions between Ta and Al were explained.
Finally, the electrical characteristics of MOCVD-TaAlN and MOCVD-TaN/PEMOCVD-AlC multistack are in-line with the observations made for PVD-TaAl. Indeed, MOCVD-TaAlN, with 20% Al presents a work function which is only slightly shifted towards p-mos, due to the significant presence of AlN in the layer. Whereas MOCVD-TaN/PEMOCVD-AlC multistack is shifted towards a n-type work function, thanks to the “free” aluminium present in the layer.

Chapter 7

Conclusions

"Any sufficiently advanced technology is indistinguishable from magic."
Arthur C. Clarke, author and inventor

7.1 Summary of the context

After more than 40 years of aggressive downsizing of MOSFETs, geometric scaling is reaching fundamental limits. New materials and novel processes are necessary in order to extend device scaling to the last CMOS technology node of the International Technology Roadmap for Semiconductors (ITRS). Traditional gate stacks based on SiO_xN_y/poly-Si were replaced by high-κ/metal gate at the 45 nm logic technology (as gate leakage became too high to manage). For sub-20 nm CMOS generations, one of the most pressing challenge is to obtain good conformity of the deposited layers on the features of the devices. For example trenches deep by 10 nm and wide by 20 nm have to be filled by the high-κ/metal stack in the Gate-Last approach. Chemically deposited materials are necessary to achieve the requirements of the advanced nodes.
Historically, thinning down the gate dielectric and increasing channel doping have been widely implemented to support the gate length shrink. However, the gate dielectric scaling has slowed down, and even with the adoption of high-κ/metal-gate it will be difficult to scale the EOT far below 1 nm. Moreover, integration of the materials has gained in interest since the amount of material at interface/surface became significant compared to the volume of the layers. Thanks to the characterisation tools available a fine analysis of the physico-chemical phenomena down to the atomic level is now at reach. Understanding of the correlations between the deposition process parameters and properties modifications of the stacks or devices are a necessity to successfully develop new materials.

So the replacement of PVD TiN gate metal for new technology nodes became a necessity with the ever more demanding conformity constraint. Furthermore, PVD impact on the substrate, resulting in a degradation of the leakage current, confirms the advantages of chemical-based deposition methods and their "softness" toward the underlayer. Titanium and tantalum nitrides metals high affinity with oxygen allows to reach the low EOT (below 1 nm) required in the 22 nm and lower nodes, when paired with HfO_2 high-κ dielectric.

7.2 Contributions

This work provides an outlook of the aforementioned issues. After the confirmation of MOCVD conformity on small size feature a detailed review of the MOCVD influential parameters is given in Chapter 3. Calculation of the deposition reaction energy activation depending on the reactant gas clearly highlights the importance of the NH_3 in the deposition mechanism. The lower activation energy obtained with Liquid Injected MOCVD, compared to the classic vapour injection, is part of the benefits of the liquid injection system. However, liquid injection also has some drawbacks, first one is the buffer effect observed after each deposition, and the second one is the precursor degradation with evaporation furnace high temperature, which can be avoided by a fine tuning of the liquid injectors temperature.
Following these findings a reaction mechanism path is proposed for both TaN and TiN MOCVD deposition. Finally, the parameters not influencing the properties of the material but having an effect upon the thickness uniformity of the layers are presented.

Similar route is followed for the PEMOCVD deposition in the Chapter 4. Succeeding the confirmation of good conformity when using PEMOCVD method, the influential parameters of the plasma enhanced deposition are discussed. Unlike MOCVD process, it is shown that decomposition of the precursor and activation of the deposition reaction is not happening at the sample surface but in the volume of the plasma. Consequently, the role of the substrate heating is only to ease the exhaust of reaction by-products, no effect is observed on the efficiency of the deposition.
A complete investigation on the plasma frequency revealed that the precursor decomposition is affected by the addition of low frequency power to a radio frequency plasma. Low frequency plasma power increase achieves an higher increase of density, growth rate and decrease of resistivity compared to a radio frequency plasma power increase.
Then, impact of H_2 plasma used for densification of the Ta(C)N layer is investigated. Density, resistivity, crystallography and chemical environments modifications of Ta(C)N indicate a change from TaN-like material with low plasma power toward TaC-like with high plasma power. Ta-C bonds formation in the layer is associated to a transposition reaction enhanced with the additional energy brought by the plasma reactive species.

Integration of Ta(C)N in an high-κ/metal gate scheme is developped in the Chapter 5. Interactions analysis between the metal and dielectric reveal a replacement of oxygen by nitrogen in the dielectric and opposite in the Ta(C)N layer. This exchange is enhanced when the power of the plasma, used for metal densification, is increased. Plasma power increase is also used for Ta-C bonds formation, as presented in Chapter 3, which was reported in literature to increase the work function. Addition of nitrogen in the HfO_2 layer and creation of HfON appear to be an advantage with EOT and leakage current decrease. Yet, oxygen removal from HfO_2 results in the creation of a TaO_x layer at the interface, which is a dielectric and thus increases the EOT. Another effect of the oxygen removal is the leakage current degradation and scattering of the measured values.
In a second part the affinity of Ta(C)N with oxygen is used for oxygen removal from TiN

layer and improvement of the electrical characteristics of the HfO_2/TiN stack. TiN is also inserted between TaCN and HfO_2 to limit the plasma damages observed earlier. With the help of quasi in-situ XPS analysis a separation of (PE)ALD steps is achieved to understand the influence of each feature from the deposition process. Surprisingly neither heating nor NH_3 reactant gas modified the chemical state of the TiN layer. Only H_2 plasma led to some oxygen removal from TiN, but not as much as what is observed after TaCN deposition. Thus, TBTDET precursor and/or TaN material interact with the TiN material to reduce the oxygen and increase the nitrogen levels. Addition of TaCN on the HfO_2/TiN high-κ/metal stack allows to reduce the EOT and TiN addition between HfO_2 and TaCN limits the plasma impact observed at plasma power increase.

Finally, benefits of new tantalum alloys are investigated in Chapter 6. A presentation of the Ta(Al)N PVD metals is given and the behaviour of the metal is discussed in link with the progressive addition of aluminium in the alloy. A clear oxidation of the Al present in the layer is shown and acts as a barrier to limit Ta oxidation. Meanwhile, AlN formation, an insulator not desired for metal-gate application, is revealed by the fast increase of the resistivity and by XPS spectra of the samples.
Then, TaN MOCVD doping with Al is investigated. However, due to the chemically driven reaction it is not possible to finely control the amount of Al in the layer. The limits of the LIMOCVD system used are given and possible improvements proposed to achieve doping of the TaN metal.
Therefore, based on the developments of TaN materials from Chapters 3 and 6 two ways to include Al to TaN material are proposed, including MOCVD-TaAlN and multistacking of MOCVD-TaN and PEMOCVD-AlC. Advantages and drawbacks of each way are developped with the support of the results from physico-chemical characterisations.
Comparison of electrical results from PVD-Ta and MOCVD-TaN metals doped with Al are examined in parallel and the differences interpreted with the support of the previously presented physico-chemical characterisations. As expected Al doping, with low levels of AlN, allows a shift of the work function towards n-mos properties.

To summarise, figure 7.1 illustrates the excellent conformity of both MOCVD and PE-MOCVD deposition techniques. The stack deposited on the Si box is made of PEMOCVD-AlC/MOCVD-TaN/ALD-HfO_2/SiO_2.

7.3 Recommendations for future research

As for every scientific study at the term of this work few answers and solutions were given, but even more questions and problems arose.
Some of the gaps found in the literature are now partially filled, i.e. few answers are given concerning the role of plasma on deposition and densification of the metalorganic materials, but the late arrival of aluminium for doping of MOCVD materials did not allow a thorough comprehension of the doping reaction mechanism and interactions.

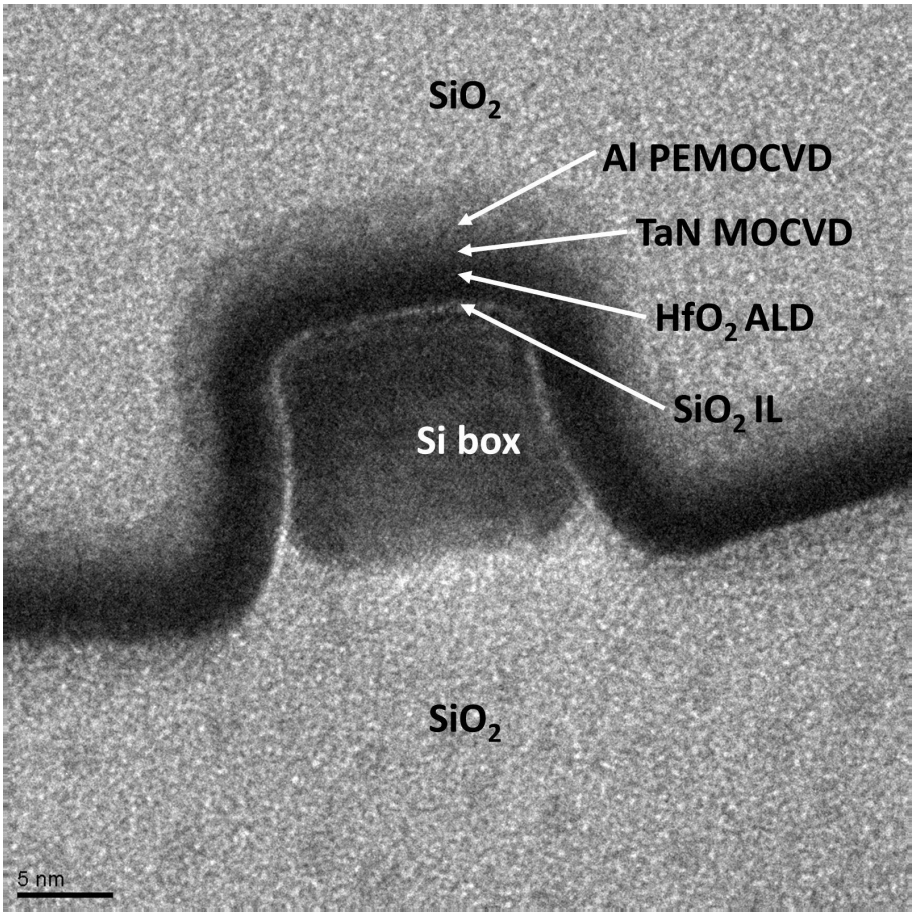

FIGURE 7.1: *Tri-gate architecture with an Al/TaN/HfO_2/SiO_2/Si stack for n-type transistor*

Some hints, concerning the behaviour of Al dopant in the TaN layer, are given by a comparison of PVD and CVD chemical bonding. A further investigation of the CVD doping would allow to complete the actual hypotheses and confirm the supposed mechanism of Ta and Al separation with the formation of Al_2O_3 at the layer extreme surface. Moreover, it was supposed that a competition exists between Al and Ta giving advantage to Al and resulting in the formation of layers mainly composed of Al. Yet, due to the Ta-Al separation and Al_2O_3 formation this competition was revealed only late in the study and the reaction mechanism was not understood.

Another important concern that was not wholly addressed was the impossibility to do the deposition of MOCVD-TaN on PEMOCVD-AlC, as revealed Chapter 6. Whereas deposition of MOCVD-TaN is possible on MOCVD-AlN and superposition of thin MOCVD-TaN and PEMOCVD-AlC layers, almost monolayers, was also possible, MOCVD-TaN did not grow on a few nanometres thick PEMOCVD-AlC. One hypothesis would need further investigation to be confirmed or refuted: it concerns the nucleation of TaN on PEMOCVD-AlC surface, if no nucleation sites are available for TaN to attach on the surface no growth of MOCVD-TaN can be achieved. It is also possible that the nucleation sites are neutralised by NH_3 reactant gas with the thermodynamically favourable formation of AlN.

Finally, the surface oxidation of the metals is another topic which has to be taken into account and needs further investigation. Indeed, surface oxidation of the metals has a growing influence on the behaviour of the devices, as a full fabrication line cannot be under vacuum, it is important to understand the vacuum break oxidation process. In this work more data would be necessary to propose a complete path for the oxidation of metals at vacuum break. For instance, to fully understand the phenomena taking place after deposition, an investigation on the effect of the sample vacuum break temperature on oxidation levels would be necessary.

Appendix A

Comparison of Gate-First and Gate-Last flows

Gate oxide thickness scaling was reaching its limits at the 40 nm node, with leakage issues and no design to work it around and bring the leakages down to acceptable levels. Already for the 28 nm node there was the need for good control over the short channel, which requires a thinner electrical gate dielectric, thus increasing the leakages. Only solution was the introduction of High-κ dielectrics/metal gate (or HKMG).
HKMG can be achieved with two main approaches: Gate-First or Gate-Last implementation. While it is well known that Intel employed the Gate Last HKMG approached for their 45 nm CPU technology, Globalfoundries concluded that this was not the most optimum approach until the 28 nm node.

Gate-Last, or Replacement Metal Gate (RMG), flow is a key factor in scaling circuit integration to sub-20nm manufacturing process technology nodes. A comparison of the Gate-First and Gate-Last integration flows for metal/high-κ deposition is presented with the next two figures.

In the gate-first flow, figure A.1, the dual-metal processing is completed prior to the polysilicon gate deposition. The metal-gates are then subtractively etched along with the poly gates prior to source/drain formation.

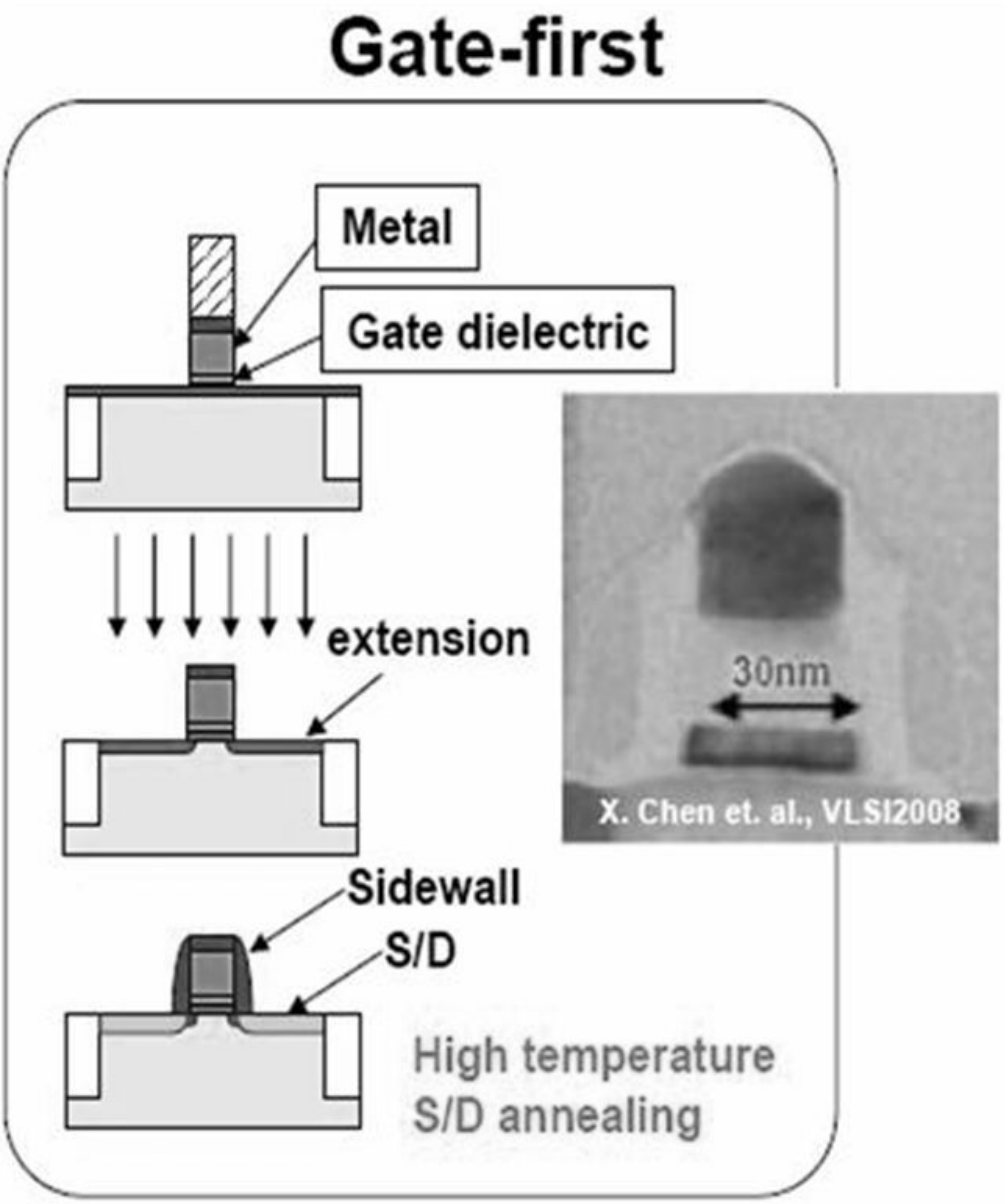

FIGURE A.1: *Metal/dielectric flow for Gate-First production*

In contrast, for the gate-last flow, a standard polysilicon gate is deposited after the high-k gate dielectric deposition, which is followed by standard polysilicon processing through the salicide and the 1st ILD deposition. The wafer is then planarized and the dummy poly gate removed. The dual-metal gates are then deposited along with a low-resistance gate fill material. The excess metal is then polished off and followed by contact processing, figure A.2.

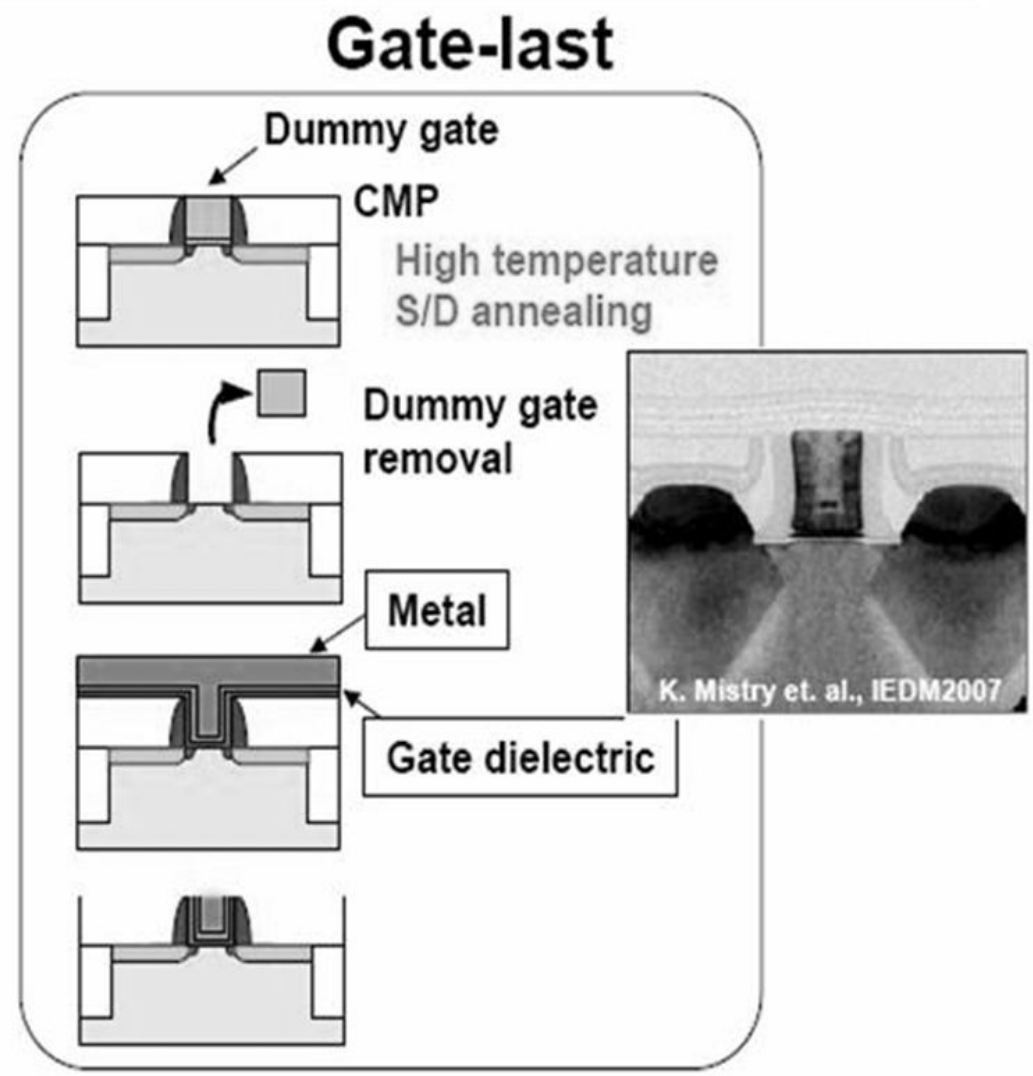

FIGURE A.2: *Metal/dielectric flow for Gate-Last production*

Appendix B

List of metals successfully deposited by CVD and ALD

Elements thermally deposited by CVD or ALD and resulting in conductive material are presented figure B.1, only reports in peer-reviewed literature are included. Metals that have been deposited by CVD or ALD are enclosed by solid black boxes. Metals (or alloys) that have been deposited only by pulsed-CVD are enclosed by dashed black boxes. Atomic numbers are shown above the atom symbols and Pauling electronegativities are shown below. Non-metals (including semi-metals) and elements without significant natural abundance are shown in white. The remaining elements are shaded.

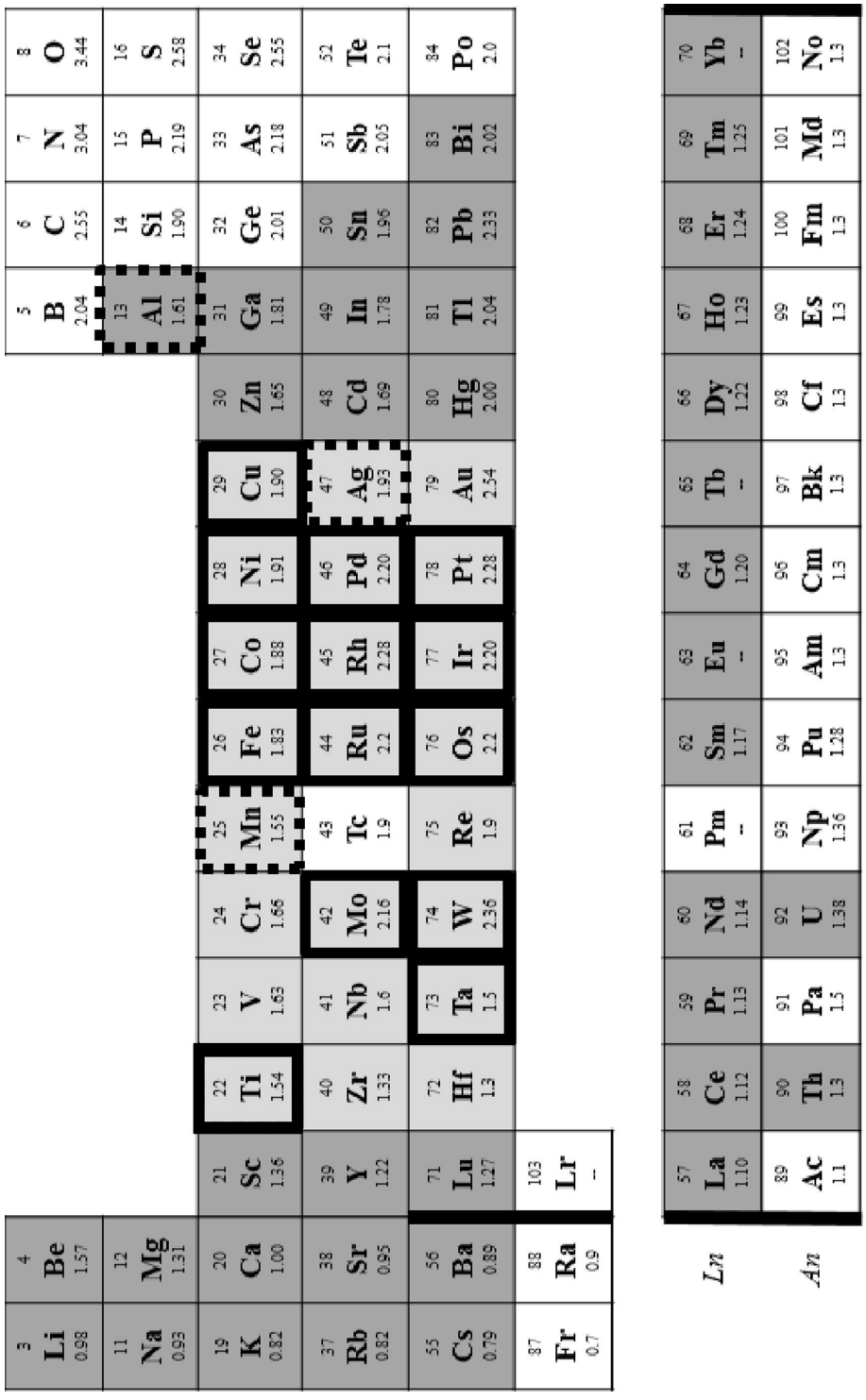

FIGURE B.1: *Thermally CVD or ALD deposited elements. Metals that have been deposited by CVD or ALD are enclosed by solid black boxes, metals (or alloys) that have been deposited only by pulsed-CVD are enclosed by dashed black boxes*

Appendix C

Principle of X-Ray generation

X-ray photons are produced by an electron beam that is accelerated to a very high speed and strikes a target. The electrons that make up the beam are emitted from a heated cathode filament. The electrons are then focused and accelerated by an electrical field towards an angled anode target. The point where the electron beam strikes the target is called the focal spot. Most of the kinetic energy contained in the electron beam is converted to heat, but around 1% of the energy is converted into X-ray photons, the excess heat is dissipated via a heat sink.
At the focal spot, X-ray photons are emitted in all directions from the target surface, the highest intensity being around 60° to 90° from the beam due to the angle of the anode target to the approaching electron beam. There is a small round window in the X-ray tube directly above the angled target. This window allows the X-ray to exit the tube with little attenuation while maintaining a vacuum seal required for the X-ray tube operation.

As presented in figure C.1, X-ray tube work by applying controlled voltage and current to a tungsten target, which results in a beam of X-rays.

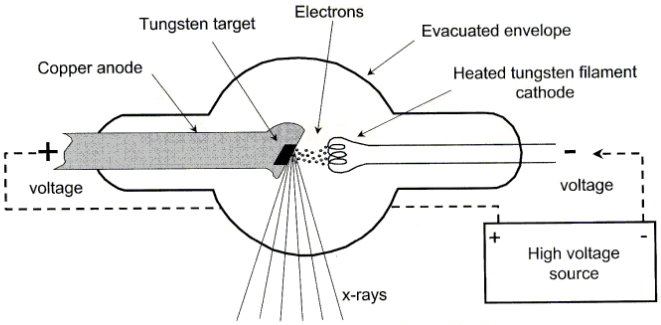

FIGURE C.1: *X-Ray generation principle*

Once created, the X-ray beam is projected on matter. Some of the X-ray beam will pass through the object, while some is absorbed. The resulting pattern of the radiation is then ultimately detected by a detection medium including rare earth screens (which surround photographic film), semiconductor detectors, or X-ray image intensifiers.

In the case of XPS, the photoelectrons emitted by the sample are going through several appliance before reaching the sensor, as presented in figure C.2.

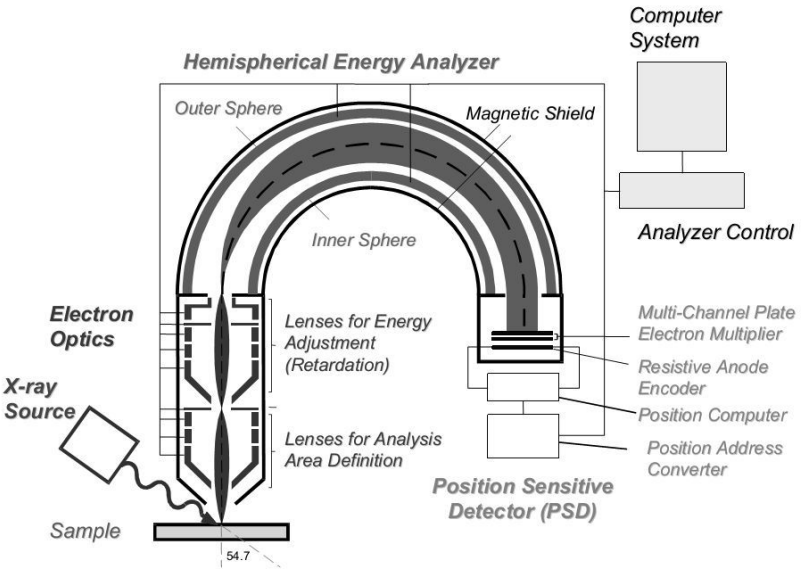

FIGURE C.2: *XPS principle schema*

Bibliography

[1] Jack Kilby. "for his part in the invention of the integrated circuit". *Nobel Prize Official Web Site*, 2000.

[2] G.E. Moore. Cramming More Components Onto Integrated Circuits. *Proceedings of the IEEE*, 86(1):82–85, 1998. ISSN 0018-9219.

[3] Cornelis Disco. *Getting new technologies together: studies in making sociotechnical order*. De Gruyter, 1998.

[4] W. Brattain J. Bardeen and W. Schockley. "for their researches on semiconductors and their discovery of the transistor effect". *Nobel Prize Official Web Site*, 1956.

[5] Paolo Spirito, Giovanni Vito Persiano, and Antonio G.M. Strollo. The bipolar mode FET: a new power device combining FET with BJT operation. *Microelectronics Journal*, 24(1):61 – 74, 1993.

[6] J Lohstroh. Devices and circuits for bipolar VLSI. *Microprocessing and Microprogramming*, 10 (2):101 – 117, 1982.

[7] J.J. Liou and F. Schwierz. RF/microwave transistors: evolution, current status, and future trend. In *Electron Devices Meeting, 2002. Proceedings. 2002 IEEE Hong Kong*, pages 5–10, 2002.

[8] G. Lucovsky, S. S. Kim, D. V. Tsu, G. G. Fountain, and R. J. Markunas. The effects of subcutaneous oxidation at the interfaces between elemental and compound semiconductors and SiO_2 thin films deposited by remote plasma enhanced chemical vapor deposition. *Journal of Vacuum Science and Technology B*, 7(4):861–869, 1989.

[9] S. S. Kim, D. J. Stephens, G. Lucovsky, G. G. Fountain, and R. J. Markunas. Substrate temperature dependence of subcutaneous oxidation at Si/SiO_2 interfaces formed by remote plasma-enhanced chemical vapor deposition. *Journal of Vacuum Science and Technology A*, 8 (3):2039–2045, 1990.

[10] T. Yasuda, Y. Ma, S. Habermehl, and G. Lucovsky. Low-temperature preparation of $SiO_2/Si(100)$ interfaces using a two-step remote plasma-assisted oxidation-deposition process. *Applied Physics Letters*, 60(4):434–436, 1992.

[11] M. Wittmer, B. Studer, and H. Melchior. Electrical characteristics of TiN contacts to N silicon. *Journal of Applied Physics*, 52(9):5722–5726, 1981.

[12] F. Fillot, T. Morel, S. Minoret, I. Matko, S. Maitrejean, B. Guillaumot, B. Chenevier, and T. Billon. Investigations of titanium nitride as metal gate material, elaborated by metal organic atomic layer deposition using TDMAT and NH_3. *Microelectronic Engineering*, 82(3):248–253, 2005.

[13] S. Kesapragada, Rongjun Wang, D. Liu, Guojun Liu, Zhigang Xie, Zhenbin Ge, Haichun Yang, Yu Lei, Xinliang Lu, Xianmin Tang, Jianxin Lei, M. Allen, S. Gandikota, K. Moraes, S. Hung, N. Yoshida, and Chorng-Ping Chang. High-k/metal gate stacks in gate first and replacement gate schemes. In *Advanced Semiconductor Manufacturing Conference (ASMC), 2010 IEEE/SEMI*, pages 256–259, 2010.

[14] H. Zhu and R. Ramprasad. The stability and work function of TaC_xN_{1-x} alloy surfaces. *Journal of Applied Physics*, 109(8):–, 2011.

[15] Ning Jiang, H.J. Zhang, S.N. Bao, Y.G. Shen, and Z.F. Zhou. XPS study for reactively sputtered titanium nitride thin films deposited under different substrate bias. *Physica B: Condensed Matter*, 352(1):118–126, 2004.

[16] F. Piallat, V. Beugin, R. Gassilloud, P. Michallon, L. Dussault, B. Pelissier, P. Morin, and C. Vallee. Evaluation of plasma parameters on PEALD deposited TaCN. *Microelectronic Engineering*, 107(0):156 – 160, 2013.

[17] Pierre Caubet, Tom Blomberg, Rym Benaboud, Christophe Wyon, Elisabeth Blanquet, Jean-Pierre Gonchond, Marc Juhel, Philippe Bouvet, Mickael Gros-Jean, Jean Michailos, Claire Richard, and Blaise Iteprat. Low-Temperature Low-Resistivity PEALD TiN Using TDMAT under Hydrogen Reducing Ambient. *Journal of The Electrochemical Society*, 155(8):H625–H632, 2008.

[18] M. H. Tsai, S. C. Sun, H.T. Chiu, C. E. Tsai, and S. H. Chuang. Metalorganic chemical vapor deposition of tantalum nitride by tertbutylimidotris(diethylamido)tantalum for advanced metallization. *Applied Physics Letters*, 67(8):1128–1130, 1995.

[19] Tae Joo Park, Jeong Hwan Kim, Jae Hyuck Jang, Kwang Duk Na, Cheol Seong Hwang, Gee-Man Kim, Kang Jun Choi, and Jae Hak Jeong. Effective work function tunability and interfacial reactions with underlying HfO_2 layer of plasma-enhanced atomic layer deposited TaC_xN_y films. *Applied Physics Letters*, 92(20):202902, 2008. ISSN 00036951.

[20] J. Westlinder, G. Sjelom, and J. Olsson. Variable work function in MOS capacitors utilizing nitrogen-controlled TiN_x gate electrodes. *Microelectronic Engineering*, 75(4):389 – 396, 2004.

[21] C. Ren, B.B. Faizhal, D.S.H. Chan, M.-F. Li, Y.-C. Yeo, A.D. Trigg, N. Balasubramanian, and D.-L. Kwong. Work function tuning of metal nitride electrodes for advanced CMOS devices. *Thin Solid Films*, 504(1):174–177, 2006.

[22] F. Y. Yen, C. L. Hung, Y.T. Hou, P.F. Hsu, V.S. Chang, P.S. Lim, L.G. Yao, J. C. Jiang, H.J. Lin, C. C Chen, Y. Jin, S.M. Jang, H.J. Tao, S-C Chen, and M-S Liang. Effective Work Function Engineering of Ta_xC_y Metal Gate on Hf-Based Dielectrics. *Electron Device Letters, IEEE*, 28(3):201–203, 2007.

[23] Jaehyoung Koo, June-Woo Lee, Taehan Doh, Yangdo Kim, Young-Do Kim, and Hyeongtag Jeon. Study on the characteristics of TiAlN thin film deposited by atomic layer deposition method. *Journal of Vacuum Science and Technology A*, 19(6):2831–2834, 2001.

[24] H.C. Kim, N.D. Theodore, K.S. Gadre, J.W. Mayer, and T.L. Alford. Investigation of thermal stability, phase formation, electrical, and microstructural properties of sputter-deposited titanium aluminide thin films. *Thin Solid Films*, 460(1):17–24, 2004.

[25] Xiao-Rong Wang, Yu-Long Jiang, Qi Xie, Christophe Detavernier, Guo-Ping Ru, Xin-Ping Qu, and Bing-Zong Li. Annealing effect on the metal gate effective work function modulation for the $Al/TiN/SiO_2/p\text{-}Si$ structure. *Microelectronic Engineering*, 88(5):573 – 577, 2011.

[26] K. Mistry, C. Allen, C. Auth, B. Beattie, D. Bergstrom, M. Bost, M. Brazier, M. Buehler, A. Cappellani, R. Chau, C.-H. Choi, G. Ding, K. Fischer, T. Ghani, R. Grover, W. Han, D. Hanken, M. Hattendorf, J. He, J. Hicks, R. Huessner, D. Ingerly, P. Jain, R. James, L. Jong, S. Joshi, C. Kenyon, K. Kuhn, K. Lee, H. Liu, J. Maiz, B. Mcintyre, P. Moon, J. Neirynck, S. Pae, C. Parker, D. Parsons, C. Prasad, L. Pipes, M. Prince, P. Ranade, T. Reynolds, J. Sandford, L. Shifren, J. Sebastian, J. Seiple, D. Simon, S. Sivakumar, P. Smith, C. Thomas, T. Troeger, P. Vandervoorn, S. Williams, and K. Zawadzki. A 45nm Logic Technology with High-k+Metal Gate Transistors, Strained Silicon, 9 Cu Interconnect Layers, 193nm Dry Patterning. In *Electron Devices Meeting, 2007. IEDM 2007. IEEE International*, pages 247–250, Dec 2007.

[27] Robert Wieland, Detlef Bonfert, Armin Klumpp, Reinhard Merkel, Lars Nebrich, Josef Weber, and Peter Ramm. 3D Integration of CMOS transistors with ICV-SLID technology. *Microelectronic Engineering*, 82(3):529 – 533, 2005.

[28] John Cartwright. Intel enters the third dimension. *Nature*, 2011.

[29] Intel. Intel to Present on 22-nm Tri-gate Technology at VLSI Symposium. In *VLSI Symposium*, 2012.

[30] ITRS 2013. International Technology Roadmap for Semiconductors 2013, December 2013.

[31] A. W. Ott S. M. George and J. W. Klaus. Surface Chemistry for Atomic Layer Growth. *The Journal of Physical Chemistry*, 100(31):13121–13131, 1996.

[32] H.-B.-R. Lee H. Kim and W.-J. Maeng. Applications of atomic layer deposition to nanofabrication and emerging nanodevices. *Thin Solid Films*, 517(8):2563 – 2580, 2009.

[33] H. Kim. Atomic layer deposition of metal and nitride thin films: Current research efforts and applications for semiconductor device processing. *Journal of Vacuum Science and Technology B: Microelectronics and Nanometer Structures*, 21(6):2231–2261, 2003.

[34] K. Nielsch M. Knez and L. Niinista. Synthesis and Surface Engineering of Complex Nanostructures by Atomic Layer Deposition. *Advanced Materials*, 19(21):3425–3438, 2007.

[35] M. Leskela and M. Ritala. Atomic Layer Deposition Chemistry: Recent Developments and Future Challenges. *Angewandte Chemie International Edition*, 42(45):5548–5554, 2003.

[36] L. Niinist, J. Nieminen, M.Pivsaari, J. Niinist, M. Putkonen, and M. Nieminen. Advanced electronic and optoelectronic materials by Atomic Layer Deposition: An overview with special emphasis on recent progress in processing of high-k dielectrics and other oxide materials. *physica status solidi (a)*, 201(7):1443–1452, 2004.

[37] Zaera Francisco. The surface chemistry of thin film atomic layer deposition ALD processes for electronic device manufacturing. *J. Mater. Chem.*, 18(30):3521–3526, 2008.

[38] P. Doppelt. Why is coordination chemistry stretching the limits of micro-electronics technology? *Coordination Chemistry Reviews*, 178, Part 2(0):1785 – 1809, 1998.

[39] J. E. Crowell. Chemical methods of thin film deposition: Chemical vapor deposition, atomic layer deposition, and related technologies. *Journal of Vacuum Science and Technology A: Vacuum, Surfaces, and Films*, 21(5):S88–S95, 2003.

[40] A. E. Kaloyeros and E. Eisenbraun. -. *Annu.Rev. Mater. Sci*, 30:363, 2000.

[41] L. McElwee-White. -. *Dalton Trans.*, page 5327, 2006.

[42] L. Niinisto M. Putkonen. -. *Top. Organomet. Chem.*, 9:125, 2005.

[43] J. G. Ekerdt, Y.-M. Sun, A. Szabo, G. J. Szulczewski, and J. M. White. Role of Surface Chemistry in Semiconductor Thin Film Processing. *Chemical Reviews*, 96(4):1499–1518, 1996.

[44] Mikko Ritala, Jaako Niinisto, Susan Krumdieck, Paul Chalker, H Aspinall, Martyn E Pemble, Wayne L Gladfelter, Barry Leese, Ronald A Fischer, Harish Parala, Ravi Kanjolia, Russell D Dupuis, S E Alexandrov, Stuart J C Irvine, Robert Palgrave, and Ivan P Parkin. *Chemical Vapour Deposition: Precursors, Processes and Applications.* The Royal Society of Chemistry, 2009.

[45] Russell D. Dupuis. Metalorganic chemical vapor deposition (mocvd). In Robert A. Meyers, editor, *Encyclopedia of Physical Science and Technology (Third Edition)*, pages 495 – 511. Academic Press, New York, third edition edition, 2003.

[46] H.O. Pierson. *Handbook of Chemical Vapor Deposition, 2nd Edition: Principles, Technology and Applications.* Elsevier Science, 1999.

[47] David J.H. Emslie, Preeti Chadha, and Jeffrey S. Price. Metal ALD and pulsed CVD: Fundamental reactions and links with solution chemistry. *Coordination Chemistry Reviews*, 257 (2324):3282 – 3296, 2013. Chemical Vapor Deposition and Atomic Layer Deposition: Precursor Design and Application.

[48] Timo Hatanp, Mikko Ritala, and Markku Leskel. Precursors as enablers of ALD technology: Contributions from University of Helsinki. *Coordination Chemistry Reviews*, 257(2324):3297 – 3322, 2013.

[49] Kyung In Choi, Byung Hee Kim, Sang Woo Lee, and Jong Myeong Lee. Characteristics of ALD-TaN thin films using a novel precursors for copper metallization. In *Interconnect Technology Conference, 2003. Proceedings of the IEEE 2003 International*, pages 129–131, June 2003.

[50] Zia Karim, Ghassan Barbar, Olivier Boissire, Peer Lehnen, Christoph Lohe, Tom Seidel, Christoph Adelmann, Thierry Conard, Barry O'Sullivan, Lars-Ake Ragnarsson, Tom Schram, Sven Van Elshocht, and Stefan De Gendt. AVD and MOCVD TaCN-based Films for Gate Metal Applications on High-κGate Dielectrics. *ECS Transactions*, 11(4):557–567, 2007.

[51] Ziwen Fang, Helen C. Aspinall, Rajesh Odedra, and Richard J. Potter. Atomic layer deposition of TaN and Ta_3N_5 using pentakis(dimethylamino)tantalum and either ammonia or monomethylhydrazine. *Journal of Crystal Growth*, 331(1):33 – 39, 2011.

[52] B. B. Burton, A. R. Lavoie, and S. M. George. Tantalum Nitride Atomic Layer Deposition Using (tert-Butylimido)tris(diethylamido)tantalum and Hydrazine. *Journal of The Electrochemical Society*, 155(7):D508–D516, 2008.

[53] H. Wojcik, M. Friedemann, F. Feustelt, M. Albert, S. Ohsiek, J. Metzgert, J. Voss, J. W Bartha, and C. Wenzel. A comparative study of thermal and plasma enhanced ALD Ta-N-C films on SiO_2, SiCOH and Cu substrates. In *International Interconnect Technology Conference, IEEE 2007*, pages 19–21, 2007.

[54] Kyung In Choi, Byung Hee Kim, Sang Woo Lee, and Jong Myeong Lee. Characteristics of ALD-TaN thin films using a novel precursors for copper metallization. In *Interconnect Technology Conference, 2003. Proceedings of the IEEE 2003 International*, pages 129–131, 2003.

[55] G. B. Rayner and S. M. George. Nucleation and growth of tantalum nitride atomic layer deposition on Al_2O_3 using TBTDET and hydrogen radicals. *Journal of Vacuum Science and Technology A*, 27(4):716–724, 2009.

[56] C. Jimnez, S. Gilles, C. Bernard, and R. Madar. Deposition of TiN thin films by organometallic chemical vapor deposition: thermodynamical predictions and experimental results. *Surface and Coatings Technology*, 7677, Part 1(0):237 – 243, 1995.

[57] V. Melnik, D. Wolanski, E. Bugiel, A. Goryachko, S. Chernjavski, and D. Krger. Influence of N2/H2 plasma treatment on chemical vapor deposited TiN multilayer structures for advanced CMOS technologies. *Materials Science and Engineering: B*, 102(13):358 – 361, 2003.

[58] Ki-Chul Park, Soo-Hyun Kim, and Ki-Bum Kim. Effect of Ion Bombardment during Chemical Vapor Deposition of TiN Films. *Journal of The Electrochemical Society*, 147(7):2711–2717, 2000.

[59] Ju-Youn Kim, Gil-Heyun Choi, Young Do Kim, Yangdo Kim, and Hyeongtag Jeon. Comparison of TiN Films Deposited Using Tetrakisdimethylaminotitanium and Tetrakisdiethylaminotitanium by the Atomic Layer Deposition Method. *Japanese Journal of Applied Physics*, 42(Part 1, No. 7A):4245–4248, 2003.

[60] J. Bonitz, S.E. Schulz, and T. Gessner. Ultra thin CVD TiN layers as diffusion barrier films on porous low-k materials. *Microelectronic Engineering*, 76(14):82 – 88, 2004.

[61] C. Marcadal, E. Richard, J. Torres, J. Palleau, L. Ulmer, L. Perroud, J. Piaguet, and G. Rolland. OMCVD TiN diffusion barrier for copper contact and via/interconnects structures. *Microelectronic Engineering*, 3738(0):197 – 203, 1997.

[62] Tae-Ho Cha, Dae-Gyu Park, Tae-Kyun Kim, Se-Aug Jang, In-Seok Yeo, Jae-Sung Roh, and Jin Won Park. Work function and thermal stability of $Ti_{1-x}Al_xN_y$ for dual metal gate electrodes. *Applied Physics Letters*, 81(22):4192–4194, 2002.

[63] Genji Nakamura, Toshio Hasegawa, Steven Consiglio, Fumitaka Amano, Vinh Luong, Ying Trickett, Cory S. Wajda, Robert D. Clark, Gert J. Leusink, and Kaoru Maekawa. EOT Scaling and Flatband Voltage Shift with Al Addition into TiN. *ECS Transactions*, 41(3):317–323, 2011.

[64] A.C. Dillon, A.W. Ott, J.D. Way, and S.M. George. Surface chemistry of Al_2O_3 deposition using $Al(CH_3)_3$ and H_2O in a binary reaction sequence. *Surface Science*, 322(13):230 – 242, 1995.

[65] L.G. Gosset, J.-F. Damlencourt, O. Renault, D. Rouchon, Ph. Holliger, A. Ermolieff, I. Trimaille, J.-J. Ganem, F. Martin, and M.-N. Smria. Interface and material characterization of thin Al_2O_3 layers deposited by ALD using TMA/H_2O. *Journal of Non-Crystalline Solids*, 303 (1):17 – 23, 2002.

[66] Manik Kumer Ghosh and Cheol Ho Choi. The initial mechanisms of Al_2O_3 atomic layer deposition on OH/Si(1 0 0)-2 x 1 surface by tri-methylaluminum and water. *Chemical Physics Letters*, 426(46):365 – 369, 2006.

[67] S. Sioncke, J. Ceuppens, D. Lin, L. Nyns, A. Delabie, H. Struyf, S. De Gendt, M. Mller, B. Beckhoff, and M. Caymax. Atomic layer deposition of Al_2O_3 on S-passivated Ge. *Microelectronic Engineering*, 88(7):1553 – 1556, 2011.

[68] Li Qiang Zhu, Yang Hui Liu, Hong Liang Zhang, Hui Xiao, and Li Qiang Guo. Atomic layer deposited Al_2O_3 films for anti-reflectance and surface passivation applications. *Applied Surface Science*, 288(0):430 – 434, 2014.

[69] D.M. Dobkin and M.K. Zuraw. *Principles of Chemical Vapor Deposition*. Springer, 2003.

[70] C.E. Morocanu. *Thin films by chemical vapour deposition*. Thin films science and technology. Elsevier, 1990.

[71] D.P. Adams, T.M. Mayer, E. Chason, B.K. Kellerman, and B.S. Swartzentruber. Island structure evolution during chemical vapor deposition. *Surface Science*, 371(2-3):445–454, 1997.

[72] Arrhenius Svante. -. *Z. phys. Chem.*, 31:197, 1899.

[73] C. Vallee. Introduction aux sciences plasma. In *Cours de 2ieme annee Polytech' Grenoble*, 2008.

[74] A. V. Eletskii and B. M. Smirnov. Dissociation of molecules in plasma and gas: the energy. *Pure and Applied Chemistry*, 57(9):1235, 19855.

[75] Ju Youn Kim, Gil Heyun Choi, Young Do Kim, Yangdo Kim, and Hyeongtag Jeon. Comparison of TiN Films Deposited Using Tetrakisdimethylaminotitanium and Tetrakisdiethylaminotitanium by the Atomic Layer Deposition Method. *Japanese Journal of Applied Physics*, 42(Part 1, No. 7A):4245–4248, 2003.

[76] Ernst Granneman, Pamela Fischer, Dieter Pierreux, Herbert Terhorst, and Peter Zagwijn. Batch ALD: Characteristics, comparison with single wafer ALD, and examples. *Surface and Coatings Technology*, 201(2223):8899 – 8907, 2007.

[77] D.M. Mattox. *Handbook of Physical Vapor Deposition (PVD) Processing*. Elsevier Science, 2010.

[78] Ingemar Olefjord and Anders Nylund. Surface analysis of oxidized aluminium. 2. oxidation of aluminium in dry and humid atmosphere studied by esca, sem, sam and edx. *Surface and Interface Analysis*, 21(5):290–297, 1994.

[79] National Institute of Standards and Technology. NIST XRD. *Database*, 2012.

[80] D. Briggs and M. P. Seah. Practical surface analysis by Auger and X-Ray photoelectron spectroscopy. *John Wiley and Sons*, 1983.

[81] J.F. Moulder and J. Chastain. *Handbook of X-Ray Photoelectron Spectroscopy: A Reference Book of Standard Spectra for Identification and Interpretation of XPS Data*. Perkin-Elmer Corporatioon, Physical Electronics Division, 1992.

[82] T. M. Duc. Analyse de surface par ESCA. Analyse élémentaire et applications. *Technique de l'Ingénieur. Analyse et caractérisation*, 2626, 1998.

[83] T. M. Duc. Analyse de surface par ESCA. Principe et instrumentation. *Technique de l'Ingénieur. Analyse et caractérisation*, 2625, 1998.

[84] A Jablonski and C.J Powell. Relationships between electron inelastic mean free paths, effective attenuation lengths, and mean escape depths. *Journal of Electron Spectroscopy and Related Phenomena*, 100(13):137 – 160, 1999.

[85] Dominik Jaeger and Jrg Patscheider. A complete and self-consistent evaluation of XPS spectra of TiN. *Journal of Electron Spectroscopy and Related Phenomena*, 185(11):523 – 534, 2012.

[86] National Institute of Standards and Technology. NIST XPS. *Database*, 2012.

[87] C.-S. Shin, Y.-W. Kim, D. Gall, J.E. Greene, and I. Petrov. Phase composition and microstructure of polycrystalline and epitaxial TaN_x layers grown on oxidized Si(001) and MgO(001) by reactive magnetron sputter deposition. *Thin Solid Films*, 402(12):172 – 182, 2002.

[88] Mikko Ritala, Pia Kalsi, Diana Riihel, Kaupo Kukli, Markku Leskel, and Janne Jokinen. Controlled Growth of TaN, Ta_3N_5, and TaO_xN_y Thin Films by Atomic Layer Deposition. *Chemistry of Materials*, 11(7):1712–1718, 1999.

[89] Tae Joo Park, Jeong Hwan Kim, Jae Hyuck Jang, Kwang Duk Na, Cheol Seong Hwang, Jong Hoon Kim, Gee-Man Kim, Jae Ho Choi, Kang Joon Choi, and Jae Hak Jeong. Improved electrical performances of plasma-enhanced atomic layer deposited TaC_xN_y films by adopting Ar/H_2 plasma. *Applied Physics Letters*, 91(25), 2007.

[90] O. van der Straten, X. Zhang, C. Penny, J. Maniscalco, S. Chiang, J. Ren, and P. Ma. Impact of Direct Plasma Densification on Resistivity and Conformality of PEALD Tantalum Nitride. *ECS Transactions*, 50(13):159–164, 2013.

[91] H. C. M. Knoops, E. Langereis, M. C. M. van de Sanden, and W. M. M. Kessels. Reaction mechanisms of atomic layer deposition of TaN_x from $Ta(NMe_2)_5$ precursor and H_2-based plasmas. *Journal of Vacuum Science and Technology A*, 30(1), 2012.

[92] H. L. Skriver and N. M. Rosengaard. Surface energy and work function of elemental metals. *Phys. Rev. B*, 46(11):7157–7168, Sep 1992.

[93] B. Pelissier, H. Kambara, E. Godot, E. Veran, V. Loup, and O. Joubert. XPS analysis with an ultra clean vacuum substrate carrier for oxidation and airborne molecular contamination prevention. *Microelectronic Engineering*, 85(1):151 – 155, 2008.

[94] Sung-Lae Cho, Ki-Bum Kim, Seok-Hong Min, Hyun-Kook Shin, and Sam-Dong Kimd. Diffusion Barrier Properties of Metallorganic Chemical Vapor Deposited Tantalum Nitride Films Against Cu Metallization. *Journal of The Electrochemical Society*, 146(10):3724–3730, 1999.

[95] G.-C. Jun, S.-L. Cho, K.-B. Kim, H.-K. Shin, and D.-H. Kim. Low temperature deposition of TaCN films using pentakis(diethylamido)tantalum. *Japanese Journal of Applied Physics, Part 2: Letters*, 37(1 PART A/B):L30–L32, 1998.

[96] Soo-Hyun Kim, Se-Joon Im, and Ki-Bum Kim. The effect of ion beam bombardment on the properties of Ta(C)N films deposited from pentakis-diethylamido-tantalum. *Thin Solid Films*, 415(1):177 – 186, 2002.

[97] Y. K. Chae, Y. Shimogaki, and H. Komiyama. The Role of Gas-Phase Reactions during Chemical Vapor Deposition of Copper from (hfac)Cu(tmvs). *Journal of The Electrochemical Society*, 145(12):4226–4233, 1998.

[98] Mermet, J.-L., Mouche, M.-J., Pires, F., Richard, E., Torres, J., Palleau, J., and Braud, F. CVD Copper Deposition from CuI(HFAC)TMVS Studied Through a Modeling Experimental Design. *J. Phys. IV France*, 05(C5):C5–517–C5–523, 1995.

[99] D.P. Brady, F.N. Fuss, and D. Gerstenberg. Thermal oxidation and resistivity of tantalum nitride films. *Thin Solid Films*, 66(3):287 – 302, 1980.

[100] MatWeb. Material Property Data @ONLINE. *http://www.matweb.com/*, 2012.

[101] Alain E. Kaloyeros, Xiaomeng Chen, Tanja Stark, Kaushik Kumar, Soon-Cheon Seo, Gregory G. Peterson, Harry L. Frisch, Barry Arkles, and John Sullivan. Tantalum Nitride Films Grown by Inorganic Low Temperature Thermal Chemical Vapor Deposition Diffusion Barrier Properties in Copper Metallization. *Journal of The Electrochemical Society*, 146(1):170–176, 1999.

[102] A. Correia Anacleto, A. Zauner, D. Cany-Canian, J. Gatineau, and M.-C. Hugon. Atomic layer deposition of tantalum nitride based thin films from cyclopentadienyl type precursor. *Thin Solid Films*, 519(1):367 – 372, 2010.

[103] T. Elangovan, S. Murugeshan, D. Mangalaraj, P. Kuppusami, Shabhana Khan, C. Sudha, V. Ganesan, R. Divakar, and E. Mohandas. Synthesis and high temperature XRD studies of tantalum nitride thin films prepared by reactive pulsed dc magnetron sputtering. *Journal of Alloys and Compounds*, 509(22):6400 – 6407, 2011.

[104] F. Ferrieu, K. Dabertrand, S. Lhostis, V. Ivanova, E. Martinez, C. Licitra, and G. Rolland. Observation of HfO_2 thin films by deep UV spectroscopic ellipsometry. *Journal of Non-Crystalline Solids*, 353(57):658 – 662, 2007.

[105] Jia-Hong Huang, Kae-Jy Yu, P. Sit, and Ge-Ping Yu. Heat treatment of nanocrystalline TiN films deposited by unbalanced magnetron sputtering. *Surface and Coatings Technology*, 200 (1415):4291 – 4299, 2006.

[106] L.T. Zhuravlev. The surface chemistry of amorphous silica. zhuravlev model. *Colloids and Surfaces A: Physicochemical and Engineering Aspects*, 173(13):1 – 38, 2000.

[107] P. Patsalas, C. Charitidis, and S. Logothetidis. The effect of substrate temperature and biasing on the mechanical properties and structure of sputtered titanium nitride thin films. *Surface and Coatings Technology*, 125(1):335 – 340, 2000.

[108] M. Bosund, A. Aierken, J. Tiilikainen, T. Hakkarainen, and H. Lipsanen. Passivation of GaAs surface by atomic-layer-deposited titanium nitride. *Applied Surface Science*, 254(17):5385 – 5389, 2008.

[109] Xingsheng Wang, G. Roy, O. Saxod, A. Bajolet, A. Juge, and A. Asenov. Simulation Study of Dominant Statistical Variability Sources in 32-nm High-$\varkappa$/Metal Gate CMOS. *Electron Device Letters, IEEE*, 33(5):643–645, May 2012.

[110] A. Bieder, A. Gruniger, and Rudolf von Rohr. Deposition of SiO_x diffusion barriers on flexible packaging materials by PECVD. *Surface and Coatings Technology*, 200(14):928 – 931, 2005.

[111] H. Surr, Ch. Gehr, H. Holzschuh, F. Schmaderer, G. Wahl, Th. Kruck, and A. Kinnen. Thermal and plasma enhanced CVD OF HTc-superconductors. *Physica C: Superconductivity*, 153155, Part 2(0):784 – 785, 1988.

[112] Chang jun Liu, Gheorghi P. Vissokov, and Ben W.-L. Jang. Catalyst preparation using plasma technologies. *Catalysis Today*, 72(34):173 – 184, 2002.

[113] J.R. Roth. *Industrial Plasma Engineering: Volume 2 - Applications to Nonthermal Plasma Processing*. Industrial Plasma Engineering. Taylor & Francis, 2001.

[114] M. Danek, M. Liao, J. Tseng, K. Littau, D. Saigal, H. Zhang, R. Mosely, and M. Eizenberg. Resistivity reduction and chemical stabilization of organometallic chemical vapor deposited titanium nitride by nitrogen RF plasma. *Applied Physics Letters*, 68(7):1015–1016, 1996.

[115] R. Smoluchowski. Anisotropy of the Electronic Work Function of Metals. *Phys. Rev.*, 60(9): 661–674, 1941.

[116] N. Mutsukura, Y. Fukasawa, Y. Machi, and T. Kubota. Diagnostics and control of radio-frequency glow discharge. *Journal of Vacuum Science and Technology A*, 12(6):3126–3130, 1994.

[117] Xiang Xu, Jie Feng, Xiang-Mei Liu, You-Nian Wang, and Jia Yan. Study of the neutral gas flow on discharges of capacitively coupled plasma in a PECVD reactor. *Vacuum*, 92:1 – 6, 2013.

[118] Hong Tak Kim, Maeng Jun Kim, and Sang Ho Sohn. Characterization of TiN thin films grown by low-frequency (60 Hz) plasma enhanced chemical vapor deposition. *Journal of Physics and Chemistry of Solids*, 73(7):931 – 935, 2012.

[119] Daniel L. Flamm. Frequency effects in plasma etching. *Journal of Vacuum Science and Technology A*, 4(3):729–738, 1986.

[120] M. Surendra and D. B. Graves. Capacitively coupled glow discharges at frequencies above 13.56 MHz. *Applied Physics Letters*, 59(17):2091–2093, 1991.

[121] Haruhiro H. Goto, Hans-Dirk Lwe, and Tadahiro Ohmi. Dual excitation reactive ion etcher for low energy plasma processing. *Journal of Vacuum Science and Technology A*, 10(5):3048–3054, 1992.

[122] Zhen hua Bi, Yong xin Liu, Wei Jiang, Xiang Xu, and You nian Wang. A brief review of dual-frequency capacitively coupled discharges. *Current Applied Physics*, 11(5, Supplement): S2 – S8, 2011.

[123] V. Georgieva and A. Bogaerts. Numerical simulation of dual frequency etching reactors: Influence of the external process parameters on the plasma characteristics. *Journal of Applied Physics*, 98(2):–, 2005.

[124] Jae Koo Lee, N.Y. Babaeva, Hyun Chul Kim, O.V. Manuilenko, and Jong Won Shon. Simulation of capacitively coupled single- and dual-frequency RF discharges. *Plasma Science, IEEE Transactions on*, 32(1):47–53, 2004.

[125] P C Boyle, A R Ellingboe, and M M Turner. Independent control of ion current and ion impact energy onto electrodes in dual frequency plasma devices. *Journal of Physics D: Applied Physics*, 37(5):697, 2004.

[126] H. C. Kim, J. K. Lee, and J. W. Shon. Analytic model for a dual frequency capacitive discharge. *Physics of Plasmas (1994-present)*, 10(11):4545–4551, 2003.

[127] M. M. Turner and P. Chabert. Collisionless Heating in Capacitive Discharges Enhanced by Dual-Frequency Excitation. *Phys. Rev. Lett.*, 96(4):205001, May 2006.

[128] J Robiche, P C Boyle, M M Turner, and A R Ellingboe. Analytical model of a dual frequency capacitive sheath. *Journal of Physics D: Applied Physics*, 36(15):1810, 2003.

[129] E. Kawamura, M. A. Lieberman, and A. J. Lichtenberg. Stochastic heating in single and dual frequency capacitive discharges. *Physics of Plasmas (1994-present)*, 13(5):–, 2006.

[130] J P Booth, G Curley, D Maric, and P Chabert. Dual-frequency capacitive radiofrequency discharges: effect of low-frequency power on electron density and ion flux. *Plasma Sources Science and Technology*, 19(1):015005, 2010.

[131] Z. Donko, J. Schulze, P. Hartmann, I. Korolov, U. Czarnetzki, and E. Schungel. The effect of secondary electrons on the separate control of ion energy and flux in dual-frequency capacitively coupled radio frequency discharges. *Applied Physics Letters*, 97(8):081501–081501–3, 2010.

[132] Ciprian Iliescu, Bangtao Chen, Daniel P. Poenar, and Yong Yeow Lee. PECVD amorphous silicon carbide membranes for cell culturing. *Sensors and Actuators B: Chemical*, 129(1):404 – 411, 2008.

[133] W.S. Tan, P.A. Houston, G. Hill, R.J. Airey, and P.J. Parbook. Electrical characteristics of AlGaN/GaN metal-insulator semiconductor heterostructure field-effect transistors on sapphire substrates. *Journal of Electronic Materials*, 32(5):350–354, 2003.

[134] C. W. Pearce, R. F. Fetcho, M. D. Gross, R. F. Koefer, and R. A. Pudliner. Characteristics of silicon nitride deposited by plasma-enhanced chemical vapor deposition using a dual frequency radio-frequency source. *Journal of Applied Physics*, 71(4):1838–1841, 1992.

[135] L. Martinu, J. E. Klemberg-Sapieha, O. M. Kttel, A. Raveh, and M. R. Wertheimer. Critical ion energy and ion flux in the growth of films by plasma-enhanced chemical-vapor deposition. *Journal of Vacuum Science and Technology A*, 12(4):1360–1364, 1994.

[136] R. Kressmann, H. Amjadi, G.M. Sessler, D. Rats, L. Martinu, J. E. Klemberg-Sapieha, and M.R. Wertheimer. Charge storage in PECVD silicon oxynitride layers. In *Electrical Insulation and Dielectric Phenomena, 1998. Annual Report. Conference on*, pages 605–608 vol. 2, 1998.

[137] Yang Lei, Xin Yu, Xu Haipeng, Yu Yiqing, and Ning Zhaoyuan. Effect of Discharge Parameters on Properties of Diamond-Like Carbon Films Prepared by Dual-Frequency Capacitively Coupled Plasma Source. *Plasma Science and Technology*, 12(1):53, 2010.

[138] Su B. Jin, Joon S. Lee, Yoon S. Choi, In S. Choi, and Jeon G. Han. High-rate deposition and mechanical properties of SiO_x film at low temperature by plasma enhanced chemical vapor deposition with the dual frequencies ultra high frequency and high frequency . *Thin Solid Films*, 519(19):6334 – 6338, 2011.

[139] M. Moisan, C. Barbeau, R. Claude, C. M. Ferreira, J. Margot, J. Paraszczak, A. B. S, G. Sauv, and M. R. Wertheimer. Radio frequency or microwave plasma reactors? Factors determining the optimum frequency of operation. *Journal of Vacuum Science and Technology B*, 9(1):8–25, 1991.

[140] S Manolache, M Sarfaty, and F Denes. RF frequency effects on molecular fragmentation. *Plasma Sources Science and Technology*, 9(1):37, 2000.

[141] Andreas Kafizas, Claire J. Carmalt, and Ivan P. Parkin. CVD and precursor chemistry of transition metal nitrides. *Coordination Chemistry Reviews*, 257(1314):2073 – 2119, 2013.

[142] T. Kitajima, Y. Takeo, N. Nakano, and T. Makabe. Effects of frequency on the two-dimensional structure of capacitively coupled plasma in Ar. *Journal of Applied Physics*, 84(11):5928–5936, 1998.

[143] V. A. Godyak and R. B. Piejak. Abnormally low electron energy and heating-mode transition in a low-pressure argon rf discharge at 13.56 MHz. *Phys. Rev. Lett.*, 65:996–999, Aug 1990.

[144] P. Chabert, N. Braithwaite, and N.S.J. Braithwaite. *Physics of Radio-Frequency Plasmas*. Physics of Radio-frequency Plasmas. Cambridge University Press, 2011.

[145] J. P. Boeuf and Ph. Belenguer. Transition from a capacitive to a resistive regime in a silane radio frequency discharge and its possible relation to powder formation. *Journal of Applied Physics*, 71(10):4751–4754, 1992.

[146] J Schulze, Z Donk, D Luggenhlscher, and U Czarnetzki. Different modes of electron heating in dual-frequency capacitively coupled radio frequency discharges. *Plasma Sources Science and Technology*, 18(3):034011, 2009.

[147] F A Haas, A Goodyear, and N St J Braithwaite. Tailoring of electron energy distributions in low temperature plasmas. *Plasma Sources Science and Technology*, 7(4):471, 1998.

[148] C Bohm and J Perrin. Spatially resolved optical emission and electrical properties of SiH_4 RF discharges at 13.56 MHz in a symmetric parallel-plate configuration. *Journal of Physics D: Applied Physics*, 24(6):865, 1991.

[149] Ph. Belenguer and J. P. Boeuf. Transition between different regimes of RF glow discharges. *Phys. Rev. A*, 41:4447–4459, Apr 1990.

[150] V.A. Godyak and A. S. Khanneh. Ion Bombardment Secondaty Electron Maintenance of Steady RF Discharge. *Plasma Science, IEEE Transactions on*, 14(2):112–123, 1986.

[151] S. K. Ahn and H.Y. Chang. Role of low-frequency power in dual-frequency capacitive discharges. *Applied Physics Letters*, 95(11):111502–111502–3, 2009.

[152] Wang You-Nian Liu Xiang-Mei, Song Yuan-Hong. Driving frequency effects on the mode transition in capacitively coupled argon discharges. *Chinese Physics B*, 20(6):65205, 2011.

[153] R.W.B. Pearse and A.G. Gaydon. *The identification of molecular spectra 4th edition*. Chapman and Hall, 1976.

[154] C. Schaffnit, L. Thomas, F. Rossi, R. Hugon, and Y. Pauleau. Plasma diagnostics of RF PACVD of boron nitride using a BCl_3-N_2-H_2-Ar gas mixture. *Surface and Coatings Technology*, 98(13): 1262 – 1266, 1998.

[155] J.L. Delcroix, C. Matos-Ferreira, and A. Ricard. *Atomes et molécules métastables dans les gaz ionisés*. Editions du Centre National de la Recherche Scientifique, 1975.

[156] Tsutomu Watanabe and Kanji Katsuura. Ionization of Atoms by Collision with Excited Atoms. ii. A Formula without the Rotating-Atom Approximation. *The Journal of Chemical Physics*, 47(2):800–811, 1967.

[157] Ewald H. Fink, Daniel Wallach, and C. Bradley Moore. Near-Resonant Electronic Energy Transfer from Argon to Hydrogen. *The Journal of Chemical Physics*, 56(7):3608–3618, 1972.

[158] K.-T. Rie and J. Whle. Plasma-CVD of TiCN and ZrCN films on light metals. *Surface and Coatings Technology*, 112(13):226 – 229, 1999.

[159] Moon-Kyun Song and Shi-woo Rhee. Phase Formation in the Tantalum Carbonitride Film Deposited with Atomic Layer Deposition Using Ammonia. *Journal of The Electrochemical Society*, 155(10):H823–H828, 2008.

[160] J.-S. Park, H.-S. Park, and S.-W. Kang. Plasma-enhanced atomic layer deposition of Ta-N thin films. *Journal of the Electrochemical Society*, 149(1):C28–C32, 2002.

[161] Shikha Somani, Atashi Mukhopadhyay, and Charles Musgrave. Atomic Layer Deposition of Tantalum Nitride Using A Novel Precursor. *The Journal of Physical Chemistry C*, 115(23): 11507–11513, 2011.

[162] P.B. Sewell, D.F. Mitchell, and M. Cohen. A kinetic study of the initial oxidation of a Ta(110) surface using oxygen ka X-ray emission. *Surface Science*, 29(1):173–188, 1972.

[163] Chang-Seok Kang, H.-J. Cho, Y.H. Kim, R. Choi, K. Onishi, A. Shahriar, and J.C. Lee. Characterization of resistivity and work function of sputtered-TaN film for gate electrode applications. *Journal of Vacuum Science Technology B: Microelectronics and Nanometer Structures*, 21(5): 2026–2028, Sep 2003.

[164] Hong Shen and Ravi Ramanathan. Fabrication of a low resistivity tantalum nitride thin film. *Microelectronic Engineering*, 83(2):206 – 212, 2006.

[165] M. A. Farooq, S. P. Murarka, C. C. Chang, and F. A. Baiocchi. Tantalum nitride as a diffusion barrier between Pd_2Si or $CoSi_2$ and aluminum. *Journal of Applied Physics*, 65(8):3017–3022, 1989.

[166] Bhola Mehrotra and Jim Stimmell. Properties of direct current magnetron reactively sputtered TaN. *Journal of Vacuum Science and Technology B*, 5(6):1736–1740, 1987.

[167] K.-E. Elers, J. Winkler, K. Weeks, and S. Marcus. $TiCl_4$ as a precursor in the TiN deposition by ALD and PEALD. *Journal of the Electrochemical Society*, 152(8):G589–G593, 2005.

[168] F. Volpi, L. Cadix, G. Berthom, E. Blanquet, N. Jourdan, and J. Torres. XPS studies of the ALD-growth of TaN diffusion barriers: Impact of the dielectric surface chemistry on the growth mechanism. *Microelectronic Engineering*, 85(10):2068–2070, 2008.

[169] Luigi Pantisano, V.V. Afanasev, S. Cimino, C. Adelmann, L. Goux, Y.Y. Chen, J.A. Kittl, D. Wouters, and M. Jurczak. Towards barrier height modulation in hfo_2/tin by oxygen scavenging dielectric defects or metal induced gap states? *Microelectronic Engineering*, 88(7):1251 – 1254, 2011.

[170] Seok-Hee Lee, Rino Choi, and Changhwan Choi. Effects of composition and thickness of TiN metal gate on the equivalent oxide thickness and flat-band voltage in metal oxide semiconductor devices. *Microelectronic Engineering*, 109(0):160 – 162, 2013.

[171] Xiongfei Yu, Chunxiang Zhu, and Mingbin Yu. Impact of nitrogen in HfON gate dielectric with metal gate on electrical characteristics, with particular attention to threshold voltage instability. *Applied Physics Letters*, 90(10):–, 2007.

[172] Chang-Seok Kang, Hag-Ju Cho, Rino Choi, Young-Hee Kim, Chang-Yong Kang, Se Jong Rhee, Changhwan Choi, M.S. Akbar, and Jack C. Lee. The electrical and material characterization of hafnium oxynitride gate dielectrics with tan-gate electrode. *Electron Devices, IEEE Transactions on*, 51(2):220–227, 2004.

[173] Ran Jiang, Erqing Xie, Zhiyong Chen, and Zhenxing Zhang. Electrical property of HfO_xN_y-HfO_2-HfO_xN_y sandwich-stack films. *Applied Surface Science*, 253(5):2421 – 2424, 2006.

[174] Tsunehiro Ino, Yuuichi Kamimuta, Masamichi Suzuki, Masato Koyama, and Akira Nishiyama. Dielectric Constant Behavior of Hf–O–N System. *Japanese Journal of Applied Physics*, 45(4B): 2908–2913, 2006.

[175] H C Shin and Chenming Hu. Thin gate oxide damage due to plasma processing. *Semiconductor Science and Technology*, 11(4):463, 1996.

[176] R. Chau, S. Datta, M. Doczy, B. Doyle, J. Kavalieros, and M. Metz. High-K/metal-gate stack and its MOSFET characteristics. *Electron Device Letters, IEEE*, 25(6):408–410, June 2004.

[177] D. H. Triyoso, M. Ramon, R. I. Hegde, D. Roan, R. Garcia, J. Baker, X.-D. Wang, P. Fejes, B. E. White, and P. J. Tobina. Physical and Electrical Characteristics of HfO_2 Gate Dielectrics Deposited by ALD and MOCVD. *Journal of The Electrochemical Society*, 152(3):G203–G209, 2005.

[178] H. N. Alshareef, M. Quevedo-Lopez, H. C. Wen, C. Huffman, M. El-Bouanani, and B. E. Gnade. Impact of Carbon Incorporation on the Effective Work Function of WN and TaN Metal Gate Electrodes. *Electrochemical and Solid-State Letters*, 11(7):H182–H184, 2008.

[179] William J. Baxter. Work Function of Tantalum Carbide and the Effects of Adsorption and Sputtering of Cesium. *Journal of Applied Physics*, 42(7):2682–2688, 1971.

[180] S. Oswald, R. Reiche, M. Zier, S. Baunack, and K. Wetzig. Depth profile and interface analysis in the nm-range. *Applied Surface Science*, 252(1):3 – 10, 2005.

[181] M. Zier, S. Oswald, R. Reiche, and K. Wetzig. XPS and ARXPS investigations of ultra thin TaN films deposited on SiO_2 and Si. *Applied Surface Science*, 252(1):234 – 239, 2005.

[182] Hyungjun Kim. Characteristics and applications of plasma enhanced-atomic layer deposition. *Thin Solid Films*, 519(20):6639 – 6644, 2011.

[183] I.-C. Chen, S. Holland, and C. Hu. Oxide breakdown dependence on thickness and hole current - enhanced reliability of ultra thin oxides. In *Electron Devices Meeting, 1986 International*, volume 32, pages 660–663, 1986.

[184] C. Gabriel and J. McVittie. How Plasma Etching Damages Thin Gate Oxides. *Solid State Technology*, 34(6):81, 1992.

[185] T. Wadanabe and Y. Yoshida. Dielectric breakdown of gate insulator due to reactive ion etching. *Solid State Technology*, -:263, 1984.

[186] W.M. Greene, J.B. Kruger, and G. Kooi. Magnetron etching of polysilicon: Electrical damage. *Journal of Vacuum Science Technology B: Microelectronics and Nanometer Structures*, 9(2): 366–369, Mar 1991.

[187] H. Shin, N. Jha, X.-Y. Qian, G. W. Hills, and C. Hu. -. *Solid State Technology*, 36(8):29, 1993.

[188] Jeon-Ho Kim, Kyu-Jeong Choi, and Soon-Gil Yoon. Electrical and reliability characteristics of HfO_2 gate dielectric treated in N_2 and NH_3 plasma atmosphere. *Applied Surface Science*, 242 (34):313 – 317, 2005.

[189] U. Kortshagen, A. Maresca, K. Orlov, and B. Heil. Recent progress in the understanding of electron kinetics in low-pressure inductive plasmas. *Applied Surface Science*, 192(14):244 – 257, 2002.

[190] Mingrong Shen, Zhenggao Dong, Zhaoqiang Gan, Shuibing Ge, and Wenwu Cao. Oxygen-related dielectric relaxation and leakage characteristics of Pt/(Ba,Sr)TiO_3/Pt thin-film capacitors. *Applied Physics Letters*, 80(14):2538–2540, 2002.

[191] Z.B. Zhang, S.C. Song, K. Choi, J.H. Sim, P. Majhi, and B. H Lee. Effects of TiN overlay on ALD TaCN metal gate/high-k MOSFET characteristics. In *Device Research Conference Digest, 2005. DRC '05. 63rd*, volume 1, pages 223–224, June 2005.

[192] R. Bs, S. Gavarini, N. Millard-Pinard, S. Cardinal, A. Perrat-Mabilon, C. Peaucelle, and T. Douillard. Influence of crystallographic orientation on the early stages of oxidation of polycrystalline titanium nitride. *Journal of Nuclear Materials*, 427(13):415 – 417, 2012.

[193] I. leR. Strydom and S. Hofmann. The contribution of characteristic energy losses in the core-level X-ray photoelectron spectroscopy peaks of TiN and (Ti, Al)N studied by electron energy loss spectroscopy and X-ray photoelectron spectroscopy. *Journal of Electron Spectroscopy and Related Phenomena*, 56(2):85 – 103, 1991.

[194] L.I. Avramenko, R.V. Kolesnikova, and N.L. Kuznetsova. Rate constant for the reaction between oxygen atoms and ammonia. *Bulletin of the Academy of Sciences of the USSR, Division of chemical science*, 11(6):918–923, 1962.

[195] Art J. Nelson, Sean Frigo, Derrick Mancini, and Richard Rosenberg. Photoemission characterization of the h2 plasma etched surface of inp. *Journal of Applied Physics*, 70(10):5619–5622, 1991.

[196] J. S. Herman and Jr. Terry, F.L. Plasma passivation of gallium arsenide. *Journal of Vacuum Science Technology A: Vacuum, Surfaces, and Films*, 11(4):1094–1098, Jul 1993.

[197] L. Pinzelli, M. Gros-Jean, Y. Brchet, F. Volpi, A. Bajolet, and J.-C. Giraudin. High-K dielectric deposition in 3D architectures: The case of Ta_2O_5 deposited with metalorganic precursor TBTDET. *Microelectronics Reliability*, 47(45):700 – 703, 2007.

[198] Hugh O. Pierson. 10 - Interstitial Nitrides: Structure and Composition. In Hugh O. Pierson, editor, *Handbook of Refractory Carbides and Nitrides*, pages 163 – 180. William Andrew Publishing, Westwood, NJ, 1996.

[199] M.V. Kuznetsov, Ju.F. Zhuravlev, V.A. Zhilyaev, and V.A. Gubanov. XPS study of the nitrides, oxides and oxynitrides of titanium. *Journal of Electron Spectroscopy and Related Phenomena*, 58(12):1 – 9, 1992.

[200] Naresh C. Saha and Harland G. Tompkins. Titanium nitride oxidation chemistry: An X-Ray Photoelectron Spectroscopy study. *Journal of Applied Physics*, 72(7):3072–3079, 1992.

[201] L. Hultman, G. Hkansson, U. Wahlstrm, J.-E. Sundgren, I. Petrov, F. Adibi, and J.E. Greene. Transmission electron microscopy studies of microstructural evolution, defect structure, and phase transitions in polycrystalline and epitaxial $Ti_{1-x}Al_xN$ and TiN films grown by reactive magnetron sputter deposition. *Thin Solid Films*, 205(2):153 – 164, 1991.

[202] Ding-Fwu Lii, Jow-Lay Huang, and Bor-Yuan Shew. Modeling of reactively sputtered TiAlN films. *Thin Solid Films*, 335(12):122 – 126, 1998.

[203] Shozo Ikeda, Sandra Gilles, and Bernard Chenevier. Electron microscopy analysis of the microstructure of $Ti_{1-x}Al_xN$ alloy thin films prepared using a chemical vapour deposition method. *Thin Solid Films*, 315(12):257 – 262, 1998.

[204] W.M. Haynes. *CRC Handbook of Chemistry and Physics, 93rd Edition*. CRC Handbook of Chemistry and Physics. Taylor & Francis, 2012.

[205] Yuki Terada, Momoko Deura, Yukihiro Shimogaki, Masakazu Sugiyama, and Yoshiaki Nakano. In situ passivation of GaAs surface with aluminum oxide with MOVPE. *Journal of Crystal Growth*, 310(23):4808 – 4812, 2008.

[206] Martin M. Frank, Chiara Marchiori, John Bruley, Jean Fompeyrine, and Vijay Narayanan. Epitaxial strontium oxide layers on silicon for gate-first and gate-last TiN/HfO_2 gate stack scaling. *Microelectronic Engineering*, 88(7):1312 – 1316, 2011.

[207] Seong Keun Kim, Gyu-Jin Choi, and Cheol Seong Hwang. Controlling the Composition of Doped Materials by ALD: A Case Study for Al-Doped TiO_2 Films. *Electrochemical and Solid-State Letters*, 11(7):G27–G29, 2008.

[208] C. A. Wilson, R. K. Grubbs, and S. M. George. Nucleation and Growth during Al_2O_3 Atomic Layer Deposition on Polymers. *Chemistry of Materials*, 17(23):5625–5634, 2005.

[209] M. D. Groner, F. H. Fabreguette, J. W. Elam, and S. M. George. Low-temperature al2o3 atomic layer deposition. *Chemistry of Materials*, 16(4):639–645, 2004.

[210] R. Hofman, R.W.J. Morssinkhof, T. Fransen, J.G.F. Westheim, and P.J. Gellings. Thin alumina and silica films by chemical vapor deposition (CVD). *Materials and Manufacturing Processes*, 8(3):315–329, 1993.

[211] Diana Riihel, Mikko Ritala, Raija Matero, Markku Leskel, Janne Jokinen, and Pekka Haussalo. Low temperature deposition of AIN films by an alternate supply of trimethyl aluminum and ammonia. *Chemical Vapor Deposition*, 2(6):277–283, 1996.

[212] HU Wei-Guo, LIU Xiang-Lin, ZHANG Pan-Feng, ZHAO Feng-Ai, JIAO Chun-Mei, WEI Hong-Yuan, ZHANG Ri-Qing, WU Jie-Jun, CONG Guang-Wei, and PAN Yi. A Comparison between AlN Films Grown by MOCVD Using Dimethylethylamine Alane and Trimethylaluminium as the Aluminium Precursors. *Chinese Physics Letters*, 24(2):516, 2007.

[213] M. E. Bartram, T. A. Michalske, J. W. Rogers, and R. T. Paine. Nucleation and growth of aluminum nitride: self-limiting reactions and the regeneration of active sites using sequential exposures of trimethylaluminum and ammonia on silica at 600 K. *Chemistry of Materials*, 5 (10):1424–1430, 1993.

[214] Velasco A., Mitsuji H., and Kim H.-J. Aluminum Nitride Film Formation Mechanism by Atmospheric Pressure Chemical Vapor Deposition using Trimethylaluminum and Ammonia. In *Proceedings of International Conference on Electrical Engineering*, 2007.

[215] Timothy Campbell, Rajiv K. Kalia, Aiichiro Nakano, Priya Vashishta, Shuji Ogata, and Stephen Rodgers. Dynamics of Oxidation of Aluminum Nanoclusters using Variable Charge Molecular-Dynamics Simulations on Parallel Computers. *Phys. Rev. Lett.*, 82:4866 – 4869, Jun 1999.

[216] B.G. Liptak. *Instrument Engineers' Handbook, Fourth Edition, Volume One: Process Measurement and Analysis*. Instrument Engineers' Handbook. Taylor & Francis, 2003.

Abstract: For the sub-20 nm technological nodes metal conformity requirements are beyond the possibilities of the currently used PVD deposition technique. CVD techniques, more specifically MOCVD and ALD, are identified as the best techniques for metal deposition. For metal-gate application, titanium and tantalum carbo-nitrides alloys are considered as the most promising. In this work, a detailed review of MOCVD and ALD deposition mechanisms and plasma influence on the deposited material is carried out. First, process windows for successful tuning of the metal properties are examined. Plasma impact on the metal and the inherent reaction mechanisms are also highlighted with the help of plasma characterisation. Then great importance is given to the integration of these metals, by careful study of the interactions taking place at the interfaces. Correlations between physico-chemical properties and electrical behaviour of the metal/high-k dielectric stack are introduced thanks to XPS characterisation. Finally, aluminium doping of MOCVD TiN and TaN is considered for n-mos and p-mos gate characteristics achievement. By comparison of the properties and behaviours of Al doped metals deposited by PVD and MOCVD, diffusion mechanisms are proposed to explain the role of Al in the observed changes.

Key words: gate stack, MOCVD, ALD, plasma, Ti(C)N, Ta(C)N, HfO_2, interface, interaction, XPS

Résumé : L'intégration du métal dans les nœuds technologiques sub-20 nm requiert une conformité supérieure à celle permise par la PVD. Les techniques de CVD, plus spécifiquement la MOCVD et l'ALD, ont été identifiées comme les meilleures solutions pour le dépôt de métal. Pour une application de métal de grille, les alliages carbo-nitrurés de titane et tantale sont considérés comme les plus prometteurs. Dans ce travail une revue détaillée des mécanismes de dépôt par MOCVD et ALD, ainsi que sur l'influence du plasma sur les matériaux déposés est réalisée. Dans un premier temps, les fenêtres de procédés possibles pour un ajustement des propriétés des métaux sont inspectées attentivement. L'accent est mis sur l'impact du plasma sur le métal et sur les mécanismes réactionnels inhérents grâce à une caractérisation poussée du plasma. Par la suite, l'intégration de ces métaux est étudiée avec une analyse précise des interactions se déroulant aux interfaces. La corrélation entre les propriétés physico-chimiques et le comportement électrique des empilements métal/diélectrique à forte permittivité est soutenue par une analyse XPS. Finalement, le dopage aluminium de dépôts de TiN et TaN MOCVD est étudié pour l'obtention de grilles n-mos et p-mos. Par comparaison des propriétés et comportements du dopage aluminium de métaux déposés par PVD et MOCVD, des mécanismes de diffusion sont proposés afin d'expliquer le rôle de l'aluminium sur les variations observées.

Mots clefs : empilement de grille, MOCVD, ALD, plasma, Ti(C)N, Ta(C)N, HfO_2, interface, interaction, XPS